Ministry of Science and Higher Education of the Russian Federation
ITMO University

ISSN 2220-8054

NANOSYSTEMS:

PHYSICS, CHEMISTRY, MATHEMATICS

2023, volume 14(6)

Наносистемы: физика, химия, математика

2023, том 14, № 6

N A N O
Ф&Х&М

NANOSYSTEMS:

PHYSICS, CHEMISTRY, MATHEMATICS

Address: ITMO University, Kronverkskiy pr., 49, St. Petersburg 197101, Russia.
Phone: +7(812)607-02-54, **Journal site:** http://nanojournal.ifmo.ru/,
E-mail: nanojournal.ifmo@gmail.com

AIM AND SCOPE

The scope of the journal includes all areas of nano-sciences. Papers devoted to basic problems of physics, chemistry, material science and mathematics inspired by nanosystems investigations are welcomed. Both theoretical and experimental works concerning the properties and behavior of nanosystems, problems of its creation and application, mathematical methods of nanosystem studies are considered.

The journal publishes scientific reviews (up to 30 journal pages), research papers (up to 15 pages) and letters (up to 5 pages). All manuscripts are peer-reviewed. Authors are informed about the referee opinion and the Editorial decision.

CONTENT

NANOSYSTEMS:
PHYSICS, CHEMISTRY, MATHEMATICS

Lobanov I.S. *Nanosystems:*
Phys. Chem. Math., 2023, **14** (6), 613–625.
http://nanojournal.ifmo.ru
DOI 10.17586/2220-8054-2023-14-6-613-625

Original article

Toward nanomagnetic implementation of energy-based machine learning

Igor S. Lobanov[1,a,b]

[1]Faculty of Physics, ITMO University, Lomonosova Str. 9, Saint Petersburg, 191002 Russia

[a]igor.lobanov@metalab.ifmo.ru, [b]lobanov.igor@gmail.com

PACS 75.78.-n, 05.65.+b

ABSTRACT Some approaches to machine learning (ML) such as Boltzmann machines (BM) can be reformulated as energy based models, which are famous for being trained by minimization of free energy. In the standard contrastive divergence (CD) learning the model parameters optimization is driven by competition of relaxation forces appearing in the target system and the model one. It is tempting to implement a physical device having natural relaxation dynamics matching minimization of the loss function of the ML model. In the article, we propose a general approach for the design of such devices. We systematically reduce the BM, the restricted BM and BM for classification problems to energy based models. For each model we describe a device capable of learning model parameters by relaxation. We compare simulated dynamics of the models using CD, Monte-Carlo method and Langevin dynamics. Benchmarks of the proposed devices on generation and classification of hand-written digits from MNIST dataset are provided.

KEYWORDS Machine learning, Boltzmann machine, energy based model, dissipative training.

ACKNOWLEDGEMENTS The work is supported by Russian Science Foundation grant 22-22-00565:
https://rscf.ru/en/project/22-22-00565/

FOR CITATION Lobanov I.S. Toward nanomagnetic implementation of energy-based machine learning. *Nanosystems: Phys. Chem. Math.*, 2023, **14** (6), 613–625.

1. Introduction

The recent machine learning (ML) development revolutionized the field of artificial intelligence and unleashed rapid progress in natural language processing, robot motion planning, art generation and so on. Part of the rapid development can be attributed to the appearance of new ML models such as transformers, but the appearance of human-like behavior is connected with the increase of capacity of the models [1]. At the moment, training of large models is an expensive task requiring 10^5 hours of A100 GPU and costs millions of dollars. To obtain even more complex models further increase of performance and memory size of hardware simulating the models is required. The state of the art hardware originates from computer graphics accelerators and is not optimal for computation of essentially analogue artificial neural networks (ANN) and similar models. This leads in particular to the huge energy consumption of electric computers based ML compared to biological neural networks.

Various new approaches for implementation of ML using new physical principles are proposed, e.g. photoelectronic circuits speed up image processing thousands times faster than Tesla A100 [2]. One of the approaches lies in designing ML models on top of magnetic devices [3, 4]. The approach extends the boundaries of spintronics, which is a likely replacement of modern electronics. Some ML models are especially appealing for implementation as magnetic devices since they originated from physical models. One approach uses topological solitons to transmit impulses between artificial neurons [5]. Probably before the emergence of such neuromorphic devices, we will see the appearance of magnetic racetrack memory working on the same principle [6, 7]. The ML model, which is most close to a physical system is the Boltzmann machine (BM) [8], that can be considered the stochastic Ising machine, and therefore can be physically implemented as interconnected spin islands [9]. BM has a variety of uses including associative memory, solving combinatorial optimization problems, generation of images, features extraction and so on.

BM consists of spins, which interact with each other and the environment, resulting in Boltzmann distribution of the spins energy. The BM is trained by variation of the interaction constants to match the probability distribution (PD) to a target one. In the simulation, sequence of states of BM are computed by Monte-Carlo methods and its weights are optimized using contrastive divergence (CD) method. The CD method implements a variant of Hebbian rule, which makes training of BM similar to the learning of biological organisms. Earlier attempts to train BM showed that it is not practical for any hard problems, but BM with restricted connections (RBM) can be efficiently simulated and are in use now especially in the form of stacked BMs.

Besides numerical simulation of BM as a variant of ANN, BM has been implemented as a number of physical devices, including the one based on tunnel magnetic junctions [10]. The Ising model also forms a basis for D-Wave quantum computer, which however uses quantum annealing instead of stochastic dynamics for computations [11]. The vast majority of BM implementations do not support training in hardware. Instead they rely on traditional computers to

solve the optimization problem. We will pursue the goal to develop a self-training device capable of adapting to continuous feed of training data. An especially simple device can be obtained, if training can be reformulated as a naturally occurring physical process.

BM belongs to the class of so-called energy-based models (EBM) [12]. A useful feature of the models is that minimization of the loss function is equivalent to energy minimization [13, 14]. The observation makes it possible to apply a physically inspired method to ML, e.g. simulation of Langevin dynamics achieving better results than other likelihood models [15].

Our initiative is to implement BM loss minimization as a relaxation in a magnetic device. In the article [16], we proposed an extended BM machine whose weights are included to degrees of freedom (DoF). We showed that the energy minimization of the system leads to memorization of the trained samples. This kind of device can be used as an associative memory, but it is not suitable for answering questions with a non-deterministic answer. In the present article we generalize the approach to a stochastic model capable of generation of arbitrary probability distributions. Similar idea was carried out in [17] that made it possible to implement plasticity of the energy landscape of a few atom BM demonstrating self-learning to some extent.

In the article, we systematically derive EBMs for BM with only visible neurons (Section 2), BM containing hidden neurons (Section 3) and BM with loss function specialized for classification problems (Section 4). For all the variants of BM, we propose an approach for physical implementation of a device, whose relaxation matches minimization of the corresponding loss functions. We also provide examples of application of the approach, studying a simple model of tuning variation of normal distribution in Section 2.1 and benchmarking hand-written digits generation (Section 3.2) and classification (Section 4.1).

2. Dissipative training

Consider an arbitrary physical system with energy functional $E[x]$ depending on the system state x. Suppose the system is in thermal equilibrium with a thermal reservoir, hence the state of the system is random and is described by Boltzmann probability distribution:

$$p(x) = Z^{-1} Z(x), \quad Z(x) = e^{-\beta E[x]},$$

where $\beta = 1/k_B T$ is the inverse temperature, and Z is the partition function:

$$Z = \sum_x Z(x) \quad \Rightarrow \quad \sum_x p(x) = 1.$$

We use notation for summation over a discrete state space for simplicity of presentation, however, the theory is valid for arbitrary measurable state space and the Lebesgue–Stieltjes integral can be substituted for sums, and an appropriate probability measure for $Z(x)$. Helmholtz free energy is defined by

$$F = -\frac{1}{\beta} \log Z \quad \Rightarrow \quad p(x) = e^{-\beta(E[x]-F)}. \tag{1}$$

The Shannon entropy is defined by

$$H(p) = \mathbb{E}_{x\sim p}[-\log p(x)] = -\sum_x p(x) \log p(x).$$

It coincides with the Gibbs entropy up to the Boltzmann constant factor: $S = k_B H$. Due to (1), the entropy is related to the free energy and mean value of energy with respect to the distribution p:

$$H(p) = \beta \mathbb{E}_p[E - F] = \beta(\mathbb{E}_p[E] - F).$$

The mean energy can be computed in terms of the partition function:

$$\frac{\partial(\beta F)}{\partial \beta} = -\frac{\partial \log Z}{\partial \beta} = -Z^{-1} \frac{\partial Z}{\partial \beta} = Z^{-1} \sum_x Z(x) E[x] = \mathbb{E}_p[E]. \tag{2}$$

In machine learning, the system can be used as a generator of samples with PD p. In practice, we want the distribution to match a given distribution $\tilde{p}$. To compare the model distribution p with a target one $\tilde{p}$, the Kullback–Leibler (KL) divergence can be used:

$$D_{KL}(\tilde{p} \parallel p) = \mathbb{E}_{x\sim\tilde{p}} \left[\log \frac{\tilde{p}(x)}{p(x)} \right] = \sum_x \tilde{p}(x) \log \frac{\tilde{p}(x)}{p(x)} = H(\tilde{p}, p) - H(\tilde{p}),$$

where $H(\tilde{p})$ is the entropy for the distribution $\tilde{p}$ and the cross-entropy is defined by:

$$H(\tilde{p}, p) = \mathbb{E}_{x\sim\tilde{p}}[-\log p(x)] = -\sum_x \tilde{p}(x) \log p(x).$$

The KL divergence is not-negative and is equal to zero if and only if the distributions p and $\tilde{p}$ coincide. Although D_{KL} is not a metric, since it is not symmetric, the two mentioned properties make the KL divergence a good choice for loss function for system parameters optimization for the system to learn the target distribution $\tilde{p}$. The learning is possible, if

the system depends on parameters θ then we can minimize loss function with respect to the parameters. The parameters will be discussed below, for the moment, we can work in very general settings.

Since the model PD p is generated by the considered system, the cross-entropy can be expressed in terms of the mean and free energy using (1):

$$H(\tilde{p}, p) = \beta \mathbb{E}_{\tilde{p}}[E - F] = \beta(\mathbb{E}_{\tilde{p}}[E] - F).$$

The expression for the cross-entropy differs from the entropy of p only by the distribution used for averaging the energy.

Suppose that the distribution $\tilde{p}$ is generated by an analogous system, but with a different expression for the energy. We will put tilde above all values related to the system with the PD $\tilde{p}$ over the states, in particular,

$$\tilde{p}(x) = \exp\Big(-\beta(\tilde{E}(x) - \tilde{F})\Big).$$

The KL divergence simplifies to:

$$D_{KL}(\tilde{p} \parallel p) = \overbrace{\beta(\mathbb{E}_{\tilde{p}}[E] - F)}^{H(\tilde{p},p)} - \overbrace{\beta(\mathbb{E}_{\tilde{p}}[\tilde{E}] - \tilde{F})}^{H(\tilde{p})} = \beta \mathbb{E}_{\tilde{p}}[E - \tilde{E}] + \beta(\tilde{F} - F).$$

Therefore, the learning of the distribution $\tilde{p}$ is equivalent to equalization of the free energies for $\tilde{p}$ and p.

Let both energies E and $\tilde{E}$ be two implementations of the same model for different parameters:

$$E(x) = E(x; \theta), \quad \tilde{E}(x) = E(x; \tilde{\theta}).$$

Then the learning is done by optimizing the loss with respect to θ. The simplest optimization procedure is the gradient descend, when the parameters are updated according to the rule:

$$\theta \mapsto \theta - \nu \frac{\partial D_{KL}}{\partial \theta},$$

where ν defines learning rate. Since the values with tilde do not depend on θ, the KL divergence simplifies:

$$\frac{\partial D_{KL}}{\partial \theta} = \beta \frac{\partial}{\partial \theta}(\mathbb{E}_{\tilde{p}}[E] - F).$$

In virtue of independence of $\tilde{p}$ on θ, the differentiation and averaging can be swapped. The free energy derivative can be computed as follows:

$$\frac{\partial F}{\partial \theta} = -\frac{1}{\beta Z}\frac{\partial Z}{\partial \theta} = -\frac{1}{\beta Z}\sum_x \frac{\partial Z(x)}{\partial \theta} = \frac{1}{Z}\sum_x Z(x)\frac{\partial E(x)}{\partial \theta} = \sum_x p(x)\frac{\partial E(x)}{\partial \theta} = \mathbb{E}_p\left[\frac{\partial E}{\partial \theta}\right]. \tag{3}$$

Finally, the parameter update rule is driven by the velocity f:

$$\theta \mapsto \theta + (\nu\beta) f, \quad f = \mathbb{E}_{\tilde{p}}\left[\frac{\partial E}{\partial \theta}\right] - \mathbb{E}_p\left[\frac{\partial E}{\partial \theta}\right]. \tag{4}$$

It is worth noting that the parameter $\tilde{\theta}$ does not present in the final expression. Moreover, the origin of $\tilde{p}$ does not matter below, so we will not restrict $\tilde{p}$ in any way below.

The key observation of the article is that the update rule coincides with the relaxation dynamics for the variable θ. Indeed, suppose θ is a DoF for the considered system, but we assume θ to be a slow variable, so that at each moment of time, the distribution of x is given by the p for the fixed θ. The relaxation dynamics of θ is described by:

$$\dot{\theta} = -\alpha \frac{\partial E}{\partial \theta},$$

where α is the damping parameter. Averaging over the ensemble, we obtain the second addendum in (4). Moreover, assuming ergodicity, the addendum can be approximated by the time average:

$$\mathbb{E}_{x\sim p}\left[\frac{\partial E(x;\theta)}{\partial \theta}\right] = \left\langle \frac{\partial E}{\partial \theta} \right\rangle_t.$$

The first addendum in (4) is more complex, since the distribution $\tilde{p}$ is external for the system. To take $\tilde{p}$ into account, we extend our system, including new degrees of freedom $\tilde{x}$. The vector $\tilde{x}$ belongs to the same state space as x, but we assume $\tilde{x}$ be externally driven, so that its distribution at every moment of time is given by $\tilde{p}$ and they are uncorrelated at different moments of time. Then the first addendum can be obtained as time averaging of:

$$\mathbb{E}_{\tilde{x}\sim\tilde{p}}\left[\frac{\partial E(\tilde{x};\theta)}{\partial \theta}\right] = \left\langle \frac{\partial E(\tilde{x};\theta)}{\partial \theta} \right\rangle_t.$$

We define total energy of the new system according to the requirements:

(1) Energy $E[\tilde{x}]$ is opposite to the energy $E[x]$.
(2) $\tilde{x}$ and x interact with the same parameters state θ.

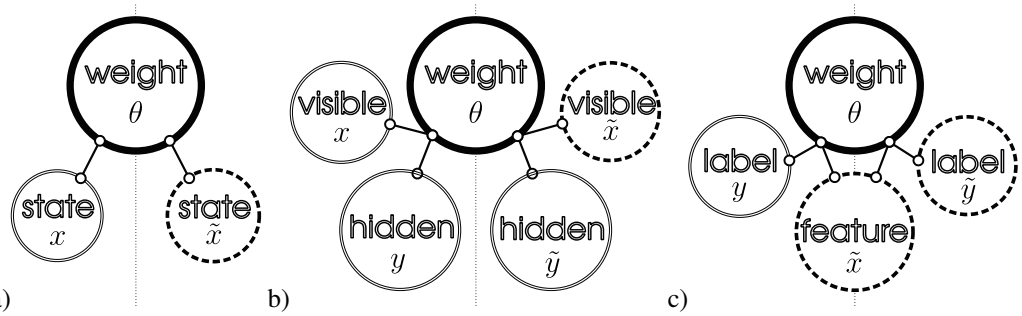

FIG. 1. Proposed designs of self-training BM. Circles represent DoF: bold line marks slow variable/weights, double-line marks fast variables, punctured boundary marks externally driven DoF. The system is split to two lobes: the right one is a copy of the left one with externally driven DoFs substituted for some fast variables. Segments between circles indicate interactions. (a) BM learning PD demonstrated on $\tilde{x}$ and generating the PD on x. (b) BM contains hidden neurons y and $\tilde{y}$; training data is demonstrated on $\tilde{x}$, the result is read from x. (c) BM for classification problem; features $\tilde{x}$ and labels $\tilde{y}$ from the training set are driven by external forces; predicted PD over labels is read from y.

Then the total energy is defined by:

$$E^T = E(x;\theta) - E(\tilde{x};\theta).$$

Summing up all properties above, we conclude that f can be obtained by averaging of the relaxation force:

$$f = \left\langle \frac{\partial E^T}{\partial \theta} \right\rangle_t.$$

We conclude that the relaxation dynamics of the extended system is a continuous version of the stochastic gradient descent for the minimization of the KL divergence. Since the approach is quite general, it opens many opportunities for implementation of self-learning devices. In the following sections, we consider several examples.

2.1. Standard deviation learning

Consider simple case of a single continuous random variable x having normal distribution with mean m and standard deviation $\sigma = \theta^{-\frac{1}{2}}$:

$$p(x) = Z^{-1} \exp\left(-\frac{\theta(x-m)^2}{2}\right).$$

The PD can be considered Boltzmann distribution for the energy

$$E = \frac{\theta(x-m)^2}{2},$$

and the constant temperature $\beta = 1$. The partition function in the case is well known:

$$Z = \sqrt{2\pi/\theta\beta}.$$

The optimization of the mean m is relatively simple and was already solved in [16]. Here we let $m = 0$ and focus on optimization of θ. The free energy of the model system:

$$F = \frac{1}{2\beta}\left(\log\theta + \log\beta - \log(2\pi)\right).$$

According to (2) the mean energy is:

$$\mathbb{E}_p[E] = \frac{\partial(\beta F)}{\partial\beta} = \frac{1}{2\beta}. \tag{5}$$

Suppose target distribution $\tilde{p}$ is also normal with standard deviation $\tilde{\sigma} = \tilde{\theta}^{-\frac{1}{2}}$. The expectation value of E with respect to $\tilde{p}$ is obtained by rescaling:

$$\mathbb{E}_{\tilde{p}}[E] = \left\langle \frac{\theta}{\tilde{\theta}}\tilde{E} \right\rangle_{\tilde{p}} = \frac{1}{2\beta}\frac{\theta}{\tilde{\theta}}.$$

KL divergence between the distributions is given by:

$$D_{KL}(\tilde{p} \parallel p) = \beta\mathbb{E}_{x\sim\tilde{p}}[E(x) - \tilde{E}(x)] + \beta(\tilde{F} - F) = \frac{1}{2}\left(\frac{\theta}{\tilde{\theta}} - 1\right) + \frac{1}{2}\left(\log\tilde{\theta} - \log\theta\right).$$

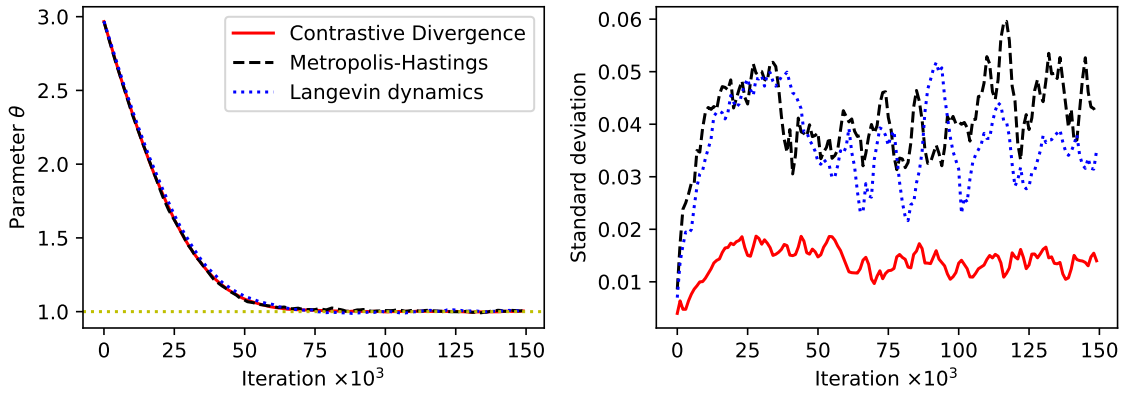

FIG. 2. Convergence of estimation of standard deviation parameter θ using EBM: CD learning (solid line), free energy minimization using Metropolis–Hastings algorithm (dashed line) and Langevin dynamics (dotted line). Target value of the parameter is 1, initial value is 3. Mean value of the parameter estimate (left panel) and standard deviation of (right panel) obtained by averaging over 20 runs and 1000 consecutive samples.

The divergence has only one minimum at $\theta = \tilde{\theta}$ as expected. The derivative of the KL divergence will be used below to make optimization algorithms:

$$\frac{\partial D_{KL}}{\partial \theta} = \frac{1}{2}\left(\frac{1}{\tilde{\theta}} - \frac{1}{\theta}\right). \tag{6}$$

2.2. Dissipative learning

Above we considered the parameter θ to be fixed. Here we suppose that θ a slow DoF of the system. Then relaxation dynamics will push θ in the direction opposite to

$$\frac{\partial E}{\partial \theta} = -\frac{x^2}{2}.$$

Assuming x is a fast variable, the derivative can averaged over x:

$$\mathbb{E}_{x\sim p}\left[\frac{\partial E(x;\theta)}{\partial \theta}\right] = -\sqrt{\frac{\theta}{2\pi}}\int_{-\infty}^{\infty}\frac{x^2}{2}\exp\left(-\frac{\theta x^2}{2}\right)\mathrm{d}x = -\frac{1}{2\theta}.$$

It is worth noting that the derivative of the mean energy with respect to θ is zero according to (5), that is the expectation value and the differentiation do not commute. It turns out that the dissipation generates the same dynamics as the second addendum in (6). The first addendum here gives a reference point and is essential to obtain the correct stationary state. The first addendum can also be interpreted as mean energy, but with respect to the target distribution $\tilde{p}$:

$$\mathbb{E}_{\tilde{x}\sim\tilde{p}}\left[\frac{\partial E(\tilde{x};\theta)}{\partial \theta}\right] = -\frac{1}{2\tilde{\theta}}.$$

Then optimization direction will coincide with mean relaxation force if we expand the system with the second part depending on $\tilde{x}$ and assuming the second part has opposite energy to the first one:

$$\frac{\partial D_{KL}}{\partial \theta} = \mathbb{E}_{x\sim p,\tilde{x}\sim\tilde{p}}\left[\frac{\partial E^T}{\partial \theta}\right], \quad E^T(x,\tilde{x};\theta) = E(x;\theta) - E(\tilde{x};\theta).$$

In the real system, the expectation values can be obtained either by averaging over ensembles or over time. The distribution $\tilde{p}$ can be enforced to the variable $\tilde{x}$ by an external force demonstrating the training set to the device. Obtaining opposite signs of energy for two parts of the system for the same value of the parameter θ is the most challenging task in designing real devices. Consider one example of such an implementation. Energy of liquid crystal interaction with an external electric field has the following form [18]:

$$E = -\frac{\Delta\epsilon(\mathbf{n}\cdot\mathbf{E})^2}{8\pi},$$

where $\mathbf{E}$ is electric field, $\mathbf{n}$ is the director vector, and $\Delta\epsilon$ is anisotropy of permittivity. Let the electric field have fixed direction $\mathbf{z}$ and be proportional to the parameter θ. Let x be projection of the director $\mathbf{n}$ to $\mathbf{z}$. Then the energy coincides with the considered above up to a constant. Sign of the constant is determined by $\Delta\epsilon$ which can be both positive and negative depending on the exact choice of the liquid crystal. It means that by choosing $\Delta\epsilon$ of opposite signs for two lobes x and $\tilde{x}$ we will obtain opposite energies for the same value of the external field θ.

2.3. Contrastive divergence training

Contrastive divergence (CD) is probably the most popular method used for training EBMs. The method belongs to the family of gradient descent methods sharing the update rule:

$$\theta \mapsto \theta + \eta f, \quad f \approx -\frac{\partial D_{KL}}{\partial \theta},$$

where $\eta > 0$ is the learning rate constant and f is an approximation to the steepest descent direction on the loss surface. The optimization algorithm here is a variant of stochastic gradient descent:

(1) Get a sample $\tilde{x}$ from the training set.
(2) Sample x from the distribution p given for the current θ.
(3) Compute dissipation force $f = \partial E(\tilde{x};\theta)/\partial\theta - \partial E(x;\theta)/\partial\theta$.
(4) Update weights $\theta \mapsto \theta + \eta f$.
(5) Repeat.

To estimate the force f more accurately, one can sample values in batches and then average the force over all batches. Nevertheless, if the learning rate η is sufficiently small, the averaging of the generated force in time gives a good enough estimate of the expectation value to obtain convergence.

2.4. Metropolis–Hastings algorithm

For complex systems sampling values x from the PD p is generally difficult since the partition function Z is not known. It is common in this case to sample values using Metropolis–Hastings (MH) algorithm. In this case, values of x are not independent between steps, but rather form a Markov chain. To define the chain we need an auxiliary probability density $g(y|x)$ called proposal density, which gives us a new candidate y given a previous value x. We will assume g symmetric: $g(x|y) = g(y|x)$. The generation of x according to MH algorithm is done as follows:

(1) Sample y according to the distribution $g(y|x)$ for the given previous value of x.
(2) Calculate the acceptance rate $\alpha = Z(y;\theta)/Z(x;\theta)$.
(3) Generate a uniform random number $u \in [0, 1]$.
(4) If $u \leq \alpha$, accept y as a new value of x.
(5) Otherwise let x preserve its value.

The optimization algorithm with MH sampling is the same as in the previous section, but the previous value of x is used to generate its new value. The emerging correlations between adjacent samples can increase spread of the optimization direction estimates f, which will require a decrease of the training rate constant to maintain convergence.

For the benchmark below we took proposal density $g(y|x)$ to be normal with the mean value y and standard deviation 0.5.

2.5. Langevin dynamics

Dynamics arising from the Monte-Carlo method described in the previous section is suitable to obtain correct estimates of expectation values, however it does not correspond to the real dynamics. In many cases, the dynamics is described by a variant Langevin equation, such as the stochastic Landau–Lifschitz–Gilbert (LLG) equation for magnetic systems. In the discretized form the Langevin equation for one variable can be written as follows:

$$x^{t+1} = x^t - \eta' \frac{\partial E(x^t;\theta^t)}{\partial x} + W^t,$$

where W^t has a normal distribution with zero mean and standard deviation $\sqrt{2/\eta'}$ and W^t for different t are independent. The distribution of x^t is the same Boltzmann distribution as above for the inverse temperature β. Dynamics of the slow variable θ are described by relaxation in the same way as above:

$$\theta^{t+1} = \theta^t - \eta f^t, \quad f^t = \frac{\partial E(\tilde{x}^t;\theta^t)}{\partial\theta} - \frac{\partial E(x^t;\theta^t)}{\partial\theta}.$$

For the benchmark below we generated training samples $\tilde{x}$ by Langevin equation with parameter θ set to the target value $\tilde{\theta}$. Time scale for the fast variable was defined by the ratio: $\eta'/\eta = 500$.

2.6. Benchmark

We compared performance of CD, dissipative learning with MH sampling and Langevin dynamics on the learning parameter θ of the normal distribution introduced in Section 2.1. The initial value of parameter was set to 3, while the target value equals 1. We set learning rate to $2 \cdot 10^{-4}$ and made $1.6 \cdot 10^5$ steps by all algorithm repeating the procedure 20 times. For each of the algorithms we averaged estimates of the parameter θ over 1000 consecutive samples, and also estimated standard deviation of the estimates on the same intervals. The results are presented in Fig. 2.2. All the methods perform equally well on average having the same convergence rate. Correlations between adjacent samples in Monte-Carlo based method and in Langevin dynamics produce $3 - 4$ times large variation of the estimate as expected. We can conclude that real-world physical dynamics is as suitable for training the ML model as a generally accepted CD method.

3. Hidden neurons

In Section 2, we described a general approach for turning arbitrary dissipative systems into a self-training machine. The class of generated PDs is defined by energy functional E. Although we have not imposed any restrictions on the energy (except of being bounded from below) and arbitrary PD can be generated under appropriate choice of the energy, in practice we have rather restricted choice of energies available for physical implementations. Standard BM is based on the Ising model, having the quadratic energy functional:

$$E[x] = \frac{1}{2}\sum_{jk} w_{jk}x_j x_k + \sum_j b_j x_j, \tag{7}$$

with x_j representing the state of a spin j (playing the role of a neuron) taking values $x_j = \pm 1$. The parameters $\theta = (w, b)$ consist of connection strengths w_{jk} between neurons j and k and biases b_j for every neuron j. The functional E allows to tune mean values and covariance of components of x, but it is impossible to obtain a nontrivial joint distributions of three and more neurons. More complex inter-dependencies between neurons can be obtained using the same quadratic energy functional, if we include new hidden DoF.

Suppose the variables x describe visible neurons, whose state is described by the training set, and which are output of the model. Introduce new DoF denoted y playing the role of hidden variables. Now the energy functional depends on x, y and θ. We do not impose any constraints on the energy functional, but for clarity of presentation we recall an example of such functional used in restricted BM (RBM):

$$E[x] = \frac{1}{2}\sum_{jk} w_{jk}x_j y_k + \sum_j a_j x_j + \sum_k b_k y_k, \tag{8}$$

where a and b are biases for visible and hidden neurons, respectively, and the interaction is nonzero only between units of different classes (visible, hidden, weight). The energy functional for RBM coincides with (7) with the vector x extended by y with additional constraints forbidding interaction between neurons of the same type.

As in Section 2, we assume θ to be slow variables, then for given θ we have joint PD

$$p(x, y; \theta) = Z^{-1}Z(x, y), \quad Z(x, y) = \exp(-\beta E[x, y; \theta]), \quad Z = \sum_{x,y} Z(x, y). \tag{9}$$

The visible neurons state is described by the marginal PD:

$$p(x) = \sum_y p(x, y) = Z^{-1}Z(x), \quad Z(x) = \sum_y Z(x, y). \tag{10}$$

For example, the marginal distribution for RBM is notably easy to compute, since for a fixed x the components of y are independent. Easy algebra leads us to the result:

$$p(x|y) = Z^{-1}\prod_j e^{-\beta a_j x_j}\prod_k \left(\sum_j e^{-\beta\Delta_j} + e^{\beta\Delta_j}\right)^{-1}, \quad \Delta_j = \sum_k w_{jk}y_k. \tag{11}$$

Introducing sufficiently many hidden neurons, an arbitrary PD $p(x)$ can be attained.

The training problem is to find parameters θ such that the marginal distribution $p(x; \theta)$ minimizes distinction with a target PD $\tilde{p}(x)$. The loss function can be defined as cross-entropy, which as we have seen above gives the same minimum as KL divergence, since entropy of $\tilde{p}$ does not depend on θ and does not affect the result:

$$H(\tilde{p}; p) = \mathbb{E}_{x\sim\tilde{p}}[-\log p(x)] = -\sum_x \tilde{p}(x)\log p(x).$$

The only change here compared to Section 2 is that $p(x)$ is a marginal distribution. In virtue of (10),

$$H(\tilde{p}; p) = F - \sum_x \tilde{p}(x)\log Z(x), \quad F = \sum_x \tilde{p}(x)\log Z, \tag{12}$$

where F is the Helmholtz free energy.

Now we compute the gradient of the loss with respect to parameters, which is used for the loss minimization. The derivative of the free energy is the same as in Equation (3):

$$\frac{\partial F}{\partial\theta} = -\beta\sum_{x,y} p(x, y)\frac{\partial E(x, y)}{\partial\theta} = -\beta\mathbb{E}_{x,y\sim p}\left[\frac{\partial E(x, y)}{\partial\theta}\right].$$

For a fixed x the second addendum in (12) is a conditional expectation of the relaxation force:

$$\frac{\partial}{\partial\theta}\log Z(x) = Z^{-1}\sum_y \frac{\partial Z(x, y)}{\partial\theta} = -\beta\sum_y p(y|x)\frac{\partial E(x, y)}{\partial\theta} = -\beta\mathbb{E}_{x,y\sim p}\left[\frac{\partial E(x, y)}{\partial\theta}\middle| x\right], \tag{13}$$

where the conditional probability is given by:

$$p(y|x) = \frac{p(x,y)}{p(x)} = \frac{Z(x,y)}{Z(x)}.$$

Taking mean over the target PD we obtain the derivative over the second addendum:

$$\frac{\partial}{\partial\theta}\sum_x \tilde{p}(x)\log Z(x) = -\beta\sum_{x,y}\tilde{p}(x)p(y|x)\frac{\partial E(x,y)}{\partial\theta} = -\beta\mathbb{E}_{x\sim\tilde{p}}\left[\mathbb{E}_{y\sim p}\left[\frac{\partial E(x,y)}{\partial\theta}\middle|x\right]\right].$$

Finally, the loss derivative is mean difference between energy gradients averaged on the target and model distributions:

$$\frac{\partial L}{\partial\theta} = \beta\left(\mathbb{E}_{x\sim\tilde{p}}\left[\mathbb{E}_{y\sim p}\left[\frac{\partial E(x,y)}{\partial\theta}\middle|x\right]\right] - \mathbb{E}_{x,y\sim p}\left[\frac{\partial E(x,y)}{\partial\theta}\right]\right). \tag{14}$$

The averaging over hidden variables y both times happens with respect to the model distribution p, hence we obtain the same result as in Section 2, but all values should be considered as values averaged over hidden DoF.

The system whose relaxation coincides with minimization of the loss can be constructed applying the same principles as in Section 2.

(1) The average over the ensemble is changed to the time average.
(2) Every addendum in (14) is generated by one of two copies of the system, which share weights θ and exchanges, but has its own examples of x and y. The energies of the copies are chosen opposite.
(3) The variables $\tilde{x}$ are controlled by external forces, which recreate distribution $\tilde{p}$.
(4) The dynamics of the weights θ are dominated by relaxation. The weights must be slow variables, x and y are fast variables.

A schematic of the proposed device with hidden variables is shown in Fig. 2.b. The exact dynamics of the device is not important as soon as it guaranties the condition (4). For example, Monte-Carlo simulation results in the contrastive divergence method widely used for training RBM in ML. Langevin dynamics can be a more adequate method for real physical system simulation.

3.1. Monte-Carlo simulation

Correct distribution of variables x, y and $\tilde{y}$ for a fixed θ can be generated using Metropolis–Hastings algorithm. The approach does not take into account exact dynamics, but generates correct mean values of energy and energy gradients, which are the only values affecting the dynamics of slow variables θ. This method allows us to cover wide range of physical implementations of BM including magnetic in the approximation of the Ising model.

Here we focus on RBM, which energy is defined by (8). By definition visible and hidden neurons in RBM do not interact, therefore for a fixed hidden neurons state y the individual components of the visible neurons state x are independent and vice versa. In particular, conditional distribution of x given y is given by (11). This allows us to efficiently generate in the parallel manner samples of y given x and x given y. For example, the following algorithm is used to generate samples of x.

(1) Compute difference of energies of states that differs by single bit j:

$$\Delta_j = 2\sum_{jk} E_{jk}y_k + 2a_j.$$

(2) Compute conditional probability of $x_j = 1$ given y:

$$p_j = p(x_j = 1|y) = \frac{1}{1+e^{\Delta_j}}.$$

(3) Generate vector ξ of uniformly distributed values $\xi_j \in [0,1]$.
(4) Set component j of the generated vector x_j to 1 if $\xi_j <= p_j$ and to -1 otherwise.

The simulation is done step by step. We put the upper index t over all values for the time step t. The initial value of x^0 is arbitrary. On each iteration all the values are updated as follows:

(1) $\tilde{x}^{t+1}$ is sampled from the training set.
(2) Random $\tilde{y}^{t+1}$ is generated by the above algorithm for the given $\tilde{x}^{t+1}$ and θ^t.
(3) Random y^t is generated by the algorithm above for the given x^t and θ^t.
(4) Random x^{t+1} is generated by the algorithm above for given y^t and θ^t.
(5) The relaxation force is computed:

$$f^{t+1} = \frac{\partial}{\partial\theta}E(x^{t+1},y^{t+1};\theta) - \frac{\partial}{\partial\theta}E(\tilde{x}^{t+1},\tilde{y}^{t+1};\theta).$$

(6) Update the parameters:

$$\theta^{t+1} = \theta^t + \eta f^{t+1} + W^t.$$

(7) Repeat.

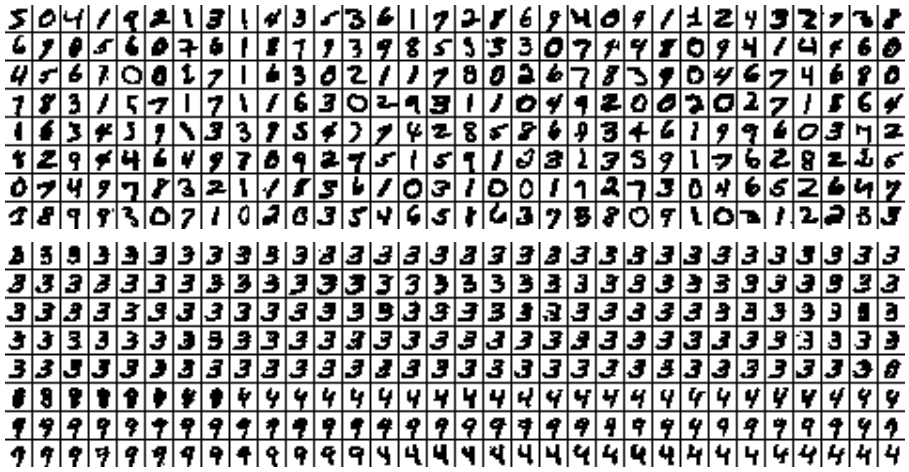

FIG. 3. (Upper panel) First 256 images of MNIST dataset scaled to 14×14 and converted to black and white. (Lower panel) State of visible neurons of the RBM after 800 epoch of training shown on every 16-th simulation step. Images are listed from left to right and from top to down.

The parameter update on step (6) is done simulating Langevin dynamics for slow variables θ. The "learning rate" parameter η should be small enough to ensure convergence, which in physical terms means that dynamics of θ must be much slower than of fast variables x and y. The addendum W is a random noise, whose amplitude is proportional to the temperature T. Since the smallest value of the error is reached at minimum of the energy, the temperature should not be large. On the other hand, small variations of θ due to the noise allows one to avoid overfitting and can be beneficial.

It is worth noting that the presented algorithm is called contrastive divergence in ML, if no noise is appended. The algorithm with the noise was earlier proposed in [15], where it was shown that it demonstrates better convergence than the CD. In most implementations of the CD the value x^{t+1} is sampled using conditional distribution $p(x|\tilde{y}^{t+1})$. In our approach, dynamics of $\tilde{x}$ and x are not directly connected, which allows us to estimate positive and negative parts of the loss gradient independently in two copies of the system.

The most difficult part of the physical implementation of the training algorithm is to obtain both positive and negative parts of the gradient as relaxation forces. In Section 2, the problem is almost non-existent, since the state of $\tilde{x}$ is externally driven and does not depend on θ, therefore, to obtain negative gradient, one can change ferromagnetic exchange to antiferromagnetic leading to negation of the energy. The trick however does not work, if there are hidden variables. Indeed, change of the exchanges energy landscape and therefore, PD of the hidden variables, which invalidates mean values of the gradient.

Pure mathematically the positive and negative terms can be considered an adversarial learning procedure, where discriminator time-flow is reversed [19]. Effective reversed time can appear in quantum mechanics [20], but it is hard to use in practice. Fortunately, the same negative gradient can be achieved by formal change of sign of β. Negative temperatures of spin systems were reported in a number of works [21–23]. Although the statistical physics for negative temperatures is studied for a long time [24, 25], a practical realization of local negative temperatures is extremely challenging.

Another possible strategy for generation of negative gradients is to shield hidden variables from the thermostat allowing its interaction only with weights and visible neurons. In the case dynamics of the hidden state y is determined exclusively by x and θ. Therefore the change of sign of all interaction constants negates energy and its gradient, but does not affect PD of y. Following this approach the self-trained system should contain two copies of x and y, with ferromagnetic exchange in one copy and antiferromagnetic in another, both interacting with the same weights θ.

One more strategy is based on reformulation of the optimization problem, abandoning the dynamics defined by (14). Considering the loss minimization method as an iterative procedure with the fixed point $p = \tilde{p}$, other energy functionals can be proposed, whose relaxation procedure has the same property. For example, let the hidden variables be shared by two parts of the system $y = \tilde{y}$. Define the total energy

$$E = -(x - \tilde{x}) \cdot wy - (x - \tilde{x}) \cdot a.$$

Here $\tilde{x}$ is defined by external impulses and x and y are subjected to Langevin dynamics. If the distributions of x and $\tilde{x}$ coincide then the system is in thermal equilibrium. The relaxation with respect to w and a can be used to adjust the PD of x, but the error measure is no longer KL divergence, and in practice leads to much worse results than the CD method. A practical choice for implementation of the negative gradient in presence of hidden variables is still an open question.

3.2. MNIST digits generation

We benchmarked performance of the proposed approach for implementation of RBM on generation of images of hand-written digits trained in MNIST dataset. MNIST dataset [26] is split to the training set of $60\,000$ and the test set of $10\,000$ gray scale images of ten different digits together with labels, which digit the image represents. We downsampled the images to size 14×14 and converted to black and white, considering the pixel black, if its luminosity is smaller than 90% of the maximum. All $60\,000$ images were used for the training, setting a new image to $\tilde{x}$ on each iteration. The beginning of the dataset is shown in the upper panel in Fig. 3.2.

The images were flattened to vectors of 196 visible neurons states, and 1000 more hidden neurons were introduced. Looping over all $60\,000$ images is considered one epoch, the training took 800 epoch in total. The training step was set $\eta = 10^{-4}$. To track convergence we calculated mean $-\log Z(x;\theta)$ over samples x taken from the test set for θ obtained on the corresponding epoch. This value is an estimation of $\mathbb{E}_{x\sim\tilde{p}}[-\log p(x;\theta)]$, which is different from the cross entropy by the absence of the free energy term $\log Z$. The applied training method does not compute free energy directly, which makes it fast, but this also prevents us from accurate estimation of the loss function. The obtained metrics are not reliable, if a lot of noise is introduced in the parameters θ on each iteration, showing rapidly decreasing loss, while real cross entropy can increase. However, in our experience the free energy does not vary significantly close to the minimum, and the metric can be used for comparison of different methods. The success of the convergence was checked by inspection of the generated images, which indeed showed close resemblance with real hand-written digits.

We run two numerical experiments: one without noise and another with normally distributed W with amplitude 0.001. The generated PD in both cases converges to the target distribution. In the presence of the noise the convergence was smooth, while without noise the loss decrease happens in step-like manner stagnating between the steps. Overall convergence rate is higher without noise. While trained BM in both cases produces correctly looking digits, the BM obtained by training without loss demonstrates faster switching between digits classes, that is smaller correlation between adjacent states.

The dynamics of the dissipative BM trained without noise is shown in Fig. 3.2 (bottom panel). The BM started from a random state, then after a burnout period of 16 steps. We recorded 256 states of the visible neurons skipping every 15 intermediate steps. The generated images reconstruct distribution of pixel colors matching MNIST dataset, but adjacent images are correlated resulting in smooth change of the digit shape. Visual inspection confirms that the dissipative BM correctly generalizes the training set producing images indistinguishable from those produced by humans.

4. BM solving classification problem

In previous sections, we considered generative models producing random values w with a learned distribution $p(x)$. For classification problems, it is often convenient to have a discriminative model, which produce random values of labels y distributed according to a learned conditional probability $p(y|x)$ given an observation of features x. This discriminative model can be implemented on top of BM with some modifications required.

The BM energy in the case is a function of features x, labels y and weights θ. The joint PD of x and y is given by Boltzmann distribution (9). In contrast to Section 3 both x and y are states of visible neurons. As shown above, addition of hidden neurons allows complex PDs, but in all formulas they are averaged out, therefore we do not list the hidden neurons explicitly in this section.

Given target distribution of labels $\tilde{p}(y|x)$ for fixed features values x, the model distribution can be compared with it using cross-entropy:

$$H(\tilde{p}, p|x) = -\sum_y \tilde{p}(y|x) \log p(y|x) = \mathbb{E}_{y\sim\tilde{p}}[-\log p(y|x)|x].$$

The loss function is commonly defined as mean of the cross-entropy over all x:

$$L = \sum_x \tilde{p}(x) H(\tilde{p}, p|x) = -\sum_{x,y} \tilde{p}(x,y) \log p(y|x) = \mathbb{E}_{x,y\sim\tilde{p}}[-\log p(y|x)].$$

Noticing (see Eq. (9)) that

$$p(y|x) = Z(x)^{-1} Z(x,y),$$

the loss function can be written in the following form:

$$L = \beta \sum_{x,y} \tilde{p}(x,y) E(x,y) + \beta \sum_{x,y} \tilde{p}(x,y) \log Z(x).$$

The first term here is the mean energy with respect to the target distribution. The second addendum is the Helmholtz free energy for a fixed x averaged over x. Consider the gradient of the loss over parameters θ. Since $\tilde{p}$ does not depend on θ, the averaging over $\tilde{p}$ can be swapped with differentiation over θ, which gives us the derivative of the first term. Using

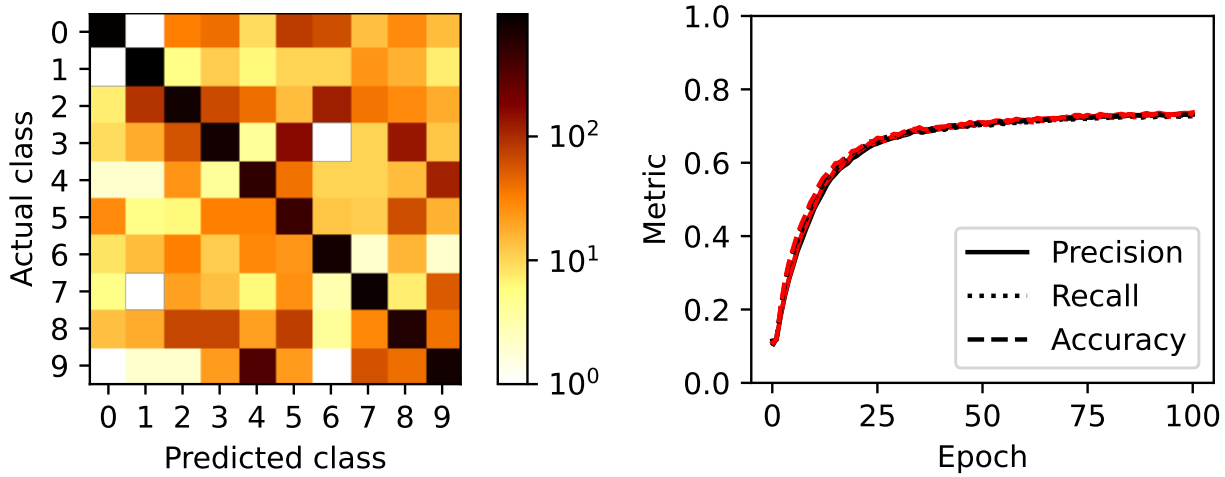

FIG. 4. Results of classification of hand-written digits from MNIST dataset. (Left panel) Confusion matrix on the test data after 100 epoch of training. (Right panel) Convergence history for accuracy and averaged over all classes precision and recall, demonstrating good agreement of all metrics. Metrics on the test set (red lines) and the training set (black lines) are almost identical.

earlier computed in (13) derivative of $\log Z(x)$, we obtain the loss derivative:

$$\frac{\partial L}{\partial \theta} = \beta \left(\sum_{x,y} \tilde{p}(x,y) \frac{\partial E(x,y)}{\partial \theta} - \sum_{x,y} \tilde{p}(x,y) \sum_{y'} p(y'|x) \frac{\partial E(x,y')}{\partial \theta} \right)$$
$$= \beta \mathbb{E}_{x\sim\tilde{p}} \left[\mathbb{E}_{y\sim\tilde{p}} \left[\frac{\partial E(x,y)}{\partial \theta} \middle| x \right] - \mathbb{E}_{y\sim p} \left[\frac{\partial E(x,y)}{\partial \theta} \middle| x \right] \right].$$

The argument of the outermost expectation value is exactly the derivative over θ of the cross-entropy $H(\tilde{p}, p)$ obtained in Section 2 assuming x fixed. Therefore, the discriminative model differs from the generative model in the way we treat the features state x: for the discriminative model x is always distributed according to the target distribution $\tilde{p}$.

The physical system whose dynamics coincides with the minimization of loss procedure, is designed using the principles stated in Section 2.

(1) The parameters θ are treated as slow DoF of the system.
(2) While the state $\tilde{x} = x$ is always driven by external forces defining target PD, a copy $\tilde{y}$ of y is introduced in such a way that interactions between x, y, θ are the same as for $x, \tilde{y}, \theta$, except for the opposite sign.
(3) Assuming ergodicity the expectation values are approximated by the time averages.
(4) The energy derivatives are treated as relaxation forces for the weight θ.

The proposed schematics of the self-training device is shown in Fig. 2.c. Its part involving labels variables y, $\tilde{y}$ is essentially the same as the schematic of the generative dissipative BM shown in Fig. 2.a, but now we have additional externally driven DoF encoding target distribution for the features $\tilde{x}$.

4.1. Digits classification benchmark

To validate the capability of the proposed method to solve complex problems, we do classification of hand-written digits from MNIST dataset using the dissipative BM. For the test, we used full size 28×28 black and white images, where the color was encoded in z projection of the spin: 1 for pure white and -1 for pure black pixel. 60 000 samples were used for training and 10 000 for testing. One loop over all training samples is considered an epoch. The training procedure took 100 epoch.

The state of the used BM consists of the features vector x, the labels vector y and the hidden units vector z. The size of the feature vector equals 784 and matches the number of pixels of the image. The labels vector y has 10 components, each component encodes the probability of the image to belong to the corresponding class, that represents one of ten digits. Both x and y compose the vector of visible neurons. For the benchmark, we set the number of hidden neurons to 200.

The energy of BM is defined by the functional:

$$E(x,y,z;\theta) = \sum_{ij} w^{xz} x_i z_k + \sum_{ij} w^{yz} y_j z_k + \sum_i b_i^x x_i + \sum_i b_i^y y_i + \sum_i b_i^z z_i,$$

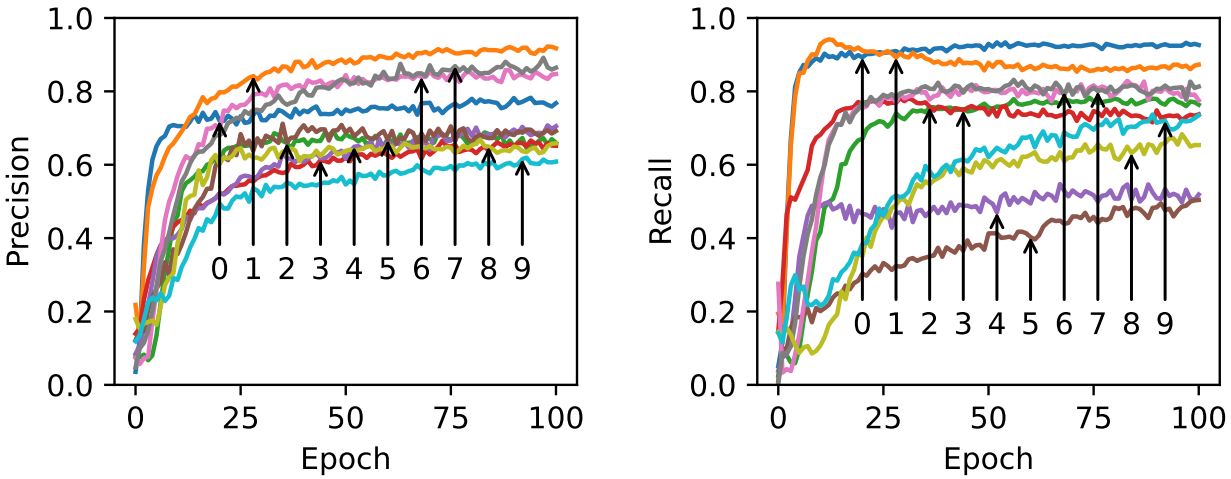

FIG. 5. Convergence history for precision (left panel) and recall (right panel) for individual classes computed on the test set.

where interaction matrices w and biases b form parameters vector $\theta = (w^{xz}, w^{yz}, b^x, b^y, b^z)$. The proposed dissipative BM contains two copies of x, y and z; we mark the second copy by tilde above the letter. The total energy of spin BM consists of energies of the two copies sharing the same parameters:

$$E^T = E(x, y, z; \theta) - E(\tilde{x}, \tilde{y}, \tilde{z}; \theta).$$

The possible strategies to negate energy of the second contribution are discussed in Section 3. During the training $\tilde{x}$ and $\tilde{y}$ are controlled by the external forces specifying training samples. The variables x, y, z and $\tilde{z}$ are distributed according to Boltzmann distribution. The dynamics was approximated by Monte-Carlo sampling of fast variables and relaxation dynamics of slow variables θ according to the algorithm:

(1) Sample new $\tilde{x}$, $\tilde{y}$ from the training set.
(2) Sample $\tilde{z}$ according to (11).
(3) Update $\theta \mapsto \theta - \eta \dfrac{\partial E^T}{\partial \theta}$.
(4) Repeat.

To reduce jitter we sample all variables in batches of 10 elements, that correspond to the physical system with 10 independent copies of each subsystem sharing the same weights.

The simulation was run on hand-written Python code using Numpy and JAX for GPU acceleration. The relaxation rate η was set to 10^{-4}. Initial weights θ were randomly sampled from the normal distribution with zero mean and standard deviation 0.1. Results of the training are shown in Fig. 4.1 and Fig. 4.1.

After 100 epoch we reached $\sim 73\%$ accuracy and very close values of precision and recall averaged over all classes. Although the metrics are much smaller than attainable by other methods, the result is comparable with the result of RBM with 200 hidden units. Increasing the number of hidden units and changing architecture of the machine including more hidden layers can significantly improve the result [15]. In the article, our main concern was comparison of the performance classical RBM and the proposed adaptation suitable for nanomagnetic implementation.

Confusion matrix shown in the left panel in Fig. 4.1 demonstrates that the most errors arise in misclassification of 9 as 4, 3 as 5 or 8, which is not much different from the errors of other methods. The same errors are confirmed by the convergence history plots shown in Fig. 4.1, pointing out that digits 4 and 5 are most confused with other digits. The metrics on the training set and on the test set are very close with precision and recall of individual digits continue to grow with every epoch, indicating the prolongation of training can lead to even better results.

Since in the proposed dissipative BM subsystem generating positive and negative update steps for the weights are generated by independent subsystems, the time required for averaging the contributions is larger than in CD method. In the BM, we are forced to use smaller training steps than in CD, therefore, convergence of simulated SBM is slower. In real magnetic nanosystems, the natural time scale defined by Larmor precession is orders of magnitude smaller than obtainable in simulation. Despite a slower convergence rate in simulation, the physical implementation of the BM is expected to be drastically faster than the ML model of BM used currently.

5. Discussion

Above, we proposed several approaches to implement energy-based ML models as physical devices. In particular, nanomagentic-devices are a natural candidate for the implementation of BM. Two problems are not completely solved and remain challenging for experimental implementation of the devices. The first problem is the necessity of three spin interactions between two neurons and the connection weight. Multispin connections in some cases give significant contribution to the total energy [27], but at the moment, it is not clear how to design magnetics with the desired multi-spin interactions. Probably more promising is creation of an effective multispin exchange by introducing auxiliary spins and averaging over them in the spirit of the work [28].

The second challenging problem is learning the weights of the hidden spins by relaxation. In this case, the introduction of lobes with opposite energies also affects the PD of the hidden neurons. The solution here can lay in avoidance of the hidden neurons interaction with the thermostat, and considering stochastic LLG dynamics of the spins, instead of Fokker–Planck equation. At least a similar approach allowed one to create a simple self-learning device experimentally [17].

References

[1] Min B., Ross H., Sulem E., et al. Recent Advances in Natural Language Processing via Large Pre-trained Language Models: A Survey. *ACM Computing Surveys*, 2023, **56**(2), P. 1–40.

[2] Chen Y., Nazhamaiti M., Xu H., et al. All-analog photoelectronic chip for high-speed vision tasks. *Nature*, 2023, **623**(7985), P. 48–57.

[3] Grollier J., Querlioz D., Camsari K.Y., et al. Neuromorphic spintronics. *Nature Electronics*, 2020, **3**(7), P. 360–370.

[4] Li S., Kang W., Zhang X., et al. Magnetic skyrmions for unconventional computing. *Materials Horizons*, 2021, **8**(3), P. 854–868.

[5] Yokouchi T., Sugimoto S., Rana B., et al. Pattern recognition with neuromorphic computing using magnetic fieldinduced dynamics of skyrmions. *Science Advances*, 2022, **8**(39), P. eabq5652.

[6] Gu K., Guan Y., Hazra B.K., et al. Three-dimensional racetrack memory devices designed from free- standing magnetic heterostructures. *Nature Nanotechnology*, 2022, 17(10), P. 1065–1071.

[7] Blasing R., Khan A.A., Filippou P.C., et al. Magnetic Racetrack Memory: From Physics to the Cusp of Applications Within a Decade. *Proceedings of the IEEE*, 2020, **108**(8), P. 1303–1321.

[8] Marullo C., Agliari E. Boltzmann Machines as Generalized Hopfield Networks: A Review of Recent Results and Outlooks. *Entropy*, 2020, **23**(1), 34 pp.

[9] Khater A., Abou Ghantous M. Magnetic properties of 2D nano-islands I: Ising spin model. *Journal of Magnetism and Magnetic Materials*, 2011, 323(22), P. 2717–2726.

[10] Yang S., Shin J., Kim T., et al. Integrated neuromorphic computing networks by artificial spin synapses and spin neurons. *NPG Asia Materials*, 2021, **13**(1), P. 1–10.

[11] Dixit V., Selvarajan R., Alam M.A., et al. Training Restricted Boltzmann Machines With a D-Wave Quantum Annealer. *Frontiers in Physics*, 2021, **9**, 589626, 10 pp.

[12] Lecun Y., Chopra S., Hadsell R., et al. A tutorial on energy-based learning. In G. Bakir, T. Hofman, B. Scholkopt, A. Smola, B. Taskar, editors, Predicting structured data. MIT Press. 2006.

[13] Dayan P., Hinton G.E., Neal R.M., et al. The Helmholtz Machine. 1999. *Neural Comput.*, 1995, **7**(5), P. 889–904.

[14] Teh Y.W., Welling M., Osindero S., et al. Energy-Based Models for Sparse Overcomplete Representa- tions. *Journal of Machine Learning Research*, 2003, **4**, P. 1235–1260.

[15] Du Y., Mordatch I. Implicit Generation and Modeling with Energy Based Models. In *Advances in Neural Information Processing Systems*, volume 32. Curran Associates, Inc.

[16] Lobanov I. Spin Boltzmann machine. *Nanosystems: Physics, Chemistry, Mathematics*, 2022, **13**(6), P. 593–607.

[17] Kiraly B., Knol E.J., Van Weerdenburg W.M.J., et al. An atomic Boltzmann machine capable of self- adaption. *Nature Nanotechnology*, 2021, **16**(4), P. 414–420.

[18] Aksenova E., Dobrun L., Kovshik A., et al. Magnetic Field-Induced Macroscopic Alignment of Liquid- Crystalline Lanthanide Complexes. *Crystals*, 2019, **9**(10), P. 499.

[19] Yair O., Michaeli T. Contrastive Divergence Learning is a Time Reversal Adversarial Game. URL/arXiv: https://doi.org/10.48550/arXiv.2012.03295.

[20] Colombo S., Pedrozo-Peafiel E., Adiyatullin A.F., et al. Time-reversal-based quantum metrology with many-body entangled states. *Nature Physics*, 2022, **18**(8), P. 925–930.

[21] Purcell E.M., Pound R.V. A Nuclear Spin System at Negative Temperature. *Physical Review*, 1951, **81**(2), P. 279–280.

[22] Hakonen P., Lounasmaa O.V. Negative Absolute Temperatures: "Hot" Spins in Spontaneous Magnetic Order. *Science*, 1994, **265**(5180), P. 1821–1825.

[23] Medley P., Weld D.M., Miyake H., et al. Spin Gradient Demagnetization Cooling of Ultracold Atoms. *Physical Review Letters*, 2011, **106**(19), 195301, 4 pp.

[24] Ramsey N.F. Thermodynamics and Statistical Mechanics at Negative Absolute Temperatures. *Physical Review*, 1956, **103**(1), P. 20–28.

[25] Baldovin M., Iubini S., Livi R., et al. Statistical mechanics of systems with negative temperature. *Physics Reports*, 2021, 923, P. 1–50.

[26] Deng L. The mnist database of handwritten digit images for machine learning research. *IEEE Signal Processing Magazine*, 2012, **29**(6), P. 141–142.

[27] Hoffmann M., Blgel S. Systematic derivation of realistic spin models for beyond-Heisenberg solids. *Physical Review B*, 2020, **101**(2), P. 024418.

[28] Yoshioka N., Akagi Y., Katsura H. Transforming generalized Ising models into Boltzmann machines. *Physical Review E*, 2019, **99**(3), P. 032113.

Submitted 10 October 2023; revised 11 November 2023; accepted 7 December 2023

Information about the authors:

Igor S. Lobanov – Faculty of Physics, ITMO University, Lomonosova Str. 9, Saint Petersburg, 191002 Russia; ORCID 0000-0001-8789-3267; igor.lobanov@metalab.ifmo.ru; lobanov.igor@gmail.com

NANOSYSTEMS:
PHYSICS, CHEMISTRY, MATHEMATICS

Original article

Vatutin A.D., et al. *Nanosystems: Phys. Chem. Math.*, 2023, **14** (2), 626–632.
http://nanojournal.ifmo.ru
DOI 10.17586/2220-8054-2023-14-2-626-632

Hidden polarization in open quantum systems

Alexander D. Vatutin, George P. Miroshnichenko, Alexander I. Trifanov

ITMO University, St.-Petersburg, Russia

Corresponding author: Alexander Vatutin, advatutin@yandex.ru

ABSTRACT In this work, we explore the master equation governing open quantum systems dynamics in an alternative form, which preserves the normal-ordered representation of the averaged normal-ordered operators. We derive a linear system of differential equations for the fourth-order moments of corresponding bosonic operators. Polarization moments of the first and the second orders are investigated using plane rotation transformation. We also evaluate the dynamics of the hidden polarization in comparison with the dynamics of usual polarization within open quantum dynamics.

KEYWORDS master equation, normal-ordered correlators, hidden polarization, fourth-order moments

FOR CITATION Vatutin A.D., Miroshnichenko G.P., Trifanov A.I. Hidden polarization in open quantum systems. *Nanosystems: Phys. Chem. Math.*, 2023, **14** (2), 626–632.

1. Introduction

The transfer, storage, and conversion of quantum information constitute three primary challenges in the field of quantum information processing. These are crucial for various quantum protocols such as quantum teleportation [1], quantum computing [2], quantum key distribution [3], dense coding, and quantum memory [4]. While numerous specific solutions address a variety of problems within these protocols, a general approach that resolves all types of issues remains unattainable.

The theory of open quantum systems addresses the problems of transport and storage of quantum information. This theory is typically articulated in terms of Completely Positive Trace-Preserving (CPTP) mappings, or trace-non-increasing linear mappings known as quantum channels. The dynamics of open quantum systems are most efficiently characterized by the master equation. Specifically, the Lindblad-type master equation [5, 6] is employed in this paper. There are two primary avenues of investigating this type of equations: the physical approach [7–9] and the mathematical techniques for the single-mode Lindblad equation [6, 10–17]. These mathematical techniques are extended to the case of multi-mode bosonic systems and have been utilized to construct the Fock-like eigenstates of Lindblad superoperators using the Lie algebras [18].

These mathematical techniques facilitate the determination of the dynamics of the averaged moments of the Stokes operators and the polarization of light [19]. Many physical processes are accurately described by these parameters. However, the averaged moments of the Stokes operator fall short in cases where not the average intensity, but other statistical parameters of the wave are recorded [20]. Therefore, higher-order moment correlators are essential for a more thorough description of these quantum processes. Furthermore, the introduction of a parameter, equivalent to polarization P_2 for higher-order moments, is both relevant and challenging. Numerous authors have demonstrated the existence of this process regardless of the existence of usual polarization [23, 24]. A more generalized approach for the determination of hidden polarization [20] is thoroughly considered in this paper.

The non-commutativity of the Stokes operators leads to quantum noise manifested through fourth-order correlators. The extent of variation in these correlators serves as an indicator of hidden polarization. The study of hidden polarization characteristics in the emission of exciton-polariton lasers is an area of research that holds fundamental interest [25]. Additionally, a comparison of the dynamics of hidden polarization to the dynamics of usual polarization in open quantum systems is meaningfully reviewed in this paper.

2. A model

We start with the master equation in the Gorini–Kossakowski–Sudarshan–Lindblad (GKSL) form for polarized light in the two-mode bosonic system in optical fibers:

$$\frac{\partial\hat{\rho}}{\partial t} = -i\sum_{n,m}\frac{1}{2}\Omega_{n,m}[\hat{a}_n^\dagger\hat{a}_m,\hat{\rho}] - \sum_{n,m}\frac{1}{2}\Gamma_{n,m}((n_T+1)(\hat{a}_n^\dagger\hat{a}_m\hat{\rho}+\hat{\rho}\hat{a}_n^\dagger\hat{a}_m-2\hat{a}_m\hat{\rho}\hat{a}_n^\dagger)+$$
$$+n_T(\hat{a}_m\hat{a}_n^\dagger\hat{\rho}+\hat{\rho}\hat{a}_m\hat{a}_n^\dagger-2\hat{a}_n^\dagger\hat{\rho}\hat{a}_m)), \quad (1)$$

where $n, m \in \{1, 2\}$, dagger denotes the Hermitian conjuration, $\hat{\rho}$ is the density matrix of a quantum state, $\hat{a}_n^\dagger$ and $\hat{a}_n$ are the creation and the annihilation operators of the n-th mode. Ω and Γ are frequency and relaxation matrixes [21], and n_T is a mean number of thermal photons:

$$n_T = \frac{1}{e^{\frac{\hbar\Omega_0}{k_B T}} - 1},$$

where Ω_0 is the bare(free-space) frequency, $\hbar$ is the reduced Planck constant, k_B is the Boltzmann constant, T is the temperature of the environment. The frequency and the relaxation matrices are given by:

$$\Omega = \begin{pmatrix} \omega_1 & \omega_3^* \\ \omega_3 & \omega_2 \end{pmatrix}, \ \Gamma = \begin{pmatrix} \gamma_1 & \gamma_3^* \\ \gamma_3 & \gamma_2 \end{pmatrix}, \tag{2}$$

where an asterisk stands for the complex conjuration. The matrices Ω and Γ are Hermitian: $\Omega = \Omega^\dagger, \Gamma = \Gamma^\dagger$. The relaxation matrix Γ is positively definite: $z^\dagger \Gamma z \geq 0$, $z \in \mathbb{C}^2$.

Equation (1) can be converted to the following form for any operator $\hat{\zeta}$ with the mean value $Z = \mathrm{tr}(\hat{\zeta}\hat{\rho}) = \langle\hat{\zeta}\rangle$:

$$\frac{\partial Z}{\partial t} = \frac{1}{2}\sum_{n,m}\left(\left\langle[\hat{\zeta}, \hat{a}_n^\dagger]\hat{a}_m\right\rangle(-i\Omega_{n,m} - \Gamma_{n,m}) + \left\langle\hat{a}_n^\dagger[\hat{a}_m, \hat{\zeta}]\right\rangle(i\Omega_{n,m} - \Gamma_{n,m})\right) - n_t\sum_{n,m}\Gamma_{n,m}\left\langle[[\hat{\zeta}, \hat{a}_n^\dagger], \hat{a}_m]\right\rangle. \tag{3}$$

If the operator $\hat{\zeta}$ with the mean value Z on the left-hand side of the equation is normal-ordered, the form of master equation (3) preserves the normal form of the moments [22].

3. Dynamics of normal-ordered forth moments

If $\hat{\zeta} = a_p^\dagger a_q^\dagger \hat{a}_s \hat{a}_t$ is the normal-ordered fourth moment, we can see that the relaxation is caused by fourth moments (the first sum) and the second moments (the second sum). Let us assume:

$$\begin{gathered}
Z_1 = \left\langle\hat{a}_1^\dagger\hat{a}_1^\dagger\hat{a}_1\hat{a}_1\right\rangle = A; \quad Z_2 = Z_4^* = \left\langle\hat{a}_1^\dagger\hat{a}_2^\dagger\hat{a}_1\hat{a}_1\right\rangle = D^*; \quad Z_3 = \left\langle\hat{a}_1^\dagger\hat{a}_2^\dagger\hat{a}_1\hat{a}_2\right\rangle = C; \\
Z_4 = \left\langle\hat{a}_1^\dagger\hat{a}_1^\dagger\hat{a}_1\hat{a}_2\right\rangle = D; \quad Z_5 = \left\langle\hat{a}_1^\dagger\hat{a}_1^\dagger\hat{a}_2\hat{a}_2\right\rangle = E; \quad Z_6 = Z_5^* = \left\langle\hat{a}_2^\dagger\hat{a}_2^\dagger\hat{a}_1\hat{a}_1\right\rangle = E^*; \\
Z_7 = \left\langle\hat{a}_2^\dagger\hat{a}_2^\dagger\hat{a}_1\hat{a}_2\right\rangle = F; \quad Z_8 = Z_7^* = \left\langle\hat{a}_1^\dagger\hat{a}_2^\dagger\hat{a}_2\hat{a}_2\right\rangle = F^*; \quad Z_9 = \left\langle\hat{a}_2^\dagger\hat{a}_2^\dagger\hat{a}_2\hat{a}_2\right\rangle = B; \\
\vec{Z} = (Z_1, Z_2, Z_3..., Z_9)^T; \\
B_1 = \left\langle\hat{a}_1^\dagger\hat{a}_1\right\rangle; \quad B_2 = \left\langle\hat{a}_1^\dagger\hat{a}_2\right\rangle; \quad B_3 = B_2^* = \left\langle\hat{a}_2^\dagger\hat{a}_1\right\rangle; \quad B_4 = \left\langle\hat{a}_2^\dagger\hat{a}_2\right\rangle; \\
\vec{B} = (B_1, B_2, B_3, B_4)^T,
\end{gathered} \tag{4}$$

where A^T denotes the transposed matrix for matrix A.

We can rewrite eq. (3) for all fourth moments like the nonhomogeneous system of linear differential equations:

$$\frac{\partial\vec{Z}}{\partial t} = H\vec{Z} + J\vec{B}, \tag{5}$$

where H is matrix 9×9 and J is 9×4 matrix. You can see matrices H and J in the Appendix. Dynamic of vector $\vec{B}$ is determined by the following equation [22]:

$$\frac{\partial\left\langle\hat{a}_p^\dagger\hat{a}_q\right\rangle}{\partial t} = \frac{1}{2}\sum_m\left\langle\hat{a}_p^\dagger\hat{a}_m\right\rangle(-i\Omega_{q,m} - \Gamma_{q,m}) + \frac{1}{2}\sum_n\left\langle\hat{a}_n^\dagger\hat{a}_q\right\rangle(i\Omega_{n,p} - \Gamma_{n,p}) + n_t\Gamma_{q,p}. \tag{6}$$

4. Polarization conversion as a rotation

If the phase factor common to the both modes is neglected, then the effect of a loss-free converter can be represented in the Heisenberg representation in the form:

$$\begin{pmatrix} \hat{a}_1' \\ \hat{a}_2' \end{pmatrix} = \begin{pmatrix} t^* & r^* \\ -r & t \end{pmatrix} \cdot \begin{pmatrix} \hat{a}_1 \\ \hat{a}_2 \end{pmatrix}, \tag{7}$$

where $t(r)$ is the amplitude transmission (conversion) coefficients of the converter. The standard parametrization can be introduced in the form:

$$\begin{aligned} t &= \cos(\theta/2) \cdot \exp[i(\phi + \psi)/2], \\ r &= -\sin(\theta/2) \cdot \exp[i(\phi - \psi)/2], \end{aligned} \tag{8}$$

where $0 \leq \theta < \pi$, $0 \leq \psi < 2\pi$ and $0 \leq \phi < 4\pi$. Using (8), we can find action of a converter on the operator $\hat{n}_1' = \hat{a}_1'^\dagger\hat{a}_1'$:

$$\hat{n}_1' = t^*t \cdot \hat{n}_1 + r^*r \cdot \hat{n}_2 + r^*t \cdot \hat{s}_+ + t^*r \cdot \hat{s}_+^*, \tag{9}$$

where $\hat{n}_1 = \hat{a}_1^\dagger \hat{a}_1$, $\hat{n}_2 = \hat{a}_2^\dagger \hat{a}_2$, and $\hat{s}_+ = \hat{a}_1^\dagger \hat{a}_2$. By averaging equations (9), one obtains the same equations for observables $N_1' = \langle \hat{n}_1' \rangle$, $N_1 = \langle \hat{n}_1 \rangle$, $N_2 = \langle \hat{n}_2 \rangle$ and $S_+ = \langle \hat{s}_+ \rangle$. We can rewrite N_1' in terms of (9):

$$N_1' = \begin{pmatrix} t & r \end{pmatrix}^* \cdot \begin{pmatrix} N_1 & S_+^* \\ S_+ & N_2 \end{pmatrix} \cdot \begin{pmatrix} t \\ r \end{pmatrix}. \tag{10}$$

If one varies one of the parameters, for example, a variation produced by rotating a $\lambda/4$ phase plate, the observed intensity varies periodically [20]: $N_1 \propto 1 + V_2 \cos(2\chi)$, $0 \le V_2 \le 1$. Here χ is the angle of the plane. The parameter V is called the *visibility factor* of the polarization interference. We can interpret Eq. (10) as a quadratic function with matrix K and normalized complex vector $(t, r)^T$, $|t|^2 + |r|^2 = 1$. Matrix K is the coherence matrix:

$$K = \begin{pmatrix} N_1 & S_+^* \\ S_+ & N_2 \end{pmatrix}. \tag{11}$$

Extremal values of the hermitian quadratic function are determined by minimum $\lambda_{\min}$ and maximum $\lambda_{\max}$ eigenvalues. These values can be found us follows:

$$(N_1')_{\max,\min} = \lambda_{\max,\min} = \frac{1}{2}\left(\operatorname{tr} K \pm [(\operatorname{tr} K)^2 - 4 \det K]^{1/2}\right).$$

Hence, the maximum possible interference visibility assumes the form:

$$V_{2_{\max}} = \frac{\lambda_{\max} - \lambda_{\min}}{\lambda_{\max} + \lambda_{\min}} = \sqrt{1 - \frac{4 \det K}{(\operatorname{tr} K)^2}} = \frac{\sqrt{S_1^2 + S_2^2 + S_3^2}}{S_0} = P_2,$$

Therefore $V_{2_{\max}}$ equals to the degree of polarization P_2. We have to mention that $S_i = \operatorname{tr}(\hat{s}_i \cdot \hat{\rho})$ for $i \in \{0, 1, 2, 3\}$ and

$$\hat{s}_0 = \hat{a}_1^\dagger \hat{a}_1 + \hat{a}_2^\dagger \hat{a}_2, \quad \hat{s}_1 = \hat{a}_1^\dagger \hat{a}_1 - \hat{a}_2^\dagger \hat{a}_2,$$
$$\hat{s}_2 = \hat{a}_1^\dagger \hat{a}_2 + \hat{a}_2^\dagger \hat{a}_1, \quad \hat{s}_3 = -i(\hat{a}_1^\dagger \hat{a}_2 - \hat{a}_2^\dagger \hat{a}_1).$$

5. Fourth-order polarization parameters

Let us similarly introduce the fourth-order polarization. Let vector $\hat{\vec{s}}$ and its average $\vec{S}$ be as follows: $\hat{\vec{s}} = (\hat{s}_1, \hat{s}_2, \hat{s}_3)$, $\vec{S} = \langle \hat{\vec{s}} \rangle = (S_1, S_2, S_3)$. The definition of fluctuations ΔS_X of the observable, for example, ΔS_1 along a definite direction of $X = (\cos(\Theta), -\sin(\Theta)\cos(\Phi), \cos(\Theta)\cos(\Phi))^T$ with coordinates (Θ, Φ) in the Stokes–Poincare space is as follows:

$$\begin{aligned}(\Delta S_X)^2 = \sum_{k,l=1}^{3} \left\langle \Delta\hat{\vec{s}}_k \Delta\hat{\vec{s}}_l \right\rangle X_k X_l = \sum_{k,l=1}^{3} (Q_{k,l} - S_k S_l + S_0 I) X_k X_l + \sum_{k,l,m=1}^{3} i\varepsilon_{k,l,m} S_m X_k X_l = \\ = \sum_{k,l=1}^{3} (Q_{k,l} - S_k S_l + S_0 I) X_k X_l = \sum_{k,l=1}^{3} (\Delta Q)_{k,l} X_k X_l,\end{aligned} \tag{12}$$

where $\Delta\hat{\vec{s}} = \hat{\vec{s}} - \vec{S}$. The second sum is always equal to zero, because of $X \in \mathbb{R}$ and antisymmetry of symbol Levi–Civita $\varepsilon_{k,l,m}$. Matrix $Q = \left\langle : \hat{\vec{s}} \otimes \hat{\vec{s}} : \right\rangle$ is the normal-ordered second moments of the Stokes operators:

$$Q = 2 \begin{pmatrix} (A+B)/2 - C & \operatorname{Re}(D-F) & \operatorname{Im}(D-F) \\ \operatorname{Re}(D-F) & C + \operatorname{Re}(E) & \operatorname{Im} E \\ \operatorname{Im}(D-F) & \operatorname{Im} E & C - \operatorname{Re} E \end{pmatrix}, \tag{13}$$

where A, B, C, D E and F are taken from Eq. (4).

The matrix $\Delta Q \equiv Q - \vec{S} \otimes \vec{S} + S_0 I$ expresses the variances of the Stokes parameters. Hence, the last expression from Eq.(12) can be reviewed as quadratic form with real vector X: $|X| = 1$. The observed S_1 varies periodically in the same way, as N_1: $\Delta S_1 \propto 1 + V_4 \cos(2\theta)$, $0 \le V_4 \le 1$, where V_4 is visibility factor of fourth moments. Hence, the degree of fourth-order polarization P_4 can be defined as the maximum possible visibility of the fourth-order interference, observed according to the fluctuations of the Stokes parameter:

$$V_{4_{\max}} = \frac{\mu_{\max} - \mu_{\min}}{\mu_{\max} + \mu_{\min}} = P_4, \tag{14}$$

where $\mu_{\max}$ and $\mu_{\min}$ are the maximum and the minimum eigenvalues of the matrix ΔQ.

It should be mentioned, that the fluctuation of any observable can be reviewed. For ΔS_2 under consideration, only the representation of direction X changes, but the most important part ΔQ and $|X| = 1$ remains the same. In addition, the fluctuations of $A = \left\langle \hat{a}_1^\dagger \hat{a}_1^\dagger \hat{a}_1 \hat{a}_1 \right\rangle$ can be taken in consideration. The formalism of quadratic forms is unusable in

this case. However, the maximum possible visibility of the fourth-order interference $V_{4_{\max}}$ gives the same result, as the fluctuations of components of Stock's vector.

6. Examples

The dissipative dynamics, as described by system (5), are governed by the frequency and the relaxation matrices introduced in Eq. (2). In this section, we compare the dynamics of hidden polarization and ordinary polarization under varying the initial conditions for these matrices and the quantum states. Diagonal frequency and the relaxation matrices are used:

$$\Omega = \begin{pmatrix} \omega - \dfrac{\delta}{2} & 0 \\ 0 & \omega + \dfrac{\delta}{2} \end{pmatrix}, \quad \Gamma = \begin{pmatrix} \gamma - \gamma_0 & 0 \\ 0 & \gamma + \gamma_0 \end{pmatrix}.$$

Parameter $\delta = 6.5 \cdot 10^6$ sec^{-1} represents the frequency difference between the two modes (beat lenght is $L = 200$ meters). Only this parameter affects the hidden polarization, similar to its effect on ordinary polarization. Hence, parameter ω can be chosen to be 0. Parameter $\gamma = 1.2 \cdot 10^6$ sec^{-1} (relaxation is 25 dB/km) and $\gamma_0 = 0.2 \cdot \gamma$ sec^{-1}. Below, we show a dynamics of ordinary polarization and hidden polarization for different initial states. Any initial state relaxes to thermal state with the number of thermal photons $n_T = 1$. Examples illustrating the initial data for common states are provided in Figs. 1–5.

A particular case under consideration is the Fock state with equal numbers of photons in the vertical and horizontal modes. The initial data yield an opening polarization of $P_2(0) = 0$ and a hidden polarization of $P_4(0) = 1$. If relaxation in the both modes is equable ($\gamma_0 = 0$), polarization $P_2(t) = 0$ for any t. Hence, the result is shown in Fig. 5.

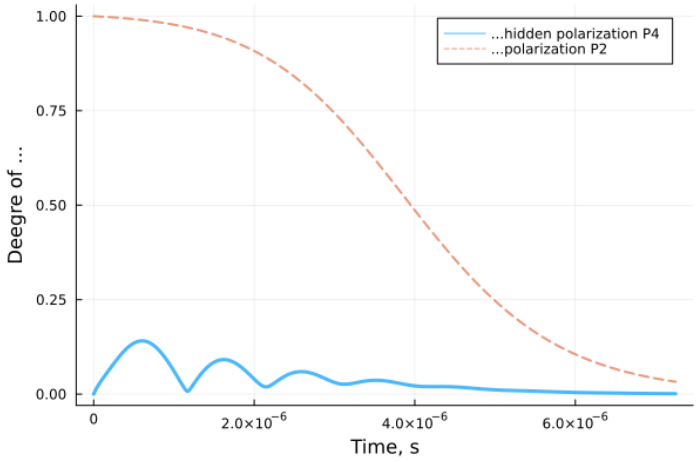

FIG. 1. Initial state is coherent state $|12, 8\rangle$

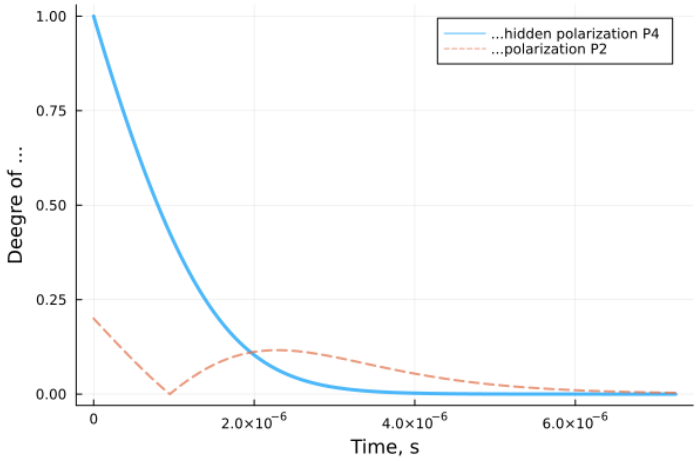

FIG. 2. Initial state is Fock state $|12, 8\rangle$

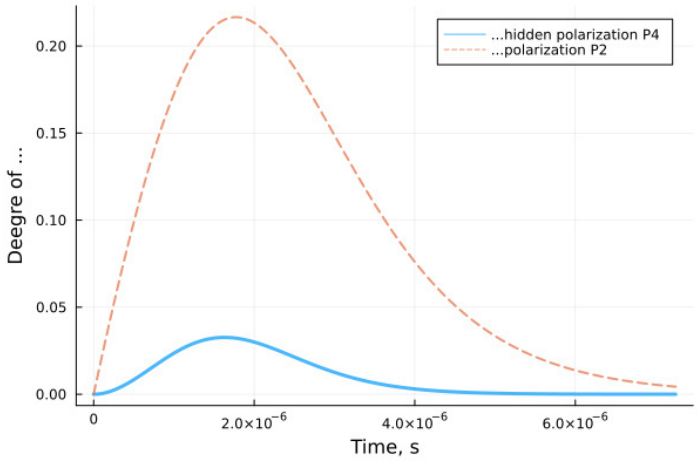

FIG. 3. Initial state is thermal state with the number of thermal photons $n_T = 10$.

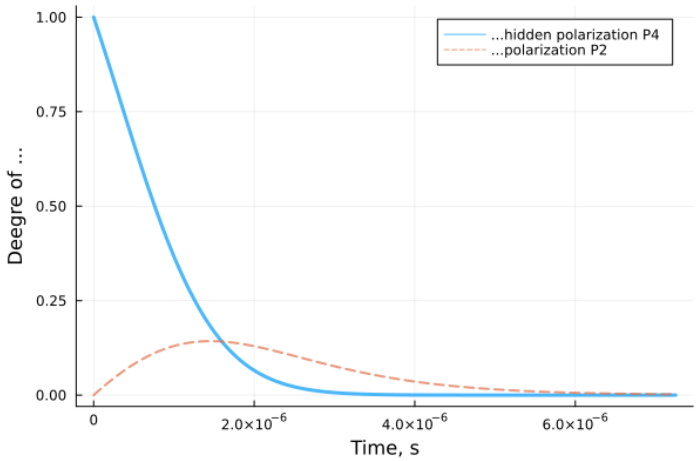

FIG. 4. Initial state is squeezed vacuum $|\xi_1, \xi_2\rangle$, where $\xi_{1(2)}$ is squeezed vacuum for 1-st(2-nd) mode. $\xi_1 = \xi_2 = 1.5 * e^{i\phi}$ is complex squeeze parameter

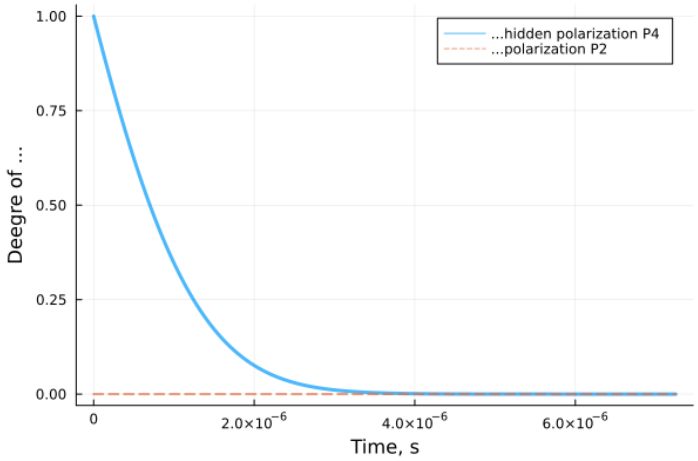

FIG. 5. Initial state is Fock state $|8, 8\rangle$. Relaxation is equal in both modes, which gives the absence of usual polarization.

7. Conclusion

In contrast to showing the existence of hidden polarization in systems without time dependence [20, 23, 24], we compare the dynamics of hidden polarization to those of usual polarization in open quantum systems. We illustrate a case where the usual polarization is absent while hidden polarization is present, as depicted in Figs. 1–4. We commence with the master equation in the GKSL form for the open quantum systems, maintain normal ordering as per equation (3). We elucidate the dynamics of the fourth-ordered observables for a more accurate description of the open quantum systems than using the dynamics of second-ordered observables [19,22]. The values of the fourth-ordered and the second-ordered observables vary depending on the plate position in the experiment. We demonstrate that both polarization P_2 and polarization P_4 can be similarly ascertained through rotation. A logical extension of this work entails the construction of quantum key distribution schemes. For instance, with the Fock state as the initial state, certain considerations regarding a qutrit arise.

Appendix

With equation (3) in use, let the operator $\hat{\zeta}$ be equal to $\hat{a}_1^\dagger\hat{a}_1^\dagger\hat{a}_1\hat{a}_1$. Then one can obtain:

$$\frac{\partial\left\langle\hat{a}_1^\dagger\hat{a}_1^\dagger\hat{a}_1\hat{a}_1\right\rangle}{\partial t}=\frac{1}{2}\sum_{n,m}\left(\left\langle[\hat{a}_1^\dagger\hat{a}_1^\dagger\hat{a}_1\hat{a}_1,\hat{a}_n^\dagger]\hat{a}_m\right\rangle(-i\Omega_{n,m}-\Gamma_{n,m})+\left\langle\hat{a}_n^\dagger[\hat{a}_m,\hat{a}_1^\dagger\hat{a}_1^\dagger\hat{a}_1\hat{a}_1]\right\rangle(i\Omega_{n,m}-\Gamma_{n,m})\right)- \\ -n_t\sum_{n,m}\Gamma_{n,m}\left\langle[[\hat{a}_1^\dagger\hat{a}_1^\dagger\hat{a}_1\hat{a}_1,\hat{a}_n^\dagger],\hat{a}_m]\right\rangle. \tag{15}$$

In the first sum of the equation (15) n equals to 1, in the second m equals to 1, in the third n and m are equal to 1. Otherwise, commutators in these sums give one 0.

$$\frac{\partial\left\langle\hat{a}_1^\dagger\hat{a}_1^\dagger\hat{a}_1\hat{a}_1\right\rangle}{\partial t}=\sum_m\left(\left\langle\hat{a}_1^\dagger\hat{a}_1^\dagger\hat{a}_1\hat{a}_m\right\rangle(-i\Omega_{1,m}-\Gamma_{1,m})+\sum_n\left\langle\hat{a}_n^\dagger\hat{a}_1^\dagger\hat{a}_1\hat{a}_1\right\rangle(i\Omega_{n,1}-\Gamma_{n,1})\right)-4n_t\Gamma_{1,1}\left\langle\hat{a}_1^\dagger\hat{a}_1\right\rangle= \\ =-2\gamma_1\left\langle\hat{a}_1^\dagger\hat{a}_1^\dagger\hat{a}_1\hat{a}_1\right\rangle+(-i\omega_3^*-\gamma_3^*)\left\langle\hat{a}_1^\dagger\hat{a}_1^\dagger\hat{a}_1\hat{a}_1\right\rangle+(i\omega_3-\gamma_3)\left\langle\hat{a}_2^\dagger\hat{a}_1^\dagger\hat{a}_1\hat{a}_2\right\rangle-4n_t\gamma_1\left\langle\hat{a}_1^\dagger\hat{a}_1\right\rangle. \tag{16}$$

This process can be continued for any operator $\hat{\zeta}=\hat{a}_p^\dagger\hat{a}_q^\dagger\hat{a}_s\hat{a}_t$. After some calculations, matrices H has the following form:

$$H=\begin{pmatrix}H_1&H_+&0&H_+^*&0&0&0&0&0\\H_-^*/2&H_2&H_+^*&0&0&H_+/2&0&0&0\\0&H_+/2&H_3&H_-^*/2&0&0&H_+/2&H_+^*/2&0\\H_-/2&0&H_+&H_4&H_+^*/2&0&0&0&0\\0&0&0&H_-&H_5&0&0&H_+&0\\0&H_-^*&0&0&0&H_6&H_+^*&0&0\\0&0&H_-^*&0&0&H_-/2&H_7&0&H_+^*/2\\0&0&H_-&0&H_-^*/2&0&0&H_8&H_+/2\\0&0&0&0&0&0&H_-&H_-^*&H_9\end{pmatrix}, \tag{17}$$

where

$$H_+=-\gamma_3+i\omega_3,\quad H_-=-\gamma_3-i\omega_3,\quad H_1=-2\gamma_1,$$
$$H_2=H_4^*=(-3\gamma_1-\gamma_2+i(-\omega_1+\omega_2))/2,\quad H_3=-\gamma_1-\gamma_2,$$
$$H_5=H_6^*=-\gamma_1-\gamma_2+i(+\omega_1-\omega_2),\quad H_7=H_8^*=(-\gamma_1-3\gamma_2+i(-\omega_1+\omega_2))/2,\quad H_9=-2\gamma_2.$$

For matrix J, one has:

$$J=n_T\begin{pmatrix}4\gamma_1&2\gamma_3^*&\gamma_2&\gamma_3&0&0&0&0&0\\0&0&\gamma_3&\gamma_1&4\gamma_3&0&0&2\gamma_2&0\\0&2\gamma_1&\gamma_3^*&0&0&4\gamma_3^*&2\gamma_2&0&0\\0&0&\gamma_1&0&0&0&2\gamma_3^*&2\gamma_3&4\gamma_2\end{pmatrix}^T. \tag{18}$$

References

[1] Pirandola S., Eisert J., Weedbrook C., Furusawa A., Braunstein S.L. Advances in quantum teleportation. *Nat. Photon.*, 2015, **9**, P. 641–652.
[2] Gyongyosi L., Imre S. A survey on quantum computing technology. *Comput. Sci. Rev.*, 2019, **31**, P. 51–71.
[3] Pirandola S., Andersen U., Banchi L., Berta M., Bunandar D., Colbeck R., Englund D., Gehring T., Lupo C., Ottaviani C., Pereira J. Advances in quantum cryptography. *Adv. Opt. Photon.*, 2020, **12**, P. 1012–1236.
[4] Lvovsky A.I., Sanders B.C., Tittel W. Optical quantum memory. *Nat. Photon.*, 2009, **3**, P. 706–714.
[5] Gaidash A., Kozubov A., Miroshnichenko G. Dissipative dynamics of quantum states in the fiber channel. *Phys. Rev. A*, 2020, **102**, 023711.
[6] Bonetti J., Hernandez S.M., Grosz D.F. Master equation approach to propagation in nonlinear fibers. *Opt. Lett.*, 2021, **46**, P. 665–668.
[7] Pearle P. Simple derivation of the Lindblad equation. *Eur. J. Phys.*, 2012, **33**, P. 805–822.
[8] Albash T., Boixo S., Lidar D.A., Zanardi P. Quantum adiabatic Markovian master equations. *New J. Phys.*, 2012, **14**, 123016.
[9] McCauley G., Cruikshank B., Bondar D.I., Jacobs K. Accurate Lindblad-form master equation for weakly damped quantum systems across all regimes. *NPJ Quantum Inf.*, 2020, **6**, P. 74.
[10] Miroshnichenko G. Decoherence of a one-photon packet in an imperfect optical fiber. *Bull. Russ. Acad. Sci.*, 2018, **82**, P. 1550–1555.
[11] Kozubov A., Gaidash A., Miroshnichenko G. Quantum model of decoherence in the polarization domain for the fiber channel. *Phys. Rev. A*, 2019, **99**, 053842.
[12] Miroshnichenko G.P. Hamiltonian of photons in a single-mode optical fiber for quantum communications protocols. *Opt. Spectrosc.*, 2012, **112**, P. 777–786.
[13] Lu H.-X., Yang J., Zhang Y.-D., Chen Z.-B. Algebraic approach to master equations with superoperator generators of su(1,1) and su(2) Lie algebras. *Phys. Rev. A*, 2003, **67**, 024101.
[14] Tay B.A., Petrosky T. Biorthonormal eigenbasis of a Markovian master equation for the quantum Brownian motion. *J. Math. Phys.*, 2008, **49**, 113301.
[15] Honda D., Nakazato H., Yoshida M. Spectral resolution of the Liouvillian of the Lindblad master equation for a harmonic oscillator. *J. Math. Phys.*, 2010, **51**, 072107.
[16] Tay B.A. Eigenvalues of the Liouvillians of quantum master equation for a harmonic oscillator. *Physica A*, 2020, **556**, 124768.
[17] Shishkov V.Y., Andrianov E.S., Pukhov A.A., Vinogradov A.P., Lisyansky A.A. Perturbation theory for Lindblad superoperators for interacting open quantum systems. *Phys. Rev. A*, 2020, **102**, 032207.
[18] Teuber L., Scheel S. Solving the quantum master equation of coupled harmonic oscillators with Lie-algebra methods. *Phys. Rev. A*, 2020, **101**, 042124.
[19] Gaidash A., Kozubov A., Miroshnichenko G., Kiselev A.D. Quantum dynamics of mixed polarization states: effects of environment-mediated intermode coupling. *JOSA B*, 2021, **38** (9), 425226.
[20] Klyshko D.M. Polarization of light: fourth-order effects and polarization-squeezed states. *Zh. Eksp. Teor. Fiz.*, 1997, **111**, P. 1955–1983.
[21] Miroshnichenko G.P. Parameterization of an interaction operator of optical modes in a single-mode optical fiber. *Nanosystems: Physics, Chemistry, Mathematics*, 2015, **6** (6), P. 857–865.
[22] Vatutin A.D., Miroshnichenko G.P., Trifanov A.I. Master equation for correlators of normal-ordered field mode operators. *Nanosystems: Physics, Chemistry, Mathematics*, 2022, **13** (6), P. 628–631.
[23] Kozlov G.G., Ryzhov I.I., Tzimis A., Hatzopoulos Z., Savvidis P.G., Kavokin A.V., Bayer M., Zapasskii V.S. Hidden polarization of unpolarized light. *Phys. Rev. A*, 2018, **98** (4), 043810.
[24] De la Hoz P., Bjork G., Klimov A.B., Leuchs G., Sanchez-Soto L.L. Unpolarized states and hidden polarization. *Phys. Rev. A*, 2014, **90**, 043826.
[25] Ryzhov I.I., Glazov M.M., Kavokin A.V., Kozlov G.G., Aßmann M., Tsotsis P., Hatzopoulos Z., Savvidis P.G., Bayer M., Zapasskii V.S. Spin noise of a polariton laser. *Phys. Rev. B*, 2016, **93**, 241307.

Submitted 27 October 2023; revised 30 October 2023; accepted 31 October 2023

Information about the authors:

Alexander D. Vatutin – ITMO University, Kronverkskiy 49, St.-Petersburg, Russia; ORCID 0000-0003-1853-2171; advatutin@yandex.ru

George P. Miroshnichenko – ITMO University, Kronverkskiy 49, St.-Petersburg, Russia; ORCID 0000-0002-4265-8818; gpmirosh@gmail.com

Alexander I. Trifanov – ITMO University, Kronverkskiy 49, St.-Petersburg, Russia; ORCID 0000-0002-5109-2086; alextrifanov@itmo.ru

Conflict of interest: the authors declare no conflict of interest.

NANOSYSTEMS:
PHYSICS, CHEMISTRY, MATHEMATICS

Original article

AlHussein H., et al. *Nanosystems: Phys. Chem. Math.*, 2023, **14** (6), 633–643.
http://nanojournal.ifmo.ru
DOI 10.17586/2220-8054-2023-14-6-633-643

Study of the electrical and electronic properties of crystalline molybdenum disulfide (MoS_2-3R) semiconductor nano using alternating current (AC) measurements

Hussein Alhussein, Jamal Qasim AlSharr, Sawsan Othman, Hassan AlKhamisy

University of Aleppo, Syria

Corresponding author: Hussein Alhussein, husianphy990@gmail.com

ABSTRACT MoS_2 nanostructures were prepared using the hydrothermal method by reacting ammonium heptamolybdate tetrahydrate ($(NH_4)_6Mo_7O_{24}4H_2O$) with citric acid monohydrate ($C_6H_8O_7H_2O$) in distilled water with the presence of sodium sulfide (Na_2S). The surface structure studies of MoS_2 showed that the size of the surface clusters of the studied tablet is of the order of 50 – 100 nm. Using measurements (Zetasizer Nano Series), we found that the particle sizes ranged from 150 – 350 nm. Alternating current (LCR) measurements were made for (tablet-MoS_2) under a constant temperature $T = 10$ °C. Measurements of the parallel electrical capacitance (C_p) in terms of frequency (F) of tablet-MoS_2 showed a sharp drop in the value of the electrical capacitance (C_p) with an increase in frequency within the range 20 Hz – 16 kHz. It is shown that the series capacitance increased with the increase of the applied potential.

KEYWORDS MoS_2-3R, atomic force microscopy (AFM), LCR measurements, electrical capacitance, Zetasizer Nano Series

FOR CITATION AlHussein H., AlSharr J., Othman S., AlKhamisy H. Study of the electrical and electronic properties of crystalline molybdenum disulfide (MoS_2-3R) semiconductor nano using alternating current (AC) measurements. *Nanosystems: Phys. Chem. Math.*, 2023, **14** (6), 633–643.

1. Introduction

When studying semi-conducting materials of silicon or its compounds in nanoscale dimensions, scientists found that they are subject to quantum constraint. Therefore, these materials seem as if they have reached their practical limits and cannot be used in modern technologies and devices that depend on nanotechnology. Therefore, scientists began searching for new materials that have properties that meet the requirements of technological progress and molybdenum disulfide was among these materials, which is characterized by multiple structural phases that give it unique properties that enable it to be used in electronic, photovoltaic, or magnetic applications. MoS_2 is considered as one of the types of semiconductors that belong to the family of transition metal chalcogenides (TMDs) that consist of layers linked by van der Waals forces that allow the formation of several crystalline phases of dichalcogen MX2, where M belongs to the metallic elements in the periodic table within the groups It represents the element chalcogen [1,2]. MoS_2 is considered as one of the important and promising compounds of this group as a result of its important physical properties, where molybdenum disulfide (MoS_2-3R) is considered as a promising alternative to silicon because of its excellent photovoltaic properties and its gap with an energy equal to the energy gap 1.2 eV of silicon [3, 4], it also has a unique multilayer or single-layer structure. These properties make it an ideal material for future applications in semiconductors, transistors, chips, and other fields of advanced science and technology. Therefore, in recent years, scientists have maintained great interest in the exploration and research of molybdenum disulfide (MoS_2-3R) [5–7].

Molybdenum disulfide exists in three patterns 3R–2H–1T, the two patterns (2H, 1T) have a semi-metallic behavior, while the pattern 3R has a semi-conducting behavior, where the pattern MoS_2-3R is characterized by an energy gap similar to the energy gap of silicon in its structural state (bulck), the sulfide is distinguished by its multi-layered structure, where we will focus in this research on studying the electrical properties of molybdenum disulfide MoS_2-3R [8–10].

2. The importance of research:

In the present work, a characterization of the electrical properties of molybdenum disulfide MoS_2 prepared chemically in the form of nanostructures with a structure of the type MoS_2-3R using alternating current measurements. We also study the nodal resistance changes with the change of temperature of the studied sample in order to employ this compound in electronic applications The molybdenum sulfide in the type MoS_2-3R has a wide optical absorption in the infrared and visible light fields. In its structural state (bulk), it has an energy gap similar to the silicon gap. Therefore, a comprehensive electrical characterization of this compound must be made.

3. Practical and experimental study

3.1. The devices and tools used: instruments & devices

(1) Zetasizer Nano-Particle size and zeta potential measurement.
(2) Atomic Force Microscopy (AFM).
(3) X-ray spectroscopy (XRD) from Phywe.
(4) LCR meter (LCR meter-microtest-6379).
(5) Chemical preparation tools (accurate electronic balance, desiccant, and thickened).
(6) Magnetic mixer with heater model (502p-2) from the American company PMC.

3.2. Materials used, method and stages of preparation

3.2.1. Materials used. Ammonium heptamolybdate tetrahydrate ($(NH_4)_6Mo_7O_{24}$ $4H_2O$), tetrathiomolybdate ammonium, distilled water, citric acid monohydrate ($C_6H_8O_7$ H_2O).

3.2.2. Method of preparation. To prepare nanostructures from 3R-MoS_2, the preparation process was carried out using the hydrothermal method [11], where in the manufacturing process, sodium sulfide was used as a source of sulfur in order to obtain molybdenum sulfide through chemical reactions, and thus we have obtained a pure powder of Molybdenum sulfide as shown in Fig. 1. Where we pressed an amount of this powder amounting to $M = 1$ gr, we obtained a MoS_2-Tablet with a diameter of 15 mm and a thickness of 2 mm for the electrical characterization, using a hydraulic compressor with a capacity of 5 ton/cm^2, and without heat treatment (the tablets have not been heat treated).

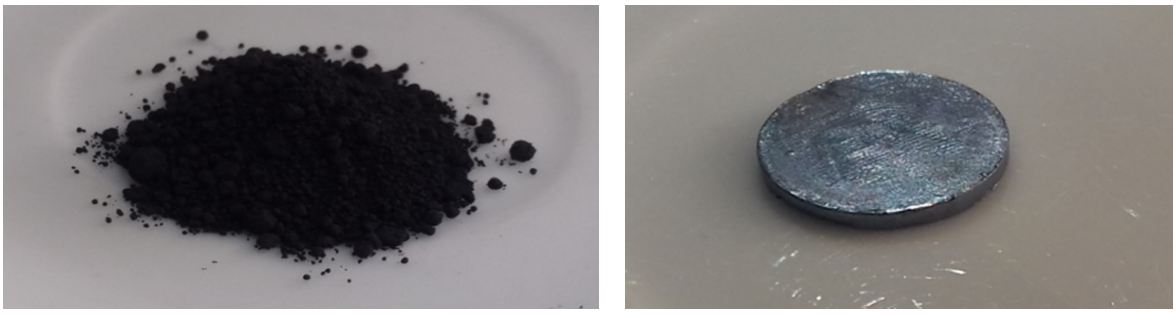

(a) (b)

FIG. 1. Pure powder prepared from MoS_2 (a); MoS_2 powder prepared and compressed into tablets (b)

3.3. Measurements (Zetasizer Nano Series) of formed nanoparticles

To determine the size of the formed nanoparticles, we measured the size of these granules using the Zetasizer Nano device, model ZS-Nano, produced by Malvern Company, using a red laser source, with a wavelength of 632.8 nm. We placed a suspension of molybdenum sulfide (MoS_2) in quartz cells designated for the device. The device is calibrated at a constant temperature of 25 °C. The dimension of the scanned cell are 5.5 mm, and a count rate is 141.8 = count rate (k_{cps}), so we found that the particle sizes ranged from 150 – 350 nm and that the average particle size was equal to 267 nm as shown in Fig. 2.

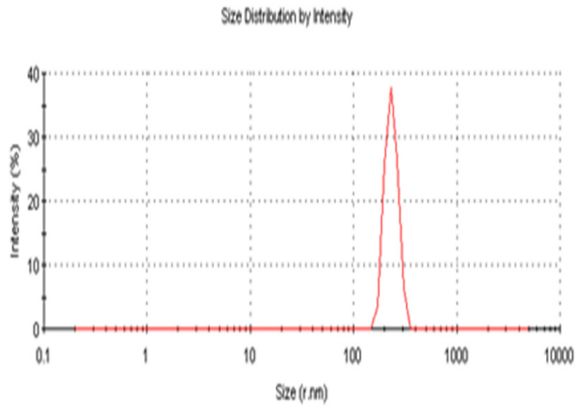

FIG. 2. Zetasizer Nano Series measurements of the size of the prepared MoS_2 granules

3.4. X-ray diffraction spectrum

In order to verify the structure of the prepared molybdenum disulfide, the crystallization of the prepared samples was studied by using an X-ray device produced by Phywe company and applying a current which intensity is 0.1 mA and an angle hop of 0.1 degrees every 10 sec). Measurements between angles 80° – 10° were taken and a copper anode which wavelength 1.541 Å was used.

X-ray spectra (XRD) of the nanopowder prepared from MoS_2 showed that there are no clear peaks, and this indicates and confirms the nanostructure of MoS_2 is amorphous, and this is consistent with the data of the card (JCPDS No. 06-0097) [12–14], as in Fig. 3(a). Since the crystallization process in the patterns (1T, 2H) is related to pressure and the degree of oxidation, we prepared tablets with diameters of 1.5 cm and thickness of 3 mm from powder-MoS_2 using a hydraulic compresser by subjecting powder-MoS_2 to a pressure of 5 ton. The X-ray diffraction measurements of these discs showed the presence of a very clear and intense peak corresponding to the crystalline plane (002) corresponding to the degree ($2\theta = 14.6°$). This is consistent with the values of the aforementioned molybdenum disulfide reference cards. Fig. 3(b) shows the presence of several diffraction peaks. It means that there are several phases within the structure of MoS_2.

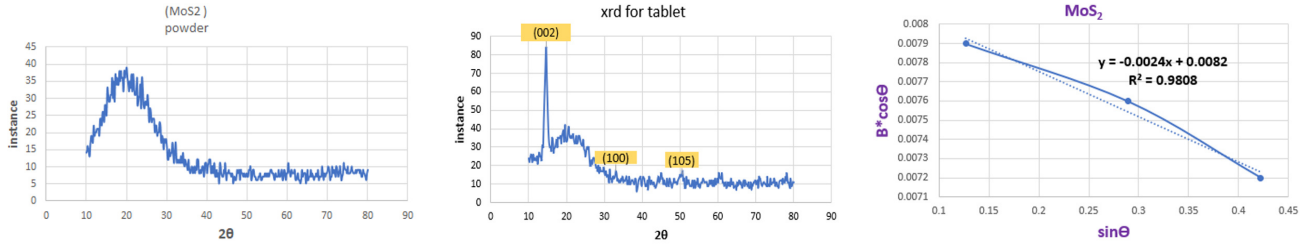

(a) (b) (c)

FIG. 3. XRD of nanopowder prepared from MoS_2 (a); XRD of nanopowder prepared from MoS_2 (b); Representing the W–H relation (c)

Table 1 shows the diffraction angles and corresponding crystal planes.

TABLE 1. The diffraction angles and corresponding crystal planes

2θ	14.6	32.5	50
(hkl)	(002)	(100)	(105)

The (002) crystal plane is the preferred crystal plane for MoS_2 crystals, as shown in Fig. 3(b). In accordance with Bragg's law of the X-rays diffraction (1), the distance between the crystal planes defined by Miller's indices (hkl) can be set:

$$2d_{hkl}\sin(\theta_{hkl}) = n\lambda. \tag{1}$$

Here d_{hkl} represents the distance between the parallel crystal planes according to the hkl direction, the angle θ_{hkl} is the diffraction angle, and n is the diffraction rank, λ represents the wavelength of the X-rays ($\lambda = 1.541$ Å). By calculation, it turns out that the value of the lattice constant is $d_{hkl} = 5.906$ Å, and by using the Williamson–Hall relation, which is given by relation (2):

$$\frac{1}{D} + \frac{2\varepsilon\sin\theta}{\lambda} = \frac{\beta\cos\theta}{\lambda}. \tag{2}$$

Other parameters can be determined from the X-ray spectra, such as the size of crystallization and strain of the crystal lattice, where β is the width of the mid-intensity of each peak estimated in radians, D is the size of crystallization, ε is the effective tension between atoms within the structure, and λ is the wavelength of the X-rays used. By plotting the previous relation, where it represents the point of interpart (λ/D) and the slope represents 2ϵ and the W–H relation can be represented in Fig. 3(c).

By calculation, we found that:

$$\frac{\lambda}{D} = 0.0082 \quad \Rightarrow \quad D = \frac{\lambda}{0.0082} = \frac{1.5418}{0.0082} = 192.7\ \mathring{A} = 19.27\ \text{nm}.$$

The value of the lattice constants (a) is calculated from relation (3):

$$d_{hkl} = \frac{a}{\sqrt{h^2 + k^2 + l^2}}. \tag{3}$$

By calculation $d_{hkl} = 5.906$ Å, the atomic dislocations within the crystal structure can be calculated based on the XRD spectrum using relation (4) [15, 16]:

$$\delta = \frac{14\beta \cos\theta}{4aD} = 0.0152 \ \left(\text{Lin nm}^{-1}\right), \tag{4}$$

where higher values of δ indicate lower crystallinity levels of the films and amount of defects in the structure.

3.5. Studying the surface structure of molybdenum disulfide MoS_2-Tablet using AFM atomic force microscopy

Using atomic force microscopy AFM, a microscopic picture of the surface of the tablets prepared from molybdenum sulfide powder (MoS_2-Tablet) was taken, where we used different sizes and the same area of the sample surface (3 μm × 3 μm) (1.01 μm × 1.01 μm).

These images showed the shape of the surface atomic clusters on the surface, where the average size of the atomic clusters formed in the structure of the surface of the MoS_2-Tablet was determined, as the formed sizes ranged between 50 – 150 nm as shown in Fig. 4, where the crystalline phases of MoS_2 are formed under the process of hydraulic pressure.

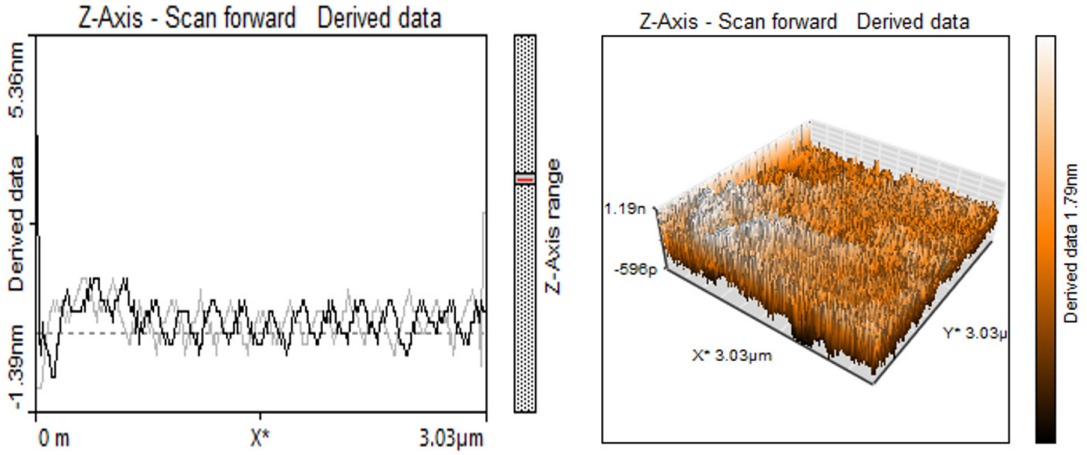

(a) (b)

FIG. 4. AFM images of tablet molybdenum disulfide at two scales (3 μm × 3 μm), (1.01 μm × 1.01 μm)

3.6. Measurements of alternating current (AC)

Alternating current measurements (capacitance, conductivity, electrical resistance, and parallel resistance (R_p values of the nanostructures were studied using a LRC meter within a frequency range 20 Hz – 1 MHz and applying an alternating potential 3 V at a room temperature $T = 11$ °C.

3.6.1. Electrical parallel capacitance C_p. Parallel capacitance (C_p) measurements as a function of frequency (F) under constant temperature ($T = 11$ °C) showed a sharp decrease in the C_p value with increasing frequency within the range 20 Hz – 16 kHz, after which it decreases. Parallel capacitance gradually as shown in Fig. 5, where the capacitance is $C_p = 4500$ pF at frequency $F = 20$ Hz, and decreases dramatically. Very close to the value $C_p = 44.8$ pF is obtained at the frequency 16 kHz, where the capacitance changes become constant with increasing frequency from 1000 –16 kHz.

But in the frequency range 16 – 300 kHz, the changes in the parallel electrical capacitance C_p become gradual, ranging from $C_p = 44.8$ – 17 pF The changes in the parallel electrical capacitance C_p become slight and almost constant in the frequency range 300 – 1000 kHz, where the changes in the capacitance corresponding to this frequency range is as follows: $C_p = 14$ – 17 pF, as shown in Fig. 6.

This change in the electrical capacitance of the molybdenum sulfide discs in terms of frequency is explained by the return to the polarization mechanisms that occur at different frequencies. At frequency less than 300 KHz, the four polarization mechanisms (electronic, ionic, orientational spacecharge) occur. This polarization includes displacement of charges either by orientation (i.e. directional polarization) or by migration of charge carriers (such as hopping polarization or space charge). The parallel capacitance relation with the loss factor is given by the relation (5) [17, 18]:

$$D = \frac{1}{W \cdot R_P \cdot C_p}. \tag{5}$$

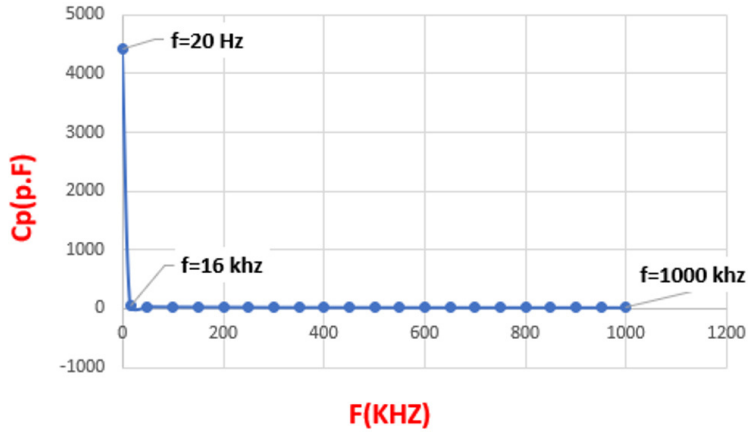

FIG. 5. Variations of the parallel electrical capacitance (C_p) with frequency (F)

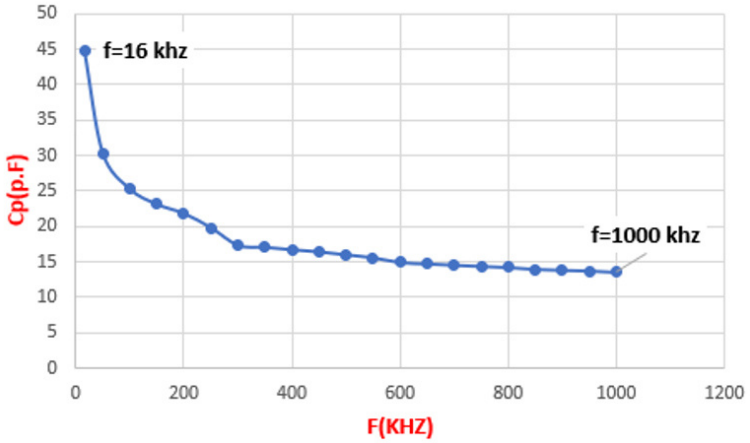

FIG. 6. Variations of the parallel electrical capacitance (C_p) with frequency (F) between 16 – 300 kHz

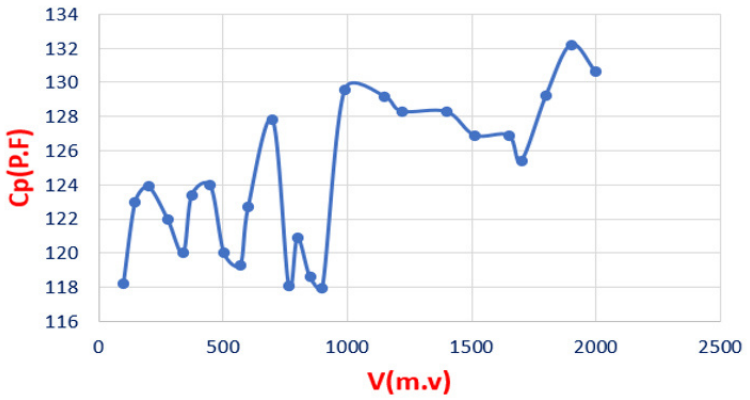

FIG. 7. Variations of the parallel electrical capacitance C_p, with the electric potential V

3.6.2. Parallel capacitance changes C_p with potential V. When studying the changes of the parallel capacitance C_p with the change in the potential applied to MoS_2-Tablet, it was shown that the electrical capacitance values of crystalline molybdenum change with the change of electrical potential as shown in Fig. 7.

For applied potentials 145 – 900 mV, it is similar to an alternating current wave, while for higher potentials in a range of 1000 – 2000 mV, the electrical capacitance changes are semi-regular and ranges between 132 –125 pF.

3.6.3. Determining the type of semiconductor. To determine the type of semiconductor, the electrical capacitance changes were studied with the electric potential within the range of 0.05 – 1.8 V, and at a frequency of $F = 1$ KHz and at a room temperature $T = 9$ °C. By plotting the changes of $\left(\frac{1}{C} - \frac{1}{2C_0}\right)^2$ in terms of V (Volt) according to the relation (8):

$$\left(\frac{1}{C} - \frac{1}{2C_0}\right)^2 = \frac{2}{\varepsilon e\,(N_d - N_a)}(\Psi + V). \tag{6}$$

From Fig. 8, we notice that the slope of the graph line representing the changes is negative and therefore $N_a \gg N_d$, and this means that the semiconductor is of type p.

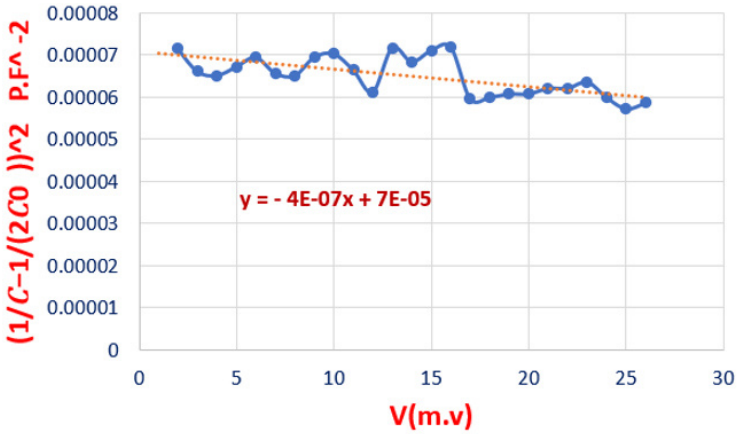

FIG. 8. $\left(\frac{1}{C} - \frac{1}{2C_0}\right)^2$ changes with potential

3.6.4. Parallel Electrical Resistance (RP) of MoS_2-Tablet. Measurements of the parallel resistance RP of crystallized molybdenum disulfide MoS_2-Tablet show semi-regular behavior which is completely different from the behavior of morpho molybdenum sulfide, where it was found that the electrical resistance RP decreases in the range 1500 – 108 KΩ in the low frequency diapason 20 Hz – 100 KHz. Then the resistance increases again at the frequency 200 KHz and the resistance value becomes 130 KΩ and then it returns to decreasing as shown in Fig. 9, the RP resistance changes become constant and range from 30 – 70 KΩ in the frequency range 1000 KHz – 250 KHz.

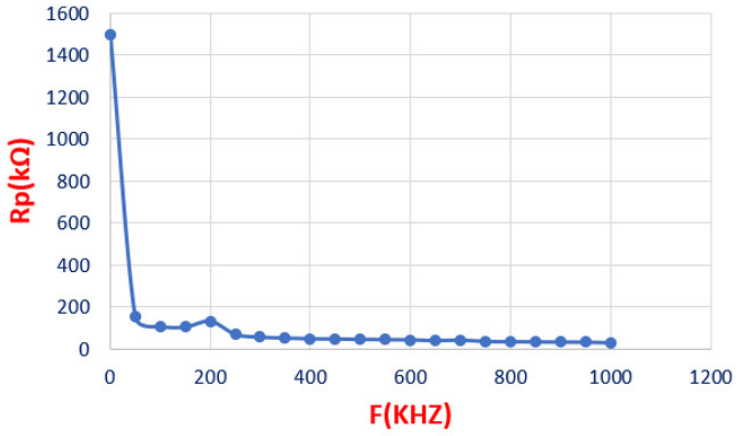

FIG. 9. Parallel resistance (R_P) changes with frequency intensity (F)

We note from the previous figure, that the resistance changes are a sharp decrease in the parallel resistance values RP at low frequencies and the parallel resistance changes become simple at high frequencies, and the parallel resistance is related to both the quality factor and the parallel inductance by the relation (7) [19]:

$$R_P = R_S\left(1 + Q^2\right) = QwL_P. \tag{7}$$

3.6.5. Capacitive Electrical Resistance (Xc) of MoS_2-Tablet. The measurements showed that the absolute value of the capacitive resistance of crystallized molybdenum disulfide (X_c) decreases sharply with the frequency at low frequencies, then the changes become small and gradual as shown in Fig. 10, where it is found that the changes of X_c are sharp with the frequency within a range of frequencies 20 Hz – 200 KHz, and in the range of frequencies 50 Hz – 3000 KHz the value of X_c changes gradually with increasing frequency.

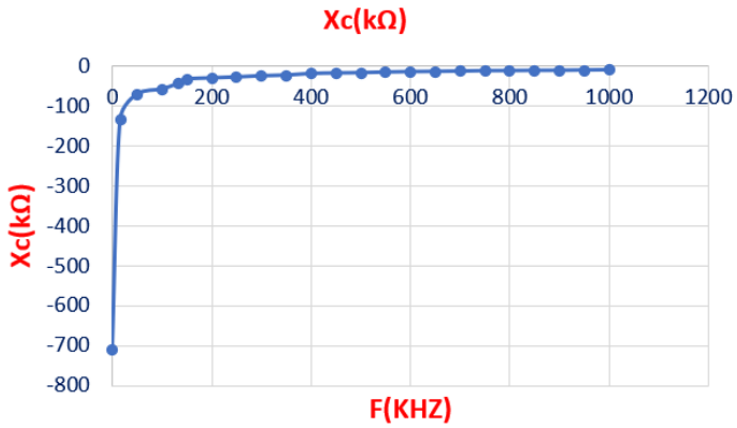

FIG. 10. Changes of capacitive resistance X_c in crystallized molybdenum disulfide with frequency F

As the frequency applied to MoS_2-Tablet increases, it leads to reducing of the capacitive resistance. Likewise, when the frequency applied to MoS_2-Tablet decreases, its capacitive resistance value increases. As the frequency increases, the MoS_2-Tablet passes more charge, which leads to a larger current flow between the electrodes, which appears as if the internal impedance (capacitive resistance) has decreased, so the value of the capacitive resistance is "frequency dependent". Whereas, the value of capacitive resistance is given by the relation:

$$X_c = \frac{-i}{\omega C},$$

where X_c is the capacitive resistance, ω is the angular frequency ($\omega = 2\pi F$), and C is the capacitance of the capacitor. Several facts are evident from this formula alone. The X_c is of an ideal capacitor, and therefore its impedance, is negative for all values of capacitance.

3.6.6. Series Electrical Capacitance (C_s). Series electrical capacitance C_s changes with frequency F. Measurements of the series electrical capacitance C_s in terms of frequency F showed a sharp drop in the value of electrical capacitance $C_p = 70 - 980$ pF (see Fig. 11) with an increase in frequency within the range 20 Hz – 16 kHz.

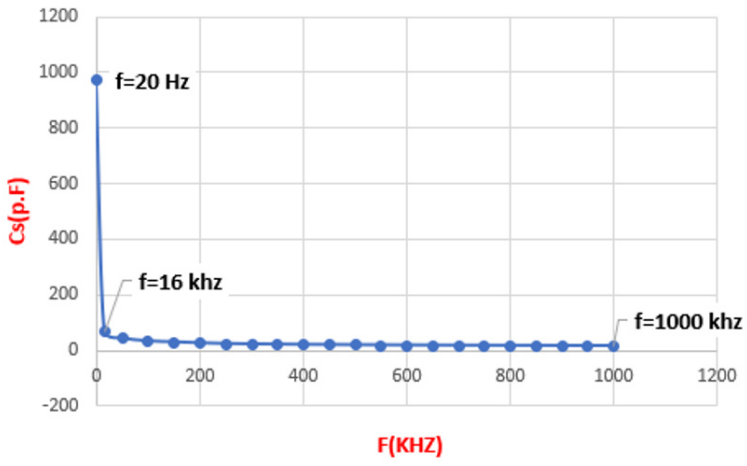

FIG. 11. Variations of series electrical capacitance C_s with frequency F

The series capacitance C_s decreases gradually with the frequency increase from 16 – 300 kHz, under a constant temperature $T = 10$ °C, as shown in Fig. 12.

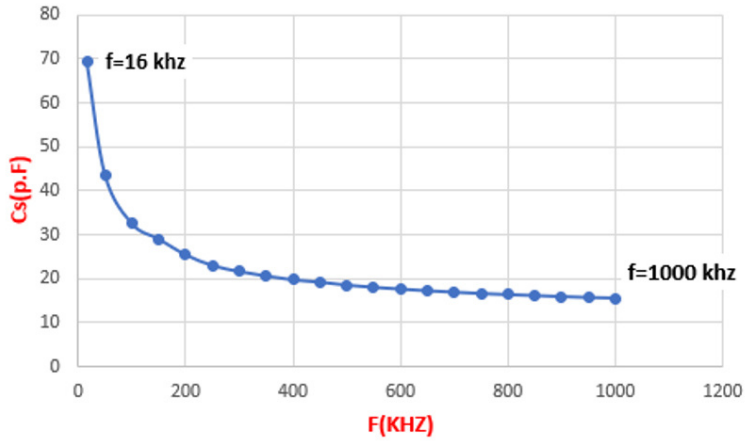

FIG. 12. Variations of series electrical capacitance C_s with frequency F between 16 – 1000 kHz

The series electrical capacitance changes C_s become slight and almost constant at the frequency range 300 – 1000 kHz, where the corresponding capacitance changes for this frequency range are $C_s = 20$ – 15 pF as shown in the Fig. 12.

3.6.7. Series electrical capacitance variations C_s with potential V. When studying the changes of the series capacitance C_s with the change of the applied potential on MoS_2-Tablet, it was found that the changes of the series electrical capacitance range from increasing and decreasing within the range of low potential 50 – 350 mV as shown in Fig. 13. The series capacitance increased gradually and slightly with the increase of the applied potential in the range 250 – 900 mV, C_s having a sharp dip for the potential 950 mV as shown in Fig. 13.

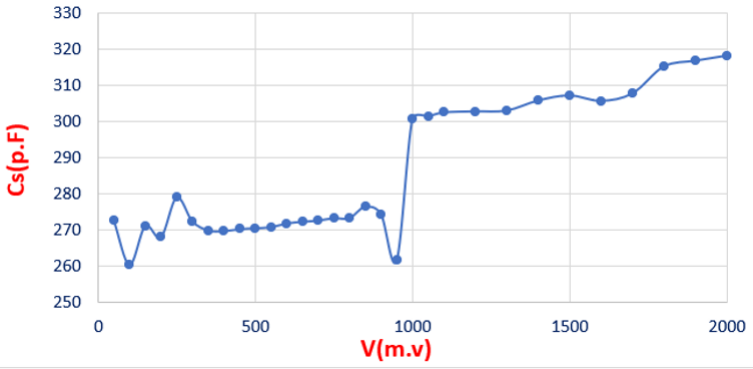

FIG. 13. Variations of the parallel electrical capacitance C_p with the electrical potential V

The series capacitance changes becomes increasing 300 – 320 pF with applied potential 1000 – 2000 mV as shown in Fig. 13.

3.6.8. Parallel induction study (L_p) of crystalline molybdenum sulfide MoS_2-Tablet. From studying the changes of the parallel inductance L_p with the frequency F, it was found that the absolute value of L_p decreases very sharply from the value 48390 mH to the value 2 mH at low frequency $F = 0.02$ – 50 KHz as shown in Fig. 14.

For values of frequency of 50 – 1000 KHz, the parallel inductance changes become decreases and slight as shown in Fig. 15, until the absolute value of the parallel inductance ranging between $L_p = 0.1$ – 0.02 mH at the frequency 1000 KHz. However, there is a response and a jump in the parallel inductance at frequency 350 KHz, where value of the parallel inductance becomes $L_p = 0.267$ mH as shown in Fig. 15. Parallel inductiveness is related to the quality factor by the relation (8) [20]:

$$Q = \frac{1}{D} = \frac{wL_S}{R_S} = \frac{R_P}{wL_P}. \tag{8}$$

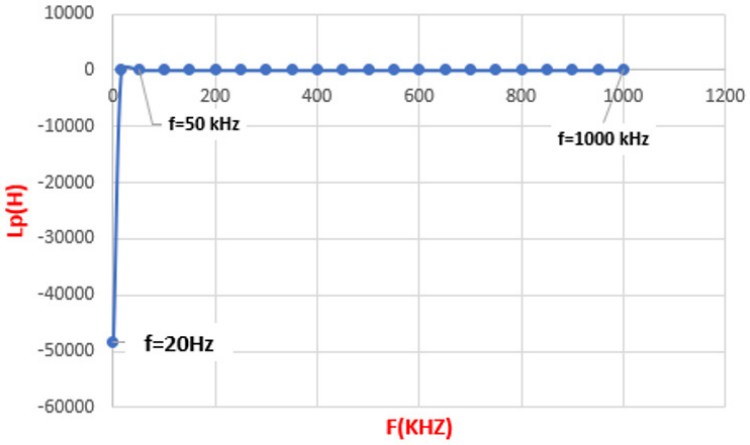

FIG. 14. Variations of parallel inductance L_p with frequency F

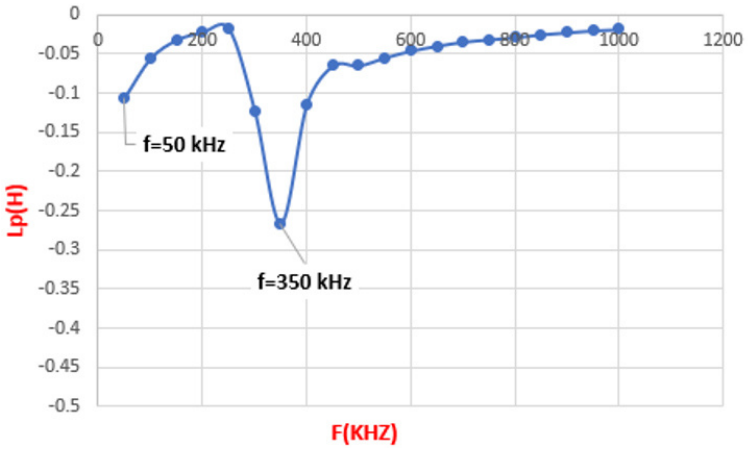

FIG. 15. Variations of Parallel Inductance L_p with Frequency F between 50 – 1000 kHz

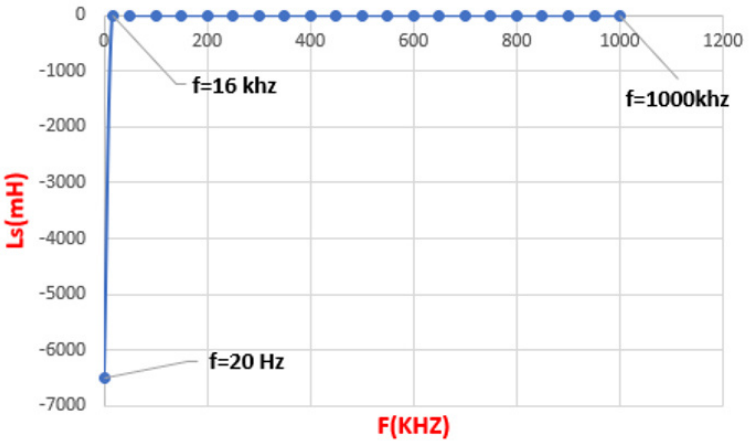

FIG. 16. Variations of series inductance L_s with frequency F

3.6.9. Series induction study Ls of crystalline molybdenum disulfide (MoS_2-Tablet). From studying the parallel inductance changes of L_s with frequency F, it was found that the absolute value of L_s decreases very sharply from the value of 6500 mH to the value of 1.3 mH at low frequency $F = 0.02 - 16$ KHz as shown in Fig. 16.

For frequencies in the range $F = 100 - 1000$ KHz we find that the changes in series inductance become slight and gradual as the absolute value of the inductivity of L_s is between 0.07 – 0.01 mH. We notice the appearance of a peak and increase in series inductance at frequency $F = 650$ KHz to value 0.367 as shown in Fig. 17.

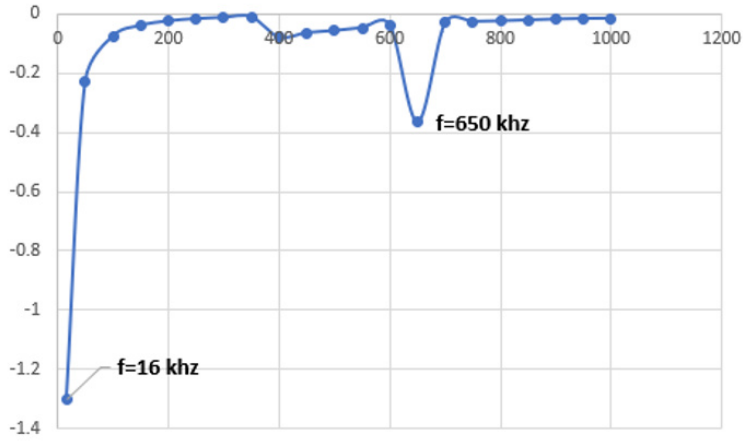

FIG. 17. Variations of series inductance L_s with frequency F between 16 – 1000 KHz

4. Conclusion

(1) The XRD spectrum of the powder prepared from MoS_2 showed that its structure is morphic and amorphous, and with a process using a hydraulic press, the structure becomes crystalline. We observe the appearance of a preferred crystallization level 200 at $2\theta = 14.6^\circ$.

(2) The AFM images show that the surface atomic clusters of the surface of the molybdenum sulfide sample (MoS_2-Tablet) range between 50 – 150 nm, where it is clear that the crystalline phases of MoS_2 are formed under the process of hydraulic pressure.

(3) Measurements of the parallel electrical capacitance (C_p) in terms of frequency (F) of (tablet-MoS_2) showed a sharp drop in the value of the electrical capacitance C_p with an increase in frequency within the range 20 Hz – 16 kHz.

(4) Measurements of the series electrical capacitance (C_s) in terms of frequency (F) showed a sharp drop in the value of electrical capacitance $C_p = 980 - 70$ pF, after which the series capacitance C_s decreases gradually, where the capacitance changes become constant with the frequency increase from 200 – 1000 KHz.

References

[1] Kuc B., Heine T. On the Stability and Electronic Structure of Transition Metal Dichalcogenide Monolayer Alloys Mo1-x Xx-S2-y Sey with X = W, Nb. *Electronics*, 2016, **5**, P. 1201–1213.

[2] Voiry D., Mohite A., Chhowalla M. Phase engineering of transition metal dichalcogenides. *Chem. Soc. Rev.*, 2015, **44**, 2702.

[3] Mak K.F., Lee C., Hone J., Shan J., Heinz T.F. Atomically thin MoS_2: anew direct-gap semiconductor. *Phys. Rev. Lett.*, 2010, **105**, 136805.

[4] Radisavljevic, Radenovic A., Brivio J., Giacometti V., Kis A. Preparation and Application of Graphene-like Tungsten Sulfide Thin Films by Chemical Vapor Deposition. *Nat Nano*, 2011, **6**, P. 147–152.

[5] Hernandez Ruiz K., Liu J., Tu R., Li M., Zhang S., Vargas Garcia J.R., Mu S., Li H., Goto T., Zhang L. Effect of microstructure on HER catalytic properties of MoS_2 vertically standing nanosheets. *J. Alloys Compd*, 2018, **747**, 100.

[6] Deng Z.H., Li L., Ding W., Xiong K., Wei Z.D. Synthesized ultrathin MoS_2 nanosheets perpendicular to graphene for catalysis of hydrogen evolution reaction. *Chem. Commun.*, 2015, **51**, 1893.

[7] Wang Y., Yu L., Lou X.W. Synthesis of highly uniform molybdenum–glycerate spheres and their conversion into hierarchical MoS_2 hollow nano spheres for lithium-ion batteries. *Angew. Chem. Int. Ed.*, 2016, **55**, 7423.

[8] Mervin Zhao, Ziliang Ye, Ryuji Suzuki, Yu Ye, Hanyu Zhu, Jun Xiao, Yuan Wang, Yoshihiro Iwasa, Xiang Zhang. Atomically phase-matched second-harmonic generation in a 2D crystal. *Light: Science & Applications*, 2016, **5**, e16131.

[9] Guo C., et al. Observation of superconductivity in 1T'-MoS_2 nanosheets. *J. of Materials Chemistry C*, 2017, **5**, 10855.

[10] Fang Y., et al. Structural determination and nonlinear optical properties of MoS_2 compound. *JACS*, 2019, **141**, 790.

[11] Al-Hussein H., Al-Sharr J., Othman S., Khamisi H. Study of the electronic, (structural and optical) properties of MoS_2 nanostructures. *Aleppo University Research J.*, 2023, **170**, 1656.

[12] Mmantsae Diale, Nolwazi Nombona, Pannan I. Kyesmen, Lebogang Manamela. Electrically Enhanced Transition Metal Dichalcogenides as Charge Transport Layers in Metallophthalocyanine-Based Solar Cells. *Frontiers in Chemistry*, 2020, **8**.

[13] Sathiyan S., Ahmad H., Chong W.Y., Lee S.H., Sivabalan S. Evolution of the Polarizing Effect of MoS_2. *IEEE Photonics J.*, 2015, **7** (6), 6100610.

[14] Callegro L. *Electrical Impedance: Principles, Measurement, and Applications*. New York: CRC Press, 2013.

[15] Sathe D.J., Chate P.A., Subrao Subrao Sargar, Kite S.V. Properties of chemically-deposited nanocrystalline MoS_2 thin films. *J. of Materials Science: Materials in Electronics*, 2016, **27** (4).
[16] Singh J., Verma N.K. Structural, optical and magnetic properties of cobalt-doped CdSe(MPA) nanoparticles. *Bull. Mater. Sci.*, 2014, **37** (3), P. 541–547.
[17] Oliver B.M., Cage J.M. *Electronic Measurement and Instrumentation*, McGraw-Hill, New York, 1971.
[18] Grover F. *Inductance Calculations (Dover Books on Electrical Engineering)*, Dover Publications, 2009.
[19] Jun He, Laizhou Song, Jiayun Yan, Ning Kang, Yingli Zhang, Wei Wang. Hydrogen Evolution Reaction Property in Alkaline Solution of Molybdenum Disulfide. *Metals*, 2017, **7** (6), 211.
[20] Pawelec B., Navarro R., Fierro J.L.G., Vasudevan P.T. Studies of molybdenum sulfide catalyst ex ammonium tetrathiomolybdate: effect of pretreatment on hydrodesulfurization of dibenzothiophene. *Applied Catalysis A: General*, 1998, **168**, P. 205–217.

Submitted 17 September 2023; revised 26 September 2023; accepted 21 November 2023

Information about the authors:

Hussein Alhussein – Department of Physics, faculty of Science, University of Aleppo, Syria; ORCID 0009-0007-4525-9664; husianphy990@gmail.com

Jamal Qasim AlSharr – Department of Physics, faculty of Science, University of Aleppo, Syria;

Sawsan Othman – Department of Physics, faculty of Science, University of Aleppo, Syria;

Hassan AlKhamisy – Institute of Health Technology, University of Aleppo, Syria; ORCID 0009-0006-5276-6560;

Conflict of interest: the authors declare no conflict of interest.

NANOSYSTEMS:
PHYSICS, CHEMISTRY, MATHEMATICS

Original article

Sozarukova M.M., et al. *Nanosystems: Phys. Chem. Math.*, 2023, **14** (6), 644–651.
http://nanojournal.ifmo.ru
DOI 10.17586/2220-8054-2023-14-6-644-651

Cerium dioxide nanoparticles modulate the oxidative metabolism of neutrophils upon blood irradiation with a pulsed broadband UV source

Madina M. Sozarukova[1,a], Polina A. Chilikina[2,b], Dmitry O. Novikov[3,c], Elena V. Proskurnina[4,d], Alexander E. Baranchikov[1,e], Vladimir K. Ivanov[1,f]

[1]Kurnakov Institute of General and Inorganic Chemistry of the Russian Academy of Sciences, Moscow, Russia
[2]Scientific and Industrial Enterprise "MELITTA" Ltd, Moscow, Russia
[3]Joint Stock Company "Experimental Factory for Scientific Engineering of the Russian Academy of Sciences", Moscow region, Chernogolovka, Russia
[4]Research Centre for Medical Genetics, Moscow, Russia

[a]s_madinam@bk.ru, [b]p.chilikina@gmail.com, [c]zerooo@list.ru, [d]proskurnina@gmail.com, [e]a.baranchikov@yandex.ru, [f]van@igic.ras.ru

Corresponding author: Vladimir K. Ivanov, van@igic.ras.ru

PACS 68.65.k, 81.20.n, 82.70.Dd, 87.85.Rs

ABSTRACT The effect of CeO_2 nanoparticles on the oxidative activity of neutrophils under UV irradiation with a pulsed broadband UV source (210 mJ/cm^2) was analyzed. The effects of citrate-stabilized CeO_2 sol on spontaneous and stimulated by phorbol-12-myristate-13-acetate (PMA) and *N*-formylmethionyl-leucyl-phenylalanine (fMLP) luminol-dependent chemiluminescence of neutrophils were evaluated. The activating effect of CeO_2 nanoparticles on the spontaneous and suppressive effect on the stimulated chemiluminescence of blood neutrophils from apparently healthy donors was shown, with the most pronounced activating effect of CeO_2 nanoparticles revealed in the blood sample with initially high radical-producing cell activity. Under UV irradiation of blood at a dose of 210 mJ/cm^2 CeO_2 nanoparticles enhance both spontaneous and stimulated radical-producing function of neutrophils. Probably, the suppressive and activating effects of citrate-stabilised cerium dioxide sol may be due to the antioxidant activity of CeO_2 nanoparticles with respect to hypochlorite ions and prooxidant activity with respect to hydrogen peroxide.

KEYWORDS nanozymes, cerium dioxide nanoparticles, neutrophils, UV radiation, pulsed xenon UV lamp, chemiluminescence

ACKNOWLEDGEMENTS This work was supported by the Russian Science Foundation (project 21-73-00251).

FOR CITATION Sozarukova M.M., Chilikina P.A., Novikov D.O., Proskurnina E.V., Baranchikov A.E., Ivanov V.K. Cerium dioxide nanoparticles modulate the oxidative metabolism of neutrophils upon blood irradiation with a pulsed broadband UV source. *Nanosystems: Phys. Chem. Math.*, 2023, **14** (6), 644–651.

1. Introduction

One of the promising inorganic nanobiomaterials possessing enzyme-like activity along with unique physical and chemical properties is nanoscale cerium dioxide [1–7]. Biochemical activity of CeO_2 nanoparticles, being similar to the functions of a number of natural enzymes, such as superoxide dismutase (SOD) [8–11], catalase [12–14], peroxidase [15–18], phosphatase [19], phospholipase [20], photolyase [21], uricase [22], etc., expands the prospects for their biomedical application for the prevention, diagnosis, and therapy of socially significant diseases [23–25] and requires a comprehensive analysis of the properties of nanoscale cerium dioxide, including its interaction with blood components, both alone, and as part of combination therapy, for example, with ultraviolet irradiation of blood (UVIB).

The increased interest in the therapeutic potential of ultraviolet irradiation of blood is due to the emergence of new viral infections, including SARS, MERS, SARS-CoV-2 and their resistance to existing antiviral drugs, vaccines, and antibacterial drugs [26–29]. The therapeutic efficacy of UVIB has been demonstrated in a number of diseases, including diseases of the biliary tract, viral hepatitis, etc. [27, 30]. One of the main targets of UVIB exposure are immune cells – lymphocytes (T- and B-cells), neutrophils, macrophages, monocytes, dendritic cells [26, 30]. This brings attention to ultraviolet irradiation of blood for the treatment of autoimmune diseases and as a new immunomodulatory method [27,30]. The great potential of UVIB could be additionally expanded by the use of various substances, including those based on redox-active nanomaterials that can regulate the effectiveness of UVIB treatment, uncontrolled activation of neutrophils, and other indicators.

When CeO_2 nanoparticles enter the bloodstream, neutrophil granulocytes (neutrophils) are among the first cells to interact with them [31, 32]. Neutrophils are one of the most important and most active cells of the innate immune system, providing the first line of defense and responding to various antigens and damaging factors [33, 34]. Activated cells are able to secrete into the extracellular medium various low and high molecular weight substances with immunomodulatory or toxic effects [35–37]. Neutrophils are one of the main sources of free radicals in the body [38], and the mechanisms of their interaction with redox-active nanomaterials, primarily CeO_2 nanoparticles, require further research.

Here, a high-intensity pulsed xenon lamp was used as a source of UV radiation. Today it is one of the promising light sources for UV therapy as an alternative to traditional low-pressure mercury lamps. The main advantages of pulsed xenon lamps are a wide spectral range and high peak power with a relatively short exposure time. Since the state of the surface of nanomaterials is a key factor in the interaction with neutrophils [39, 40], citrate ions were used to functionalize cerium dioxide nanoparticles. Cerium dioxide nanoparticles stabilized by citrate ions possess high biocompatibility and low toxicity, and prevent hemocoagulation [41]. Though the bioactivity of CeO_2 nanoparticles modified with citrate ions has been widely studied, there are no data on their effect on blood neutrophils under ultraviolet irradiation.

In this study, we analyzed for the first time the effect of CeO_2 nanoparticles functionalized with citrate ions on the radical-producing activity of neutrophils upon UV irradiation of blood with a high-intensity pulsed xenon lamp.

2. Materials and methods

Cerium dioxide nanoparticles functionalized with ammonium citrate in a molar ratio of 1:1 were obtained in two stages. The initial electrostatically stabilized CeO_2 sol was synthesized by the thermal hydrolysis of an aqueous solution of cerium(IV) ammonium hexanitrate ($(NH_4)_2Ce(NO_3)_6$, #215473, Sigma) [42]. A solution of $(NH_4)_2Ce(NO_3)_6$ (100 g/L) was heated at 95 °C for 24 h. The resulting yellow precipitate was washed three times with isopropanol and then redispersed in deionized water. To remove residual isopropanol, a colloidal solution of cerium dioxide was boiled for 1 h under constant stirring. The concentration of the resulting CeO_2 sol, according to thermogravimetric analysis, was 20.6 g/L (0.12 M).

At the second stage, the surface of CeO_2 nanoparticles was functionalized with ammonium citrate (#247561, Sigma). An electrostatically stabilized CeO_2 sol was added to an aqueous solution of ammonium citrate (0.12 mol/L) under stirring. After addition of CeO_2 nanoparticles to the ligand solution, stirring was continued for 30 min.

Powder X-ray diffraction analysis (XRD) of powders obtained by drying colloidal solutions of cerium dioxide at 50 °C was carried out on a Bruker D8 Advance diffractometer (CuKα radiation, θ–2θ geometry).

Analysis of the microstructure of samples of CeO_2 sols was carried out by transmission electron microscopy (TEM) on a Leo 912 AB Omega electron microscope at the accelerating voltage of 100 kV.

UV-visible absorbance spectra were obtained on a SF-2000 spectrophotometer (OKB Spektr, Russia). The wavelength range was 200 – 700 nm, the scanning step was 0.1 nm.

The average hydrodynamic particle diameter of colloidal solutions of CeO_2 and the ζ-potential were determined at 20 °C using a Photocor Complex analyzer (25 mW, diode laser, $\lambda = 650$ nm).

As a source of neutrophilic granulocytes, we used venous blood of apparently healthy donors ($n = 3$, donors 1–3) aged 22 $\pm$ 1 years, sampled in tubes with an anticoagulant – lithium heparin (17 IU/mL). Biomaterial sampling was carried out by the qualified personnel. Donors signed an informed consent to participate in the study. The design of the study was approved by the Ethics Committee of the Research Centre for Medical Genetics (Protocol #5, May 2019). The samples were stored at $+4$ °C for no more than 1.5 – 2 hours from the moment of blood sampling.

The blood samples (600 μl) were preincubated with 30 μl of 1 mM citrate-stabilized CeO_2 sol for 30 min. A device for UV irradiation of blood (UVIB) based on an L11937 pulsed lamp (Hamamatsu, Japan) (device power 30 W, nominal lamp power 20 W) was used as a source of high-intensity pulsed broadband radiation. The distance from the radiation source to the sample was 10 cm. To assess the effect of CeO_2 nanoparticles on the functional activity of blood neutrophils during irradiation, a UV irradiation dose was chosen that did not cause significant activation of neutrophils, equal to 210 mJ/cm^2.

Analysis of the radical-producing function of blood neutrophils was performed by luminol-enhanced chemiluminescence [43]. We used the protocol of two-stage stimulation of the functional activity of cells: a primer + a main stimulus. Phorbol-12-myristate-13-acetate (PMA, #P148, Sigma) was used as a primer, and *N*-formylmethionyl-leucyl-phenylalanine (fMLF, #F3506, Sigma) was used as a main stimulus. The measurements were carried out in a medium consisting of Hank's buffer (PanEco, with glucose without phenol red) with Hepes (50 μM, 4-(2-hydroxyethyl)-1-piperazineethanesulfonic acid, #H3375, Sigma).

Cell luminescence was recorded at room temperature on a 12-channel Lum-1200 chemiluminometer (DISoft, Russia). An aliquot of 450 μl of medium (Hanks/Hepes) with 25 μl of blood was previously incubated with CeO_2 citrate sol. Next, 25 μl of 1 mM luminol solution (#123072, Sigma) was added to a cuvette. Spontaneous chemiluminescence of blood cells was recorded for 10 min. Next, neutrophils were primed by adding PMA (50 ng/mL) without interrupting the recording of the analytical signal (20 min after the addition of PMA). At the final stage, the main stimulus fMLF (10 μM) was added to the blood cells, registering the chemiluminescent response of the cells for at least 60 min.

PowerGraph software (version 3.3) was used to process chemiluminograms. Both for the spontaneous chemiluminescence and for PMA+fMLF-stimulated chemiluminescence we calculated the area under the curve (AUC) (S_{lum}, $S_{\text{PMA+fMLF}}$), which is proportional to the number of produced free radicals. To assess the effects of CeO_2 nanoparticles and UV irradiation, the activation (> 1) and suppression (< 1) coefficients were calculated as the ratio of the corresponding AUC S_{lum} or $S_{\text{PMA+fMLF}}$ to the control value (S_0). The response of neutrophils without exposure to CeO_2 nanoparticles and UV irradiation was considered as a control.

3. Results and discussion

3.1. Physicochemical characteristics of CeO_2 nanoparticles

The X-ray patterns of the dried initial CeO_2 sol (pH $\sim$ 3) obtained by the thermal hydrolysis of cerium(IV) ammonium hexanitrate and the citrate-stabilized colloidal solution of cerium dioxide are shown in Fig. 1a.

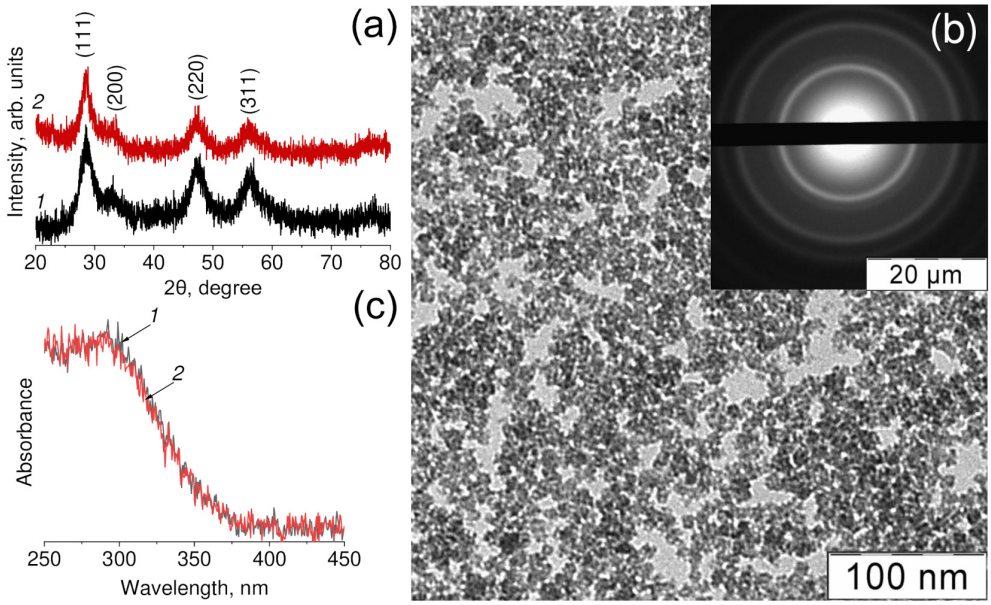

FIG. 1. XRD patterns of CeO_2 nanopowders (a); TEM images and electron diffraction data (inset) of CeO_2 nanoparticles (b); UV-visible absorption spectra of CeO_2 sols (c). Samples of nanoscale cerium dioxide: bare CeO_2 sol (1) and citrate-stabilized CeO_2 sol (2).

According to XRD data (Fig. 1a), CeO_2 sols contain single-phase cerium dioxide (PDF2 34-0394). The size of CeO_2 nanoparticles, estimated from the Scherrer equation, was 3.2 nm. The data on the particle size and the phase composition of the obtained material were confirmed by the results of analysis of the colloidal solution of CeO_2 by transmission electron microscopy (TEM) and electron diffraction (Fig. 1b).

Absorption spectra in the UV-visible region of the CeO_2 sols are shown in Fig. 1c. The appearance of an absorption band in the region of 280 – 300 nm confirms that the sols do contain nanoscale cerium dioxide.

The average hydrodynamic diameters of particles equal to 11 nm and 14 nm, respectively, were determined by dynamic light scattering for the samples of initial and citrate-stabilized CeO_2 sols. Small changes in the hydrodynamic diameter upon the interaction of cerium dioxide nanoparticles with the ligand indicate approximately the same degree of particle aggregation in colloidal solutions of CeO_2. Analysis of the electrokinetic properties of CeO_2 sols showed that functionalization of the surface of nanoscale cerium dioxide with citrate ions leads to a decrease in the absolute value of ζ-potential from $+41.2 \pm 1.5$ mV to $+15.3 \pm 0.9$ mV.

3.2. Analysis of the effect of CeO_2 nanoparticles on the radical-producing activity of neutrophils

Radical-producing activity of neutrophilic leukocytes was analyzed by luminol-enhanced chemiluminescence method using a two-step stimulation protocol [43, 44].

In the first series of experiments, we measured spontaneous chemiluminescence of neutrophils (Fig. 2a,c). In the second series, we measured chemiluminescence stimulated by the sequential addition of PMA and fMLF (Fig. 2b,d).

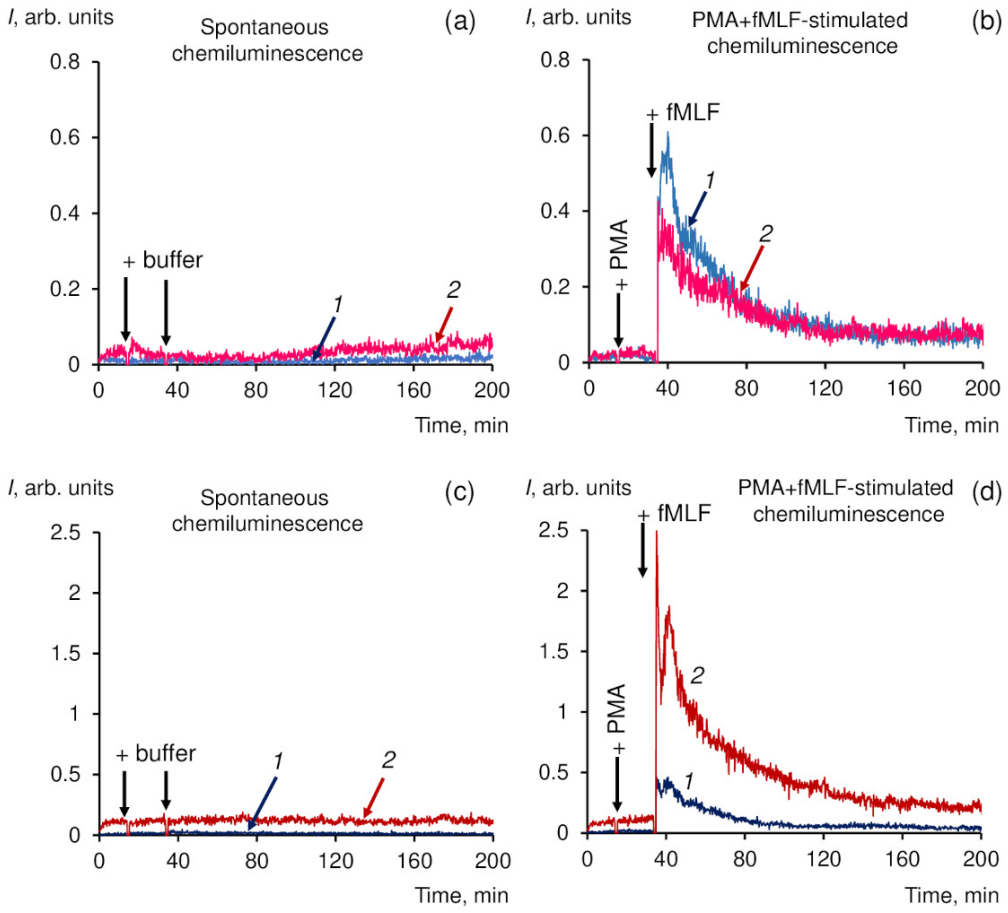

FIG. 2. The chemiluminograms of neutrophil response before (a, b) and after (c, d) exposure to UV irradiation (210 mJ/cm^2). Samples: control (without CeO_2) (1), with citrate-stabilized CeO_2 sol (2).

As for spontaneous chemiluminescence, the signal intensity was low ($I < 0.5$ arb. units, Fig. 2a,c). The sequential addition of the stimuli (PMA and fMLF) with various stimulation mechanisms leads to the extended chemiluminescent response of neutrophils (Fig. 2b,d). Stimulated chemiluminescence is a result of neutrophil priming (pre-activation) with PMA and subsequent activation with fMLF (Fig. 2b,d). As a result, neutrophils produce various types of reactive oxygen species (ROS), mainly, hydrogen peroxide and hypochlorite [45]. An increase in the intensity of chemiluminescence qualitatively indicates an increase in the radical-producing function of neutrophils after the addition of stimuli (Fig. 2b,d).

The used concentration of the colloidal CeO_2 solution of 50 μm does not affect cell viability [46–48]. To quantitatively assess the effect of CeO_2 nanoparticles on the neutrophils response before and after UV exposure, we calculated the AUC values (S_{lum}, $S_{\text{PMA+fMLF}}$), which are proportional to the amount of formed free radicals (Fig. 3).

To assess the effect of CeO_2 nanoparticles, including in combination with UV radiation, based on the ROS-producing activity of neutrophils (S_{lum}, $S_{\text{PMA+fMLF}}$, Fig. 3), the activation and suppression coefficients were calculated. A coefficient value > 1 indicates activation of the radical-producing function of neutrophils, and a coefficient value < 1 indicates suppression of the function (Table 1).

In the absence of UV radiation, the citrate-stabilized CeO_2 sol had an activating effect on the spontaneous chemiluminescence of neutrophils (Fig. 3a, Table 1). The most prominent effect of enhancing the ROS-producing activity of cells in the presence of CeO_2 nanoparticles was demonstrated by the sample from donor 3. It should be noted that in a series of control measurements (without CeO_2 nanoparticles), the sample from donor 3 was characterized by approximately 3.5 times higher radical-producing activity compared to the samples from donor 1 and donor 2. In turn, this could be the reason for the enhancement of stimulated chemiluminescence by CeO_2 nanoparticles from donor 3 (Fig. 3b, Table 1). At the same time, in the samples from donor 1 and donor 2, the suppressor effect of the citrate-stabilised CeO_2 sol was registered (Fig. 3b, Table 1). The most probable explanation for the observed effect is the competition between immunomodulatory and antioxidant effects caused by CeO_2 nanoparticles. On the one hand, nanoscale CeO_2 should induce an immune response; on the other hand, having antioxidant properties [49–51], CeO_2 nanoparticles are able to prevent the activation of the radical-producing function of neutrophils. Preincubation of neutrophils with citrate-stabilized CeO_2 sol demonstrates that cerium dioxide nanoparticles themselves can act as stimuli (Fig. 3a, Table 1). Obviously, the stimulating ability of nanoscale CeO_2 depends on the state of neutrophils and the immune system (presence of cytokines, etc.).

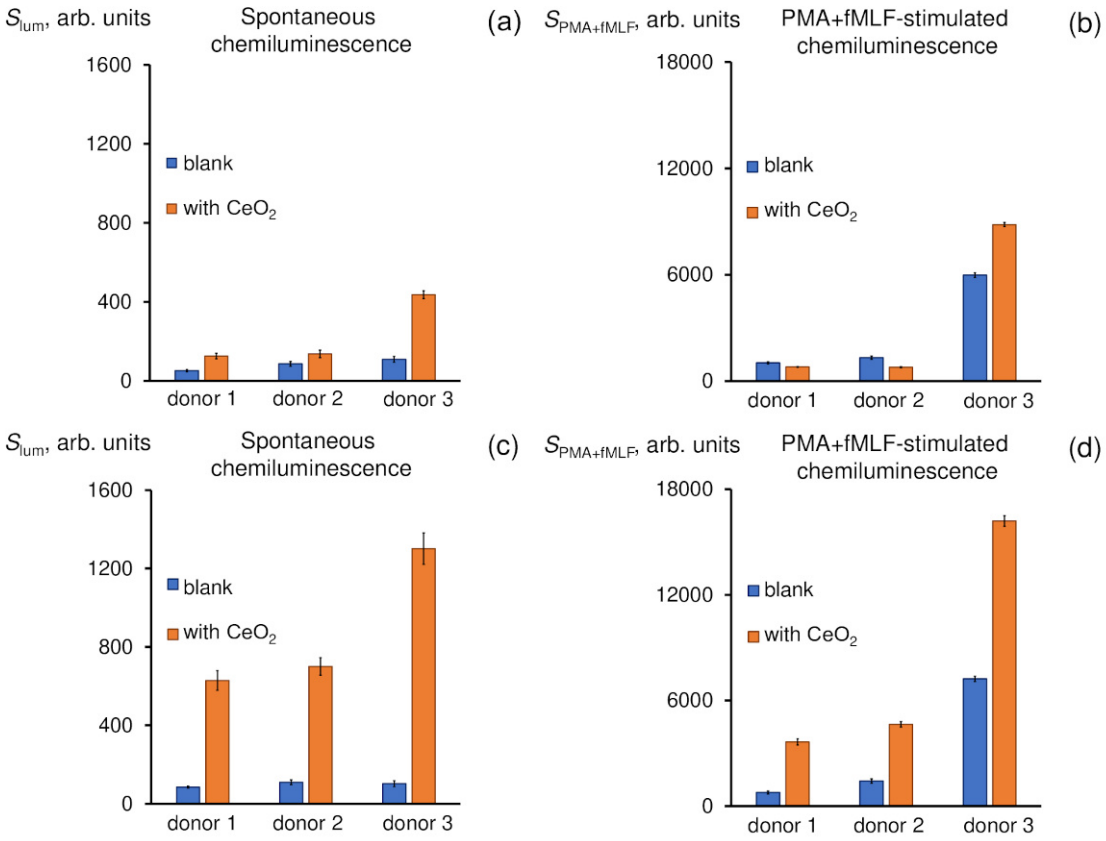

FIG. 3. Distribution histograms of indicators of radical-producing activity of neutrophils S_{lum} and $S_{PMA+fMLF}$, calculated from the data of spontaneous and stimulated chemiluminescence, respectively; before (a, b) and after (c, d) UV exposure (210 mJ/cm^2).

TABLE 1. Effect of citrate-stabilized CeO_2 nanoparticles (CeO_2 NPs) on spontaneous and stimulated chemiluminescence (CL) of neutrophils before and after UV exposure (average values of the activation and suppression coefficients are given)

CL	Spontaneous CL	PMA+fMLF-stimulated CL	Spontaneous CL	PMA+fMLF-stimulated CL
Factor determining the effect	CeO_2 NPs		CeO_2 NPs + UV exposure	
donor 1	2.4	0.8	12.2	4.5
donor 2	1.6	0.6	8.1	6.0
donor 3	4.0	*1.5	12.0	1.8

* – activation

The few available studies demonstrate the opposite effect – a decrease in ROS production by immune cells in the presence of CeO_2 nanoparticles [52,53]. Eriksson *et al.* showed that CeO_2 nanoparticles did not induce the production of free radicals in isolated neutrophils activated by PMA [52]. In these samples, nanoscale CeO_2 exhibited significant radical-scavenging properties [52]. Registration of the luminol-enhanced response of neutrophils makes it possible to trace the formation of the main types of free radicals. Luminol is a sensitive probe for hydrogen peroxide and hypochlorite ions [54–56] produced by NADPH oxidase (NOX2) and neutrophil myeloperoxidase. Moreover, in the absence of peroxidases, the luminescence of luminol can be caused by interaction with the superoxide anion radical [57]. In this study, it is likely that the suppressor effect in stimulated chemiluminescence in the samples from donor 1 and donor 2 could be due to the antioxidant activity of CeO_2 nanoparticles with respect to hypochlorite ions. The antioxidant activity of CeO_2 nanoparticles in relation to HOCl/ClO^- was demonstrated elsewhere [53]. The ability of nanoscale cerium dioxide to catalyze the decomposition of ClO^- ions by a reaction involving the reduction of Ce^{4+} to Ce^{3+} and the formation of

oxygen was confirmed in a series of *in vitro* and *in vivo* experiments [53, 58]. A significant decrease in myeloperoxidase activity in hepatocytes under the action of CeO_2 nanoparticles was also demonstrated [59]. Thus, the regulation of the oxidative activity of neutrophils by CeO_2 nanoparticles can occur both by direct inactivation of ROS and by suppressing the activity of cellular enzymes that produce free radicals.

In this study, it was found that the combined action of CeO_2 nanoparticles and pulsed broadband UV radiation at a dose of 210 mJ/cm^2 causes activation of neutrophils (Fig. 3c,d, Table 1). Irradiation of blood in the presence of citrate-stabilised CeO_2 sol significantly enhances both spontaneous and stimulated chemiluminescence (Fig. 3c,d). This effect can probably be due to the prooxidant activity of CeO_2 nanoparticles with respect to hydrogen peroxide. There are only few works devoted to the modulation of the oxidative metabolism of neutrophils by CeO_2 nanoparticles under UV radiation. Exposure of neutrophils to a low dose of UV radiation (500 mJ/cm^2) can enhance ROS formation due to NADPH oxidase activation [31]. In the same report, the ability of CeO_2 nanoparticles to significantly reduce the activity of NADPH oxidase and inhibit free radical processes was demonstrated. The inactivating effect of CeO_2 nanoparticles with respect to free radicals is explained by their catalase- and SOD-like properties [31]. The protective effect of CeO_2 nanoparticles against the damaging effect of UV radiation, due to the enzyme-like activity inherent in nanoscale cerium dioxide, was also observed in experiments with L929 fibroblasts [60]. According to the data, the protective effect also included an increase in the activity of cellular antioxidant enzymes in the presence of CeO_2 nanoparticles when compared with the control.

Thus, CeO_2 nanoparticles can have a variety of effects on living cells. The results obtained demonstrate the ability of CeO_2 nanoparticles to modulate the oxidative metabolism of the main cells of the immune system, neutrophils, and also to enhance the effects of UV radiation.

4. Conclusions

For the first time, the effect of CeO_2 nanoparticles (with or without UV irradiation) on free-radical producing activity of neutrophils was demonstrated. The modulating effect of citrate-stabilized CeO_2 nanoparticles reveals itself either as enhancement or inhibition of the production of free radicals by neutrophils. In the absence of additional stimuli, CeO_2 nanoparticles activate neutrophils. However, this activating effect is less than that of artificial stimuli. As for stimulated chemiluminescence of neutrophils, nanoscale cerium dioxide has the suppressive effect. Under UV irradiation of blood at a dose of 210 mJ/cm^2, CeO_2 nanoparticles enhance the radical-producing function of neutrophils. Hypothetically, the suppressing and activating effects of citrate-stabilised cerium dioxide sol may be due to the antioxidant activity of CeO_2 nanoparticles with respect to hypochlorite ions and their prooxidant activity with respect to hydrogen peroxide, respectively.

References

[1] Singh S. Cerium oxide based nanozymes: Redox phenomenon at biointerfaces. *Biointerphases*, 2016, **11** (4), 04B202.

[2] Jiang D., Ni D., et al. Nanozyme: new horizons for responsive biomedical applications. *Chem. Soc. Rev.*, 2019, **48** (14), P. 3683–3704.

[3] Singh K.R., Nayak V., et al. Cerium oxide nanoparticles: properties, biosynthesis and biomedical application. *RSC Adv.*, 2020, **10** (45), P. 27194–27214.

[4] Filippova A.D., Sozarukova M.M., et al. Peroxidase-like activity of CeO_2 nanozymes: particle size and chemical environment matter. *Molecules*, 2023, **28** (9), 3811.

[5] Ivanov V.K., Polezhaeva O.S., Tret'yakov Y.D. Nanocrystalline ceria: synthesis, structure-sensitive properties, and promising applications. *Russ. J. Gen. Chem.*, 2010, **80** (3), P. 604–617.

[6] Shcherbakov A.B., Reukov V.V., et. al. CeO_2 nanoparticle-containing polymers for biomedical applications: A review. *Polymers*, 2021, **13** (6), 924.

[7] Popov A.L., Shcherbakov A.B., et. al. Cerium dioxide nanoparticles as third-generation enzymes (nanozymes). *Nanosyst: Phys, Chem, Math.*, 2017, **8** (6), P. 760–781.

[8] Korsvik C., Patil S., et al. Superoxide dismutase mimetic properties exhibited by vacancy engineered ceria nanoparticles. *Chem. Commun. (Camb.)*, 2007, **10**, P. 1056–1058.

[9] Heckert E.G., Karakoti A., et al. The role of cerium redox state in the SOD mimetic activity of nanoceria. *Biomaterials*, 2008, **29** (18), P. 2705–2709.

[10] Baldim V., Bedioui F., et al. The enzyme-like catalytic activity of cerium oxide nanoparticles and its dependency on Ce^{3+} surface area concentration. *Nanoscale*, 2018, **10** (15), P. 6971–6980.

[11] Sozarukova M.M., Shestakova M.A., et al. Quantification of free radical scavenging properties and SOD-like activity of cerium dioxide nanoparticles in biochemical models. *Rus. J. Inorg. Chem.*, 2020, **65**, P. 597–605.

[12] Pirmohamed T., Dowding J.M., et al., Nanoceria exhibit redox state-dependent catalase mimetic activity. *ChemComm.*, 2010, **46** (16), P. 2736–2738.

[13] Singh R., Singh S. Role of phosphate on stability and catalase mimetic activity of cerium oxide nanoparticles. *Colloids Surf. B Biointerfaces*, 2015, **132**, P. 78–84.

[14] Singh R., Singh S. Redox-dependent catalase mimetic cerium oxide-based nanozyme protect human hepatic cells from 3-AT induced acatalasemia. *Colloids Surf. B Biointerfaces*, 2019, **175**, P. 625–635.

[15] Jiao X., Song H., et al., Well-redispersed ceria nanoparticles: promising peroxidase mimetics for H_2O_2 and glucose detection. *Anal. Methods*, 2012, **4** (10), P. 3261–3267.

[16] Ansari A.A., Solanki P.R., Malhotra B. Hydrogen peroxide sensor based on horseradish peroxidase immobilized nanostructured cerium oxide film. *J. Biotechnol.*, 2009, **142** (2), P. 179–184.

[17] Sozarukova M.M., Proskurnina E.V., Ivanov V.K. Prooxidant potential of CeO_2 nanoparticles towards hydrogen peroxide. *Nanosyst: Phys, Chem, Math.*, 2021, **12** (3), P. 283–290.
[18] Filippova A.D, Sozarukova M.M., et al. Low-Temperature Inactivation of Enzyme-like Activity of Nanocrystalline CeO_2 Sols. *Rus. J. Inorg. Chem.*, 2022, **67** (12), P. 1948–1955.
[19] Liu H., Liu J. Self-limited Phosphatase-mimicking CeO_2 Nanozymes. *Chem.Nano.Mat*, 2020, **6** (6), P. 947–952.
[20] Khulbe K., Karmakar K., et al. Nanoceria-based phospholipase-mimetic cell membrane disruptive antibiofilm agents. *ACS Appl. Bio Mater.*, 2020, **3** (7), P. 4316–4328.
[21] Tian Z., Yao T., et al. Photolyase-like catalytic behavior of CeO_2. *Nano Lett.*, 2019, **19** (11), P. 8270–8277.
[22] Liu D., Yang P., et al. Study on performance of mimic uricase and its application in enzyme-free analysis. *Anal. Bioanal. Chem.*, 2021, **413** (26), P. 6571–6580.
[23] Celardo I., Pedersen J.Z., et al. Pharmacological potential of cerium oxide nanoparticles. *Nanoscale*, 2011, **3** (4), P. 1411–1420.
[24] Ciccarese F., Raimondi V., et al. Nanoparticles as tools to target redox homeostasis in cancer cells. *Antioxidants*, 2020, **9** (3), 211.
[25] Sun W., Yang Y. Recent advances in redox-responsive nanoparticles for combined cancer therapy. *Nanoscale Adv.*, 2022, **4** (17), P. 3504–3516.
[26] Hamblin M.R. Ultraviolet irradiation of blood: "the cure that time forgot"? *Adv. Exp. Med. Biol.*, 2017, **996**, P. 295–309.
[27] Ahmad S.I. *Ultraviolet light in human health, diseases and environment*. Springer International Publishing, Cham, 2017, 365 p.
[28] Heilingloh C.S., Aufderhorst U.W., et al. Susceptibility of SARS-CoV-2 to UV irradiation. *Am. J. Infect. Control*, 2020. **48** (10), P. 1273–1275.
[29] Hessling M., Hönes K., et al. Ultraviolet irradiation doses for coronavirus inactivation–review and analysis of coronavirus photoinactivation studies. *GMS Hyg. Infect. Control*, 2020, **15**.
[30] Boretti A., Banik B., Castelletto S. Use of ultraviolet blood irradiation against viral infections. *Clin. Rev. Allergy Immunol.*, 2021, **60**, P. 259–270.
[31] Peloi K.E., Ratti B.A., et al. Engineered nanoceria modulate neutrophil oxidative response to low doses of UV-B radiation through the inhibition of reactive oxygen species production. *J. Biomed. Mater. Res. A*, 2021, **109** (12), P. 2570–2579.
[32] Lin M.-H., Lin C.-F., et al. The interplay between nanoparticles and neutrophils. *J. Biomed. Nanotechnol.*, 2018, **14** (1), P. 66–85.
[33] Nauseef W.M., Borregaard N. Neutrophils at work. *Nat. Immunol.*, 2014, **15** (7), P. 602–611.
[34] Mayadas T.N., Cullere X., Lowell C.A. The multifaceted functions of neutrophils. *Annu. Rev. Pathol.*, 2014, **9**, P. 181–218.
[35] Knaapen A.M., Güngör N., et al. Neutrophils and respiratory tract DNA damage and mutagenesis: a review. *Mutagenesis*, 2006, **21** (4), P. 225–236.
[36] Deniset J.F., Kubes P. Recent advances in understanding neutrophils. *F1000Res.*, 2016, **5**, 2912.
[37] Boni B.O.O., Lamboni L. Immunomodulation and cellular response to biomaterials: the overriding role of neutrophils in healing. *Mater. Horiz.*, 2019, **6** (6), P. 1122–1137.
[38] Nguyen G.T., Green E.R., Mecsas J. Neutrophils to the ROScue: mechanisms of NADPH oxidase activation and bacterial resistance. *Front. Cell. Infect. Microbiol.*, 2017, **7**, 373.
[39] Chakraborty A., Boer J.C., et al. Amino acid functionalized inorganic nanoparticles as cutting-edge therapeutic and diagnostic agents. *Bioconjug. Chem.*, 2017, **29** (3), P. 657–671.
[40] Sur S., Rathore A., et al. Recent developments in functionalized polymer nanoparticles for efficient drug delivery system. *Nano-Struct. Nano-Objects*, 2019, **20**, 100397.
[41] Zhang W., Bai M., et al. Safety and efficacy of regional citrate anticoagulation for continuous renal replacement therapy in liver failure patients: a systematic review and meta-analysis. *Crit. Care*, 2019, **23** (1), P. 1–11.
[42] Shcherbakov A.B., Teplonogova M.A. et al. Facile method for fabrication of surfactant-free concentrated CeO_2 sols. *Mater. Res. Express*, 2017, **4** (5), 055008.
[43] Obraztsov I.V., Godkov M.A., et al. An evaluation of neutrophil function in whole blood samples with two-step stimulation: a new approach to chemiluminescence analysis. *Rus. J. Immun.*, 2015, **9**, P. 418–425.
[44] Allen R.C. Role of oxygen in phagocyte microbicidal action. *Environ. Health Perspect.*, 1994, **102** (Suppl 10), P. 201–208.
[45] Tarafdar A., Pula G. The role of NADPH oxidases and oxidative stress in neurodegenerative disorders. *Int. J. Mol. Sci.*, 2018, **19** (12), 3824.
[46] Darroudi M., Sarani, M. et al. Nanoceria: Gum mediated synthesis and in vitro viability assay. *Ceram. Int.*, 2014, **40** (2), P. 2863–2868.
[47] Li C., Zhao W., et al. Cytotoxicity of ultrafine monodispersed nanoceria on human gastric cancer cells. *J. Biomed. Nanotechnol.*, 2014, **10** (7), P. 1231–1241.
[48] Shokrzadeh M., Abdi H., et al. Nanoceria attenuated high glucose-induced oxidative damage in HepG2 cells. *Cell J.*, 2016, **18** (1), 97.
[49] Ivanov V.K., Usatenko A.V., Shcherbakov A.B. Antioxidant activity of nanocrystalline ceria to anthocyanins. *Russ. J. Inorg. Chem.*, 2009, **54**, 1522.
[50] Ivanov V.K., Shcherbakov A.B., et al. Inactivation of the nitroxyl radical by ceria nanoparticles. *Dokl. Chem.*, 2010, **430**, P. 43–46.
[51] Zholobak N.M., Shcherbakov A.B., et al. Direct monitoring of the interaction between ROS and cerium dioxide nanoparticles in living cells. *RSC Adv.*, 2014, **4**, P. 51703–51710.
[52] Eriksson P., Tal A.A., et al. Cerium oxide nanoparticles with antioxidant capabilities and gadolinium integration for MRI contrast enhancement. *Sci. Rep.*, 2018, **8** (1), P. 6999.
[53] Pulido-Reyes G., Das S., et al. Hypochlorite scavenging activity of cerium oxide nanoparticles. *RSC Adv.*, 2016, **6** (67), P. 62911–62915.
[54] Brestel E.P. Co-oxidation of luminol by hypochlorite and hydrogen peroxide implications for neutrophil chemiluminescence. *Biochem. Biophys. Res. Commun.*, 1985, **126** (1), P. 482–488.
[55] Edwards, S. Luminol-and lucigenin-dependent chemiluminescence of neutrophils: role of degranulation. *J. Clin. Lab. Immunol.*, 1987, **22** (1), P. 35–39.
[56] Gorudko I., Mikhalchik E., Sokolov A., Grigorieva D., Kostevich V., Vasilyev V., Cherenkevich S., Panasenko O. The production of reactive oxygen and halogen species by neutrophils in response to monomeric forms of myeloperoxidase. *Biophysics*, 2017, **62**, P. 919–925.
[57] Bedouhène S., Moulti-Mati F., et al. Luminol-amplified chemiluminescence detects mainly superoxide anion produced by human neutrophils. *Am. J. Blood Res.*, 2017, **7** (4), 41.
[58] Seminko V., Maksimchuk P., et al. Catalytic Decomposition of Hypochlorite Anions by Ceria Nanoparticles Visualized by Spectroscopic Techniques. *J. Phys. Chem. C*, 2019, **123** (33), P. 20675–20681.
[59] Adebayo O.A., Akinloye O., Adaramoye O.A. Cerium oxide nanoparticles attenuate oxidative stress and inflammation in the liver of diethylnitrosamine-treated mice. *Biol. Trace Elem. Res.*, 2020, **193**, P. 214–225.
[60] Peloi K.E., Lancheros C.A.C., et al. Antioxidative photochemoprotector effects of cerium oxide nanoparticles on UVB irradiated fibroblast cells. *Colloids Surf. B Biointerfaces*, 2020, **191**, P. 111013.

Submitted 26 April 2023; accepted 10 May 2023

Information about the authors:

Madina M. Sozarukova – Kurnakov Institute of General and Inorganic Chemistry of the Russian Academy of Sciences, Leninsky av., 31, Moscow, 119991, Russia; ORCID 0000-0002-5868-4746; s_madinam@bk.ru

Polina A. Chilikina – Scientific and Industrial Enterprise "MELITTA" Ltd, Miklukho-Maklaya Str., 16/10, Moscow, 117997, Russia; ORCID 0009-0005-6923-6120; p.chilikina@gmail.com

Dmitry O. Novikov – Joint Stock Company "Experimental Factory for Scientific Engineering of the Russian Academy of Sciences", Moscow region, Chernogolovka, Russia; ORCID 0009-0005-5806-9603; zerooo@list.ru

Elena V. Proskurnina – Research Centre for Medical Genetics, ul. Moskvorechye 1, Moscow, 115522, Russia; ORCID 0000-0002-8243-6339; proskurnina@gmail.com

Alexander E. Baranchikov – Kurnakov Institute of General and Inorganic Chemistry of the Russian Academy of Sciences, Leninsky av., 31, Moscow, 119991, Russia; ORCID 0000-0002-2378-7446; a.baranchikov@yandex.ru

Vladimir K. Ivanov – Kurnakov Institute of General and Inorganic Chemistry of the Russian Academy of Sciences, Leninsky av., 31, Moscow, 119991, Russia; ORCID 0000-0003-2343-2140; van@igic.ras.ru

Conflict of interest: the authors declare no conflict of interest.

NANOSYSTEMS:
PHYSICS, CHEMISTRY, MATHEMATICS

Original article

Larionov K.S., et al. *Nanosystems: Phys. Chem. Math.*, 2023, **14** (6), 652–659.
http://nanojournal.ifmo.ru
DOI 10.17586/2220-8054-2023-14-6-652-659

Slow zinc release from carboxymethylcellulose gels filled with humic zinc oxide nanocomposites

Konstantin S. Larionov[1,a], Alexander Volikov[1,b], Nikita A. Sobolev[1,c], Daniil A. Kozlov[2,d], Irina V. Perminova[1,e]

[1]Lomonosov Moscow State University, 119991 Moscow, Russia

[2]Kurnakov Institute of General and Inorganic Chemistry of RAS, 119991 Moscow, Russia

[a]konstantin.larionov@chemistry.msu.ru, [b]ab.volikov@gmail.com, [c]n.a.sobolev@outlook.com, [d]kozlov@inorg.chem.msu.ru, [e]iperm@med.chem.msu.ru

Corresponding author: Irina V. Perminova, iperm@med.chem.msu.ru

ABSTRACT The study is focused on characterization of humic zinc oxide nanocomposites and their potential application in wound healing as antibacterial agent. Zinc oxide nanoparticles were synthesized with varying concentrations of humic substances (HS) and analyzed using PXRD, TEM, SEM and UV-Vis techniques. The nanoparticle sizes based on the PXRD data decreased ranged from 50 to 15 nm along with an increase in humic ligand concentration. TEM images revealed that the star-shaped aggregates of 200–500 nm ZnO particles were formed in the absence of HS, whereas the presence of humic ligands led to shapeless smaller particles ranging from 20 to 200 nm. UV-Vis spectra showed increasing of zinc oxide band gap caused with an rise of HS concentration. The band gap of ZnO nanoparticles increased from 3.19 eV to 3.40 eV as the concentration of HS increased up to 15 g/L. The synthesized ZnO-HS nanocomposites were used for filling in the hydrogels of carboxymethylcellulose (CMC). The release studies of zinc ions from the gel into different buffers were conducted to imitate wound conditions. The measurements of Zn concentrations over time in buffer showed a gradual release over time making these gels potentially suitable for long-term wound treatment.

KEYWORDS humic substances, zinc oxide nanoparticles, release, wound healing.

ACKNOWLEDGEMENTS This work was funded by the Russian Science Foundation (grant #20-63-47070). The research was carried out using the equipment of MSU Shared Research Equipment Centre "Technologies for obtaining new nanostructured materials and their complex study", "Nanochemistry and Nanomaterials" and purchased by MSU in the frame of the Equipment Renovation Program (National Project "Science and Universities") and in the frame of the MSU Program of Development.

FOR CITATION Larionov K.S., Volikov A., Sobolev N.A., Kozlov D.A., Perminova I.V. Slow zinc release from carboxymethylcellulose gels filled with humic zinc oxide nanocomposites. *Nanosystems: Phys. Chem. Math.*, 2023, **14** (6), 652–659.

1. Introduction

Development of novel biologically active and reactive nanomaterials is a dynamic field of research that has emerged in recent decades due to the intensive development of nanotechnology. Nanoparticles (NPs) have attracted considerable attention in both biomedicine and environmental remediation because of their high reactivity connected to high area-to-volume ratio and the presence of a large number of active sites. Recent reviews on the use of engineered nanomaterials as antimicrobial agents and for wound healing show the great potential of nanoparticles for biomedical applications [1–3]. Among synthetic nanoparticles, zinc oxide nanoparticles are of substantial importance [4]. A use of zinc oxide NPs as a source of slow-release zinc was shown to accelerate healing of chronic wounds [1, 5, 6]. There are many mechanisms of antimicrobial activity of zinc oxide nanoparticles including binding to thiol groups of bacterial proteins, participation in generation of reactive oxygen species (ROS), and physical interaction with bacteria [7]. Zinc oxide NPs are produced by a variety of methods [8] including thermal evaporation [9], hydrothermal synthesis [10], sol-gel technique [11], microwave synthesis [12], wet chemical precipitation [2], etc. Still, the most common method includes wet chemical precipitation because it is cheap, simple and allow to obtain high yields of NP [2]. This technique implies precipitation of $Zn(OH)_2$ from a solution of Zn^{2+} precursor (sulphate, chloride, acetate) by interaction with an alkali followed by decomposition into ZnO NPs [8].

Along with beneficial reactive properties, the use of NPs in biomedicine is of great public concern due to nanotoxicity [13]. Due to their size they can penetrate through cellular barriers. To solve this problem, the NPs are packed into "nanocontainers" made of polymeric materials by modifying the surface of NPs. For this purpose, NPs are prepared in

the presence of surfactants or ligand exchange is applied on the surface of synthesised NPs [14]. Polyethyleneglycol, polyethylene-vinylacetate, polyvinylpyrrolidone, polylactate-glycolic acid, and polyvinyl alcohol are often used as polymer compounds [15]. Among natural polymers, chitosan occupies the leading position [16], followed by collagen [17], gelatin [18], and hyaluronic acid [19]. They are usually used to stabilise NPs in aqueous media, which are most widely used in biomedical technologies. The advantage of packing NPs in nanocontainers is a significant decrease in cytotoxicity of nanoparticles with passivated surface compared to nonstabilised NPs [15]. Another promising class of natural polyelectrolytes is humic substances (HS), which are present in all natural environments and can be obtained on an industrial scale from oxidised lignite, peat, and other natural resources. Šebesta et al., 2019 [20] showed the positive effect of HS ligands in sol-gel synthesis of ZnO NPs. However, the authors conducted synthesis at one concentration of HS, whereas systematic studies at different conditions are essential.

HS are natural polyelectrolytes dominated with carboxyl and hydroxyl groups [21]. Polyfunctional character determines a wide range of their chemical interactions. They can be oxidized by strong oxidizing agents, act as reducing agents, participate in protolytic, ion exchange, and complexation reactions, participate in donor-acceptor interactions, form hydrogen bonds, and participate in van der Waals interactions [22]. The unique combination of these properties indicates high potential of HS use for biomedical and environmental applications [23–25]. A lot of publications are dedicated to a use of HS for modification of NPs [26, 27]. They can act as stabilizing agents preventing aggregation of magnetic iron oxide nanoparticles in aqueous solutions [28], they inhibit growth and crystallinity of iron oxide NPs [29, 30]. The advantage of using HS over synthetic polymers is its biocompatibility, which reduces the risk of harm to living organisms due to the release of nanoparticles [31], as well as the immunostimulatory properties of HS [32].

Another concern with the use of zinc nanoparticles is how they are applied to wounds. Usually, gels or ointments are used, which are easy to apply because of their viscosity, and the nanoparticles are also consumed evenly, which is also an advantage. Many of the biomaterials used in the synthesis of ZnO nanoparticles are also good matrices due to their gel-forming properties, such as alginate [33], chitosan [16], gelatin [34], and sago starch [35]. There is also an approach in which synthesized zinc oxide nanoparticles are placed in a gel after synthesis, for example, using amphiphilic polymers such as Carbopol [36] or N,N-dimethylacrylamide (DMAA) [37]. Carboxymethylcellulose (CMC) has also found wide application, both as a direct agent in the synthesis of zinc oxide nanoparticles [38, 39] and as a separate matrix [40]. The advantage of CMC is its availability, low cost, and nontoxicity, which allows it to be widely used in the medical and food industries.

Thus, the production of nanocompositions based on zinc nanoparticles is an urgent task. The use of humic substances will expand the possibilities of zinc oxide nanoparticles. In view of the lack of humic substances of gel-forming properties, in this work a CMC was used as one of the most convenient gel matrices.

2. Materials and methods

2.1. Materials

Commercial potassium humate (Powhumus, Humintech GmbH, Germany) isolated from leonardite has been used as a humic material (CHP). Sodium carboxymethylcellulose (CMC) with a substitution of 1.03 degrees (FL9, Wuxi, China) was used to create gels. All water solutions were prepared using the Simplicity 185 system using deionised water (Millipore, Merck KGaA, Darmstadt, Germany). The pH of the solution was measured with the Ecotest-2000 pH meter (Econix, Moscow, Russia), equipped with a universal glass electrode. Analytical grade reagents ($Zn(OAc)_2$, NaOH) were used to synthesise zinc oxide nanoparticles and adjust pH.

2.2. Synthesis of humic zinc oxide nanocomposites

ZnO-NPs were synthesized by the method of alkaline precipitation in aqueous solution of HS using an approach described by [20]. The experimental setup is shown in Fig. 1.

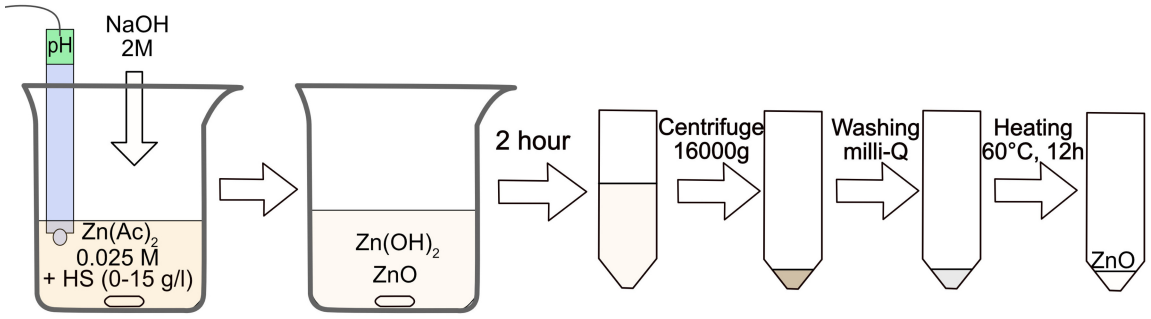

FIG. 1. Scheme of synthesis of Humic-ZnO nanocomposites in media containing humic substances

We prepared a solution of sodium humate in Milli-Q water at concentrations of 0.1, 0.5, 1, 2, 4, 8, and 15 g/L. Then, a volume of 50 ml of the prepared CHP solution was placed into a glass equipped with a dropping funnel filled with 2M NaOH and an electrode was inserted for pH measurements during synthesis. A volume of 50 mL of 0.025M zinc acetate was prepared and added dropwise to the CHP solution under continued stirring and pH adjustment to 12 by adding 2M NaOH. The resulting solution was stirred with a magnetic stirrer for 2 hours at room temperature. Then, the settled down sediment was separated and washed by multiple centrifugations at 16000 g with Milli-Q water to remove salts and unbound humic material. The precipitate was dried in a vacuum oven at 60°C for 12 hours. The obtained precipitates were from light grey to light brown in color. They were designated as ZnO–PX, where X is the concentration of CHP during synthesis (g/L).

2.3. Characterisation of humic zinc oxide nanocomposites

The obtained products were characterized using powder X-ray diffraction (PXRD) analysis to determine phase composition and crystallite size of the synthesized ZnO-HS-nanocomposites. We used a D/MAX 2500 (Rigaku, Japan) rotating anode diffractometer (Rigaku, Tokyo, Japan) in reflection geometry (Bragg-Brentano) with Cu $Ka_{1,2}$ radiation and a graphite monochromator. The PXRD patterns were collected in a range from 5 to 80°2θ with a step of 0.02. Phase analysis was performed using Match 3 software, whereas corresponding to zinc oxide nanoparticles size coherent scattering region (CSR) was evaluated with anisotropic model using MAUD software [41].

Size and morphology of the ZnO-HS nanocomposites were investigated using a high-resolution transmission electron microscope (TEM) JEM-2100 F (JEOL, Japan) at an accelerating voltage of 200 kV. Prior to analysis, the dry ZnO-NPs samples were ultrasonically dispersed in Milli-Q water, and a drop of sample was applied to carbon coated copper grid and dried.

UV-vis spectroscopy Cary 50 (Varian, USA) was used to measure the absorbance of ZnO–NPs to determine the band gap width and exciton energy. For the measurements, powder samples of all ZnO–NPs were ultrasonically treated in Milli-Q water.

Conversion degree of ionic Zn was determined by measuring Zn concentration in the supernatants after separation of sediments using inductively coupled plasma atomic emission spectrometry (ICP–AES) on an Agilent 5100 instrument. The concentration of Zn in the supernatants ranged from 0.1 to 0.5 mM, which corresponds to a conversion degree of 98–99% of ionic Zn to ZnO under the conditions used in the described above experimental setup.

2.4. Preparation of gels filled with ZnO-HS nanocomposites

For gel preparation, a weight of ZnO-NP-HS was ultrasonically dispersed in Milli-Q water to yield a concentration of 2% on metallic zinc basis. Then a weight of CMC (2% by mass) was added to the solution with dispersed nanocomposites and vigorously mixed with a glass rod to obtain homogeneous solution. Intense gelation started within first 10 minutes, and continued until complete homogenization was achieved in 30 minutes under continued mechanical agitation.

2.5. Setup of zinc release experiments from gels

A nitrocellulose membrane (0.5, 3, 13.5 kDa, Merck, Germany) was used to study zinc release. The membrane was attached to one end of a plastic tube, 1.5 cm in diameter and 2 cm long. An amount of gel having a weight of 2 g was placed in a tube. The tube filled with gel was placed atop of a 50 mL tube filled with a buffer solution, so that only the membrane surface touched the solution. We used Mueller-Hinton broth (Dehydrated infusion from beef 0.3 g/L, Casein hydrolysate 0.0175 g/L, Starch 0.0015 g/L, Agar, pH 7.3), 0.1M acetate buffer (pH 5.5) and Milli-Q water for release experiments. To imitate conditions of human body, the test compositions were kept in a thermostat at 37°C. The samples were collected after 2, 4, 6, 8, 24, 48, 56.5, 79, 145.5, 247 hours. The aliquot was diluted with 5% nitric acid and analyzed after a thorough mixing and settled for 1 h using an Agilent 5100 inductively coupled plasma spectrometer (ICP-AES). The scheme and photo of the experiment installation are shown in Fig. 2. All experiments were carried out in three replicates. To account for measurement error mean percent standard deviation was evaluated.

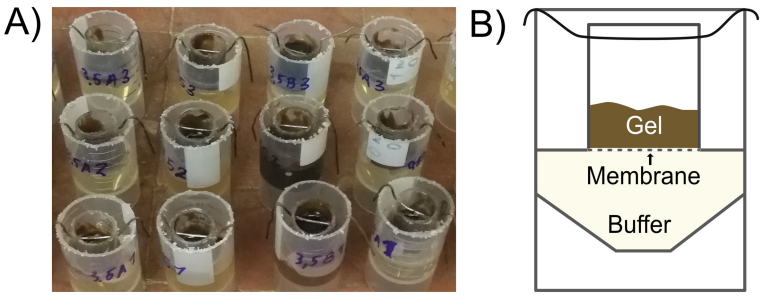

FIG. 2. Photo (A) and scheme (B) of equipment for the investigation of zinc release

3. Results and discussion

3.1. Characterisation of ZnO-NP-HS nanocomposites

ZnO-HS nanocomposites were synthesized using concentrations of HS in the range from 0.1 to 15 g/L. The PXRD results (Fig. 3A) confirmed the presence of characteristic peaks of ZnO in the samples obtained. At the same time, at high concentrations of HS – 4, 8, and 15 g/L, characteristic peaks of $Zn(OH)_2$ of low intensity were also detected, which may be associated with its binding and stabilization with HS.

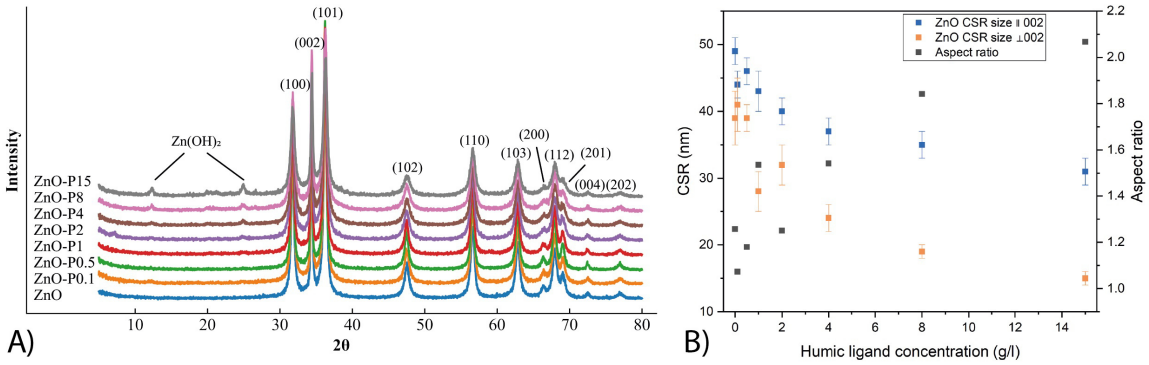

FIG. 3. PXRD patterns of ZnO-HS nanocomposites synthesised in the presence of increasing concentrations of HS (0, 0.1, 2, 4, 8, 15 g/L) (A), HS concentration effect on the calculated CSR sizes and aspect ratio of ZnO nanoparticles (B)

The NP sizes calculated from the PXRD data (Fig. 3B) ranged from 15 to 45 nm decreasing gradually with an increase in concentration of the humic ligand. In this case, the sizes of ZnO nanoparticles monotonously decrease both along the 002 direction and in the perpendicular direction, whereas aspect ratio rises. The observed phenomenon could be caused by an inhibition of $Zn(OH)_2$ crystallite growth due to blocking growth facets via binding with humic ligands similar to mechanism for feroxyhyte NPs which was described by [42]. However, when measured with TEM (Fig. 4), the synthesized composites turned out to be composed of the NPs aggregated into much larger – micron size, star-shaped particles. It can be explained by the peculiarity of ZnO particle size determination with X-ray diffraction, where the size of the coherent scattering region is calculated. In contrast, TEM measures size of the whole aggregate.

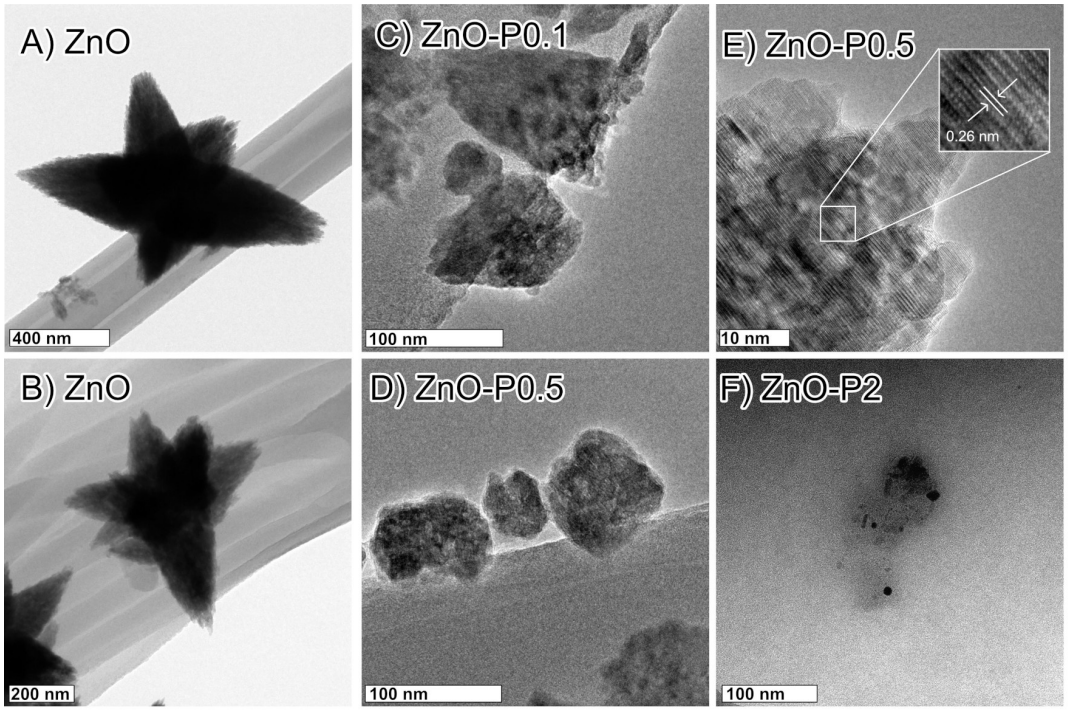

FIG. 4. TEM images of ZnO synthesized in the absence of HS (A, B), in the presence of 0.1 g/L HS (C), 0.5 g/L HS (D, E) and 2 g/L HS (F)

The TEM images show that the sizes of the obtained particles are in the micrometer range. The largest particles (near 1 μm) are observed for the preparations obtained without humic ligands. In the presence of humic ligands, particles are formed with sizes of 50–200 nm. Humic ligands change not only size, but morphology of particles as well. In the absence of humic ligands (Fig. 4A,B), star-shaped aggregates are formed, which consist of single ZnO particles of 400–800 nm in size (Fig. 4B). In the presence of HS (Fig. 4C-F), both large aggregates and small particles are visible. As HS concentration increases, the particle size decreases down to 50–100 nm (0.1 g/L), 30–100 nm (0.5 g/L), and 10–30 nm (2 g/L), which is consistent with the PXRD data. When examining the large-scale images (Fig. 3E), the crystal structure with an interplanar distance of 0.26 nm perpendicular to the plane 002 of ZnO can be seen.

To evaluate the band gap width of zinc oxide nanoparticles obtained with humic substance addition optical absorption spectra were collected. Absorption coefficients (α) were calculated from measured spectra using Kubelka-Munk theory:

$$F(R) = \frac{(1-R)^2}{2R^2} = \frac{\alpha}{s},$$

where $F(R)$ is the Kubelka-Munk function, R is the reflectance, s is the scattering coefficient.

The obtained spectra were transformed into the Tauc plot for allowed direct electron transition (Fig. 5A):

$$\alpha h\nu \sim (h\nu - E_g)^{1/2},$$

where E_g is the band gap.

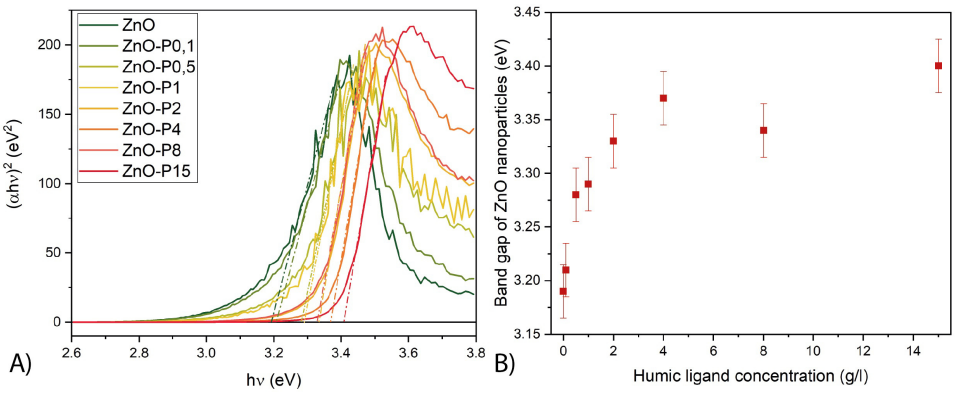

FIG. 5. Tauc plot of the humic zinc oxide nanocomposites UV-vis absorbance spectra (A). The HS concentration effect on the ZnO nanoparticles band gap (B)

The UV-vis absorption curves have a typical for ZnO characteristic absorption edge and exciton peak at 3.2–3.6 eV range. With increasing concentration of the humic ligand during synthesis, the observed absorption edge shifts to the larger energies. Also calculated zinc oxide nanoparticles band gap monotonously rises, that possibly is caused by the decrease in the size of individual crystallites of zinc oxide crystallites (Fig. 5B).

The calculated band gap values for ZnO nanoparticles and their size-dependent behavior are in good agreement with the reported data [43, 44]. It can be explained by decreasing the ZnO nanoparticles sizes caused by addition with HS during synthesis. Thus, the presence of HS allows us to control the ZnO nanoparticles sizes and to tune their band gap width, increasing it up to 3.40 eV at HS concentration of 15 g/L.

As can be seen from the above data, the use of humic substances leads to a significant change in the morphology of zinc oxide nanoparticles. The presence of humic substance both stabilizes the smaller ZnO crystallites and prevents its further aggregation. It also should be emphasised that a relatively high concentration of humic substances, from 4 g/L, is needed to observe a significant effect. This concentration is much higher than the typical maximum for natural content in water (up to 0.2 g/L), and the effect of this concentration range on ZnO nanoparticles was investigated earlier [20]. However, for the directed synthesis of drugs, the use of these concentrations is quite justified, since humic substances retain their neutral properties even at high concentrations.

3.2. Filling gels with ZnO-HS nanocomposites and zinc slow release

When the humic ZnO nanocomposites are dispersed, a non-viscous suspension is obtained, which is inconvenient to apply in the case of wounds. For wound treatment, gels and ointments are widely used, the advantage of which is high viscosity and more prolonged exposure of active substances to the wound. Therefore, in this work, we used commercially available preparations of carboxymethylcellulose (CMC) as gel carriers, which are widely used to create gels that are convenient and safe, including for the creation of medical preparations for external use. For gel preparation, ZnO samples were dispersed in water at a concentration of 2% zinc and then the gel matrix was added and stirred vigorously for 30 minutes until the gel swelled to a halt. Fig. 6 shows photo (A, B) of gel making filled with ZnO-P15 nanocomposites and SEM image (C, D).

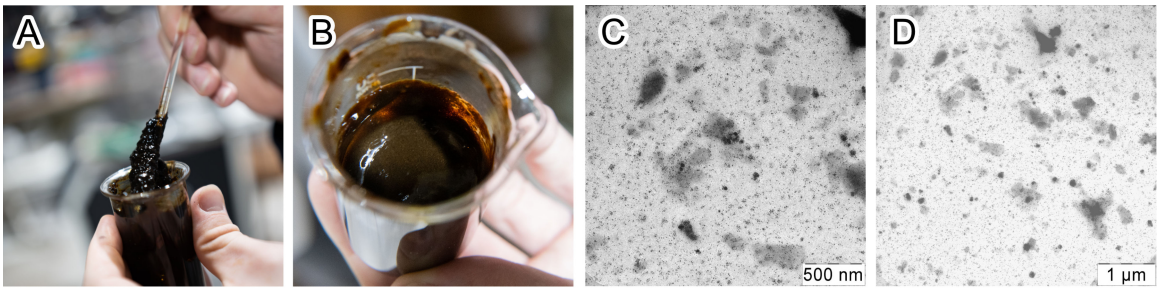

FIG. 6. Photo of Gel preparations filled with ZnO-P15 nanocomposites (A, B) and SEM image of them (C, D)

The resulting gels are quite dense, do not spread on the surface, and are able to hold the liquid containing active ingredients in its composition. The TEM results (Fig. 6 C,D) for this gel show the presence of a wide distribution of particle size in it, from small, 10–20 nm, to large 200–500 nm aggregates.

For wound healing dressing, the active ingredients must be slowly released. In this case, as a result of the influence of the wound environment and various anions, zinc nanoparticles are gradually destroyed with the release of zinc, which has an antibacterial and wound-healing effect. The anions diffuse into the gel and dissolve the zinc oxide, resulting in the release of zinc as a Zn^{2+} ions. To study kinetics of this process, the release of zinc in Mueller-Hinton broth and 0.1M acetate buffer (pH 5.5) was studied through membranes with different pore diameters: large (13.5 kDa) intermediary (3.5 kDa) and small (0.5 kDa), and the data obtained are shown in Fig. 7.

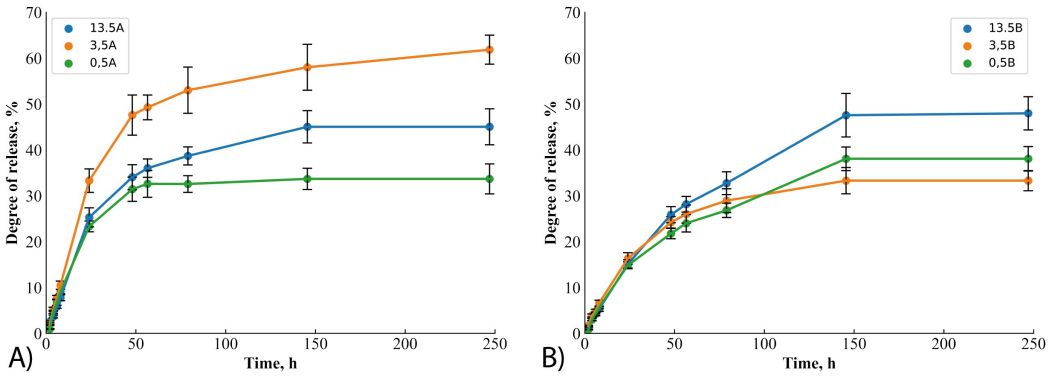

FIG. 7. Kinetics of the zinc release from CMC gel, A - acetate buffer, B - Mueller-Hinton broth, pore diameter of the dialysis membrane: 13.5 (highlighted in blue), 3.5 (highlighted in orange) and 0.5 kDa (highlighted in green), respectively

It can be seen that zinc is released into the acetate buffer at the higher rate (Fig. 7A) as compared to the Mueller-Hinton broth (Fig. 7B), which is manifested as the steeper slope of the release plots in Fig. 7B. At the same time, the total amount of zinc released is larger for the Mueller-Hinton broth as compared to the acetate buffer. Against the expectations, the largest zinc release was observed for the membrane with intermediary pore size (3.5 kDa) in case of the acetate buffer, where it achieved (50±10) %. At the same time, this very membrane was characterized with the minimum zinc release into the Muller Hinton broth of (30 ±5%). Such a discrepancy in the expected and factual values of zinc release through this membrane might be indicative of its biased behavior for the systems used in this study.

The zinc release from the gel reached its equilibrium after 150 hours of exposure on all three permeable membranes used in this study. The amount of zinc transferred into the solution over this exposure time accounted for (40 ± 10) % of its total content in the gel both for the large and small membranes. For the intermediary membrane, the released amount varied substantially for Mueller-Hinton broth versus acetate buffer and accounted for 30 and 60%, respectively. Of importance is that a substantial portion of zinc (from 10 to 15% of its total content in the gel) zinc was released during the first 24 hours, which gives good promise for the long-term effect of the carboxymethylcellulose gels filled with ZnO-HS nanocomposites.

4. Conclusions

In this work, we showed that the humic substances can be used effectively in the wet precipitation synthesis of zinc oxide nanoparticles within concentrations up to 15 g/L facilitating the formation and stabilization of zinc oxide nanoparticles. HS inhibits the growth of ZnO nanoparticles by blocking growth facets similar to mechanism described in the

literature for feroxyhyte NPs [41]. This phenomenon brings about formation of smaller nanoparticles. These nanosize-effects of HS with respect to ZnO particles were experimentally evidenced with a use of PXRD and UV-vis spectroscopy measurements. The nanocomposites obtained can be efficiently used for the treatment of wounds due to beneficial combination of properties of the both components: ZnO-NPs might act as antibacterial agents, whereas HS could prevent cytotoxicity and rapid consumption of Zn-NPs. The most preferable treatment form for wound healing applications are hydrogels. This is why we filled in 2% solution of carboxymethylcellulose with the ZnO–HS nanocomposites and studied zinc release from the filled gels. The results showed that zinc is released slowly, about 10–30% of the total amount for the first day. This allowed us to conclude that the CMC gels filled with ZnO-HS nanocomposites could be used as a slow-release zinc applications in wound healing.

References

[1] Nandhini S.N., Sisubalan N., Vijayan A., Karthikeyan C., Gnanaraj M., Gideon D.A.M., Jebastin T., Varaprasad K., Sadiku R. Recent advances in green synthesized nanoparticles for bactericidal and wound healing applications. *Heliyon*, 2023, **9**, P. e13128.

[2] Pino P., Bosco F., Mollea C., Onida B. Antimicrobial Nano-Zinc Oxide Biocomposites for Wound Healing Applications: A Review. *Pharmaceutics*, 2023, **15**, P. 970.

[3] Singh M., Thakur V., Kumar V., Raj M., Gupta S., Devi N., Upadhyay S.K., Macho M., Banerjee A., Ewe D., Saurav K. Silver Nanoparticles and Its Mechanistic Insight for Chronic Wound Healing: Review on Recent Progress. *Molecules*, 2022, **27**, P. 5587.

[4] Mishra P.K., Mishra H., Ekielski A., Talegaonkar S., Vaidya B. Zinc oxide nanoparticles: a promising nanomaterial for biomedical applications. *Drug Discovery Today*, 2017, **22**, P. 1825–1834.

[5] Vasile B.S., Oprea O., Voicu G., Ficai A., Andronescu E., Teodorescu A., Holban A. Synthesis and characterization of a novel controlled release zinc oxide/gentamicin–chitosan composite with potential applications in wounds care. *International journal of pharmaceutics*, 2014, **463**, P. 161–169.

[6] Mohandas A., PT S.K., Raja B., Lakshmanan V.K., Jayakumar R. Exploration of alginate hydrogel/nano zinc oxide composite bandages for infected wounds. *International journal of nanomedicine*, 2015, **10**, P. 53–66.

[7] Sirelkhatim A., Mahmud S., Seeni A., Kaus N.H.M., Ann L.C., Bakhori S.K.M., Hasan H., Mohamad D. Review on Zinc Oxide Nanoparticles: Antibacterial Activity and Toxicity Mechanism. *Nano-Micro Lett*, 2015, **7**, P. 219–242.

[8] Shaba E.Y., Jacob J.O., Tijani J.O., Suleiman M.A.T. A critical review of synthesis parameters affecting the properties of zinc oxide nanoparticle and its application in wastewater treatment. *Appl Water Sci*, 2021, **11**, P. 48.

[9] Zheng J.H., Jiang Q., Lian J.S. Synthesis and optical properties of flower-like ZnO nanorods by thermal evaporation method. *Applied Surface Science*, 2011, **257**, P. 5083–5087.

[10] Gerbreders V., Krasovska M., Sledevskis E., Gerbreders A., Mihailova I., Tamanis E., Ogurcovs A. Hydrothermal synthesis of ZnO nanostructures with controllable morphology change. *CrystEngComm*, 2020, **22**, P. 1346–1358.

[11] Hasnidawani J.N., Azlina H.N., Norita H., Bonnia N.N., Ratim S., Ali E.S. Synthesis of ZnO Nanostructures Using Sol-Gel Method. *Procedia Chemistry*, 2016, **19**, P. 211–216.

[12] Wojnarowicz J., Chudoba T., Lojkowski W. A Review of Microwave Synthesis of Zinc Oxide Nanomaterials: Reactants, Process Parameters and Morphologies. *Nanomaterials*, 2020, **10**, P. 1086.

[13] Zhang F. Grand Challenges for Nanoscience and Nanotechnology in Energy and Health. *Front. Chem.*, 2017, **5**, P. 80.

[14] Arati Sharma S.V.M., Robertson G.P. Toxicological considerations when creating nanoparticle-based drugs and drug delivery systems. *Expert Opinion on Drug Metabolism & Toxicology*, 2012, **8**, P. 47–69.

[15] Hühn D., Kantner K., Geidel C., Brandholt S., De Cock I., Soenen S.J.H., Rivera Gil P., Montenegro J.-M., Braeckmans K., Müllen K., Nienhaus G.U., Klapper M., Parak W.J. Polymer-Coated Nanoparticles Interacting with Proteins and Cells: Focusing on the Sign of the Net Charge. *ACS Nano*, 2013, **7**, P. 3253–3263.

[16] Sathiyaseelan A., Vishven Naveen K., Zhang X., Han K., Wang M.-H. Research progress on chitosan-zinc oxide nanocomposites fabrication, characterization, biomedical and environmental applications. *Coordination Chemistry Reviews*, 2023, **496**, P. 215398.

[17] Agban Y., Mugisho O.O., Thakur S.S., Rupenthal I.D. Characterization of Zinc Oxide Nanoparticle Cross-Linked Collagen Hydrogels. *Gels*, 2020, **6**, P. 37.

[18] Shahvalizadeh R., Ahmadi R., Davandeh I., Pezeshki A., Seyed Moslemi S.A., Karimi S., Rahimi M., Hamishehkar H., Mohammadi M. Antimicrobial bio-nanocomposite films based on gelatin, tragacanth, and zinc oxide nanoparticles – Microstructural, mechanical, thermo-physical, and barrier properties. *Food Chemistry*, 2021, **354**, P. 129492.

[19] Parani M., Lokhande G., Singh A., Gaharwar A.K. Engineered Nanomaterials for Infection Control and Healing Acute and Chronic Wounds. A*CS Appl. Mater. Interfaces*, 2016, **8**, P. 10049–10069.

[20] Šebesta M., Kolenčík M., Urík M., Bujdoš M., Vávra I., Dobročcka E., Smilek J., Kalina M., Diviš P., Pavúk M., Miglierini M., Kratošová G., Matúš P. Increased Colloidal Stability and Decreased Solubility—Sol—Gel Synthesis of Zinc Oxide Nanoparticles with Humic Acids. *J. Nanosci. Nanotechnol*, 2019, **19**, P. 3024–3030.

[21] Hayes M., MacCarthy P., Malcolm R., Swift R. The search for structure: setting the scene. Humic substances II, in search of struture. *Chichester, John, Wiley & Sons*, 1989, P. 3–33.

[22] Nebbioso A., Piccolo A. Basis of a Humeomics Science: Chemical Fractionation and Molecular Characterization of Humic Biosuprastructures. *Biomacromolecules*, 2011, **12**, P. 1187–1199.

[23] Ji Y., Zhang A., Chen X., Che X., Zhou K., Wang Z. Sodium humate accelerates cutaneous wound healing by activating TGF-β/Smads signaling pathway in rats. *Acta Pharmaceutica Sinica B*, 2016, **6**, P. 132–140.

[24] Lipczynska-Kochany E., Kochany J. Humic substances in bioremediation of industrial wastewater—Mitigation of inhibition of activated sludge caused by phenol and formaldehyde. *Journal of Environmental Science and Health, Part A*, 2008, **43**, P. 619–626.

[25] Wan J., Dong W., Tokunaga T.K. Method to Attenuate U(VI) Mobility in Acidic Waste Plumes Using Humic Acids. *Environ. Sci. Technol.*, 2011, **45**, P. 2331–2337.

[26] Liu J.F., Zhao Z.S., Jiang G.B. Coating Fe_3O_4 magnetic nanoparticles with humic acid for high efficient removal of heavy metals in water. *Environmental science & technology*, 2008, **42**, P. 6949–6954.

[27] Polyakov A.Yu., Lebedev V.A., Shirshin E.A., Rumyantsev A.M., Volikov A.B., Garshev A.V., Goodilin E.A., Perminova I.V. Non-classical growth of water-redispersible spheroidal gold nanoparticles assisted by leonardite humate. *Cryst. Eng. Comm.*, 2017, **19**, P. 876–886.

[28] Ghosh S., Jiang W., McClements J.D., Xing B. Colloidal stability of magnetic iron oxide nanoparticles: Influence of natural organic matter and synthetic polyelectrolytes. *Langmuir*, 2011, **27**, P. 8036–8043.
[29] Kulikova N.A., Polyakov A.Y., Lebedev V.A., Abroskin D.P., Volkov D.S., Pankratov D.A., Klein O.I., Senik S.V., Sorkina T.A., Garshev A.V., Veligzhanin A.A., Garcia Mina J.M., and Perminova I.V. Key roles of size and crystallinity of nanosized iron (hydr)oxides stabilized by humic substances in iron bioavailability to plants. *Journal of Agricultural and Food Chemistry*, 2017, **65**(51), P. 11157–11169.
[30] Sorkina T.A., Polyakov A.Yu., Kulikova N.A., Goldt A.E., Philippova O.I., Aseeva A.A., Veligzhanin A.A., Zubavichus Ya.V., Pankratov D.A., Goodilin E.A., Perminova I.V. Nature-inspired soluble iron-rich humic compounds: new look at the structure and properties. *Journal of Soils and Sediments*, 2014, **14**(2), P. 261–268.
[31] Perminova I.V. Humic substances-assisted synthesis of nanoparticles in the nature and in the lab. In Functions of Natural Organic Matter in Changing Environment. Eds. J. Xu, J. Wu, Y. He. Zhejiang University Press and Springer Science+Business Media, Dordrecht, 2013 P. 735–740.
[32] Schepetkin I.A., Khlebnikov A.I., Ah S.Y., Woo S.B., Jeong C.-S., Klubachuk O.N., Kwon B.S. Characterization and biological activities of humic substances from mumie. *J. Agric. Food Chem.*, 2003, **51**, P. 5245–5254.
[33] Jayakumar R., Sudheesh Kumar P., Mohandas A., Lakshmanan V.-K., Biswas R. Exploration of alginate hydrogel/nano zinc oxide composite bandages for infected wounds. *IJN*, 2015, **53**.
[34] Sherafatkhah Azari S., Alizadeh A., Roufegarinejad L., Asefi N., Hamishehkar H. Preparation and characterization of gelatin/β-glucan nanocomposite film incorporated with ZnO nanoparticles as an active food packaging system. *J. Polym. Environ*, 2021, **29**, P. 1143–1152.
[35] Nafchi A.M., Alias A.K., Mahmud S., Robal M. Antimicrobial, rheological, and physicochemical properties of sago starch films filled with nanorod-rich zinc oxide. *Journal of Food Engineering*, 2012 **113**, P. 511–519.
[36] Ismail S.H., Hamdy A., Ismail T.A., Mahboub H.H., Mahmoud W.H., Daoush W.M. Synthesis and characterization of antibacterial Carbopol/ZnO hybrid nanoparticles gel. *Crystals*, 2021, **11**, 1092.
[37] Sakohara S., Mori K. Preparation of ZnO nanoparticles in amphiphilic gel network. *J Nanopart Res*, 2008, **10**, P. 297–305.
[38] Rakhshaei R., Namazi H. A potential bioactive wound dressing based on carboxymethyl cellulose/ZnO impregnated MCM-41 nanocomposite hydrogel. *Materials Science and Engineering: C*, 2017, **73**, P. 456–464.
[39] Yadollahi M., Gholamali I., Namazi H., Aghazadeh M. Synthesis and characterization of antibacterial carboxymthyl cellulose/ZnO nanocomposite hydrogels. *International Journal of Biological Macromolecules*, 2015, **74**, P. 136–141.
[40] Zafar A., Khosa M.K., Noor A., Qayyum S., Saif M.J. Carboxymethyl Cellulose/Gelatin Hydrogel films loaded with Zinc Oxide nanoparticles for sustainable food packaging applications. *Polymers*, 2022, **14**, P. 5201.
[41] Lutterotti L. Total pattern fitting for the combined size–strain–stress–texture determination in thin film diffraction. *Nuclear Instruments and Methods in Physics Research Section B: Beam Interactions with Materials and Atoms*, 2010, **268**(3-4), P. 334–340.
[42] Polyakov A.Yu, Goldt A.E., Sorkina T.A., Perminova I.V., Pankratov D.A., Goodilin E.A., Tretyakov Y.D. Constrained growth of anisotropic magnetic δ-FeOOH nanoparticles in the presence of humic substances *CrystEngComm*, 2012, **14**(23), P. 8097–8102.
[43] Goh E.G., Xu X., McCormick P.G. Effect of particle size on the UV absorbance of zinc oxide nanoparticles. *Scripta Materialia*, 2014, **78–79**, P. 49–52.
[44] Arif A., Belahssen O., Gareh S., Benramache S. The calculation of band gap energy in zinc oxide films. *J. Semicond*, 2015, **36**, P. 013001.

Submitted 9 November 2023; revised 19 November 2023; accepted 20 November 2023

Information about the authors:

Konstantin S. Larionov – Department of Chemistry, Lomonosov Moscow State University, Leninskiye Gory 1-3, 119991 Moscow, Russia; ORCID 0009-0009-1635-3648; konstantin.larionov@chemistry.msu.ru

Alexander Volikov – Department of Chemistry, Lomonosov Moscow State University, Leninskiye Gory 1-3, 119991 Moscow, Russia; ORCID 0000-0002-8475-8091; ab.volikov@gmail.com

Nikita A. Sobolev – Department of Chemistry, Lomonosov Moscow State University, Leninskiye Gory 1-3, 119991 Moscow, Russia; ORCID 0000-0002-8210-8263; n.a.sobolev@outlook.com

Daniil A. Kozlov – Kurnakov Institute of General and Inorganic Chemistry of RAS, Leninsky Prospect 31, 119991 Moscow, Russia; ORCID 0000-0003-0620-8016; kozlov@inorg.chem.msu.ru

Irina V. Perminova – Department of Chemistry, Lomonosov Moscow State University, Leninskiye Gory 1-3, 119991 Moscow, Russia; ORCID 0000-0001-9084-7851; iperm@med.chem.msu.ru

Conflict of interest: the authors declare no conflict of interest.

NANOSYSTEMS:
PHYSICS, CHEMISTRY, MATHEMATICS

Enikeeva M.O., et al. *Nanosystems: Phys. Chem. Math.*, 2023, **14** (6), 660–671.
http://nanojournal.ifmo.ru

Original article

DOI 10.17586/2220-8054-2023-14-6-660-671

Synthesis under hydrothermal conditions and structural transformations of nanocrystals in the $LaPO_4$–YPO_4–(H_2O) system

Maria O. Enikeeva[1,2,a], Olga V. Proskurina[1,2,b], Evgeny Yu. Gerasimov[3,c], Vladimir N. Nevedomskiy[1,d], Victor V. Gusarov[1,e]

[1]Ioffe Institute, 194021 St. Petersburg, Russia

[2]St. Petersburg State Institute of Technology, 190013 St. Petersburg, Russia

[3]Federal Research Center, Boreskov Institute of Catalysis SB RAS, Novosibirsk 630090, Russia

[a]odin2tri45678@gmail.com, [b]proskurinaov@mail.ru, [c]gerasimov@catalysis.ru,
[d]nevedom@mail.ioffe.ru, [e]gusarov@mail.ioffe.ru

Corresponding author: M. O. Enikeeva, odin2tri45678@gmail.com

ABSTRACT Structural transformations of nanocrystals in the $LaPO_4$–YPO_4–(H_2O) oxide system were investigated under hydrothermal conditions at 230°C, depending on isothermal holding times (2 hours, 7 days and 28 days). It was shown that before hydrothermal processing, phases crystallize in the system with rhabdophane structures $La_{1-x}Y_xPO_4 \cdot nH_2O$ ($0 \leq x \leq 0.80$) and xenotime YPO_4. It has been determined that increasing the duration of isothermal treatment under hydrothermal conditions leads to the transformation of the rhabdophane phase into phases with monazite and equilibrium xenotime structures, with an intermediate crystallization of the metastable monazite phase. It is noted that only after 28 days of hydrothermal treatment at 230°C, the system approaches the equilibrium composition of the phases with monazite structures $La_{0.97}Y_{0.03}PO_4$ (with crystal sizes of 18–50 nm) and xenotime YPO_4 (with crystal sizes of 45–90 nm). In a single-phase sample with a monazite structure $La_{0.75}Y_{0.25}PO_4$, the average crystal size remains unchanged at around 20 nm after 2 hours, 7 days and 28 days of hydrothermal treatment at 230°C.

KEYWORDS nanocrystals, monazite, xenotime, rhabdophane, structural transformations, yttrium phosphate, lanthanum phosphate.

ACKNOWLEDGEMENTS Powder XRD measurements, Rietveld refinement of crystal structures and EDX analysis have been carried out with using the equipment and software of the Engineering Department of the St. Petersburg State University of Technology (Technical University). TEM investigations carried out with using the equipment of the Joint Research Center 'Materials science and characterization in advanced technology' (Ioffe Institute, St. Petersburg) and HRTEM study was carried out using the facilities of the "National center of investigation of catalysts" at Boreskov Institute of Catalysis. The present work of M.O.E., O.V.P. and V.V.G. was supported by the Russian Science Foundation (project no. 21-13-00260).

FOR CITATION Enikeeva M.O., Proskurina O.V., Gerasimov E.Yu., Nevedomskiy V.N., Gusarov V.V. Synthesis under hydrothermal conditions and structural transformations of nanocrystals in the $LaPO_4$–YPO_4–(H_2O) system. *Nanosystems: Phys. Chem. Math.*, 2023, **14** (6), 660–671.

1. Introduction

Materials based on nanocrystalline rare-earth phosphates are of significant interest due to their wide range of applications in optics [1–4], catalysis [2,5,6], medicine [7–9], fabrication of gas sensors [10] and other fields [11–13]. Special attention is given to the binary- and multi-component systems based on rare-earth orthophosphates, as they are used as luminescent materials [14, 15] and matrices for immobilizing toxic and radioactive waste [16–18].

Depending on the synthesis conditions, rare-earth phosphates can be obtained in the form of phases with a monazite structure (*LRE*PO_4, *LRE*=La→Gd, space group (SG): $P2_1/n$) [19–21], xenotime structure (*HRE*PO_4, *HRE*=Tb→Lu, Y, Sc; SG: $I4_1/amd$) [19, 21], rhabdophane structure (*RE*$PO_4 \cdot nH_2O$, *RE*=La→Gd, Y, n=0-1; SG: $C2$ or $P6_222$) [22, 23] and churchite or weinschenkite structure (*HRE*$PO_4 \cdot 2H_2O$, *HRE*=Tb→Lu, Y; SG: $C2/c$) [24–26]. Hydrated phases with rhabdophane and churchite structures are often considered as precursors for the formation of anhydrous phases with monazite and xenotime structures. It was found that the loss of structurally bound water with increasing temperature leads to the transition of the rhabdophane structure to monazite and the churchite structure to xenotime for individual compounds of the *RE*$PO_4 \cdot nH_2O$ type [27, 28]. An exception is yttrium orthophosphate, which crystallizes under certain conditions into a phase with a rhabdophane structure that can transform into a phase with a xenotime structure [29]. However, it is also possible to form anhydrous phases with monazite and xenotime structures without the use of high temperatures [30, 31].

For the synthesis of nanocrystalline materials based on rare-earth orthophosphates, soft chemistry methods are commonly used, such as precipitation [28, 32–34], sol-gel [3, 35–38], hydrothermal and hydrothermal-microwave synthesis [1, 4, 38–41]. At times, precipitates obtained by soft chemistry methods are annealed at temperatures $\geq 500^{\circ}$C to obtain samples with monazite and xenotime structures [18, 20, 43].

Studies of structural transformations in the $LaPO_4$–YPO_4–(H_2O) system were investigated in works [34, 36, 44–49]. During heat treatment at temperatures of 1000–1600°C, phases with monazite and xenotime structures are formed in the system. There is a wide homogeneity range of solid-solution with a monazite structure (up to 42 mol. % YPO_4 at $T = 1600^{\circ}$C), while the solubility of $LaPO_4$ in the xenotime phase is extremely low (less than a few percent at $T = 1600^{\circ}$C). Phases with rhabdophane, monazite and xenotime structures were obtained in the $LaPO_4$–YPO_4–H_2O system using soft chemistry synthesis methods. However, research in the low-temperature range remains poorly systematic and has little focus on phase transformations in the system with varying synthesis durations. This information can be valuable for improving the understanding of phase stability in the $LaPO_4$–YPO_4–H_2O system and predicting the behavior of functional materials based on it.

Taking into account the above considerations, this study aims to investigate the structural transformations of nanocrystals in the oxide system $LaPO_4$–YPO_4–(H_2O) under hydrothermal conditions, focusing on the influence of the duration of isothermal holding times.

2. Experimental

The following chemical reagents were used for the synthesis of nanopowders with the composition $La_{1-x}Y_xPO_4 \cdot nH_2O$ (x =0-1): lanthanum (III) nitrate hexahydrate $La(NO_3)_3 \cdot 6H_2O$ (puriss.), yttrium (III) nitrate hexahydrate $Y(NO_3)_3 \cdot 6H_2O$ (puriss.) and ammonium dihydrogen phosphate $NH_4H_2PO_4$ (puriss.).

The precipitation was carried out from solutions of the reagents in distilled water by adding the $NH_4H_2PO_4$ solution to the rare-earth nitrate solution with continuous stirring at $T = 25 \pm 5^{\circ}$C.The resulting white suspension with pH=1 was constantly stirred for 15 minutes.

For hydrothermal synthesis, the suspension obtained by precipitation was transferred into a Teflon-lined autoclave (filling factor 0.7) and hydrothermally treated at $T = 230^{\circ}$C and $P \sim 10$ MPa with isothermal holding times: 2 hours, 7 days and 28 days.

Samples obtained by both precipitation and hydrothermal treatment were washed with distilled water until reaching a pH of 7, centrifuged (at 10,000 rpm), dried at $T = 75^{\circ}$C for 24 hours and subsequently ground using an agate mortar.

The elemental composition of the samples was determined using energy-dispersive X-ray spectroscopy (EDS) with a Tescan Vega 3 SBH scanning electron microscope (Tescan, Czech Republic) equipped with an Oxford Instruments INCA x-act microanalysis system (UK). The measurements were conducted in the energy range up to 20 keV in five different areas and the obtained values were averaged.

X-ray diffraction (XRD) analysis of the samples was performed based on the powder diffraction patterns obtained using a Rigaku SmartLab 3 X-ray diffractometer (Cu $_{K\alpha}$- radiation) in the angular range of 2θ = 10–90° with a step size of 0.01° and scan speeds of 0.2°/min and 0.8°/min. Phase analysis of the samples was carried out using the ICSD PDF-2 and CSD databases. Quantitative phase analysis was performed using the *SmartLab Studio SmartLab Studio II* v4.4.241.0 (Rigaku Corporation, Japan). The average crystallite sizes were determined using non-overlapping reflections for each phase: the 200 reflection for the monazite structure phase, the 101 reflection for the xenotime structure phase and the $11\bar{1}$ reflection for the rhabdophane structure phase. The average crystallite size of xenotime phase in the samples obtained by precipitation was determined using the Scherrer formula [50] based on 101 and 200 reflections. The composition of the variable composition phase with a monazite structure was determined using Retgers law [51] and literature data [20, 46].

The investigation of the crystal structure and microstructure of the samples was carried out using high-resolution transmission electron microscopy (HRTEM) on an electron microscope ThemisZ (Thermo Fisher Scientific, USA), which provided a maximum lattice resolution of 0.07 nm and on an electron microscope JEM- 2100F (JEOL Ltd., Akishima, Tokyo, Japan) with an accelerating voltage of 200 kV. During the operation of the ThemisZ microscope, images were recorded using a Ceta 16 CCD sensor (Thermo Fisher Scientific, USA). The microscope ThemisZ was also equipped with an EDX Super-X spectrometer (Thermo Fisher Scientific, Bleiswijk, The Netherlands) with a semiconductor Si detector providing an energy resolution of 128 eV.

To construct particle size distribution histograms, particle images were analyzed by the *ImageJ* software. There were at least 40 particles in the samples. The distribution histogram was processed using the lognormal distribution law.

3. Results and discussions

According to the elemental analysis data, the molar ratio of *RE*:P is close to 1:1 in all samples, which corresponds to the stoichiometry of rare-earth phosphate. For the designation of the samples, an experimentally determined molar ratio of yttrium and lanthanum is used, expressed as Yn%, where n%= n(Y)/(n(Y) + n(La))·100% Yn% - represents the molar percentage of yttrium relative to the sum of rare-earth elements, n(Y) is the molar fraction of yttrium in the sample and n(La) is the molar fraction of lanthanum in the sample.

Figure 1 shows the X-ray diffraction patterns of the samples obtained by precipitation. Nanocrystalline samples with compositions of 0%–Y73% exhibit a rhabdophane structure. In the Y81% sample, reflections of the rhabdophane structure are present, as well as broadened reflections corresponding to the xenotime structure, which are also observed in the Y93%–Y100% samples.

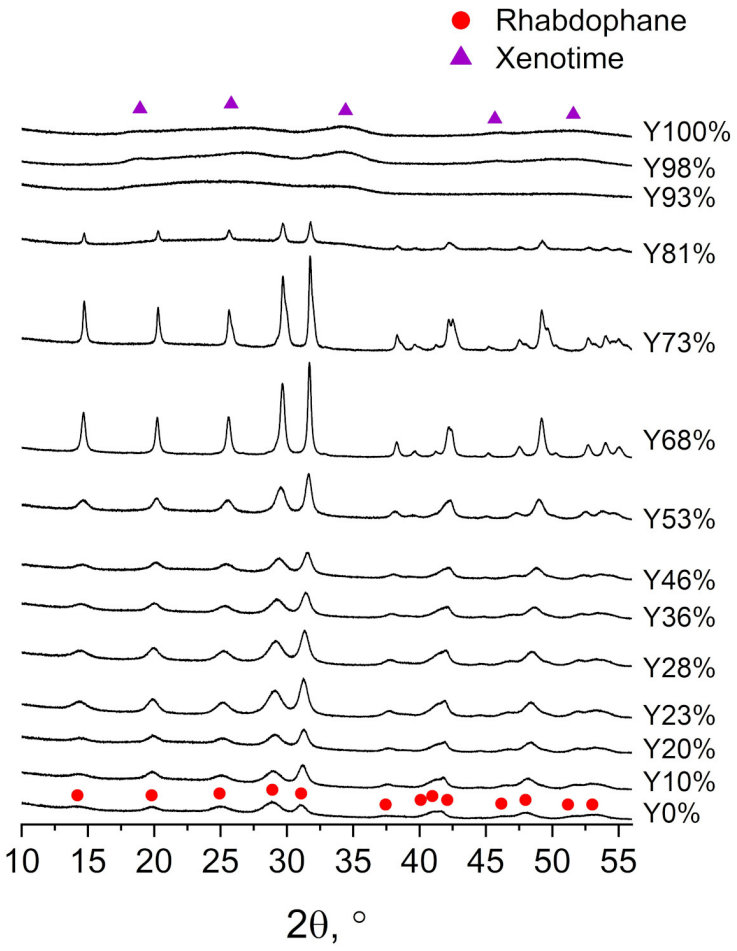

FIG. 1. The X-ray diffraction patterns of the samples obtained by precipitation

Figure 2(a) present the dependency of the unit cell volume per formula unit on the composition of the system for the rhabdophane and xenotime structure phases in the samples obtained by precipitation method. In the system, a solid solution with a rhabdophane structure $La_{1-x}Y_xPO_4 \cdot nH_2O$ ($x < 0.81$) is formed. In the Y81% sample, the obtained values of the V/z parameter for the rhabdophane structure have larger values compared to those for the Y73% sample, which is due to the crystallization of the YPO_4 xenotime-structured phase in this sample as well. The presence of an amorphous phase containing lanthanum cannot be excluded in the Y93%–Y98% samples.

The dependence of the weighted average crystallite size with rhabdophane structure on the YPO_4 content in the system is shown in Fig. 2(b). For $La_{1-x}Y_xPO_4 \cdot nH_2O$ ($x < 0.5$), the formation of nanocrystals with an average size of 5–10 nm. Further increase in the molar fraction of yttrium orthophosphate in the system leads to an increase in the sizes of rhabdophane-structured crystals several times. In the Y81% sample, the value $D = 45 \pm 30$ nm. The average size of xenotime-structured phase crystals in Y93%–Y100% samples, determined by the Scherrer formula, does not exceed 5 nm.

Figure 3(a,c,e) present microphotographs of Y23%, Y73% and Y100% nanoparticles obtained by precipitation method. Microphotographs for the $LaPO_4$ sample obtained by precipitation method are presented in the work [32]. Based on the analysis of the images, histograms of particle size distribution according to their cross-sectional area (thickness) were constructed, as shown in the Appendix (Supporting Materials Fig. S1(a,b,c)). The Y23% nanoparticles with rhabdophane structure have a rod-like shape (Fig. 2(a)) with a narrow distribution of particle thicknesses (Fig. S1(a)). The thickness of the nanorods varies in the range of 5–10 nm.

In the Y73% sample (Fig. 3(c)), the particles have an prolate form with a significantly lower aspect ratio of geometric parameters compared to the $LaPO_4$ sample [32]. The particle size distribution for the Y73% sample with rhabdophane structure, shown in Fig. S1(b), is considerably wider than that of the Y23% sample. The particle thickness varies in the

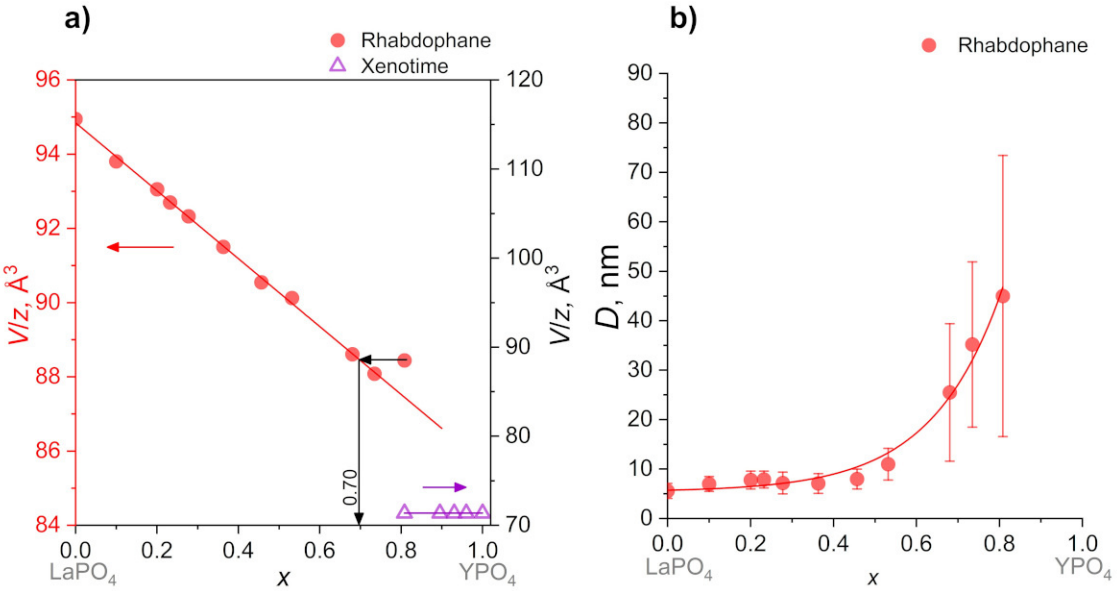

FIG. 2. a) The dependence of unit cell per formula unit of structure on the yttrium content; b) The mean volume weighted crystallite size (D) of the rhabdophane-structured nanocrystals $La_{1-x}Y_xPO_4 \cdot nH_2O$ ($x \leq 0.81$), obtained by precipitation method, on the composition of the system

range of 10 to 50 nm. The average crystal sizes for the Y23% and Y73% samples (Fig. 2(b)) with rhabdophane structure correlate quite well with the average particle thicknesses (Fig. S1(a,b)) of these samples. This was also shown in the work [45] for samples with the composition $LaPO_4$:YPO_4=1:3.

In the Y100% sample (Fig. 3(e)), there are nanocrystals with interplanar distances $d \approx 3.45$ Å and $d \approx 2.56$ Å corresponding to the (200) and (112) planes of the xenotime structure. The cross-sectional size of the nanoparticles in the sample does not exceed 10 nm (distribution shown in Fig. S1(c)) and correlates with the crystal size of the xenotime-structured phase, as determined by the Scherrer formula (~ 5 nm).

The microdiffraction patterns of the Y23%, Y73% and Y100% samples are shown in Fig. 3(b,d,f). In the Y23% and Y73% samples, only rhabdophane structure reflections are observed, while in the Y100% sample, only xenotime-structured phase reflections are presented.

Figure 4(a) shows a microphotograph of particles from the Y73% sample with rhabdophane structure, synthesized by precipitation method. The results of elemental mapping are shown in Fig. 4(b). Despite the Y73% sample with rhabdophane structure being single-phase, the distribution of elements La(L_α-series) and Y(K_α-series) in each particle is not homogeneous. Energy-dispersive analysis of an individual particle showed that the Y:La ratio at the edges of the particle is close to 4:1, while in the central part of the particle, it is approximately 3:2. The total amount of yttrium in all particles corresponds to the composition determined by energy-dispersive X-ray analysis using SEM, i.e., close to 73 mol.% YPO_4. Apparently, the compositional inhomogeneity of the particles in the Y73% sample can be attributed to the difference in the solubility product of lanthanum and yttrium phosphates in an acidic media. This leads to the formation of nanocrystals with a rhabdophane structure containing a relatively higher amount of La than indicated by the stoichiometry of the precipitated phase. As a result, the mother liquid becomes depleted in La^{3+} ions and an yttrium-enriched rhabdophane phase crystallizes on the periphery of the particles. Fig. S2 shows the image of an individual particle from the Y73% sample with complete elemental mapping, where the presence of lanthanum can also be observed predominantly in the central part of the particle.

In the $LaPO_4$–YPO_4–(H_2O) system, after hydrothermal treatment (HT) at 230°C with different isothermal holding times (2 hours, 7 days and 28 days), phases with monazite, rhabdophane and xenotime structures crystallize. The diffraction patterns of the samples are presented in the Supporting Materials in Fig. S3, S4 and S5.

The phase quantities and the dependence of the unit cell per formula unit of structure on the yttrium content after hydrothermal treatment are shown in Fig. 5(a-f). HT of samples for 2 hours (Fig. 5(a,b)) leads to the formation of a solid solution with a monazite structure $La_{1-x}Y_xPO_4$ ($x \leq 0.38$), the formation of a solid solution with a rhabdophane structure and the formation of a phase with a xenotime structure. The single-phase solid solution with a monazite structure has a composition of $0 < x \leq 0.25$. Partial phase transformation the rhabdophane structure to the monazite structure occurs in the samples $0.25 < x < 0.70$, which is consistent with the data on the $LaPO_4$:YPO_4=1:1 sample obtained under hydrothermal-microwave conditions [49]. In samples Y71%–Y80%, one phase with the rhabdophane structure is formed, similar to before HT (Fig. 2(a)). For samples with a composition of $0.85 \leq x \leq 0.92$ after 2 hours of HT, the initial precipitate, which contains not only amorphous phase but also nanocrystalline xenotime, transforms into phases with

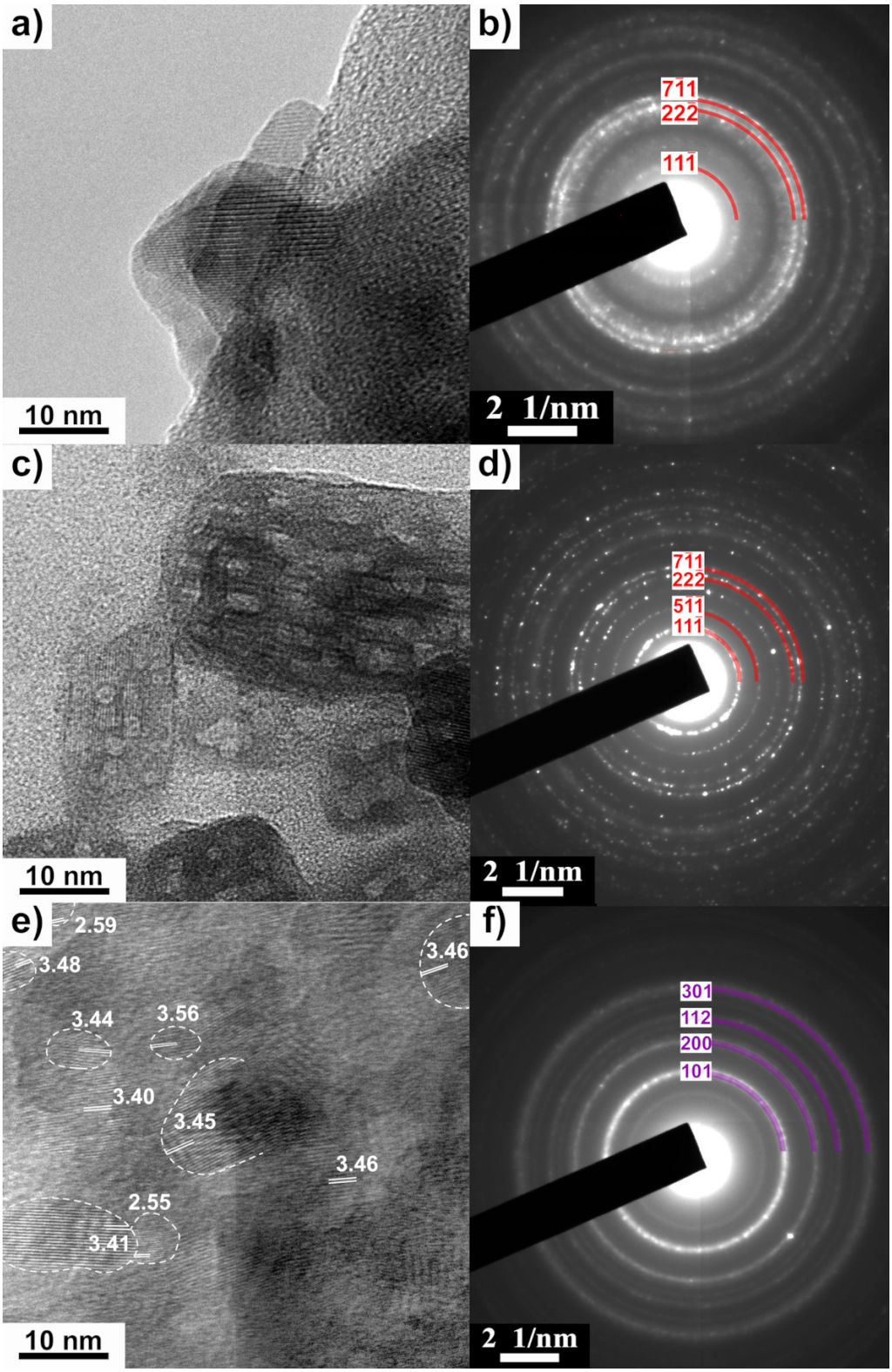

FIG. 3. TEM images and microdiffraction patterns samples synthesized by precipitation method: a,b) Y23%; c,d) Y73% and e,f) Y100% (YPO_4)

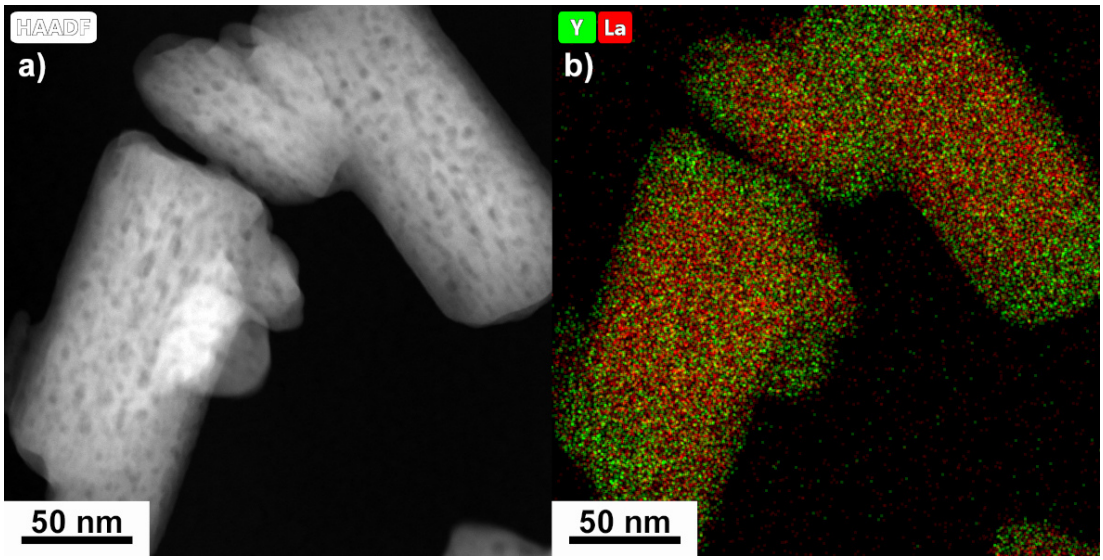

FIG. 4. a) TEM image and b) element mapping particles from the Y73% sample, synthesized by precipitation method

structures of monazite, rhabdophane and xenotime. The monazite phase is depleted in YPO_4 component compared to the nominal composition of the samples and has the composition $La_{1-x}Y_xPO_4$ ($x \leq 0.28$). The fraction of monazite phase in samples containing $0.85 \leq x \leq 0.92$ is approximately 10%. The composition of the xenotime phase can be considered close to YPO_4 within the experimental error. The composition of the rhabdophane phase $La_{1-x}Y_xPO_4 \cdot nH_2O$ is difficult to determine accurately due to the narrow concentration range of a single-phase region after hydrothermal treatment. The fraction of xenotime phase in samples with a composition of $0.85 \leq x \leq 0.92$ increases along with the fraction of yttrium phosphate in the system. In samples Y97% and Y100%, only the xenotime phase is observed in the diffraction patterns.

Figure 5(c,d) shows the phase ratios and changes in the unit-cell volume normalized to the number of formula units for the monazite and xenotime phases in samples after 7 days of HT. The samples have completely transformed from the rhabdophane structure to phases with monazite and xenotime structures. For samples with a composition of $x \leq 0.25$, the formation of the solid solution with a monazite structure is observed, similar to that after 2 hours of HT. Samples Y53%, Y74% and Y84% contain two phases with different compositions but with a monazite structure, as well as a phase with a xenotime structure. The diffraction patterns of the samples, presented in Fig. S4, show reflections of two monazite phases with the different dissolved yttrium, as well as reflections of the xenotime structure. For the Y53% sample, the profiles of the reflections of the two monazite phases heavily overlap, indicating their similar composition and a relatively large error in determining the parameters of the unit cell. In the Y74% and Y84% samples, the fraction of the monazite phase enriched in yttrium, with a composition of $0.28 \leq x \leq 0.37$, does not exceed 30% and decreases with an increase in the amount of yttrium in the system. The fraction of the second monazite phase, with a composition of $0.09 \leq x \leq 0.12$, does not exceed 8%.

The phase ratios and changes in the volume of the unit cell, normalized to one formula unit, for the monazite and xenotime phases in samples after 28 days of HT, are shown in Fig. 5(e,f). Samples Y54%, Y74% and Y84% contain a xenotime phase and a single phase with a variable composition monazite structure. The phase ratio in the entire two-phase region has a linear character, indicating a nearly equilibrium phase ratio in the $LaPO_4$–YPO_4–(H_2O) system. It is worth noting that the composition of the monazite phase $La_{1-x}Y_xPO_4$ ($x \approx 0.03$) in the Y84% sample can be considered as the closest to the equilibrium at $T = 230^{\circ}$C, $P \sim 10$ MPa (hydrothermal conditions). At compositions closer to this ratio of $LaPO_4$:YPO_4, phase transformations occur more slowly and in samples after 28 days HT, solid solutions with a monazite structure $La_{1-x}Y_xPO_4$ exist with a composition of $0.07 \leq x \leq 0.17$.

The dependencies of the mean volume weighted crystallite size of phases in the samples after 2 hours of HT are shown in Fig. 6(a), after 7 days in Fig. 6(b) and after 28 days in Fig. 6(c). After 2 hours of HT, the crystallites with a monazite structure do not exceed 20 nm in samples with compositions of $x \leq 0.60$. The crystallites of the rhabdophane phase, which coexist with the monazite phase, have similar values of the mean crystallite size (around 20 nm). In the single-phase region under these HT conditions, the rhabdophane crystallites reach 80 nm. It should be noted that the dependence of the mean volume weighted crystallite size of the rhabdophane phase after HT-treated similar to samples, obtained by precipitation method and, tends to increase with an increase in the molar fraction of YPO_4 in the system. The crystallites with a monazite structure in samples Y86%–Y92% exhibit significant variation in size, ranging from 20 to 100 nm. The xenotime phase crystallites have the mean volume weighted size of $D \approx 60$ nm with a fairly wide range of values.

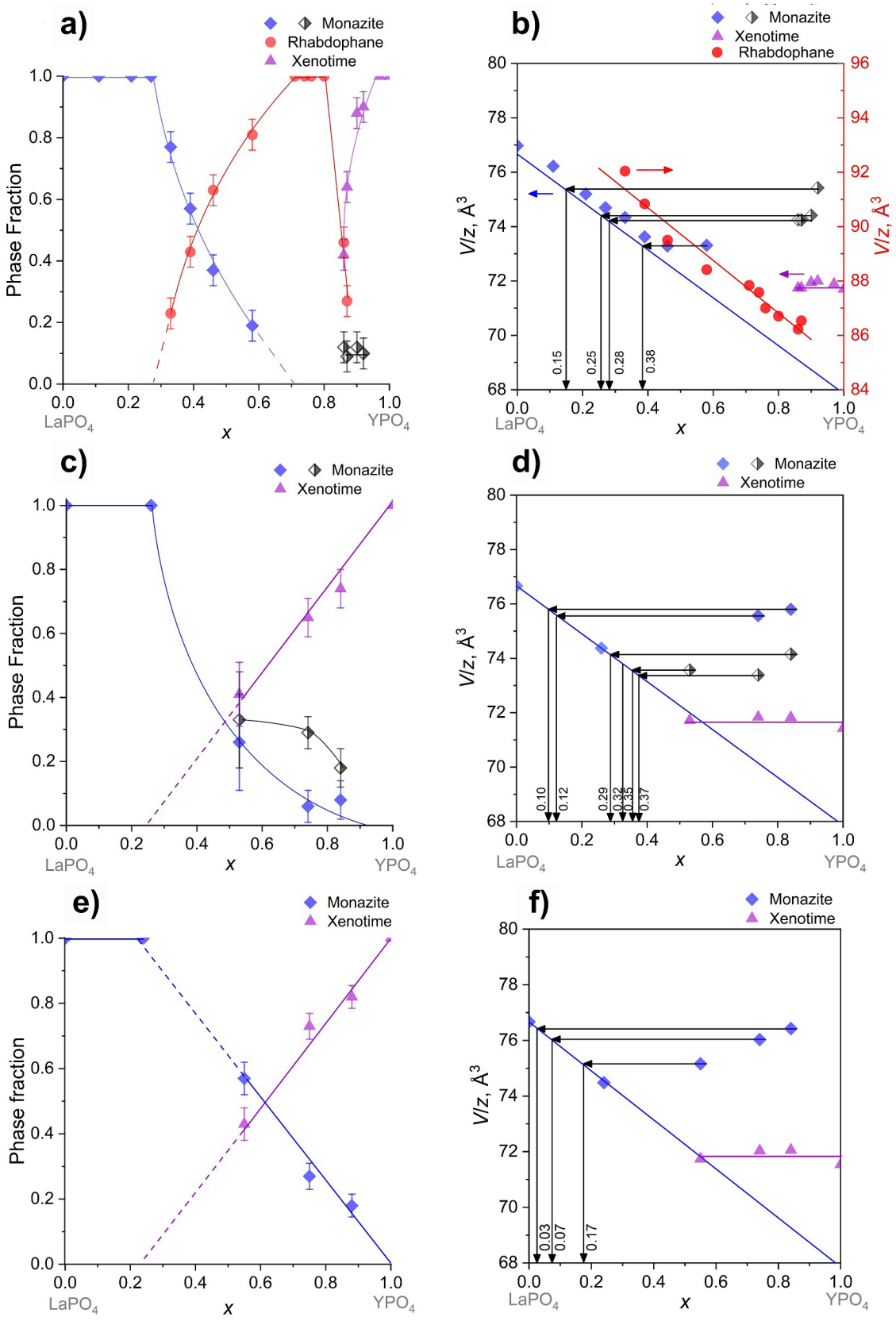

FIG. 5. Phase ratio and change in the unit-cell volume normalized to the number of formula units for rhabdophane, monazite and xenotime structures on the yttrium content of samples after HT: a,b) 2 hours; c,d) 7 days; e,f) 28 days

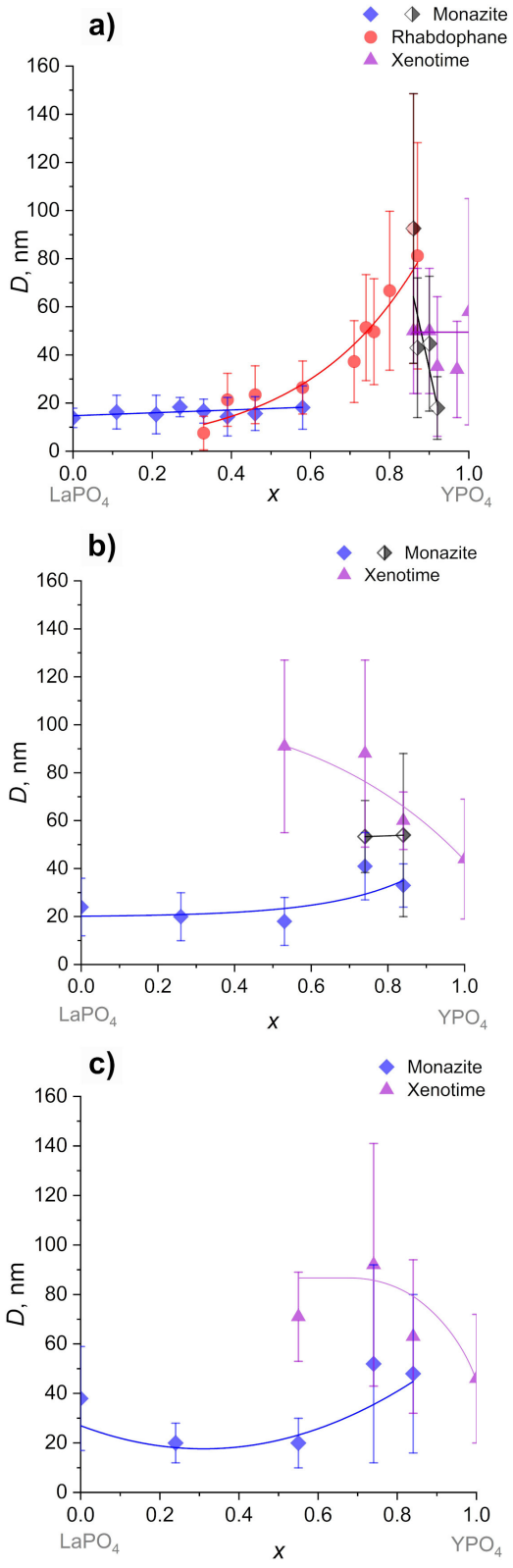

FIG. 6. The dependence of the mean volume weighted crystallite size on the composition of the system of samples after HT: a,b) 2 hours; c,d) 7 days; e,f) 28 days

After 7 days of HT, the mean volume weighted crystallite size of the monazite phase in samples with $x \leq 0.50$ was found to be 20 ± 10 nm (Fig. 6(b)). In samples with a $LaPO_4$:YPO_4 ratio close to 1:1, there is a tendency for the weighted average crystallite size of the xenotime phase to increase to 90 ± 35 nm compared to the Y100% sample ($D = 45 \pm 25$ nm). The weighted average crystallite sizes of the monazite phase in the Y74% and Y84% samples are quite close, averaging 50 ± 20 nm. The determination of the average crystallite size of the monazite phase in the Y53% sample has a larger error due to the overlap of two reflections from monazite phases with different compositions. It is worth noting that the crystallite sizes may be smaller than 20 nm for both compositions of the monazite phase.

After 28 days under hydrothermal conditions, the mean volume weighted crystallite size of the monazite phase in the Y0% sample twofold increase compared to that after 2 hours of HT, reaching 38 ± 21 nm. The average crystallite sizes of the xenotime structure in samples with a $LaPO_4$:YPO_4 ratio of approximately 1:1 tend to increase, similar to the samples after 7 days of HT. The decrease value of the mean volume weighted crystallite sizes of the xenotime structure in the Y54% sample is likely caused by the transformation of the metastable phase with a monazite structure into phases with xenotime and monazite structures. As a result of the transformation process, new nanocrystals with a smaller size and a xenotime structure are formed, which affects the size distribution characteristics. The weighted average crystallite sizes of the monazite and xenotime structures in the Y74% and Y84% samples have a larger range of values compared to samples of the same composition after 7 days of HT. This fact is likely also caused by the transformation of the metastable phase with a monazite structure into more stable phases - a monazite phase with a different composition and a xenotime phase. It is worth noting that there was no increase in the mean volume weighted crystallite size of the monazite structure in the Y25% sample after 28 days of HT ($D \approx 20$ nm).

Figure 7 shows TEM image of nanoparticles and their distribution in the cross-sectional sizes of a sample with a composition of $La_{0.75}Y_{0.25}PO_4$ with monazite structure after 28 days of HT. The monazite nanoparticles have rod-like shapes with a relatively high aspect ratio. The distribution of particles according to their smaller dimensions ranges from 10 to 40 nm, with a weighted average thickness of about 18 nm. It should be noted that a significant systematic error was most likely introduced into the particle size distribution during the sample preparation. It is due to the fact that upon completion of the ultrasonic dispersion of a suspension of particles in alcohol, the particles begin to settle to the bottom and the settling rate of large heavy particles is obviously higher. Nevertheless, the mean volume weighted crystallite size determined from the X-ray diffraction line profile ($D = 20 \pm 8$ nm) correlates well with the TEM data on the average particle thickness.

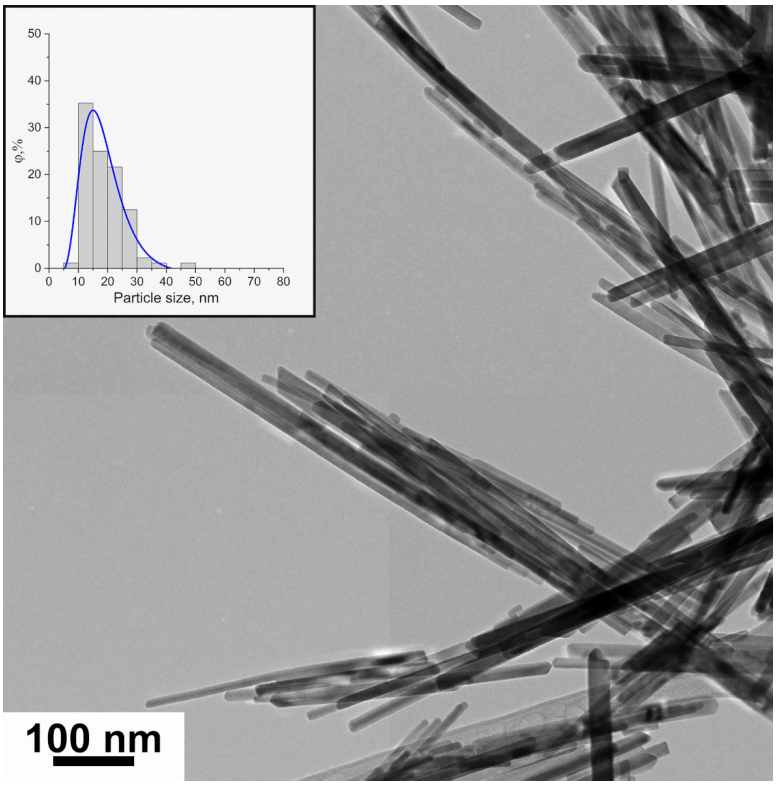

FIG. 7. TEM image of the $La_{0.75}Y_{0.25}PO_4$ sample synthesized by the hydrothermal method at 230°C for 28 days and the histogram of particle size distribution (on inset)

Hydrothermal treatment at 230°C for 28 days leads to the formation of phases with compositions close to the equilibrium state of the system: a monazite-structured phase $La_{1-x}Y_xPO_4$ ($x \leq 0.03$) and a xenotime-structured phase YPO_4.

With increasing isothermal holding time of HT from 2 hours to 7 days and 28 days, a transformation of the rhabdophane-structured phase into the monazite-structured and xenotime-structured phases was observed in the system, along with a gradual redistribution of the YPO_4 component between the monazite-structured and xenotime-structured phases. The $La_{0.75}Y_{0.25}PO_4$ sample, crystallizing in the monazite-structured phase, does not change its phase composition or crystal size ($D \approx 20$ nm) with increasing duration of isothermal holding time under hydrothermal condition. Based on the obtained data, it can be presumed that the $La_{0.75}Y_{0.25}PO_4$ sample also crystallizes in a metastable monazite-structured phase, and that increasing the duration of HT will lead to transformations of this metastable phase into phases with more equilibrium compositions, such as the monazite-structured and xenotime-structured phases. On the other hand, analysis of literature data for the $LaPO_4$–YPO_4 system at $T \geq 1000^\circ$C [46, 48] has shown that only one phase with a monazite structure is observed for the $La_{0.75}Y_{0.25}PO_4$ sample. It is likely that the stability of the monazite-structured phase $La_{0.75}Y_{0.25}PO_4$ is related to the prehistory of the initial sample and homogenization of the La and Y atoms in the rhabdophane-structured phase. However, without a phase diagram for the $LaPO_4$–YPO_4–(H_2O) system, extrapolating the literature data to low temperature ranges would still have significant uncertainty.

4. Conclusions

It has been shown that in the $LaPO_4$–YPO_4–(H_2O) system, nanocrystalline samples of a solid solution with rhabdophane structure $La_{1-x}Y_xPO_4 \cdot nH_2O$ ($0 \leq x \leq 0.80$) were obtained using a precipitation method. The average thickness of the nanocrystals with rhabdophane structure correlates well with the mean volume weighted crystallite size for the samples after precipitation, indicating their single-crystalline structure in cross-sectional size of the nanorods. After hydrothermal treatment at 230°C for 2 hours, phases with monazite, rhabdophane, and xenotime structures are formed in the system in various ratios. After hydrothermal synthesis for 7 days in the system, phase transformation from a rhabdophane-structured phase to nanocrystals of two different compositions with monazite structure and to a xenotime-structured phase occurs. The phase fraction of the metastable phase with higher yttrium solubility in monazite structure after 7 days of HT ranged from ∼20 to ∼35%. With an increase in the duration of isothermal holding time to 28 days, the metastable phase with higher yttrium solubility in monazite structure is completely transformed into phases with structures of YPO_4 xenotime and $La_{1-x}Y_xPO_4$ monazite with compositions close to equilibrium.

Thus, it is shown that in the $LaPO_4$–YPO_4–H_2O system at low temperatures, the phase with variable composition with a high yttrium content and a monazite structure, and the phase of indefinite composition containing a significant amount of lanthanum with a rhabdophane structure, are not in equilibrium. The stability of the monazite phase in a sample with a composition of $La_{0.75}Y_{0.25}PO_4$ after 2 hours, 7 days and 28 days of HT at 230°C, which does not change its composition and remains in the form of nanocrystals with an average crystal size of about 20 nm, can be explained by the presence of this phase in a metastable state.

References

[1] Pawłów J., Zdończyk M., Guzik M., Boulon G., Guyot Y., Wilk-Kozubek M., Mudring A.-V., Cybińska J. Influence of ionic liquid and oleic acid assisted methods on the spectroscopic properties of Nd^{3+}-doped $GdPO_4$ nano-particles. *J. Mater. Chem.*, 2023, **11**(22), P. 7227–7242.

[2] Bouddouch A., Amaterz E., Taoufyq A., Bakiz B., Guinneton F., Villain S., Valmalette J.C., Gavarri J.R., Benlhachemi A. Photocatalytic and photoluminescent properties of a system based on $SmPO_4$ nanostructure phase. *Mater. Today Proc.*, 2020, **27**(4), P. 3139–3144.

[3] Kahouadji B., Guerbous L., Boukerika A., Dolić S.D., Jovanović D.J., Dramićanin M.D. Sol gel synthesis and pH effect on the luminescent and structural properties of YPO_4:Pr^{3+} nanophosphors. *Opt. Mater.*, 2017, **70**, P. 138–143.

[4] Yang J., Wang X., Song L., Luo N., Dong J., Gan S., Zou L. Tunable luminescence and energy transfer properties of $GdPO_4$:Tb^{3+}, Eu^{3+} nanocrystals for warm-white LEDs. *Opt. Mater.*, 2018, **85**, P. 71–78.

[5] Zhao R., Chen Z., Li Q., Wang X., Tang Y., Fu G., Li H., Lee J.M., Huang S. N-doped $LaPO_4$: An effective Pt-free catalyst for electrocatalytic oxygen reduction. *Chem Catal.*, 2022, **2**(12), P. 3590–3606.

[6] Ramesh K., Zheng J., Ling E.G.Y., Han Y.F., Borgna A. Synthesis, Characterization and Catalytic Activity of Uniformly Crystalline $LaPO_4$ Nanofiber Catalysts for Ethanol Dehydration. *J. Phys. Chem. C*, 2009, **113**(37), P. 16530–16537.

[7] Woodward J., Kennel S.J., Stuckey A., Osborne D., Wall J., Rondinone A.J., Standaert R.F., Mirzadeh S. $LaPO_4$ nanoparticles doped with actinium-225 that partially sequester daughter radionuclides. *Bioconjug. Chem.*, 2011, **22**(4), P. 766–776.

[8] Sadowska K., Ragiń T., Kochanowicz M., Miluski P., Dorosz J., Leśniak M., Dorosz D., Kuwik M., Pisarska J., Pisarski W., Rećko K., Żmojda J. Analysis of Excitation Energy Transfer in $LaPO_4$ Nanophosphors Co-Doped with Eu^{3+}/Nd^{3+} and Eu^{3+}/Nd^{3+}/Yb^{3+}. *Ions. Mater.*, 2023, **16**(4), P. 1588.

[9] Zhang L., Bai S., You H., Wu H., Peng Q., Li W., Cao K., Zhou Y. Submicrometre-sized $EuPO_4$ hollow spheres: template-directed synthesis and luminescent properties. *Micro Nano Lett.*, 2019, **14**(3), P. 309–312.

[10] Michel C.R., Martínez-Preciado A.H., Rivera-Tello C.D. CO2 gas sensing response of YPO_4 nanobelts produced by a colloidal method. *Sensors Actuators B Chem.*, 2015, **221**, P. 499–506.

[11] Zhang P., Wang E., Guo C., Yang T., Hou X. High-entropy rare earth phosphates ($REPO_4$, RE = Ho, Tm, Yb, Lu, Dy, Er and Y) with excellent comprehensive properties. *J. Eur. Ceram. Soc.*, 2023, **35**(12), P. 2892–2896.

[12] Mezentseva L.P., Osipov A.V., Ugolkov V.L., Koptelova L.A., Khamova T.V. Comparative Study of the Synthesis of Ceramic Composites Based on Lanthanum Orthophosphate. *Glas. Phys. Chem.*, 2023, **49**, P. 379–385.

[13] Yorov K.E., Shekunova T.O., Baranchikov A.E., Kopitsa G.P., Almásy L., Skogareva L.S., Kozik V.V., Malkova A.N., Lermontov S.A., Ivanov V.K. First rare-earth phosphate aerogel: sol–gel synthesis of monolithic ceric hydrogen phosphate aerogel. *J. Sol-Gel Sci. Technol.*, 2018, **85**, P. 574–584.

[14] Chaudan E., Kim J., Tusseau-Nenez S., Goldner P., Malta O.L., Peretti J., Gacoin T. Polarized Luminescence of Anisotropic $LaPO_4$:Eu Nanocrystal Polymorphs. *J. Am. Chem. Soc.*, 2018, **140**(30), P. 9512–9517.

[15] Makowski M., Witkowski M.E., Drozdowski W., Wojtowicz A.J., Wisniewski K., Boatner L.A. Luminescence and scintillation properties of XPO_4:Nd^{3+}(X = Y, Lu, Sc, La) crystals. *Opt. Mater.*, 2018, **79**, P. 273–278.

[16] Mezentseva L.P., Osipov A.V., Ugolkov V.L., Akatov A.A., Doil'nitsyn V.A. Physicochemical Properties of Ceramics Based on a $LaPO_4$–$DyPO_4$ System. *Glas. Phys. Chem.*, 2019, **45**, P. 268–271.

[17] Heuser J.M., Palomares R.I., Bauer J.D., Rodriguez M.J.L., Cooper J., Lang M., Scheinost A.C., Schlenz H., Winkler B., Bosbach D., Neumeier S., Deissmann G. Structural characterization of (Sm,Tb)PO_4 solid solutions and pressure-induced phase transitions. *J. Eur. Ceram. Soc.*, 2018, **38**(11), P. 4070–4081.

[18] Kamel N., Remil K., Arabi M., Kamel Z., Zahri A., Metahri S. Effect of the synthesis method on the properties of a Pb-bearing (Y–Gd–Ce) rare-earth phosphate used for the confinement of high-level radioactive waste. *J. Nucl. Mater.*, 2010, **401**(1-3), P. 104–112.

[19] Ni Y., Hughes J.M., Mariano A.N. Crystal chemistry of the monazite and xenotime structures. *Am. Mineral.*, 1995, **80**(1-2), P. 21–26.

[20] Heuser J.M., Neumeier S., Peters L., Schlenz H., Bosbach D., Deissmann G. Structural characterisation of metastable Tb- and Dy-monazites. *J. Solid State Chem.*, 2019, **273**, P. 45–52.

[21] Kijkowska R. Thermal decomposition of lanthanide orthophosphates synthesized through crystallisation from phosphoric acid solution. *Thermochim. Acta.*, 2003, **404**(1-2), P. 81–88.

[22] Mooney R.C.L. X-ray diffraction study of cerous phosphate and related crystals. I. Hexagonal modification. *Acta Crystallogr.*, 1950, **3**, P. 337–340.

[23] Mesbah A., Clavier N., Elkaim E., Szenknect S., Dacheux N. In pursuit of the rhabdophane crystal structure: from the hydrated monoclinic $LnPO_4 \cdot 0.667H_2O$ to the hexagonal $LnPO_4$ (Ln = Nd, Sm, Gd, Eu and Dy). *J. Solid State Chem.*, 2017, **249**, P. 221–227.

[24] Subramani T., Rafiuddin M.R., Shelyug A., Ushakov S., Mesbah A., Clavier N., Qin D., Szenknect S., Elkaim E., Dacheux N., Navrotsky A. Synthesis, Crystal Structure and Enthalpies of Formation of Churchite-type $REPO_4 \cdot 2H_2O$ (RE = Gd to Lu) Materials. *Cryst. Growth Des.*, 2019, **19**(8), P. 4641–4649.

[25] Hikichi Y., Sasaki T., Murayama K., Nomura T., Miyamoto M. Mechanochemical Changes of Weinschenkite-Type $RPO_4 \cdot 2H_2O$ (R = Dy, Y, Er, or Yb) by Grinding and Thermal Reactions of the Ground Specimens. *J. Am. Ceram. Soc.*, 1989, **72**(6), P. 1073–1076.

[26] Ivashkevich L.S., Lyakhov A.S., Selevich A.F. Preparation and structure of the yttrium phosphate dihydrate $YPO_4 \cdot 2H_2O$. *Phosphorus Res. Bull.*, 2013, **28**, P. 45–50.

[27] Shelyug A., Mesbah A., Szenknect S., Clavier N., Dacheux N., Navrotsky A. Thermodynamics and stability of rhabdophanes, hydrated rare earth phosphates $REPO_4 \cdot nH_2O$. *Front. Chem.*, 2018, **6**, P. 604.

[28] Ochiai A., Utsunomiya S. Crystal Chemistry and Stability of Hydrated Rare-Earth Phosphates Formed at Room Temperature. *Miner.*, 2017, **7**(5), P. 84.

[29] Hikichi Y., Ota T., Hattori T., Imaeda T. Synthesis and Thermal Reactions of Rhabdophane-(Y). *Mineral. J.*, 1996, **18**(3), P. 87–96.

[30] Bryukhanova K.I., Nikiforova G.E., Gavrichev K.S. Synthesis and study of anhydrous lanthanide orthophosphate (Ln = La, Pr, Nd, Sm) nanowhiskers. *Nanosystems: Phys. Chem. Math.*, 2016, **7**(3), P. 451–458.

[31] Enikeeva M.O., Proskurina O.V., Motaylo E.S., Danilovich D.P., Gusarov V.V. The influence of condition of the monazite structured $La_{0.9}Y_{0.1}PO_4$ nanocrystals sintering on thermal and mechanical properties of the material. *Nanosystems: Phys. Chem. Math.*, 2021, **12**(6), P. 799–807.

[32] Proskurina O.V., Sivtsov E.V., Enikeeva M.O., Sirotkin A.A., Abiev R. Sh., Gusarov V.V. Formation of rhabdophane-structured lanthanum orthophosphate nanoparticles in an impinging-jets microreactor and rheological properties of sols based on them. *Nanosystems: Phys. Chem. Math.*, 2019, **10**(2), P. 206–214.

[33] Rafiuddin M.R., Tyagi C., Haq M.A. Synthesis and structural investigation of churchite-type $REPO_4 \cot 2H_2O$ (RE = Y, Gd, Dy) nanocrystals. *J. Solid State Chem.*, 2022, **311**, P. 123150.

[34] Lucas S., Champion E., Bregiroux D., Bernache-Assollant D., Audubert F. Rare earth phosphate powders $RePO_4 \cdot nH_2O$ (Re=La, Ce or Y)—Part I. Synthesis and characterization. *J. Solid State Chem.*, 2004, **177**(4-5), P. 1302–1311.

[35] Sankar S., Warrier K.G. Aqueous sol-gel synthesis of lanthanum phosphate nano rods starting from lanthanum chloride precursor. *J. Sol-Gel Sci. Technol.*, 2011, **58**, P. 195–200.

[36] Mezentseva L.P., Osipov A.V., Ugolkov V.L., Akatov A.A., Doilnitsyn V.A., Maslennikova T.P., Yakovlev A.V. Sol-Gel Synthesis, Thermal Behavior of Nanopowders and Chemical Stability of $La_{1-x}Ho_xPO_4$ Ceramic Matrices. *Glas. Phys. Chem.*, 2018, **44**, P. 440–449.

[37] Ugolkov V.L., Mezentseva L.P., Osipov A.V., Popova V.F., Maslennikova T.P., Akatov A.A., Doil'nitsyn V.A. Synthesis of nanopowders and physicochemical properties of ceramic matrices of the $LaPO_4$–YPO_4–(H_2O) and $LaPO_4$–$HoPO_4$–(H_2O) systems. *Russ. J. Appl. Chem.*, 2017, **90**, P. 28–33.

[38] Ahmadzadeh M.A., Chini S.F., Sadeghi A. Size and shape tailored sol-gel synthesis and characterization of lanthanum phosphate ($LaPO_4$) nanoparticles. *Mater. Des.*, 2019, **181**, P. 108058.

[39] Colomer M.T., Ortiz A.L., Effect of Tb^{3+} doping and self-generated pressure on the crystallographic/morphological features and thermal stability of $LaPO_4 \cdot nH_2O$ single-crystal nanorods obtained by microwave-assisted hydrothermal synthesis. *Ceram. Int.*, 2016, **42**(16), P. 18074–18086.

[40] Palma-Ramírez D., Domínguez-Crespo M.A., Torres-Huerta A.M., Dorantes-Rosales H., Ramírez-Meneses E., Rodríguez E. Microwave-assisted hydrothermal synthesis of $CePO_4$ nanostructures: Correlation between the structural and optical properties. *J. Alloys Compd.*, 2015, **643**, P. S209–S218.

[41] Enikeeva M.O., Kenges K.M., Proskurina O.V., Danilovich D.P., Gusarov V.V. Influence of Hydrothermal Treatment Conditions on the Formation of Lanthanum Orthophosphate Nanoparticles of Monazite Structure. *Russ. J. Appl. Chem.*, 2020, **93**, P. 540–548.

[42] Meyssamy H., Riwotzki K., Kornowski A., Naused S., Haase M. Wet-Chemical Synthesis of Doped Colloidal Nanomaterials: Particles and Fibers of $LaPO_4$:Eu, $LaPO_4$:Ce and $LaPO_4$:Ce,Tb. *Adv. Mater.*, 1999, **11**(10), P. 840–844.

[43] Leys J.M., Ji Y., Klinkenberg M., Kowalski P.M., Schlenz H., Neumeier S., Bosbach D., Deissmann G. Monazite-Type $SmPO_4$ as Potential Nuclear Waste Form: Insights into Radiation Effects from Ion-Beam Irradiation and Atomistic Simulations. *Materials*, 2022, **15**(10), P. 3434

[44] Lucas S., Champion E., Bernache-Assollant D., Leroy G. Rare earth phosphate powders $RePO_4 \cdot nH_2O$ (Re=La, Ce or Y) II. Thermal behavior. *J. Solid State Chem.*, 2004, **177**(4-5), P. 1312–1320.

[45] Enikeeva M.O., Proskurina O.V., Levin A.A., Smirnov A.V., Nevedomskiy V.N., Gusarov V.V. Structure of $Y_{0.75}La_{0.25}PO_4 \cdot 0.67H_2O$ rhabdophane nanoparticles synthesized by the hydrothermal microwave method. *J. Solid State Chem.*, 2023, **319**, P. 123829.

[46] Mogilevsky P., Boakye E.E., Hay R.S. Solid solubility and thermal expansion in a $LaPO_4$–YPO_4 system. *J. Am. Ceram. Soc.*, 2007, **90**(6), P. 1899-1907.

[47] Emden B. V., Thornber M., Graham J., Lincoln F.J. Solid Solution Behaviour of Synthetic Monazite and Xenotime from Structure. Proceeding pf "45th Annual Denver X-ray Conference". Denver, Colorado, USA, 1996.

[48] Mogilevsky P. On the miscibility gap in monazite-xenotime systems. *Phys. Chem. Miner.*, 2007, **34**, P. 201–214.

[49] Enikeeva M.O., Proskurina O.V., Danilovich D.P., Gusarov V.V. Formation of nanocrystals based on equimolar mixture of lanthanum and yttrium orthophosphates under microwave-assisted hydrothermal synthesis. *Nanosystems: Phys. Chem. Math.*, 2020, **11**(6), P. 705–715.

[50] Scherrer P.. Bestimmung der Größe und der inneren Struktur von Kolloidteilchen mittels Röntgenstrahlen. *Nachrichten von Der Gesellschaft Der Wissenschaften Zu Göttingen Math.Klasse.*, 1918, P. 98–100.
[51] Retgers J. W. The Specific Gravity of Isomorphic Mixtures. *Zeitschrift Für Phys. Chemie.*, 1889, **3**, P. 497–497.

Submitted 10 October 2023; revised 15 November 2023; accepted 16 November 2023

Information about the authors:

Maria O. Enikeeva – Ioffe Institute, 194021 St. Petersburg, Russia; St. Petersburg State Institute of Technology, 190013 St. Petersburg, Russia; ORCID 0000-0002-9633-4421; odin2tri45678@gmail.com

Olga V. Proskurina – Ioffe Institute, 194021 St. Petersburg, Russia; St. Petersburg State Institute of Technology, 190013 St. Petersburg, Russia; ORCID 0000-0002-2807-375X; proskurinaov@mail.ru

Evgeny Yu. Gerasimov – Federal Research Center, Boreskov Institute of Catalysis SB RAS, Novosibirsk 630090, Russia; ORCID 0000-0002-3230-3335; gerasimov@catalysis.ru

Vladimir N. Nevedomskiy – Ioffe Institute, 194021 St. Petersburg, Russia; ORCID 0000-0002-7661-9155; nevedom@mail.ioffe.ru

Victor V. Gusarov – Ioffe Institute, 194021 St. Petersburg, Russia; ORCID 0000-0003-4375-6388; gusarov@mail.ioffe.ru

Conflict of interest: the authors declare no conflict of interest.

NANOSYSTEMS:
PHYSICS, CHEMISTRY, MATHEMATICS

Original article

Malyshev S.A., et al. *Nanosystems: Phys. Chem. Math.*, 2023, **14** (6), 672–678.
http://nanojournal.ifmo.ru
DOI 10.17586/2220-8054-2023-14-6-672-678

Formation of the metal-oxide nanocomposites during the partial reduction of Nd-Sr nickelates

Sergey A. Malyshev[1,2,a], Oleg A. Shlyakhtin[1,b], Grigorii M. Timofeev[1,c], Galina N. Mazo[1,d], Ilya V. Roslyakov[3,4,e], Aleksander V. Vasiliev[1,f], Tatiana B. Shatalova[1,g], Aleksander L. Kustov[1,h]

[1]Department of Chemistry, M. V. Lomonosov Moscow State University, 119991 Moscow, Russia

[2]Department of Materials Sciences, Shenzhen MSU-BIT University, Shenzhen 518172, China

[3]Department of Materials Sciences, M. V. Lomonosov Moscow State University, 119991 Moscow, Russia

[4]N. S. Kurnakov Institute of General and Inorganic Chemistry, Russian Academy of Sciences, 119991 Moscow, Russia

[a]malyshev12sa@yandex.ru, [b]oleg@inorg.chem.msu.ru, [c]timofeevg@inbox.ru, [d]mazo@inorg.chem.msu.ru, [e]Ilya.roslyakov@gmail.com, [f]a.vasiliev@inorg.chem.msu.ru, [g]shatalovatb@gmail.com, [h]kyst@list.ru

Corresponding author: O. A. Shlyakhtin, oleg@inorg.chem.msu.ru

ABSTRACT A thermal reduction of $Nd_{2-x}Sr_xNiO_{4-\delta}$ ($x = 0$–1.4) solid solutions in an Ar/H_2 gas mixture occurs in several separate stages. The initial stages of reduction presumably related to the reduction of Ni^{3+} to Ni^{2+} cause only minor changes in the initial K_2NiF_4 type structure and retain the morphology of the complex oxide particles. Occasionally, this process is accompanied by the appearance of Ni metal nanoparticles at the surface of oxide grains. As-obtained Ni/metal oxide nanocomposites similar to the products of redox exsolution demonstrate noticeable catalytic activity in the reaction of CO_2 hydrogenation at T = 350–400°C.

KEYWORDS nanoparticles, nanocomposites, thermal reduction, redox exsolution, catalysis, CO_2 hydrogenation.

ACKNOWLEDGEMENTS This study is supported by the Russian Science Foundation (grant 22-23-00460). The Moscow State University program of development is gratefully acknowledged for the partial support of instrumental studies. SEM images were obtained at the IGIC RAS Joint Research Center for Physical Methods of Research.

FOR CITATION Malyshev S.A., Shlyakhtin O.A., Timofeev G.M., Mazo G.N., Roslyakov I.V., Vasiliev A.V., Shatalova T.B., Kustov A.L. Formation of the metal-oxide nanocomposites during the partial reduction of Nd-Sr nickelates. *Nanosystems: Phys. Chem. Math.*, 2023, **14** (6), 672–678.

1. Introduction

Most of the modern chemical synthesis methods of metal-oxide nanocomposites are based on the soaking of refractory substrates with solutions containing transition metals followed by the thermal reduction of the dried substrate [1]. However, the growing attention has been attracted in recent years by the new synthesis techniques based on the formation of metal-oxide nanocomposites in situ, by the thermal decomposition of solid multicomponent precursors in the reductive environment. Along with polynuclear complex compounds and metal-organic frameworks (MOF), complex oxides of transition elements could be also used as precursors in this synthesis [2–4].

An original synthesis technique was proposed last years based on the partial reduction of several complex oxides at elevated temperatures in the reducing environment. Despite retaining the crystal structure of the initial complex oxide with minor changes only, this process is accompanied by the formation of the isolated spherical nanoparticles of the transition or noble metals at the surface of larger grains of the precursor compound [5–7]. An essential feature of nanocomposites obtained by this technique called redox exsolution is their enhanced thermal stability due to socketing the metal particles to the surface of precursor grains. This effect was observed for a limited number of rather specific complex oxides like cation-deficient perovskites or solid solutions containing a small amount of transition metals only [8–10]. Due to the low rate of metal particle formation, this process usually takes processing for several hours at elevated temperatures, usually at T > 700°C.

Recent studies demonstrated that metal-oxide nanocomposites with morphology rather similar to the products of redox exsolution could be obtained by the complete thermal reduction of complex oxides of rare earth, cobalt, and nickel with K_2NiF_4 structure [11–13]. Another feature of these nanocomposites that makes them similar to the redox exsolution products is their excellent catalytic activity, selectivity, and stability of the catalytic properties in the processes of partial oxidation and dry reforming of methane at T = 750–850°C.

During these studies, it was found that complex oxides $Nd_{2-x}Sr_xNiO_{4-\delta}$ with K_2NiF_4 structure used as precursors could be obtained for $x \leq 1.4$ though the formation of these compounds is rather complicated; some of them could be obtained at $T > 1100^\circ$C only [14]. A complete reduction of these compounds is usually completed at T > 800°C; this temperature usually increases with an increase in Sr content. All these processes are realized in two distinct stages.

The first step of this process has never been studied before. Taking into account an expected similarity of this stage – partial reduction of $Nd_{2-x}Sr_xNiO_{4-\delta}$ – with redox exsolution processes and, hence, the possibility to observe the formation of Ni nanoparticles at the surface of partial reduction products, the present study was aimed at the investigation of the processes and products of the partial reduction of $Nd_{2-x}Sr_xNiO_{4-\delta}$. Due to the limited thermal stability of these products, the evaluation of their catalytic properties was performed in the CO_2 hydrogenation process usually realized at 300–400°C [15–18].

2. Experimental

A series of complex oxide precursors $Nd_{2-x}Sr_xNiO_{4-\delta}$ (x = 0; 0.5; 1; 1.2; 1.4) was obtained by the freeze drying synthesis method. The details of the synthesis technique can be found elsewhere [14]. Briefly, the aqueous solutions of Nd nitrate, Ni nitrate, and Sr acetate taken in the stoichiometric ratio were mixed with an aqueous solution of polyvinyl alcohol (5 mass. %) to avoid melting during freeze drying. As-obtained solutions with different x values were flash-frozen by liquid nitrogen and freeze dried at P = 0.7 mbar for 2 days. According to the results of previous studies [14], thermal processing of freeze dried precursors was performed in air at T = 1200°C for 6 h to ensure the complete phase formation of all K_2NiF_4-like solid solutions in this series. A reduction of these complex oxides was performed in 10% H_2/Ar gas mixture at different temperatures for 1 h followed by slow cooling in Ar/H_2 stream to room temperature.

XRD analysis of precursors and their reduction products was implemented with a Rigaku D/MAX-2500PC diffractometer (Rigaku, Tokyo, Japan) with Cu $K_{\alpha 1,2}$ radiation generated on a rotating Cu anode (40 kV, 250 mA). The profile analysis of the powder XRD data was carried out by the Le Bail method using the Jana 2006 program package. The TG-DSC thermal analysis of samples was performed in a 10% H_2/Ar gas mixture by STA 409PC/PG (NETZSCH) at T = 40°C – 1000°C and a 5°C/min heating rate. The morphology of the powders was studied using a Carl Zeiss NVision 40 scanning electron microscope (Carl Zeiss SMT AG, Oberkochen, Germany). The magnetic properties were studied using the Faraday balance magnetometer at room temperature. The instrumentation was manufactured at the Institute of Solid-State Chemistry of the Ural Branch of the Russian Academy of Sciences. The magnetic field varied from -17.9 to 17.9 kOe. The relative error in determining the magnetization was 3%. The error in determining the coercive force was ± 100 Oe.

The catalytic properties of the partial reduction products in a CO_2 hydrogenation were studied in a flow-through catalytic apparatus equipped with a stainless steel reactor (4 mm inner diameter) with a fixed catalyst bed. The catalyst sample (200 mg of a catalyst and mixed with quartz glass powder in a 1:2.5 mass ratio) in the form of 0.25–0.5 mm particles was placed in a vertically placed reactor. Hydrogen and carbon dioxide were fed by Bronkhorst EL-FLOW Prestige flow controllers in H_2/CO_2 = 2/1 gas mixture at atmospheric pressure in the absence of dilution with inert gas at 250–400°C at the total reaction mixture flow rate of 100 ml/min.

The total CO_2 conversion (X, %) was calculated from the carbon dioxide loss:

$$x = \left(\frac{G^0 X^0_{CO_2} - G X_{CO_2}}{G^0 X^0_{CO_2}} \right) \cdot 100\%,$$

where $X^0_{CO_2}$ and X_{CO_2} are fractions of carbon dioxide before and after the reactor, and $G^0 X^0_{CO_2}$ and $G X_{CO_2}$ are the carbon dioxide gas flows before and after the reactor.

The product selectivity (S, %) was determined by the equation:

$$S_i = \left(\frac{X_i}{\sum X} \right) \times 100\%,$$

The CO_2 performance was calculated using the equation:

$$P = \frac{G^0 X^0_{CO_2} - G X_{CO_2}}{m_{cat}},$$

where m_{cat} is the catalyst mass.

3. Results and discussion

According to the results of previous studies, all $Nd_{2-x}Sr_xNiO_{4-\delta}$ complex oxides with K_2NiF_4 structure belong to the space group I4/mmm except Nd_2NiO_4 ($x = 0$) belonging to the space group Fmmm [14]. A complex dependence of lattice parameters during the substitution of Nd with Sr in these solid solutions could be explained by the interplay of the difference in ionic radii of Nd^{3+} and Sr^{2+}, different ratio Ni^{3+}/Ni^{2+} and rather different oxygen stoichiometry in these complex oxides. However, the temperature of thermal reduction of these compounds in an H_2/Ar gas mixture resulted in the formation of Ni metal, Nd_2O_3, and SrO demonstrates a systematic increase with the growing amount of strontium

in their composition [14]. The precise oxygen stoichiometry of Nd_2O_3 and SrO allows one to use the total mass change during this reduction for a rather exact evaluation of the oxygen stoichiometry in $Nd_{2-x}Sr_xNiO_{4-\delta}$.

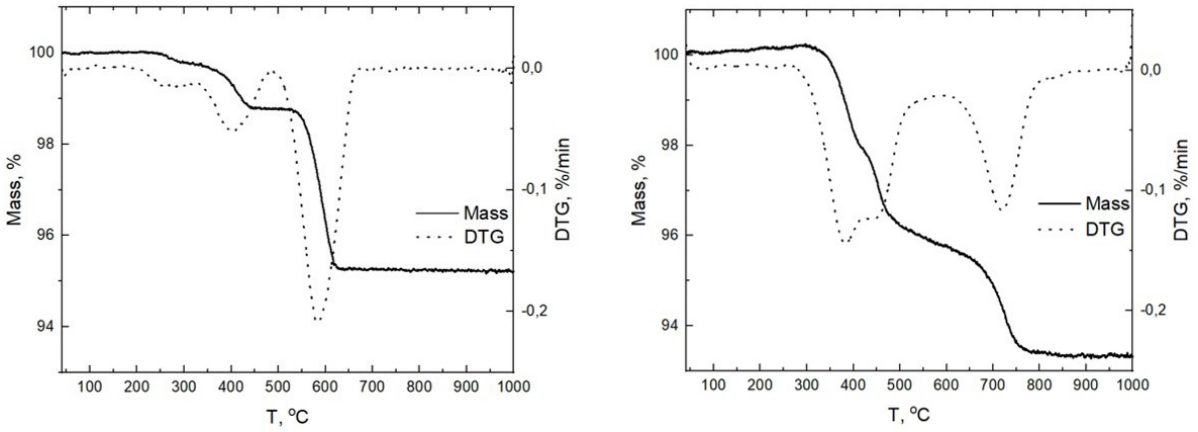

FIG. 1. TG and DTG curves of the reduction of Nd_2NiO_4 ($x = 0$) and $NdSrNiO_{4-\delta}$ ($x = 1$) in the 10% H_2/Ar gas mixture

Another essential feature of these thermal reduction processes deals with their multistage character in all these products (Fig. 1). The mass loss ratio of the first to last steps in TG increases with x. Taking into account that the substitution of Nd with Sr in Nd_2NiO_4 causes a systematic increase of Ni oxidation state from Ni^{2+} to Ni^{3+}, the first stages of the thermal reduction could be affiliated with the reduction of Ni^{3+} to Ni^{2+}.

To study the products of these stages in more detail, the products of the partial reduction of $Nd_{2-x}Sr_xNiO_{4-\delta}$ for $x = 0$–1.4 were obtained by the isothermal treatment of initial complex oxides in Ar/H_2 at T = 500°C, just before the beginning of the last stage of reduction. Analysis of their XRD patterns (Fig. 2, Supplementary, Fig. S1,S2) demonstrated the formation of the new individual complex oxides; their lattice parameters are given in Table 1. The partial reduction product of Nd_2NiO_4 belongs to orthorhombic space group Aema while in other cases the reduced complex oxides belong to Immm structure. A small amount of Nd_2O_3 in this sample could be attributed to the beginning of the second stage of reduction of Nd_2NiO_4 (Fig. 2 ($x = 0$), Fig. S1).

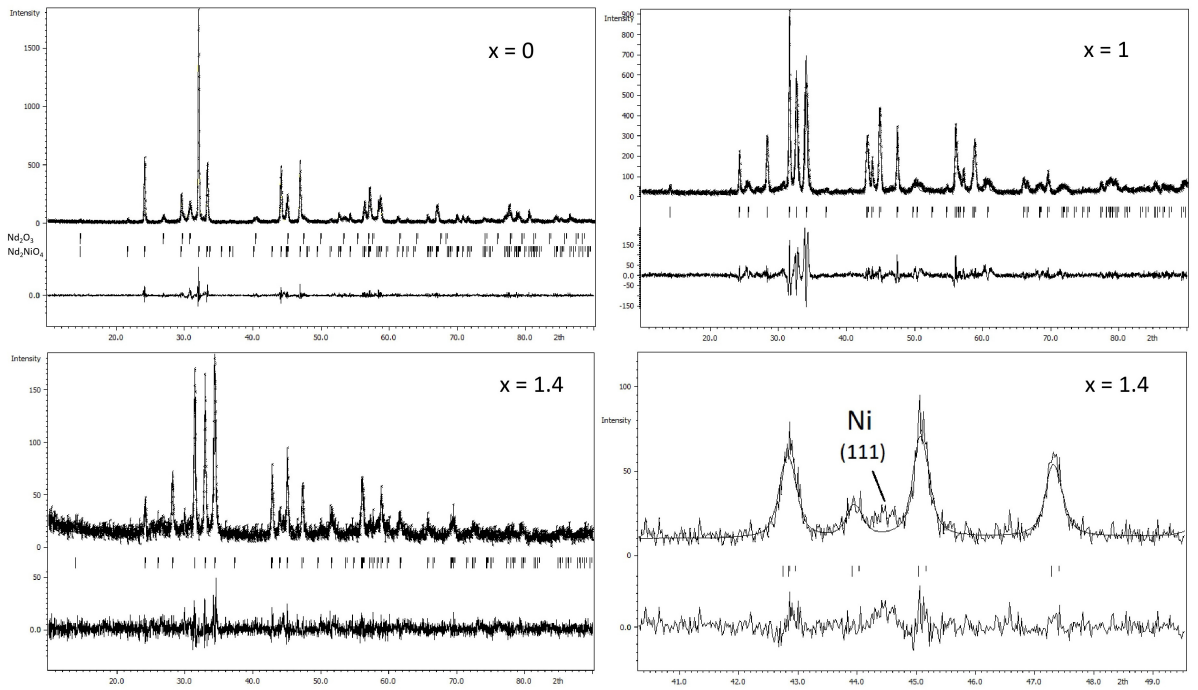

FIG. 2. Le Bail profile refinement plots of the partial reduction products of $Nd_{2-x}Sr_xNiO_{4-\delta}$ – ($x = 0, 1$ and 1.4) at 500°C

A comparison of these data with the lattice parameters of the corresponding precursor compounds described in [14] shows that the minimal changes in lattice volume are observed for Nd_2NiO_4 ($x = 0$) and $Nd_{1.5}Sr_{0.5}NiO_{4-\delta}$ ($x = 0.5$),

TABLE 1. Lattice parameters of the partial reduction products of $Nd_{2-x}Sr_xNiO_{4-\delta}$

Sample	Space group	a, Å	b, Å	c, Å	V, Å
$x = 0$	Aema	5.8335(5)	5.3830(4)	12.119(18)	364.24(6)
$x = 0.5$	Immm	3.7114(2)	3.8232(2)	12.501(17)	177.40(3)
$x = 1$	Immm	3.622(19)	3.8303(5)	12.591(2)	174.68(5)
$x = 1.2$	Immm	3.5503(4)	3.8324(3)	12.665(17)	172.33(4)
$x = 1.4$	Immm	3.538(18)	3.835(18)	12.630(3)	171.38(8)

where the amount of Ni^{3+} and, hence, the intensity of reduction processes were rather small. For complex oxides with $x \geq 1$, the volume is changed more significantly which indicates a difference in the topochemical mechanisms of reduction processes. This difference could be attributed both to a larger amount of Ni^{3+} in the precursor oxide and/or to a more significant effect of strontium with its rather specific chemistry of high temperature processes. Another intriguing feature observed in the XRD pattern of $Nd_{0.6}Sr_{1.4}NiO_{4-\delta}$ reduction product is a small peak attributed to Ni^0 metal that was not identified in other samples.

Analysis of the morphology of the partial reduction products demonstrated retaining the initial morphology of precursor powders with their large micron-sized crystallites formed during their synthesis at 1200°C (Fig. 3). The most important feature of these micrographs is that there is a large number of tiny nanospheres at the surface of large grains of oxide reduction products with $x = 0.5$, 1, and 1.2. It is worth noting, that the sample with $x = 1.2$ is characterized by a slightly larger average particle diameter along with significantly increased size distribution width (Fig. 3F).

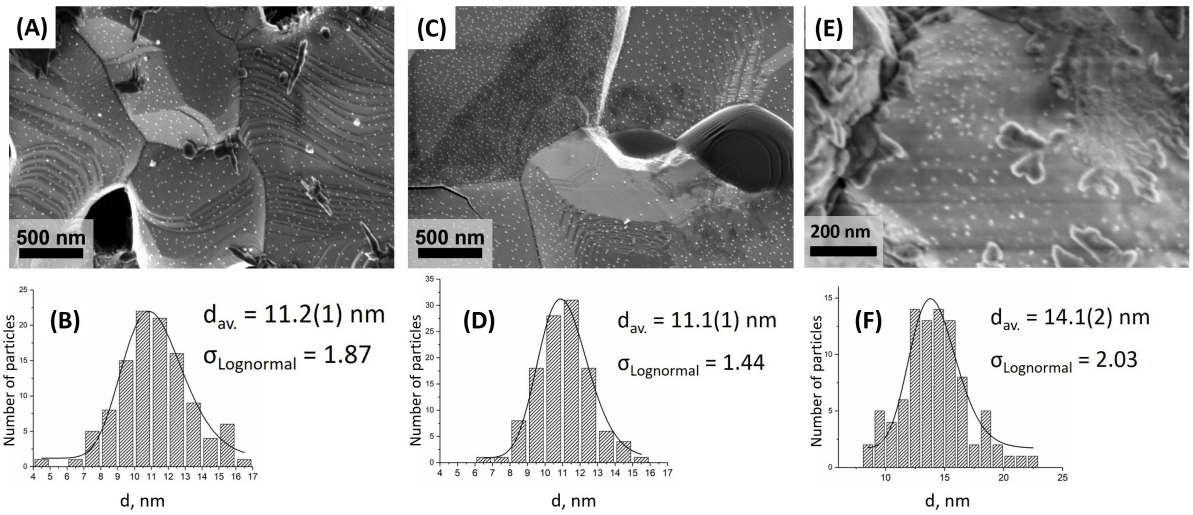

FIG. 3. SEM micrographs of the partial reduction products of $Nd_{2-x}Sr_xNiO_{4-\delta}$ at 500°C for $x = 0.5$ (A,B), $x = 1$ (C,D) and $x = 1.4$ (E,F)

Similar spherical nanoparticles have been observed before during previous studies of $(R,Ca)_2(Co,Ni)O_4$ reduction products [11–14] but they were observed in the products of complete reduction only and have been identified as nanoparticles of Ni metal being one of the main natural products of the complete reduction. The appearance of Ni metal in the products of partial reduction of $Nd_{2-x}Sr_xNiO_{4-\delta}$ affiliated with a reduction of Ni^{3+} to Ni^{2+} and accompanied by the minor changes of the initial K_2NiF_4 structure looks rather unusual.

It should be mentioned, however, that similar particles have been also observed during another partial reduction process that occurred in other complex oxides at much higher temperatures, during redox exsolution [7–10]. Hence, it is rather probable that the nanoparticles observed in Fig. 3 belong to the nickel metal too. Taking into account that the Ni metal is the only ferromagnetic among possible reaction products, the appearance of nickel at the early stages of $Nd_{2-x}Sr_xNiO_{4-\delta}$ reduction was confirmed by the results of magnetic measurements. The observed magnetization curves usual for the soft ferromagnetic materials clearly confirmed the appearance of a significant amount (several mass. %) of magnetic phase in all products of partial reduction in the study (Fig. 4) while the initial compounds demonstrated the common paramagnetic behavior.

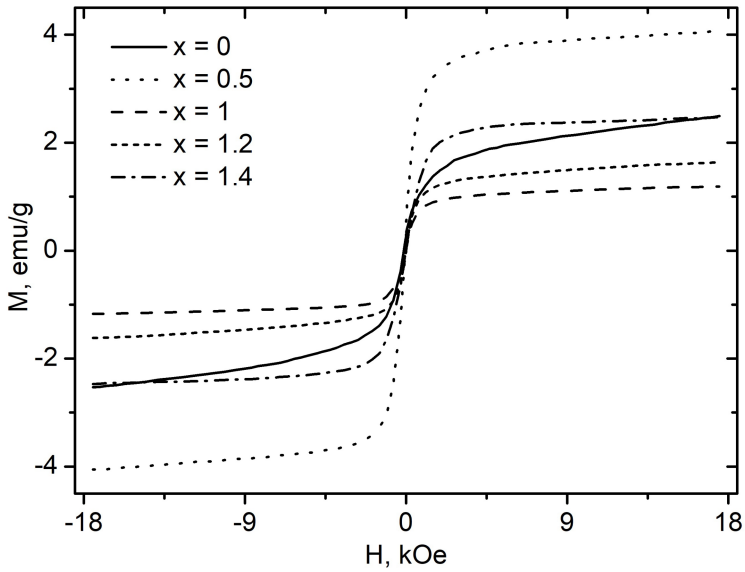

FIG. 4. Magnetization curves of the partial reduction products of $Nd_{2-x}Sr_xNiO_{4-\delta}$

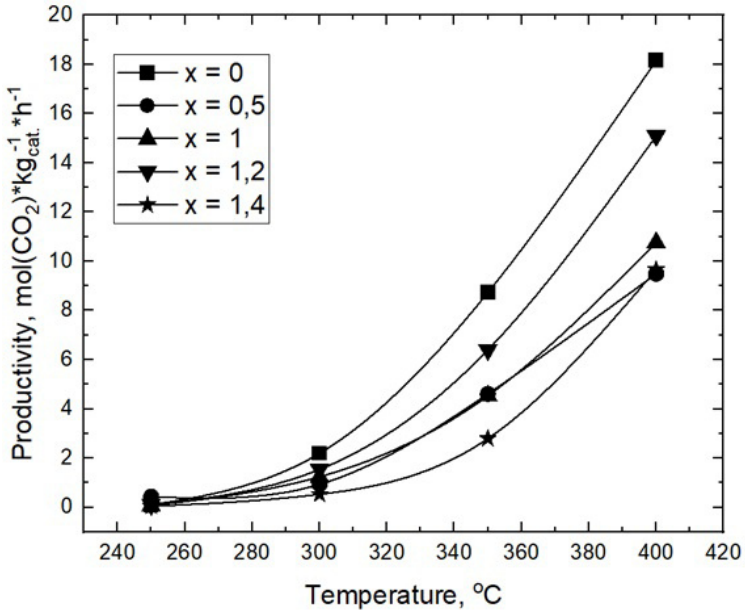

FIG. 5. The productivity of the partial reduction products of $Nd_{2-x}Sr_xNiO_{4-\delta}$ as catalysts of CO_2 hydrogenation at various temperatures

The amount of magnetic phase in these samples is rather different and doesn't demonstrate any obvious correlations with the composition of the precursor compound. This feature clearly indicates that several different topochemical processes could occur during the partial reduction of complex oxides. One of them deals with a soft transformation of the crystal lattice of precursor compound caused by the reduction of Ni^{3+} to Ni^{2+}. Another process involves a more intensive reduction of Ni^{3+} to Ni^0. The ratio between these two reaction pathways could depend on several factors that are not clear right now, and more detailed mechanistic studies are needed to control the nanoparticle formation process.

Despite these obstacles, this interesting process could be used right now as one more synthesis technique to obtain functional metal-oxide nanocomposites. To demonstrate the potential usefulness of these materials, their catalytic properties have been evaluated in the reaction of CO_2 hydrogenation usually occurring at T = 300–400°C. All the materials in the study demonstrated a significant catalytic activity usual for Ni-based catalysts (Fig. 5); the main reduction products are CO and CH_4 (Supplementary, Table S1). The highest catalytic activity is demonstrated by the Sr-free partial reduction product of Nd_2NiO_4 which could be associated with the smallest size of Ni nanoparticles in this composite. A correlation of catalytic activity of other composites with x, amount of magnetic particles, or their size doesn't look obvious that could

be caused by the different reduction mechanisms of different precursor compounds and different spatial distribution of Ni nanoparticles inside the particles of reduction product.

Finally, we have to note that the processes of metal nanoparticles during the partial reduction of complex nickelates have been observed for the first time in the present study. These processes occur simultaneously with a soft transformation of the crystal lattice of matrix oxide at the first stages of reduction. Apart from another kind of partial reduction processes, redox exsolution, these processes occur in a short time at rather moderate temperatures. The complex character of these processes deserves more detailed study by modern instrumental methods. The potential practical usefulness of these processes for materials synthesis could be confirmed by the significant catalytic activity of Ni-based metal-oxide nanocomposites obtained by this method.

References

[1] Ray C., Pal T. Recent advances of metal-metal oxide nanocomposites and their tailored nanostructures in numerous catalytic applications. *J. Mater. Chem. A*, 2017, **5**, P. 9465–9487.

[2] Zhou L.X., Yang Y.Y., Zhu H.L., Zheng Y.Q. In situ synthesis of Ag/NiO derived from hetero-metallic MOF for supercapacitor application. *Chem Papers*, 2021, **75**, P. 1795–1807.

[3] Konnerth H., Matsagar B.M., Chen S.S., Prechtl M.H.G., Shieh F.K., Wu K.C.W. Metal-organic framework (MOF)-derived catalysts for fine chemical production. *Coord. Chem. Rev*, 2020, **416**, P. 213319.

[4] Bhattar S., Abedin M.A., Kanitkar S., Spivey J.J. A review on dry reforming of methane over perovskite derived catalysts. *Catal.Today*, 2021, **365**, P. 2–23.

[5] Kwon O., Joo S., Choi S., Sengodan S., Kim G. Review on exsolution and its driving forces in perovskites. *J. Phys. Energy*, 2020, **2**, P. 032001.

[6] Fan W., Sun Z., Bai Y. Manipulating Electrocatalytic Activity of Perovskite Oxide Through Electrochemical Treatment, *Small*, 2022, **18**, P. 2107131.

[7] Neagu D., Tsekouras G., Miller D.N., Mernard H., Irvine J.T.S. In situ growth of nanoparticles through control of non-stoichiometry. *Nature Chem.*, 2013, **5**, P. 916–923.

[8] Han H., Park J., Nam S.Y., Kim K.J., Choi G.M., Parkin S.S.P., Jang H.M., Irvine J.T.S. Lattice strain-enhanced exsolution of nanoparticles in thin films. *Nature Comm.*, 2019, **10**, P. 1471.

[9] Shah S., Sayono S., Ynzunza J., Pan R., Xu M., Pan X., Gilliard-AbdulAziz K.L. The effects of stoichiometry on the properties of exsolved Ni-Fe alloy nanoparticles for dry methane reforming. *AIChE J.*, 2020, **66**, P. e17078.

[10] Gao Y., Chen D., Saccoccio M., Lu Z., Ciucci F. From material design to mechanism study: Nanoscale Ni exsolution on a highly active A-site deficient anode material for solid oxide fuel cells. *Nano Energy*, 2016, **27**, P. 499–508.

[11] Shlyakhtin O.A., Malyshev S.A., Loktev A.S., Mazo G.N., Garshev A.V., Chumakov R.G., Dedov A.G. Synthesis and Decomposition of $Nd_{2-y}Ca_yCo_{1-x}Ni_xO_4$: The Effect of Resynthesis on the Catalytic Performance of Decomposition Products in the Partial Oxidation of Methane. *ACS Appl. Energy Mater.*, 2021, **4**(8), P. 7661–7673.

[12] Malyshev S.A., Shlyakhtin O.A., Loktev A.S., Mazo G.N., Timofeev G.M., Mukhin I.E., Kaplin I.Yu., Svetogorov R.D., Valeev R.G., Dedov A.G. Exsolution-like synthesis of Ni/(Nd_2O_3,CaO) nanocomposites from $Nd_{2-x}Ca_xNiO_4$ precursors for catalytic applications. *J. Solid State Chem.*, 2022, **312**, P. 123267.

[13] Malyshev S.A., Shlyakhtin O.A., Loktev A.S., Mazo G.N., Timofeev G.M., Mukhin I.E., Svetogorov R.D., Roslyakov I.V., Dedov A.G., Ni/(R_2O_3,CaO) Nanocomposites Produced by the Exsolution of $R_{1.5}Ca_{0.5}NiO_4$ Nickelates (R = Nd, Sm, Eu): Rare Earth Effect on the Catalytic Performance in the Dry Reforming and Partial Oxidation of Methane. *Materials*, 2022, **15**, P. 7265(1-11).

[14] Shlyakhtin O.A., Timofeev G.M., Malyshev S.A., Loktev A.S., Mazo G.N., Shatalova T.B., Arkhipova V.A., Roslyakov I.V., Dedov A.G., $Nd_{2-x}Sr_xNiO_4$ solid solutions: synthesis, structure and enhanced catalytic properties of their reduction products in the dry reforming of methane, *Catalysts*, 2023, **13**, P. 966.

[15] Stangeland K., Kalai D., Li H., Yu Z. The effect of temperature and initial methane concentration on carbon dioxide methanation on Ni based catalysts. *Energy Procedia*, 2017, **105**, P. 2016–2021.

[16] Zhang T., Liu Q. Perovskite LaNiO3 Nanocrystals inside Mesostructured Cellular Foam Silica: High Catalytic Activity and Stability for CO_2 Methanation. *Energy Technol.*, 2020, **8**, P. 1901164.

[17] Evdokimenko N., Ermekova Zh., Roslyakov S., Tkachenko O., Kapustin G., Bindiug D., Kustov A., Mukasyan A.S. Sponge-like CoNi Catalysts Synthesized by Combustion of Reactive Solutions: Stability and Performance for CO_2 Hydrogenation. *Materials*, 2022, **15**, P. 5129.

[18] Vikanova K.V., Kustov A.L., Makhov E.A., Tkachenko O.P., Kapustin G.I., Kalmykov K.B., Mishin I.V., Nissenbaum V.D., Dunaev S.F., Kustov L.M. Rhenium-contained catalysts based on superacid ZrO_2 supports for CO_2 utilization. *Fuel*, 2023, **351**, P. 128956.

Submitted 18 October 2023; revised 20 November 2023; accepted 22 November 2023

Information about the authors:

Sergey A. Malyshev – Department of Materials Sciences, Shenzhen MSU-BIT University, Shenzhen 518172, China; Department of Chemistry, M. V. Lomonosov Moscow State University, 119991 Moscow, Russia; ORCID 0009-0005-0132-4466; malyshev12sa@yandex.ru

Oleg A. Shlyakhtin – Department of Chemistry, M. V. Lomonosov Moscow State University, 119991 Moscow, Russia; ORCID 0000-0001-8362-1002; oleg@inorg.chem.msu.ru

Grigorii M. Timofeev – Department of Chemistry, M. V. Lomonosov Moscow State University, 119991 Moscow, Russia; ORCID 0009-0002-4855-7935; timofeevg@inbox.ru

Galina N. Mazo – Department of Chemistry, M. V. Lomonosov Moscow State University, 119991 Moscow, Russia; ORCID 0000-0001-7036-5927; mazo@inorg.chem.msu.ru

Ilya V. Roslyakov – N. S. Kurnakov Institute of General and Inorganic Chemistry, Russian Academy of Sciences, 119991 Moscow, Russia; Department of Materials Sciences, M. V. Lomonosov Moscow State University, 119991 Moscow, Russia; ORCID 0000-0002-9958-6659; Ilya.roslyakov@gmail.com

Aleksander V. Vasiliev – Department of Chemistry, M. V. Lomonosov Moscow State University, 119991 Moscow, Russia; ORCID 0000-0003-4108-9040; a.vasiliev@inorg.chem.msu.ru

Tatiana B. Shatalova – Department of Chemistry, M. V. Lomonosov Moscow State University, 119991 Moscow, Russia; ORCID 0000-0002-4304-8624; shatalovatb@gmail.com

Aleksander L. Kustov – Department of Chemistry, M. V. Lomonosov Moscow State University, 119991 Moscow, Russia; ORCID 0000-0003-0869-8784; kyst@list.ru

Conflict of interest: the authors declare no conflict of interest.

NANOSYSTEMS:
PHYSICS, CHEMISTRY, MATHEMATICS

Original article

Matveyeva A.N., et al. *Nanosystems: Phys. Chem. Math.*, 2023, **14** (6), 679–689.
http://nanojournal.ifmo.ru
DOI 10.17586/2220-8054-2023-14-6-679-689

Alumina and silica supported Ce–Fe–O systems obtained by the solution combustion method and their performance in CO_2 hydrogenation to syngas

Anna N. Matveyeva[1], Shamil O. Omarov[1], Marianna A. Gavrilova[1,2]

[1]Ioffe Institute, St.-Petersburg, Russia

[2]St.-Petersburg State Institute of Technology (Technical University), St.-Petersburg, Russia

Corresponding author: Anna N. Matveyeva, anna.matveyeva@mail.ioffe.ru

PACS 61.46.+w, 82.65.+r

ABSTRACT This study presents Ce–Fe–O systems supported on γ-Al_2O_3 or SiO_2 to enhance the reactivity of an oxygen-deficient $CeFeO_3$ perovskite phase, which are promising catalysts for the production of fuels and chemicals from CO_2 as feedstock. The synthesis was carried out by the glycine-nitrate solution combustion method at various fuel-to-oxidizer ratios, and with or without the addition of ammonium nitrate. The obtained composites were characterized by XRD, SEM, EDX, N_2-physisorption, H_2-TPR, and CO_2-TPD to study the relationship of physicochemical properties with catalytic CO_2 hydrogenation (rWGS) activity. γ-Al_2O_3 was found to be a more suitable support than SiO_2 due to its ability to form a higher content of the perovskite phase, significantly reduce the size of $CeFeO_3$ crystallites, and increase oxygen defectiveness and CO_2 adsorption capacity. Combustion in the presence of silica results in the binding of most of cerium into a silicate phase, which is inactive for rWGS.

KEYWORDS perovskites, cerium orthoferrite, $CeFeO_3$, alumina, silica, solution combustion synthesis, glycine, carbon dioxide, CO_2 hydrogenation, rWGS

ACKNOWLEDGEMENTS This research was funded by the Russian Science Foundation (grant number 22–23–20094, https://rscf.ru/project/22-23-20094/, accessed on 26 October 2023) and the St.-Petersburg Science Foundation (agreement number 26/2022 from 14 April 2022).

FOR CITATION Matveyeva A.N., Omarov S.O., Gavrilova M.A. Alumina and silica supported Ce–Fe–O systems obtained by the solution combustion method and their performance in CO_2 hydrogenation to syngas. *Nanosystems: Phys. Chem. Math.*, 2023, **14** (6), 679–689.

1. Introduction

Reducing CO_2 concentrations in the atmosphere is a complex task which requires the search and development of optimal technologies for capturing and further converting CO_2 into useful chemicals for industrial processes or high value-added products [1]. In this regard, CO_2 hydrogenation is a suitable and actively studied method for recycling carbon dioxide, especially in a combination with hydrogen produced from renewable energy sources [2]. In particular, efficient conversion of CO_2 into synthesis gas (a mixture of CO and H_2) is possible at temperatures above 500 °C and atmospheric pressure through the reverse water gas shift (rWGS) reaction [3, 4]. In steam reforming of alcohols, the excess of which can become a serious problem for the biodiesel industry [5–7], rWGS can close the carbon cycle and reduce emissions of CO_2, which is a by-product [8].

This is hampered by the difficulties of finding and developing effective and low-cost catalytic materials with excellent thermal and long-term stability under redox conditions [9, 10]. Among various systems, perovskites, in particular ferrites, which have the above-mentioned advantages, can be promising materials for use in rWGS. This phenomenon is associated with enhanced self-diffusion of oxygen, the creation and regulation of oxygen defectiveness, the low energy barrier of the $Fe^{3+} \longleftrightarrow Fe^{2+}$ transition under redox conditions, and the possibility of reuse of perovskites [11–14]. Partial reduction of ferrites, including under reaction conditions, allows one to *in situ* obtain highly dispersed metal nanoparticles from the perovskite phase [11, 12, 14].

Currently, ferrite-perovskite composite materials based on $LaFeO_3$ and its analogues doped at A and/or B sites are being widely studied for CO_2 hydrogenation [11–19]. A detailed study of such systems made it possible to establish that, firstly, increasing the number of oxygen vacancies contributes toward an increase of the CO_2 binding strength and the rate of CO_2 hydrogenation on the perovskite surface. Secondly, the partial substitution of A cations improves redox properties and the tendency to form oxygen vacancies. Thirdly, the presence of oxygen vacancies, FeO_x, and metal (Ni or Co) nanoparticles on the perovskite surface leads to a synergistic effect and a significant increase in rWGS activity of such systems.

However, simple ferrites with unsubstituted cations, especially cerium orthoferrite, have been studied much less as catalysts than substituted perovskites, despite the extensive literature on their preparation [20–26]. A feature of o-$CeFeO_3$

compared to other lanthanide ferrites is the possibility of a reversible $Ce^{3+} \longleftrightarrow Ce^{4+}$ electronic transition, which can affect the redox properties of the perovskite and its defectiveness. Recently, a sample containing 94 wt% $CeFeO_3$, obtained by the solution combustion synthesis (SCS) method, was found to be highly active in rWGS [20]. Moreover, its activity is superior to $LaFeO_3$, previously studied in [18]. Compared to other methods to prepare cerium orthoferrite [27–32], the SCS method is much less labor-intensive and allows one to regulate the conditions for obtaining phase-pure and homogeneous powders. An important advantage of obtaining $CeFeO_3$ by this method is also the option of carrying out synthesis in a reducing atmosphere created by the gaseous products of a thermochemical reaction, which is important to prevent the oxidation of perovskite at $T > 350$ °C [20, 26].

The SCS synthesis approach has been already proven to be an effective tool for fine control of the microstructure and morphology of materials, which makes it possible to obtain foam-like [20, 26, 33, 34] or globular [33, 35] powders, including core-shell structure type [34, 36]. The main way of such control is to change the ratio of fuel and nitrates, the pH value and the final treatment temperature [37, 38]. For $CeFeO_3$ perovskite, the influence of the fuel-to-oxidizer ratio, the fuel type, as well as post-calcination temperature has been mainly studied [20, 39].

However, all these parameters did not change the extremely low specific surface area of perovskites. Therefore, another way to create porosity is the template-assisted SCS, where either a colloidal solution or powders (as external microstructure templates) with a developed pore system (Al_2O_3, SiO_2, etc.) are used [13, 37, 38]. The use of a colloid/template makes it possible to significantly moderate combustion by reducing the maximum temperature, and the reaction is localized in nanodomains between colloid/template particles [40]. This leads to a decrease in the crystallite size of the supported phase compared to its bulk form and homogeneously distributes the resulting target product throughout the volume of the support matrix [37, 40–44]. The obtained composite system can be additionally treated with alkali to remove the silicon- or aluminum-containing template [40–42, 45] or used in such form [43, 44, 46, 47], in which the template becomes a support for the second component, similar to traditional supported catalysts. For example, the use of a template leads to an increase in the photocatalytic activity of $LaFeO_3$ [46, 47].

It was previously found that even a mechanical mixture of 25 wt% $La_{0.75}Sr_{0.25}FeO_3$ perovskite with SiO_2 increases the CO yield compared to unsupported and CeO_2, ZrO_2, α-Al_2O_3, TiO_2 (rutile)-supported perovskites [48, 49]. This is explained by the formation of the smallest size of perovskite crystallites, which led to the highest content of oxygen defects and activity in rWGS compared to other supports. In the case of using Al_2O_3 and TiO_2, the observed decrease in activity of the composites is due to the encapsulation of perovskite nanoparticles, which prevents the adsorption of CO_2 and its participation in the catalytic cycle.

Thus, in this study, an oxide support (template) was used for the first time to obtain composites based on $CeFeO_3$ perovskite by the SCS method. The influence of the support type (Al_2O_3 or SiO_2) on the catalytic behavior of the Ce–Fe–O system in the rWGS process has been established. Additionally, the fuel-to-oxidizer ratio was varied by changing the amount of glycine or adding ammonium nitrate and compared with the bulk $CeFeO_3$ obtained previously in [20].

2. Experimental

2.1. Catalyst preparation

The $CeFeO_3$-containing system was prepared by solution combustion synthesis in the absence and the presence of a support, as well as ammonium nitrate (AN, 98.5 % (St.-Petersburg, Russia)). γ-Al_2O_3 was obtained by calcination of Pural SB Lot. N. 233144 (Sasol) pseudoboehmite at 700 °C for 2 h, silica gel of KSKG grade (Russia, the BET specific surface area of 190 m^2/g and the total pore volume of 0.61 cm^3/g [50]) was crushed to a fraction of 10 – 300 μm.

In total, glycine ($C_2H_5NO_2$, 99.2 %, LenReactiv (St. Petersburg, Russia)) and the corresponding metal nitrates (MeN) $Ce(NO_3)_3 \cdot 6H_2O$ (99.8 %, Chemcraft (Kaliningrad, Russia); or 99.1 %, LenReactiv), $Fe(NO_3)_2 \cdot 9H_2O$ (98.3 %, LenReactiv; or 98.0 %, NevaReactiv (St.-Petersburg, Russia)), were dissolved in DI water in a wide 250 mL glass beaker to obtain one gram of cerium ferrite. For every gram of raw material there was 1 mL of water. In the solution, nitrates acted as oxidizing agents, and glycine as a fuel. Additionally, if necessary, γ-Al_2O_3 or SiO_2 (1 g per 1 g perovskite), and NH_4NO_3 were added. For 1 g of calculated perovskite, from 0.1 to 1 g of NH_4NO_3 was used. The bulk system is denoted as CeFe, and systems supported on Al_2O_3 and SiO_2 are denoted as CeFeAl and CeFeSi, respectively.

When the ratio between the reagents changes, the ratio of fuel-to-oxidizer (φ), calculated from the reducing and oxidizing valence states (RV and OV, respectively), also changes, as follows [38]:

$$\varphi = (-1)\frac{\Sigma(\text{coeff} \cdot \text{RV of fuel})}{\Sigma(\text{coeff} \cdot \text{OV of nitrate})}. \quad (1)$$

The methodology for calculating reducing and oxidizing valence states can be found in [51]. The resulting aqueous solution or suspension was heated on a 1 kW electric plate until boiling and subsequent combustion to form a solid powder. Previously, reproducibility was tested on two or three batches of samples [20, 33]. Reaction equations for each synthesis can be found in [20].

2.2. Characterization

XRD analysis was partially performed on a SmartLab 3 Diffractometer (Rigaku, Japan) equipped with 1D DteX250 detector and NiK_β filter at 30 mA, 40 kV, a 4 °/min scan speed, and a 0.01° step width. For other samples (CeFeAl (0.1 – 0.25 g AN) and CeFeSi) was used XRD-6100 diffractometer (Shimadzu, Japan) with Cu$K\alpha$ radiation at 40 kV, 30 mA, scan speed of 1 °/min, step width of 0.02°, and D(divergence):S(scatter):R(receiving) = 1:1:0.3. The diffraction data were analyzed by the Rietveld method. The refinement procedure and software are similar to those given in [20].

SEM and energy-dispersive X-ray (EDX) spectroscopy were carried out on a VEGA 3 SBH microscope (TESCAN, Czech Republic) equipped with INCAx–act detector (Oxford instruments, UK).

N_2-physisorption data were obtained on Quantachrom's Autosorb-6iSA (USA) unit. The samples were preliminarily degassed at 250 °C under vacuum. The specific surface area and the total pore volume were determined using the BET equation, and the pore size distribution was determined by the NLDFT method.

H_2-TPR (temperature programmed reduction by H_2) and CO_2-TPD (temperature programmed desorption) were performed on a Chemosorb (SOLO, Russia) equipped with a TCD (thermal conductivity detector) and a MC7-200D quadrupole mass analyzer (Institute for Analytical Instrumentation of Russian Academy of Sciences). For H_2-TPR experiments, ca. 30 mg of a powder (calcined at 350 °C) was reduced from 100 to 800 °C at a 10 °/min rate under 20 mL/min of 10 vol% H_2/Ar (99.998 vol% purity). Propanol-2 cooled in the liquid N_2 was used as a water vapor trap.

Before CO_2-TPD, ca. 100 mg of a sample (calcined at 350 °C) was reduced *in situ* by a 50 vol% H_2/He flow (40 mL/min) at a ramp rate of 20 °/min to 510 °C and 10 °/min to 600 °C and held for 20 – 30 min. Then it was cooled to 350 °C in 50 % H_2/He (40 mL/min) and to 110 °C in He, after which it was saturated with CO_2 (CO_2/He flow, 10:90 vol%, 20 mL/min) for 20 min. After removing the physically adsorbed CO_2 by purging with He (20 mL/min), the sample was heated to 600 °C at a ramping rate of 10 °C/min.

2.3. Catalytic tests

The experiments were performed in a fixed-bed reactor at 1 atm and 600 °C. The reactor was a cylindrical quartz tube (37 cm in length, 15 mm in inner diameter), in which the sample was placed on a SiO_2 diffuser grid. The gases were fed into the reactor from top to bottom. A thermocouple pocket with a diameter of 5 mm was located in the center of the tube.

35 mg of the powder sample was initially heated in the air flow (50 mL/min) to 300 °C, then flushed with N_2 (99.999 vol. % purity, 40 mL/min) up to 400 °C. Thereafter, 50 vol% H_2 in N_2 was fed with a total flow of 80 mL/min for 0.5 h. After reduction, the sample was heated to 600 °C and exposed to the reactants (H_2:CO_2:N_2=1:1:1, 120 mL/min) at a weight hourly space velocity (WHSV) of 205.7 $L{\cdot}g^{-1}{\cdot}h^{-1}$ for 30 – 90 min. Nitrogen in the gas flow was used as the internal standard for gas chromatography, allowing establishing the mass balance. In order to prevent water from entering the GC, the outlet pipe passed through a cooling trap.

The outlet gases were analyzed on a GC-2010 Plus chromatograph (Shimadzu, Japan) with a TCD (capillary column RT-Msieve 5A (30 m, dinner = 0.53 mm) and capillary column Rt-Q-BOND (30 m, dinner = 0.53 mm); temperature program: 30 °C – 5 min; 30 – 60 °C with a heating rate 4 °/min; 60 – 100 °C with a heating rate 15 °/min; 100 – 150 °C with a heating rate 30 °/min; 150 °C – 3 min; 150 – 180 °C with a heating rate 5 °/min; 180 °C – 23.9 min).

Catalytic behavior was assessed by CO_2 conversion (X_{CO_2}, %):

$$X_{CO_2} = \frac{\text{Molar flow C from CO}}{\text{Molar flow C from CO}_2 + \text{CO}} \cdot 100\ \%, \tag{2}$$

where molar flow C from CO_2 or CO – molar flow of the compound multiplied by the number of carbon atoms in the compound, mol/h. Selectivity to CO in all test was 100 %.

3. Results and discussion

3.1. Phase composition and crystal structure

XRD patterns of various series of catalysts synthesized by the SCS method using glycine as a fuel are presented in Fig. 1. The first series (Fig. 1a) consists of the bulk Ce–Fe–O system (denoted CeFe) and several CeFe composites on alumina (CeFeAl) obtained at different fuel-to-oxidizer ratios (φ). A more detailed study of the bulk Ce–Fe–O system prepared with various fuels, additives, and φ was carried out in [20], therefore, it is presented here for comparison. The selected CeFe contains mainly orthorhombic $CeFeO_3$ perovskite (94 wt%) with a Pbnm space group (ICDD PDF-2 card No. 00-022-0166) and small amounts of iron and cerium oxides (Table 1). $CeFeO_3$ reflections observed for CeFeAl systems at 22.8°, 32.6 – 32.7°, 40.2 – 40.3°, 46.5 – 46.6°, and 58.1 – 58.2° 2θ, corresponding to the planes (110), (112), (202), (004), and (024, 204), have more broadening and are shifted towards higher angles compared to bulk CeFe.

The second series (Fig. 1b) represents CeFeAl and CeFeSi systems synthesized with an additional oxidizing agent NH_4NO_3 in various quantities. Previous studies have shown [20] that the addition of ammonium nitrate (AN) to the reaction mixture promotes the formation of the target perovskite. Indeed, according to the data obtained by the Rietveld refinement method, samples obtained using AN have an increased content of $CeFeO_3$ (Table 1).

The crystallographic parameters of the synthesized systems based on $CeFeO_3$ are also presented in Table 1. The $CeFeO_3$ unit cell volume (239.93 $\pm$ 0.01 Å^3) in bulk CeFe was found to be in better agreement with the cell volume

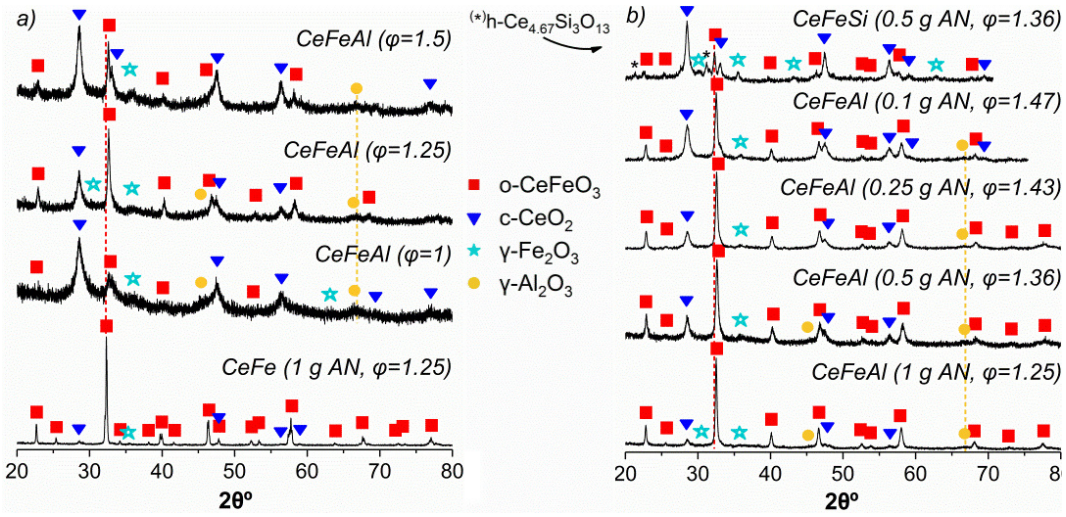

FIG. 1. XRD patterns of bulk Ce–Fe–O (a) or supported CeFe on γ-Al_2O_3 and SiO_2 (a,b), synthesized by glycine–nitrate solution combustion using different ratios of fuel-to-oxidizer (φ) and the amounts of ammonium nitrate (AN). ICDD PDF-2 card No. for: orthorhombic(o)-$CeFeO_3$ – 00-022-0166; cubic(c)-CeO_2 – 01-075-8371; γ-Fe_2O_3 – 00-039-1346; γ-Al_2O_3 – 00-056-0457; hexagonal(h)-$Ce_{4.67}Si_3O_{13}$ – 00–043–441.

presented in [52] (238.9 Å^3), than in [28] (241.3 Å^3). The combustion of the glycine–nitrates mixture in the presence of Al_2O_3 leads to the formation of $CeFeO_3$ with an even smaller unit cell volume of 233.67 – 235.60 Å^3 (Fig. 2a). Such a significant change in lattice parameters is confirmed by the shift of diffraction peaks towards larger angles compared to bulk CeFe. This can be the result of replacing Ce (site A) or Fe (site B) ions in the perovskite structure with aluminum having a smaller ionic radius ($_{VI}Al^{3+}$, 0.535 Å [53]) compared to $_{VIII}Ce^{3+}$ (1.143 Å) and $_{VI}Fe^{3+}$ (0.55 – 0.645 Å), which was previously shown in [54–56] for $La_{1-x}Al_xFeO_3$ and $LaAl_yFe_{1-y}O_3$. However, according to [55], Al^{3+} ions have a strong site preference for the B site.

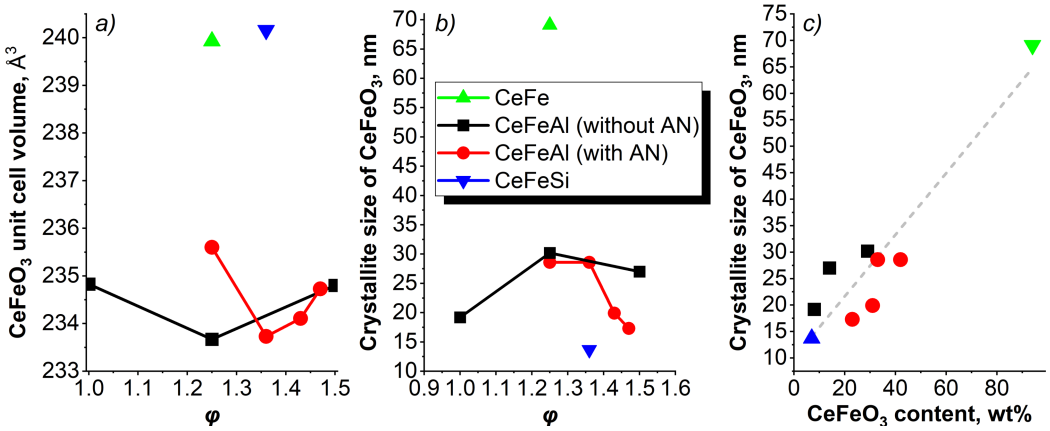

FIG. 2. Dependence of the $CeFeO_3$ unit cell volume on the fuel-to-oxidizer ratio (φ) (a). Dependence of the $CeFeO_3$ crystallite size on φ (b) and $CeFeO_3$ content (c).

The unit cell parameter of the cubic phase of alumina also deviates upward from the reference value (Table 1), which indicates a distortion of the Al_2O_3 lattice. In this case, a shift in the peak position of the (440) plane towards lower angles 2θ is observed. The discrepancy between the ionic radii of rare earth elements and Al^{3+}, leading to an extremely low equilibrium solubility limit of rare earth elements $\sim 10^{-3}$ % [57], makes it possible to exclude the introduction of cerium ions into the Al_2O_3 matrix. Therefore, the most probable is the substitution of Al^{3+} by Fe^{3+} [58].

Interestingly, replacing the alumina support by silica gel under the same synthesis conditions negatively affects the content of the perovskite phase. Moreover, from previous studies of SiO_2-supported perovskite oxides, it is known that the interface region of the SiO_2-based composite is the most vulnerable to solid-phase reactions [41,49]. A more detailed examination of the range of 20 – 35 $2\theta^\circ$ for CeFeSi (Fig. 1b) shows the formation of a secondary phase of cerium oxide silicate in a significant amount (17 wt% $Ce_{4.67}Si_3O_{13}$).

The size of crystallites in Ce–Fe–O based systems was also analyzed. With a decrease in the fraction of cerium ferrite, the mean size of perovskite crystallites also decreases by more than 2 times (Fig. 2b) depending on the synthesis

TABLE 1. Data on the phase composition, crystallite sizes, and lattice parameters of Ce–Fe–Al(Si) and Ce–Fe oxide systems obtained by the glycine–nitrate SCS method

N	m(AN); n(AN)/ n(MeN)	φ	Phase composition according to the Rietveld method/corrected*, wt%					D_1, nm; V_1, Å^3	D_2, nm; a_2, Å	D_3, nm; a_3, Å	D_4, nm; a_4, Å	R_{wp}/R_e
			o-$CeFeO_3$	c-CeO_2	γ-Fe_2O_3	γ-Al_2O_3 (SiO_2**)	CeSiO					
Ref. v.	—	—	50 or 100	—	—	50 or 0	—	—; 241.31	—; 5.4126	—; 8.3342	—; 7.9142	—
1	0	1	4/8	18/33	5/9	73/50	0	19.2; 234.83	8.7; 5.4088	10.4; 8.2901	5.3; 7.9153	2.7
2	0	1.25	29	16	5	50	0	30.2; 233.67	11.6; 5.4094	7.4; 8.3419	8.2; 7.9205	1.1
3	0	1.5	15/14	25/23	15/13	45/50	0	27.0; 234.80	12.5; 5.4100	8.9; 8.3216	9.1; 7.9106	1.0
4	1 g; 1.5	1.25	45/42	4/4	4/4	47/50	0	28.6; 235.60	17.8; 5.4050	5.8; 8.3192	5.1; 7.9229	1.0
5	0.5 g; 0.75	1.36	40/33	10/8	10/8	40/50	0	28.6; 233.73	14.9; 5.4095	6.8; 8.3469	8.7; 7.9461	1.1
6	0.25 g; 0.375	1.43	57/31	19/10	16/9	8/50	0	19.9; 234.11	8.5; 5.4062	4.9; 8.2790	20.1; 7.7264	1.3
7	0.1 g; 0.15	1.47	23	19	8	50	0	17.3; 234.73	6.9; 5.4049	6.6; 8.3049	3.0; 7.9320	1.1
8	0.5 g; 0.75	1.36	13/7	37/20	17/9	0/47**	32/17	13.7; 240.16	9.7; 5.4120	19.9; 8.3728	—	1.1
9	1 g; 1.5	1.25	96/94	4/4	0/2	0	0	69.1; 239.93	15.6; 5.3970	—	—	1.1

Note: *correction of fitting inaccuracies based on the specified alumina content or including amorphous iron oxide according to the equation wt% (Fe_2O_3)= wt%(CeO_2)/2.156, where 2.156 is the CeO_2/Fe_2O_3 weight ratio obtained from $CeFeO_3$; **SiO_2 instead of Al_2O_3; ref.v. – a reference value (expected); m(AN) – the mass of NH_4NO_3; n(AN)/n(MeN) – the ratio of stoichiometric coefficients of ammonium nitrate and metal nitrates (Ce and Fe); φ – the fuel-to-oxidizer ratio; CeSiO – h-$Ce_{4.67}Si_3O_{13}$ (ICSD 9378); D – the mean crystallite size; 1 – o-$CeFeO_3$ (modified ICSD 93611); 2 – c-CeO_2 (ICSD 193169); 3 – γ-Fe_2O_3 (ICSD 247036); 4 – γ-Al_2O_3 (ICSD 66558); the ratio of the weighted (R_{wp}) and expected (R_e) R-factors characterizes goodness of fit, if the squared value is equal to one or constant the refinement procedure is complete.

conditions. In this case, a linear correlation is observed between the Ce ferrite content and the mean size of its crystallites (Fig. 2c).

3.2. Structural and textural properties

The results of N_2 physisorption measurements are presented in Fig. 3 and Table 2. Data corresponding to the alumina support are also included for comparison. All presented systems display a IV type isotherm (Fig. 3a), which is usually ascribed to mesoporous materials according to the IUPAC classification [59]. The bulk system based on $CeFeO_3$ *per se* is non-porous, and small volumes of mesopores are apparently formed due to secondary porosity, namely, aggregation of small crystalline particles [20]. Most pore sizes for Al_2O_3- and SiO_2-supported CeFe systems are less than 20 nm and are uniformly distributed (the average pore diameter (d_p) is 10 nm), while the pore size distribution for the perovskite-based system is relatively wide, with two maxima of ca. 15 and 40 nm (Fig. 3b). As expected, the total pore volume decreased after loading the support with the perovskite-containing system, which leads to a decrease in the peak height of the pore size distribution compared to pure alumina. In the presence of a high surface area support, the specific surface area (S_{BET}) and the total pore volume (ΣV_p) of the supported Ce–Fe–O systems are 92 – 123 m^2/g and 0.32 – 0.34 cm^3/g, respectively.

According to SEM, phases of cerium ferrite and secondary oxides formed during combustion, due to the large amount of released gaseous reaction products, are organized into a crystalline foam-like nanostructure (Fig. 4a), surrounding individual particles of the support (Fig. 4b,c). The surface atomic ratios of Ce:Fe:Al, given in Table 2, turned out to be higher than the corresponding theoretical values, which can be explained by the heterogeneity of phase distribution.

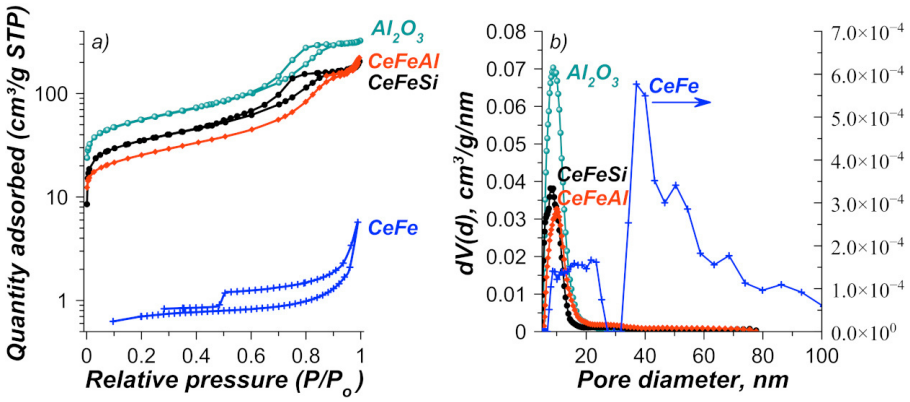

FIG. 3. N_2 physisorption isotherms and the pore size distribution for Al_2O_3, CeFe (1 g AN, $\varphi = 1.25$), CeFeAl (0.5 g AN, $\varphi = 1.36$), and CeFeSi (0.5 g AN, $\varphi = 1.36$). For CeFeAl, the desorption branch of the isotherm is not completely recorded.

TABLE 2. Elemental composition (in at%) according to the EDX analysis and textural characteristics for Al_2O_3, Ce–Fe and Ce–Fe–Al(Si) oxide systems

Sample	Ce	Fe	Al	Ce:Fe:Al	S_{BET}, m^2/g	ΣV_p, cm^3/g	d_p, nm
CeFe (1 g AN, $\varphi = 1.25$)	48.36	51.64	—	1:1.07	2.3	0.01	15
CeFeAl ($\varphi = 1$)	10.76	12.21	77.03	1:1.13:7.16	—	—	—
CeFeAl ($\varphi = 1.25$)	10.59	11.88	77.53	1:1.12:7.32	—	—	—
CeFeAl ($\varphi = 1.5$)	11.19	12.55	76.26	1:1.12:6.82	—	—	—
CeFeAl (1 g AN, $\varphi = 1.25$)	13.02	14.36	72.62	1:1.10:5.58	—	—	—
CeFeAl (0.5 g AN, $\varphi = 1.36$)	12.09	13.24	74.67	1:1.10:6.18	92	0.34	15
CeFeSi (0.5 g AN, $\varphi = 1.36$)	—	—	—	—	123	0.32	10
Al_2O_3	—	—	—	—	200	0.50	10

EDX mapping of morphologically distinct areas showed that the CeFeAl sample consists of dark subangular particles (Fig. 5, area 1) and bright foam-like particles (Fig. 5, area 2). The dark particles were found to contain more aluminum than bright ones, which indicates the formation of different thicknesses of the Ce–Fe–O layer on the surface of alumina. Similar results were obtained for the silica-supported CeFe system.

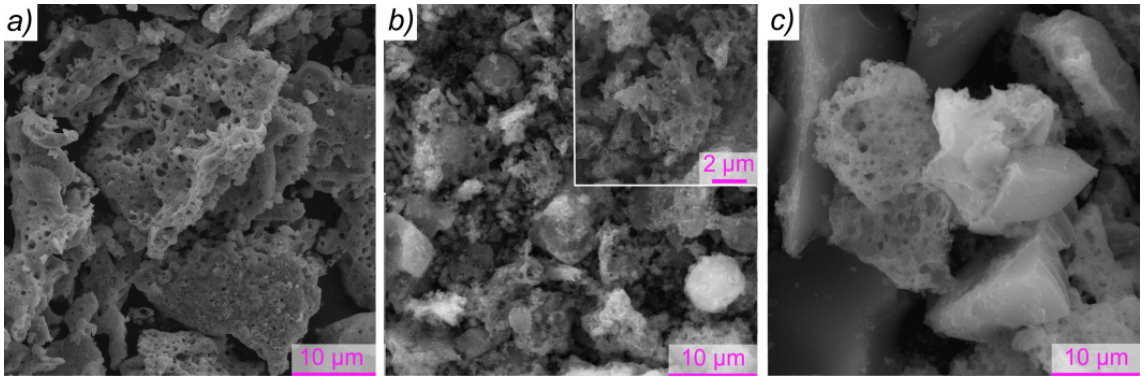

FIG. 4. Microphotographs of as-prepared (a) CeFe (1 g AN, $\varphi = 1.25$), (b) CeFeAl ($\varphi = 1.5$), (c) CeFeSi (0.5 g AN, $\varphi = 1.36$)

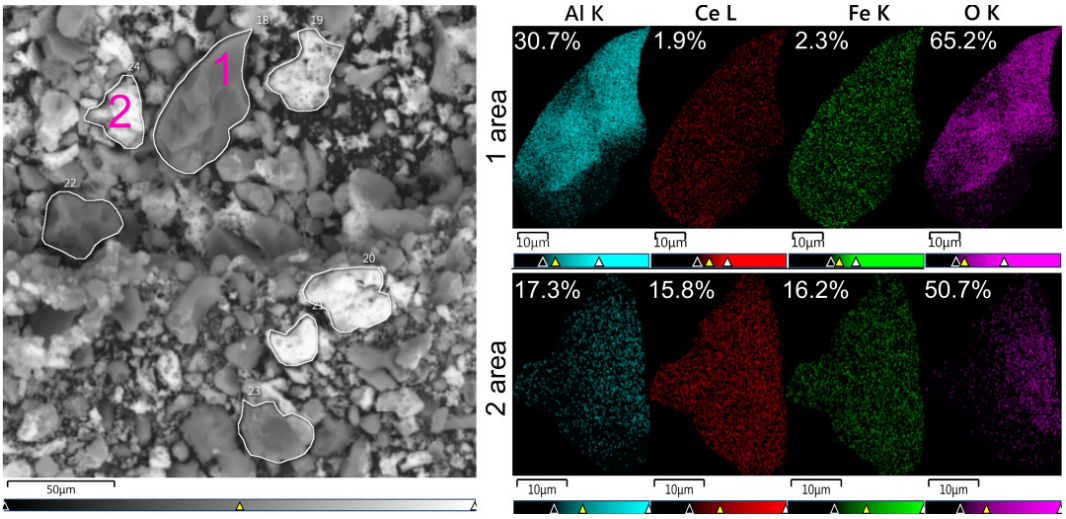

FIG. 5. EDX spectroscopy elemental maps (Al, Ce, Fe, and O) for CeFeAl ($\varphi = 1.5$)

3.3. Reducibility

The presented systems contain elements that are prone to changes in the degree of oxidation under redox conditions. H_2-TPR makes it possible to characterize the stability of catalysts, as well as to identify the features of reduction depending on the synthesis conditions, phase composition, etc. Fig. 6 presents hydrogen consumption curves for the samples listed in Table 1.

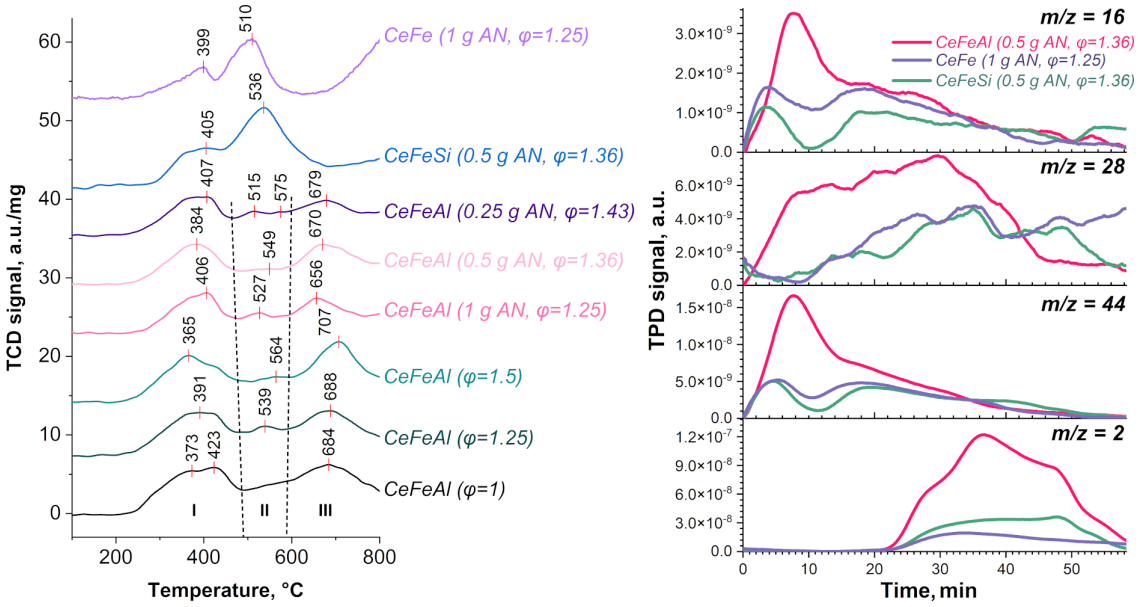

FIG. 6. H_2-TPR (left) and CO_2-TPD+MS (right) spectra for Ce–Fe and Ce–Fe–Al(Si) oxide systems (after preliminary calcination at 350 °C). In some cases, in H_2-TPR experiments, after 800 °C, the samples were cooled until the TCD signal reached the baseline. CO_2-TPD+MS was recorded at temperature from 110 °C to 600 °C.

It was previously shown that the cerium ferrite-rich sample (CeFe) is characterized by two-stage reduction at 200 – 415 °C and 415 – 600 °C [20]. This occurs due to the partial reduction of Fe^{3+} in Fe_2O_3 nanoparticles and on the $CeFeO_3$ surface to Fe^{2+} (Fe_3O_4) with its subsequent reduction to FeO and Fe^0 at 415 – 600 °C, as well as surface Ce^{4+} to Ce^{3+} with additional formation of oxygen vacancies [20, 26]. The reduction profile of CeFe supported on SiO_2 is close to the reduction profile obtained for bulk CeFe. However, a more complex phase composition, low perovskite content and the presence of cerium silicate suggest that the main contribution to hydrogen consumption comes from unbound Fe_2O_3.

CeFeAl samples of both series (obtained with or without ammonium nitrate) are characterized by complex reduction profiles, namely, at temperatures above 600 °C the third reduction region appears. XRD data of CeFeAl (sample No. 5 in Table 1) after reduction at 800 °C showed that destruction of o-$CeFeO_3$ does not occur under these conditions and metallic

iron is present, which is absent after reduction at 600 °C. At the same time, metallic Fe was discovered for CeFeSi after reduction at 600 °C. This allows one to partially associate the observed peaks with reduction of bulk γ-Fe_2O_3 and/or a solid solution $Al_2O_3(Fe^{3+})$ to Fe_3O_4, further reduction of which to FeO continues at temperatures up to 600 °C [20, 26].

A quantitative comparison of H_2-TPR results (Table 3) shows that increasing φ for CeFeAl systems, obtained with or without AN, increases the fraction of easily reducible components, as well as the overall reducibility of these systems due to an increase in dispersion of Fe_2O_3 and CeO_2 and the fraction of bound iron and cerium in the perovskite (Table 1). CeFeAl samples synthesized with AN at $\varphi = 1.36$ and $\varphi = 1.43$ can be considered optimal in terms of $CeFeO_3$ content and reducibility. The use of γ-Al_2O_3 compared to SiO_2 makes it possible to obtain a larger amount of $CeFeO_3$, as well as more highly dispersed and easily reduced phases.

TABLE 3. Hydrogen consumption (% of peak area) in different temperature regions

Region	CeFe	CeFeAl ($\varphi = 1$)	CeFeAl ($\varphi = 1.25$)	CeFeAl ($\varphi = 1.5$)	CeFeAl (1 g AN, $\varphi = 1.25$)	CeFeAl (0.5 g AN, $\varphi = 1.36$)	CeFeAl (0.25 g AN, $\varphi = 1.43$)	CeFeSi
I (200 – 475 °C)	34	39	40	28	35	40	39	31
II (475 – 600 °C)	66	18	19	38	15	14	19	69
III (600 – 825 °C)	–	43	41	34	51	46	42	0
Total amount H_2, mmol/g*	1.8	4.6	4.2	4.6	3.1	3.7	3.8	4.5

Note. *For all samples (except of CeFe), the amount of consumed H_2 is calculated on 50 wt% Ce–Fe–O.

3.4. CO_2-TPD with mass-spectrometry

According to previous studies (see Introduction section), CO_2 adsorption is a critical step in the rWGS reaction, because it occurs at surface oxygen defects. Therefore, the CO_2-TPD method was used for studying the features of CO_2 desorption and characterizing the surface defects in the bulk and alumina- and silica-supported Ce–Fe–O systems, similar to other perovskite-based systems [15, 16, 18, 19, 48, 49]. Fig. 6 (right) shows the curves of changes in mass number signals over time (temperature from 100 to 600 °C) during TPD experiments for three different systems. Based on the known mass spectra of CO_2, CO, and H_2, the following correspondence can be established between m/z and the detected ions: $m/z = 16$ – O· or O_2·· (separately or as part of CO_2 and/or CO spectrum), $m/z = 28$ – CO· (separately or as part of the CO_2 spectrum), $m/z = 44$ – CO_2·, $m/z = 2$ – H_2·. Thus, the amount of desorbed CO_2 ($m/z = 44$) increases in the following order: CeFeSi < CeFe < CeFeAl.

The discrepancy between the profiles of $m/z = 44$ and $m/z = 28$ evidences the presence in the $m/z = 28$ signal of a contribution from CO desorption, caused by the reaction between adsorbed CO_2 and oxygen vacancies. The amount of desorbed CO ($m/z = 28$) and O/O_2 ($m/z = 16$) increases in the order CeFeSi < CeFe < CeFeAl, suggesting a higher number of oxygen vacancies in CeFe supported on γ-Al_2O_3. In [49], the opposite result was obtained for $LaFeO_3$, which, as the authors explained, takes place due to the higher energy of vacancy formation in the presence of Al_2O_3 compared to SiO_2. The difference in the results with the data obtained in this study is apparently due to using a different synthesis method. This led to different regularities of interaction between the system components, which, in turn, affected the amount of formed $CeFeO_3$.

Calculation of the amount of desorbed CO_2, CO, and O/O_2 per S_{BET} shows that the surface density of oxygen vacancies increases in the order: CeFeSi < CeFeAl < CeFe, which corresponds to the $CeFeO_3$ content. At the same time, the amount of desorbed hydrogen remaining on the surface after the preliminary reduction stage increases in the order from CeFe to CeFeAl, which coincides with the amount of consumed hydrogen according to H_2-TPR data (Table 3). Apparently, this is associated with the formed solid solution of Fe^{3+} in γ-Al_2O_3, reduction of which leads to the formation of small metallic Fe nanoparticles that interact with neighboring phases and are capable of adsorbing hydrogen [60, 61]. Consequently, the low dispersion of the obtained Fe nanoparticles during the reduction of CeFeSi leads to a smaller amount of desorbed H_2.

3.5. Catalytic performance in CO_2 hydrogenation

The catalytic activity in terms of conversion of CO_2 to CO via the reverse water gas shift (rWGS) reaction for the bulk and supported Ce–Fe–O systems is presented in Fig. 7. It can be seen that perovskite-containing systems on alumina provide higher CO_2 conversion compared to the bulk CeFe system (Fig. 7a). In this case, there is no correlation with the content of the perovskite phase, because the bulk CeFe system contains 94 wt% $CeFeO_3$, while the alumina-supported

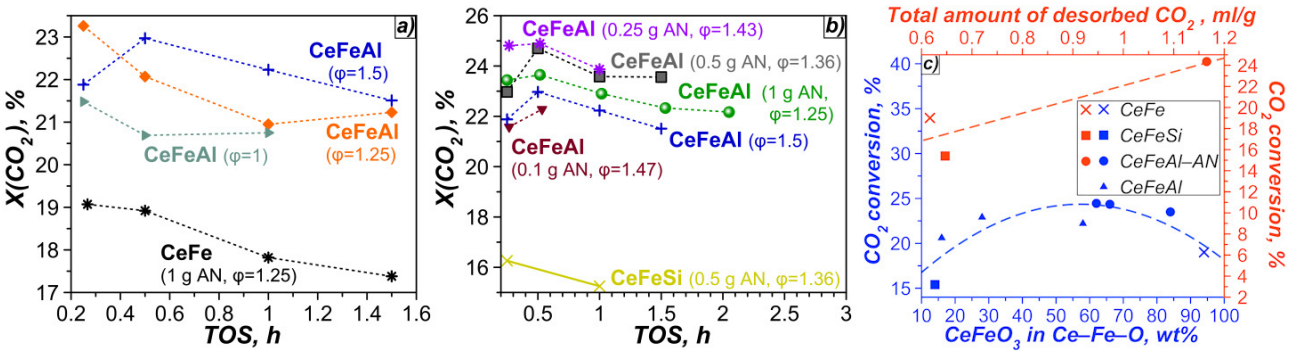

FIG. 7. Dependence of CO_2 conversion on time-on-stream (TOS) for the bulk Ce–Fe–O system and Al_2O_3- and SiO_2-supported CeFe obtained in the presence and the absence of NH_4NO_3 by the SCS method using glycine as a fuel (a,b). Conditions: 600 °C, H_2:CO_2:N_2 = 1:1:1, WHSV = 205.7 $L \cdot g^{-1} \cdot h^{-1}$. Influence of the total amount of desorbed CO_2 and the $CeFeO_3$ content in the Ce–Fe–O system on CO_2 conversion after 1 h of TOS (c).

systems – from 8 to 29 wt%. A slight increase in conversion for CeFeAl catalysts is observed with increasing the fuel-to-oxidizer ratio.

Combustion in the presence of ammonium nitrate (AN) also has a generally positive effect on the catalytic performance of alumina-supported CeFe systems (Fig. 7b). Maintaining the fuel-to-oxidizer ratio, the use of AN has a clear advantage in achieving higher CO_2 conversion on CeFeAl. However, adding 0.25 – 0.5 g of ammonium nitrate was found to be the most effective compared to smaller and larger amounts (0.1 g and 1 g, respectively). Interestingly, the silica supported CeFe system, also obtained with NH_4NO_3, has the lowest activity among the all presented catalysts.

The presented discussions correlate with the obtained CO_2-TPD results, where combustion in the presence of SiO_2 reduces the number of oxygen vacancies in the system compared to CeFeAl (Fig. 7c). At the same time, having recalculated the fraction of perovskite in the Ce–Fe–O system, the following dependence with a maximum was obtained, as shown in Fig. 7c.

4. Conclusions

Currently, rare earth ferrites are increasingly finding their use in thermocatalytic redox processes, in particular in CO_2 hydrogenation to CO (the rWGS reaction) as a potential way to utilize carbon dioxide. This study demonstrates improved rWGS activity by using perovskite-based composites. The Ce–Fe–O (CeFe) systems supported on γ-Al_2O_3 (CeFeAl) or SiO_2 (CeFeSi) were prepared via the glycine-nitrate solution combustion synthesis (SCS), a simple, energy- and time-effective method for the production of nanomaterials.

γ-Al_2O_3 has proven to be a suitable support for application in the SCS technology due to its ability to form a higher content of the $CeFeO_3$ perovskite phase compared to SiO_2. On silica, in turn, during combustion, most of cerium is bound into a low-active silicate phase, thereby limiting the formation of perovskite. On the contrary, reduction of a solid solution of Fe^{3+} in Al_2O_3, formed in small quantities, leads to the formation of small Fe nanoparticles capable of adsorbing hydrogen.

The use of alumina as a support significantly reduces the size of $CeFeO_3$ crystallites, but increases oxygen defectiveness and ability to CO_2 adsorption, which was determined by CO_2-TPD with mass spectrometry. CeFeAl has the highest amount of desorbed CO_2 ($m/z = 44$) and CO ($m/z = 28$) compared to bulk and SiO_2-supported CeFe. According H_2-TPR, in the presence of γ-Al_2O_3 makes it possible to obtain more highly dispersed and easily reduced phases compared to SiO_2. The obtained regularities serve as a prediction of the catalytic activity of these systems. The most active Ce–Fe–Al oxide system is obtained by using an additional oxidizer NH_4NO_3, the amount of which also affects φ and, consequently, CO_2 conversion.

References

[1] Mirzakhani S., Yin B.H., Masteri-Farahani M., Yip A.C.K. Heterogeneous catalytic systems for carbon dioxide hydrogenation to value-added chemicals. *ChemPlusChem*, 2023, **88** (7), e202300157.

[2] Malik F.R., Yuan H.B., Moran J.C., Tippayawong N. Overview of hydrogen production technologies for fuel cell utilization. *JESTECH*, 2023, **43**, 101452.

[3] Ebrahimi P., Kumar A., Khraisheh M. A review of CeO_2 supported catalysts for CO_2 reduction to CO through the reverse water gas shift reaction. *Catalysts*, 2022, **12** (10), 1101.

[4] Zhu M., Ge Q., Zhu X. Catalytic reduction of CO_2 to CO via reverse water gas shift reaction: Recent advances in the design of active and selective supported metal catalysts. *Transactions of Tianjin University*, 1234, **26**, P. 172–187.

[5] Charisiou N.D., Polychronopoulou K., Asif A., Goula M.A. The potential of glycerol and phenol towards H_2 production using steam reforming reaction: A review. *Surf. Coat. Technol.*, 2018, **352**, P. 92–111.

[6] Roslan N.A., Abidin S.Z., Ideris A., Vo D.V.N. A review on glycerol reforming processes over Ni-based catalyst for hydrogen and syngas productions. *Int. J. Hydrogen Ener.*, 2020, **45** (36), P. 18466–18489.

[7] Adeniyi A.G., Ighalo J.O. A review of steam reforming of glycerol. *Chem. Pap.*, 2019, **73** (11), P. 2619–2635.

[8] Falkowski P., Scholes R.J., Boyle E., Canadell J., Canfield D., Elser J., Gruber N., Hibbard K., Högberg P., Linder S., Mackenzie F.T., Moore B., Pedersen T., Rosenthal Y., Seitzinger S., Smetacek V., Steffen W. The global carbon cycle: A test of our knowledge of earth as a system. *Science*, 2000, **290** (5490), P. 291–296.

[9] Mathew T., Saju S., Raveendran S.N. Survey of heterogeneous catalysts for the CO_2 reduction to CO via reverse water gas shift. In: *Engineering solutions for CO_2 conversion*. John Wiley & Sons, Ltd, 2021, P. 281–316.

[10] Wang Y., Winter L.R., Chen J.G., Yan B. CO_2 hydrogenation over heterogeneous catalysts at atmospheric pressure: from electronic properties to product selectivity. *Green Chem.*, 2021, **23** (1), P. 249–267.

[11] Li F., Zhan H., Zhao N., Xiao F. Copper-based perovskite design and its performance in CO_2 hydrogenation to methanol. In: *Perovskite materials – Synthesis, characterisation, properties, and applications*. IntechOpen, Rijeka, 2016.

[12] Lindenthal L., Popovic J., Rameshan R., Huber J., Schrenk F., Ruh T., Nenning A., Löffler S., Opitz A.K., Rameshan C. Novel perovskite catalysts for CO_2 utilization – Exsolution enhanced reverse water-gas shift activity. *Appl. Catal. B*, 2021, **292**, 120183.

[13] Chen X., Chen Y., Song C., Ji P., Wang N., Wang W., Cui L. Recent advances in supported metal catalysts and oxide catalysts for the reverse water-gas shift reaction. *Front. Chem.*, 2020, **8**.

[14] Neagu D., Tsekouras G., Miller D.N., Ménard H., Irvine J.T.S. In situ growth of nanoparticles through control of non-stoichiometry. *Nat. Chem.*, 2013, **5** (11), P. 916–923.

[15] Hou Y., Wang X., Chen M., Gao X., Liu Y., Guo Q. $Sr_{1-x}K_xFeO_3$ perovskite catalysts with enhanced RWGS reactivity for CO_2 hydrogenation to light olefins. *Atmosphere (Basel)*, 2022, **13** (5), 760.

[16] Ma L.H., Gao X.H., Zhang J.L., Ma J.J., Hu X. De, Guo Q.J. Effects of metal doping on the catalytic performance of LaFe-based perovskites for CO_2 hydrogenation to light olefins. *J. of Fuel Chemistry and Technology*, 2023, **51** (1), P. 101–110.

[17] Han Kim D., Layng Park J., Ji Park E., Dok Kim Y., Uhm S. Dopant effect of barium zirconate-based perovskite-type catalysts for the intermediate-temperature reverse water gas shift reaction. *ACS Catal.*, 2014, **4** (9), P. 3117–3122.

[18] Zhang J., Wang Y., Tian J., Yan B. Cu/$LaFeO_3$ as an efficient and stable catalyst for CO_2 reduction: Exploring synergistic effect between Cu and $LaFeO_3$. *AIChE Journal*, 2022, **68** (6), P. 1–11.

[19] Daza Y.A., Maiti D., Hare B.J., Bhethanabotla V.R., Kuhn J.N. More Cu, more problems: Decreased CO_2 conversion ability by Cu-doped $La_{0.75}Sr_{0.25}FeO_3$ perovskite oxides. *Surf. Sci.*, 2016, **648**, P. 92–99.

[20] Matveyeva A.N., Omarov Sh.O., Gavrilova M.A., Sladkovskiy D.A., Murzin D.Yu. $CeFeO_3$–CeO_2–Fe_2O_3 systems: Synthesis by solution combustion method and catalytic performance in CO_2 hydrogenation. *Materials*, 2022, **15** (22), 7970.

[21] Bachina A., Ivanov V.A., Popkov V.I. Peculiarities of $LaFeO_3$ nanocrystals formation via glycine-nitrate combustion. *Nanosystems: Physics, Chemistry, Mathematics*, 2017, **8** (5), P. 647–653.

[22] Popkov V.I., Tugova E.A., Bachina A.K., Almyasheva O. V. The formation of nanocrystalline orthoferrites of rare-earth elements $XFeO_3$ (X = Y, La, Gd) via heat treatment of coprecipitated hydroxides. *Russ. J. Gen. Chem.*, 2017, **87** (11), P. 2516–2524.

[23] Popkov V.I., Almjasheva O.V, Panchuk V.V, Semenov V.G., Gusarov V.V. The role of pre-nucleus states in formation of nanocrystalline yttrium orthoferrite. *Doklady Chemistry*, 2016, **471** (2), P. 356–359.

[24] Popkov V.I., Almjasheva O. V. Yttrium orthoferrite $YFeO_3$ nanopowders formation under glycine-nitrate combustion conditions. *Russ. J. Appl. Chem.*, 2014, **87** (2), P. 167–171.

[25] Popkov V.I., Almjasheva O.V., Nevedomskiy V.N., Sokolov V.V., Gusarov V.V. Crystallization behavior and morphological features of $YFeO_3$ nanocrystallites obtainedby glycine-nitrate combustion. *Nanosystems: Physics, Chemistry, Mathematics*, 2015, **6** (6), P. 866–874.

[26] Cam T.S., Omarov S., Trofimuk A., Lebedev V., Panchuk V., Semenov V., Nguyen A.T., Popkov V. Foam-like Ce–Fe–O-based nanocomposites as catalytic platforms for efficient hydrogen oxidation in air. *J. of Science: Advanced Materials and Devices*, 2023, **8** (3), 100596.

[27] Choong C.E., Park C.M., Chang Y.Y., Yang J. kyu, Kim J.R., Oh S.E., Jeon B.-H., Choi E.H., Yoon Y., Jang M. Interfacial coupling perovskite $CeFeO_3$ on layered graphitic carbon nitride as a multifunctional Z-scheme photocatalyst for boosting nitrogen fixation and organic pollutants demineralization. *Chem. Eng. J.*, 2022, **427**, 131406.

[28] Robbins M., Wertheim G.K., Menth A., Sherwood R.C. Preparation and properties of polycrystalline cerium orthoferrite ($CeFeO_3$). *J. Phys. Chem. Solids*, 1969, **30** (7), P. 1823–1825.

[29] Ameta J., Kumar A., Ameta R., Sharma V.K., Ameta S.C. Synthesis and characterization of $CeFeO_3$ photocatalyst used in photocatalytic bleaching of gentian violet. *J. of the Iranian Chemical Society*, 2009, **6** (2), P. 293–299.

[30] Pandya H.N., Kulkarni R.G., Parsania P.H. Study of cerium orthoferrite prepared by wet chemical method. *Mater. Res. Bull.*, 1990, **25** (8), P. 1073–1077.

[31] Surendran A., Gupta N.K., Aziz F., Kushwaha K.K. Synthesis and characterization of Ce–Fe composite nanoparticles via sol–gel method. *J. of Nano- and Electronic Physics*, 2020, **12** (1).

[32] Opuchovic O., Kreiza G., Senvaitiene J., Kazlauskas K., Beganskiene A., Kareiva A. Sol-gel synthesis, characterization and application of selected sub-microsized lanthanide (Ce, Pr, Nd, Tb) ferrites. *Dyes and Pigments*, 2015, **118**, P. 176–182.

[33] Matveyeva A.N., Omarov S.O., Gavrilova M.A., Trofimuk A.D., Wärna J., Murzin D.Yu. CeO_2-supported Ni and Co catalysts prepared by a solution combustion method for H_2 production from glycerol: the effect of fuel/oxidizer ratio and oxygen excess. *Catal. Sci. Technol.*, 2023, **13** (18), P. 5387–5406.

[34] Seroglazova A.S., Lebedev L.A., Chebanenko M.I., Sklyarova A.S., Buryanenko I. V., Semenov V.G., Popkov V.I. Ox/Red-controllable combustion synthesis of foam-like $PrFeO_3$ nanopowders for effective photo-Fenton degradation of methyl violet. *Adv. Powder Technol.*, 2022, **33** (2), 103398.

[35] Omarov Sh.O., Martinson K.D., Matveyeva A.N., Chebanenko M.I., Nevedomskiy V.N., Popkov V.I. Renewable hydrogen production via glycerol steam reforming over Ni/CeO_2 catalysts obtained by solution combustion method: The effect of Ni loading. *Fuel Process. Technol.*, 2022, **236**, 107429.

[36] Uzunoglu A., Kose D.A., Stanciu L.A. Synthesis of CeO_2-based core/shell nanoparticles with high oxygen storage capacity. *Int. Nano. Lett.*, 2017, **7** (3), P. 187–193.

[37] Siddique F., Gonzalez-Cortes S., Mirzaei A., Xiao T., Rafiq M.A., Zhang X. Solution combustion synthesis: the relevant metrics for producing advanced and nanostructured photocatalysts. *Nanoscale*, 2022, **14** (33), P. 11806–11868.

[38] Deganello F., Tyagi A.K. Solution combustion synthesis, energy and environment: Best parameters for better materials. *Progr. Cryst. Growth Charact. Mater.*, 2018, **64** (2), P. 23–61.

[39] Zaboeva E.A., Izotova S.G., Popkov V.I. Glycine-nitrate combustion synthesis of $CeFeO_3$-based nanocrystalline powders. *Russ. J. Appl. Chem.*, 2016, **89** (8), P. 1228–1236.

[40] A. Voskanyan A., Chan K.-Y., Vanessa Li C.-Y. Colloidal solution combustion synthesis: Toward mass production of a crystalline uniform mesoporous CeO_2 catalyst with tunable porosity. *Chem. Mater.*, 2016, **28** (8), P. 2768–2775.
[41] Deganello F., Testa M.L., La Parola V., Longo A., Tavares A.C. $LaFeO_3$-based nanopowders prepared by a soft–hard templating approach: the effect of silica texture. *J. Mater. Chem. A*, 2014, **2** (22), P. 8438–8447.
[42] Manukyan V.K., Chen Y.-S., Rouvimov S., Li P., Li X., Dong S., Liu X., Furdyna J.K., Orlov A., Bernstein G.H., Porod W., Roslyakov S., Mukasyan A.S. Ultrasmall α-Fe_2O_3 superparamagnetic nanoparticles with high magnetization prepared by template-assisted combustion process. *J. Phys. Chem. C*, 2014, **118** (29), P. 16264–16271.
[43] Scholz J., Etter M., Haas D., Meyer A., Kornowski A., Sazama U., Mascotto S. Pore geometry effect on the synthesis of silica supported perovskite oxides. *J. Colloid. Interface. Sci.*, 2017, **504**, P. 346–355.
[44] Yu T.F., Chang C.W., Chung P.W., Lin Y.C. Unsupported and silica-supported perovskite-type lanthanum manganite and lanthanum ferrite in the conversion of ethanol. *Fuel Process. Technol.*, 2019, **194**, P. 106117.
[45] Yuan Y., Liu C., Zhang Y., Shan X. Sol–gel auto-combustion synthesis of hydroxyapatite nanotubes array in porous alumina template. *Mater. Chem. Phys.*, 2008, **112** (1), P. 275–280.
[46] Peng K., Fu L., Yang H., Ouyang J. Perovskite $LaFeO_3$/montmorillonite nanocomposites: synthesis, interface characteristics and enhanced photocatalytic activity. *Sci. Rep.*, 2016, **6** (1), 19723.
[47] Wang K., Niu H., Chen J., Song J., Mao C., Zhang S., Gao Y. Immobilizing $LaFeO_3$ nanoparticles on carbon spheres for enhanced heterogeneous photo-Fenton like performance. *Appl. Surf. Sci.*, 2017, **404**, P. 138–145.
[48] Hare B.J., Maiti D., Daza Y.A., Bhethanabotla V.R., Kuhn J.N. Enhanced CO_2 conversion to CO by silica-supported perovskite oxides at low temperatures. *ACS Catal.*, 2018, **8** (4), P. 3021–3029.
[49] Hare B.J., Maiti D., Ramani S., Ramos A.E., Bhethanabotla V.R., Kuhn J.N. Thermochemical conversion of carbon dioxide by reverse water-gas shift chemical looping using supported perovskite oxides. *Catal. Today*, 2019, **323**, P. 225–232.
[50] Kharlamova T.S., Urazov Kh.Kh., Vodyankina O.V. Effect of modification of supported V_2O_5/SiO_2 catalysts by lanthanum on the state and structural peculiarities of vanadium. *Kinet. Catal.*, 2019, **60** (4), P. 465–473.
[51] González-Cortés S.L., Imbert F.E. Fundamentals, properties and applications of solid catalysts prepared by solution combustion synthesis (SCS). *Appl. Catal. A Gen.*, 2013, **452**, P. 117–131.
[52] Bertaut F., Forrat F. Sur les deformations dans les perovskites à base de terres rares et d'elements de transition trivalents. *J. de Physique et le Radium*, 1956, **17** (2), P. 129–131.
[53] Shannon R.D. Revised effective ionic radii and systematic studies of interatomie distances in halides and chaleogenides. *Acta Cryst.*, 1976, **32**, 751.
[54] Janbutrach Y., Hunpratub S., Swatsitang E. Ferromagnetism and optical properties of $La_{1-x}Al_xFeO_3$ nanopowders. *Nanoscale Res. Lett.*, 2014, **9** (1), 498.
[55] Ahmed M.A., Okasha N., Hussein B. Synthesis, characterization and studies on magnetic and electrical properties of $LaAl_yFe_{1-y}O_3$ nanomultiferroic. *J. Alloys Compd.*, 2013, **553**, P. 308–315.
[56] Yang F., Yang X., Su K., Lin J., He Y., Lin Q. Structural and magnetic properties of perovskite functional nanomaterials $La_{1-x}R_xFeO_3$ (R = Co, Al, Nd, Sm) obtained using sol-gel. *Molecules*, 2023, **28** (15), 5745.
[57] Penilla E.H., Sellappan P., Duarte M.A., Wieg A.T., Wingert M.C., Garay J.E. Bulk polycrystalline ceria–doped Al_2O_3 and YAG ceramics for high-power density laser-driven solid-state white lighting: Effects of crystallinity and extreme temperatures. *J. Mater. Res.*, 2020, **35** (8), P. 958–971.
[58] Farahmandjou M., Khodadadi A., Yaghoubi M. Low concentration iron-doped alumina (Fe/Al_2O_3) nanoparticles using co-precipitation method. *J. Supercond. Nov. Magn.*, 2020, **33** (11), P. 3425–3432.
[59] Thommes M., Kaneko K., Neimark A. V., Olivier J.P., Rodriguez-Reinoso F., Rouquerol J., Sing K.S.W. Physisorption of gases, with special reference to the evaluation of surface area and pore size distribution (IUPAC Technical Report). *Pure Appl. Chem.*, 2015, **87** (9–10), P. 1051–1069.
[60] Zhong C., Yang Y., Fang Y., Chen J., Feng B., Wang H., Luo W., Yao Y. Insights into the enhanced hydrogen adsorption on M/La_2O_3 (M = Ni, Co, Fe). *Phys. Chem. Chem. Phys.*, 2023, **25** (22), P. 15547–15554.
[61] Carraro P.M., Sapag K., Oliva M.I., Eimer G.A. Comparative study of hydrogen storage on metal doped mesoporous materials. *Chem. Phys. Lett.*, 2018, **701**, P. 93–97.

Submitted 28 July 2023; revised 11 October 2023; accepted 30 October 2023

Information about the authors:

Anna N. Matveyeva – Ioffe Institute, Politekhnicheskaya st., 28, St.-Petersburg, 194021, Russia; ORCID 0000-0001-6689-1430; anna.matveyeva@mail.ioffe.ru

Shamil O. Omarov – Ioffe Institute, Politekhnicheskaya st., 28, St.-Petersburg, 194021, Russia; ORCID 0000-0002-6862-128X; somarov@mail.ioffe.ru

Marianna A. Gavrilova – Ioffe Institute, Politekhnicheskaya st., 28, St.-Petersburg, 194021, Russia; St.-Petersburg State Institute of Technology (Technical University), Moskovskiy av., 26, St.-Petersburg, 190013, Russia; ORCID 0000-0001-6163-9316; amonrud@yandex.ru

Conflict of interest: the authors declare no conflict of interest.

NANOSYSTEMS:
PHYSICS, CHEMISTRY, MATHEMATICS

Bukina V., et al. *Nanosystems: Phys. Chem. Math.*, 2023, **14** (6), 690–698.
http://nanojournal.ifmo.ru
DOI 10.17586/2220-8054-2023-14-6-690-698

Original article

Optical glass-ceramics based on Fe^{2+}: $MgAl_2O_4$ nanocrystals and nucleated by TiO_2 and ZrO_2

Vasilisa S. Bukina[1,a], Olga S. Dymshits[1,2,b], Irina P. Alekseeva[1,c], Anna A. Volokitina[1,d], Svetlana S. Zapalova[1,e], Aleksandr A. Zhilin[3,f]

[1]Vavilov State Optical Institute, 36 Babushkina St., St. Petersburg, 192171, Russia

[2]Ioffe Institute, 26 Politekhnicheskaya, St Petersburg, 194021, Russia

[3]D.V. Efremov Institute of Electrophysical Apparatus, 3 Doroga na Metallostroi, pos. Metallostroi, St Petersburg, 196641, Russia

[a]nakara.orihara@mail.ru, [b]vodym1959@gmail.com, [c]vgolub19@gmail.com, [d]anna.itmo@gmail.com, [e]zenii99@yandex.ru, [f]zhilin1311@yandex.ru

Corresponding author: Olga S. Dymshits, vodym1959@gmail.com

PACS 78.67.Bf, 61.46.Hk, 42.70.Ce, 64.75.Jk, 81.10.Aj, 78.20.Ci

ABSTRACT Transparent glass-ceramics of magnesium aluminosilicate system based on Fe^{2+}:$MgAl_2O_4$ spinel nanocrystals nucleated by a mixture of TiO_2 and ZrO_2 and doped with 0.6 mol% FeO were developed. The glass was melted at 1580 °C with stirring and heat-treated in the temperature range from 800 to 1300 °C. The structure and spectroscopic properties of the glass and glass-ceramics were studied by DSC and XRD methods, Raman and absorption spectroscopy. $ZrTiO_4$ nanocrystals 6 nm in size precipitate during the nucleation heat-treatment at 800 °C. Spinel nanocrystals 9–14 nm in size are formed during heat-treatments at 850–1000 °C. Intense absorption at ∼2 μm is observed due to Fe^{2+} ions in tetrahedral positions in these crystals. Iron-doped sapphirine crystallization in transparent glass-ceramics at 1000–1050 °C results in a decrease of absorption in this spectral range. The glass-ceramics are important for the development of saturable absorbers for the spectral range of 2–3 μm.

KEYWORDS Nanocrystals, spinel, transparent glass-ceramics, ferrous ions, nucleating agents.

ACKNOWLEDGEMENTS This work was partly supported by the Russian Science Foundation (Grant 23-23-00446).

FOR CITATION Bukina V.S., Dymshits O.S., Alekseeva I.P., Volokitina A.A., Zapalova S.S., Zhilin A.A. Optical glass-ceramics based on Fe^{2+}: $MgAl_2O_4$ nanocrystals and nucleated by TiO_2 and ZrO_2. *Nanosystems: Phys. Chem. Math.*, 2023, **14** (6), 690–698.

1. Introduction

Nanosecond lasers emitting in the short-wave infrared spectral range of 2–3 μm can be used for range finding, remote sensing, medical applications, and meteorology. ZnS and ZnSe crystals doped with Fe^{2+} ions located in tetrahedral (T_d) sites are employed as saturable absorbers of such lasers [1]. Crystals of magnesium aluminate spinel with promising thermo-mechanical properties are alternative matrices for the accommodation of Fe^{2+} ions [2]. Glass-ceramics for optical applications are more cost efficient than corresponding single crystals and optical ceramics. They are easy and flexible in manufacturing and demonstrate high optical quality. Glass-ceramics, in contrast to glasses, have optical properties similar to those of the single crystals [3]. Magnesium aluminate spinel nanocrystals doped with Fe^{2+} ions were recently obtained in transparent glass-ceramics nucleated by titania, TiO_2 [4]. The drawback of glass-ceramics is that in these multiphase materials active ions are not only located in the desired crystal phase, but may also be distributed between and at the interfaces of different crystalline and amorphous phases. In [4] we demonstrated that in spinel-based magnesium aluminosilicate glass-ceramics, iron ions are distributed between the target spinel phase, the phase of the nucleating agent, magnesium aluminotitanate crystalline phase, and the residual highly siliceous glass. For the development of spinel-based glass-ceramics selectively doped with ferrous ions, Fe^{2+}, it is important to know how the nature of the nucleating agent influences the structure, phase composition and absorption properties of transparent spinel based glass-ceramics. The role of these agents was previously studied in the $MgO–Al_2O_3–SiO_2$ ternary system [5], in which nucleation and internal bulk spinel crystallization is achieved using TiO_2 [6] or a mixture of TiO_2 and ZrO_2 [5, 7].

The aim of the present study is the development of transparent glass-ceramics of magnesium aluminosilicate system based on Fe^{2+}:$MgAl_2O_4$ spinel nanocrystals nucleated by a mixture of TiO_2 and ZrO_2 and the study of their structure and

spectral properties. In future, we are planning to compare the properties of these glass-ceramics with those nucleated by titania. These glass-ceramics are important for the development of saturable absorbers for the spectral range of 2–3 μm.

2. Experimental

2.1. Sample preparation

Model magnesium aluminosilicate glass with the composition (mol%) 20 MgO, 20 Al_2O_3, 60 SiO_2 [6] was prepared with the addition of two nucleating agents, TiO_2 and ZrO_2, [5, 7] and FeO. The nominal glass composition was (mol%) 18.1 MgO, 18.1 Al_2O_3, 54.2 SiO_2, 4.5 TiO_2, 4.5 ZrO_2, and 0.6 FeO.

The raw materials were reagent grade. The batch for producing 400 g of glass was melted in a crucible made of quartz ceramics at 1580 °C for 4 hours (h) with stirring. The glass was poured onto a cold metal plate and annealed at 660 °C. The transparent yellow glass, Fig. 1, was subjected to one- and two-stage secondary heat-treatments. The first nucleation stage was at 800 °C for 6 h and the temperature of the second stage ranged from 850 to 1300 °C with the same holding time of 6 h. As a result, transparent glass-ceramics were prepared by heat-treatments with the temperature of the second stage from 850 to 1050 °C, Their color changed with the heat-treatment temperature from the yellow to the brown, see Fig. 1. The glass heat-treated at the second stage at 1100 °C becomes translucent. The glass-ceramics prepared at 1200 and 1300 °C are opaque.

FIG. 1. Photographs of the polished glass, glass produced by the heat-treatment at 800 °C and glass-ceramics produced by two-stage heat-treatments with the first hold at 800 °C and the second hold from 850 to 1300 °C. Holding time at each stage is 6 h. The thickness of the polished samples is 1 mm.

2.2. Methods

XRD patterns of powdered samples were measured with a Shimadzu XRD-6000 diffractometer with nickel-filtered Cu Kα radiation. The average crystal sizes were estimated from broadening of X-ray peaks according to Scherrer's equation [8]. The error in the average crystal size estimation is about 5%. The average size of $ZrTiO_4$ nanocrystals was estimated using the peak with Miller's indices (111); the size of magnesium aluminate spinel was estimated using the peak with indices (440). The average size of petalite-like phase was estimated using the peak with indices (211) and (210). The size of sapphirine of the 2M modification was estimated using the peaks with indices (122) and (1 10 0). The size of indialite crystals was estimated using the peak with Miller's indices (211), the size of cristobalite crystals was estimated using the peak with the indices (111). The unit cell parameter a was estimated from the position of the (440) plane of the spinel crystal.

Bulk samples of about 15 mg in weight were used for differential scanning calorimetry (DSC) study with help of a simultaneous thermal analyzer NETZSCH STA 449 F3 Jupiter with a dynamic flow atmosphere of Ar. The heating rate was 10 °C/min. The samples were the initial glass and the glass heat-treated at 800 °C for 6 h. For assigning the exothermic DSC peaks to certain crystalline phases, bulk samples of about 90 mg in weight were heated in the DSC furnace with the same heating rate of 10 °C/min up to the temperature of an appearance of a certain exothermic peak, cooled down to room temperature and subjected to powder XRD analysis.

Unpolarized Raman spectra were measured in backscattering geometry on an InVia (Renishaw, England) Micro-Raman spectrometer equipped with the multichannel detector cooled up to −70 °C. The spectra were excited by Ar+ CW laser line of 514 nm. Leica 50× (N.A. = 0.75) objective was used for illuminating the sample; the scattered light was collected by the same objective. Edge filter was placed before the spectrograph entrance slit; a spatial resolution was of 2 cm^{-1}. Every spectrum was averaged over 30 acquisitions with duration of 20 s.

Room-temperature absorption spectra were recorded by using a double-beam spectrophotometer Shimadzu UV 3600 in the range from 250 to 3300 nm. The samples were polished plates with a thickness of 1 mm. Absorbance spectra were normalized to the sample thickness.

3. Results and discussion

Figure 2 shows the DSC curve of the quenched glass and the curve of the same glass heat-treated at 800 °C for 6 h (the nucleation stage). From the DSC curve of the initial glass, the glass transition temperature, T_g = 765 °C, is determined. Several exothermic peaks associated with appearance of different crystalline phases are also observed. In the low temperature region, two exothermic peaks are formed, the crystallization onset temperatures, T_{on}, of which are T_{on1} = 845 °C and T_{on2} = 918 °C, and the crystallization maximum temperatures, $T_{\max}$, are $T_{\max 1}$ = 877 °C and $T_{\max 2}$ = 965 °C. High-temperature exothermic peaks have complex shapes, the temperatures of their crystallization maxima are as follows: $T_{\max 3}$ =1101 °C, $T_{\max 4}$ = 1212 °C, and $T_{\max 5}$ =1290 °C.

The glass transition temperature of the glass heat-treated at 800 °C for 6 h is higher than that of the initial glass, T_g = 793 °C. On the DSC curve of this sample, there is no peak in the range of 900 °C, observed on the DSC curve of the initial glass. In the region of high temperatures, the shapes and temperatures of maxima of exothermic peaks on the DSC curves of the initial and heat-treated glasses are near similar.

We determined the origin of the peaks for both DSC curves. After the crystallization maximum temperatures were found, the samples of the quenched glass and the glass preliminary heat-treated at 800 °C for 6 h, ∼90 mg in weight, were heated in the DSC instrument up to the temperatures of the appearance of exothermic peaks. According to the XRD data, Fig. 3(a), the first exothermic peak in the DSC curve of the initial glass is associated with crystallization of zirconium titanate, $ZrTiO_4$, with orthorhombic structure. The sample heat-treated up to the temperature of the second exothermic peak (969 °C) has the phase composition of zirconium titanate and magnesium aluminate spinel, $MgAl_2O_4$, with the cubic structure, see Fig. 3(a).

An absence of the exothermic peak of $ZrTiO_4$ at ∼880 °C on the DSC curve of the sample preheated at 800 °C for 6 h, see Fig. 2, suggests that almost all of $ZrTiO_4$ that crystallized during the heating of the initial glass in the DSC furnace, evolves during the preliminary heat-treatment of this glass at 800 °C for 6 h. This suggestion is confirmed by the similarity of the XRD patterns of the quenched glass heated in the DSC furnace up to 878 °C and the glass heat-treated in isothermal conditions at 800 °C for 6 h, see Fig. 4. The sample preheated at 800 °C for 6 h and heat-treated up to the temperature of the peak at 965 °C had the same phase composition as the quenched glass heated up to 969 °C. It is a mixture of zirconium titanate and magnesium aluminate spinel, see Fig. 3(b).

Taking into account the similarity of the high-temperature parts of the DSC curves of the both samples, we determined phase compositions only of the materials preheated at 800 °C for 6 h and heated in the DSC furnace to the temperatures of near 1300 °C, see Fig. 3(b). We believe the phase compositions of both materials heated up to these temperatures are similar.

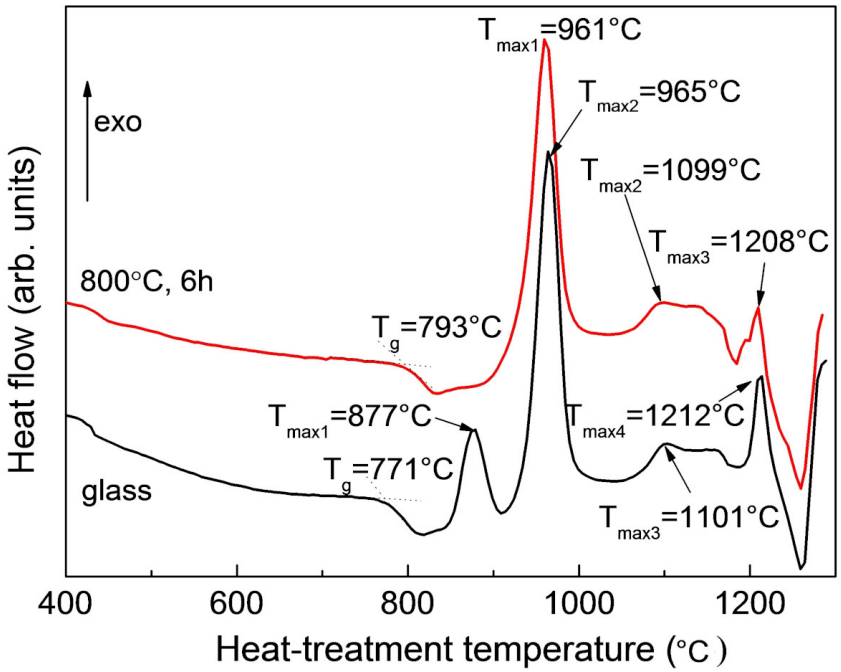

FIG. 2. DSC curves of the quenched glasses and the glass heat-treated at 800 °C for 6 h. T_g stands for the glass transition temperature, $T_{\max}$ stands for the maximum crystallization temperature. The curves are shifted for the convenience of observation

According to XRD data presented in Fig. 3(b), the broad exothermic peak in the temperature range from ∼1100 to ∼1200 °C is related to the transformation of magnesium aluminate spinel into sapphirine, the magnesium aluminosilicate

with monoclinic structure, which is in accordance with our previous study [4]. The preheated sample heat-treated up to the temperature of the $T_{\max 4}$ (1212 °C) has a rich phase composition of the $ZrTiO_4$, sapphirine, and magnesium aluminosilicate with a quartz-like structure. The minimum on the DSC curve at about 1255 °C is related to the beginning of decomposition of the magnesium aluminosilicate with a quartz-like structure and appearance of traces of indialite, a high-temperature modification of cordierite. The sample also contained the crystals of $ZrTiO_4$ and sapphirine. The material heated to 1290 °C has the phase composition of $ZrTiO_4$, indialite, sapphirine, and traces of the magnesium aluminosilicate with a quartz-like structure.

The heat-treatments in isothermal conditions were conducted based on the results of the DSC –XRD study. According to the XRD patterns presented in Fig. 5, nanocrystals of zirconium titanate, $ZrTiO_4$, are formed during the heat-treatment at 800 °C for 6 h. Their average size is 6 nm, see Table 1. During heat-treatments at the second stage at temperature in the range from 850 to 1000 °C, magnesium aluminate spinel with average size of 8.5 – 13.5 nm is additionally formed. The variation of its unit cell parameter with heat-treatment is presented in Table 1. Traces of magnesium aluminosilicate with petalite structure with the average size of 16 nm are detected on the XRD pattern of the sample obtained by the heat-treatment at the second stage at 850 °C. In the temperature range from 1000 to 1100 °C, sapphirine crystals with the average size from 17 to 25 nm are formed at the expense of spinel, the intensity of zirconium titanate peaks increases.

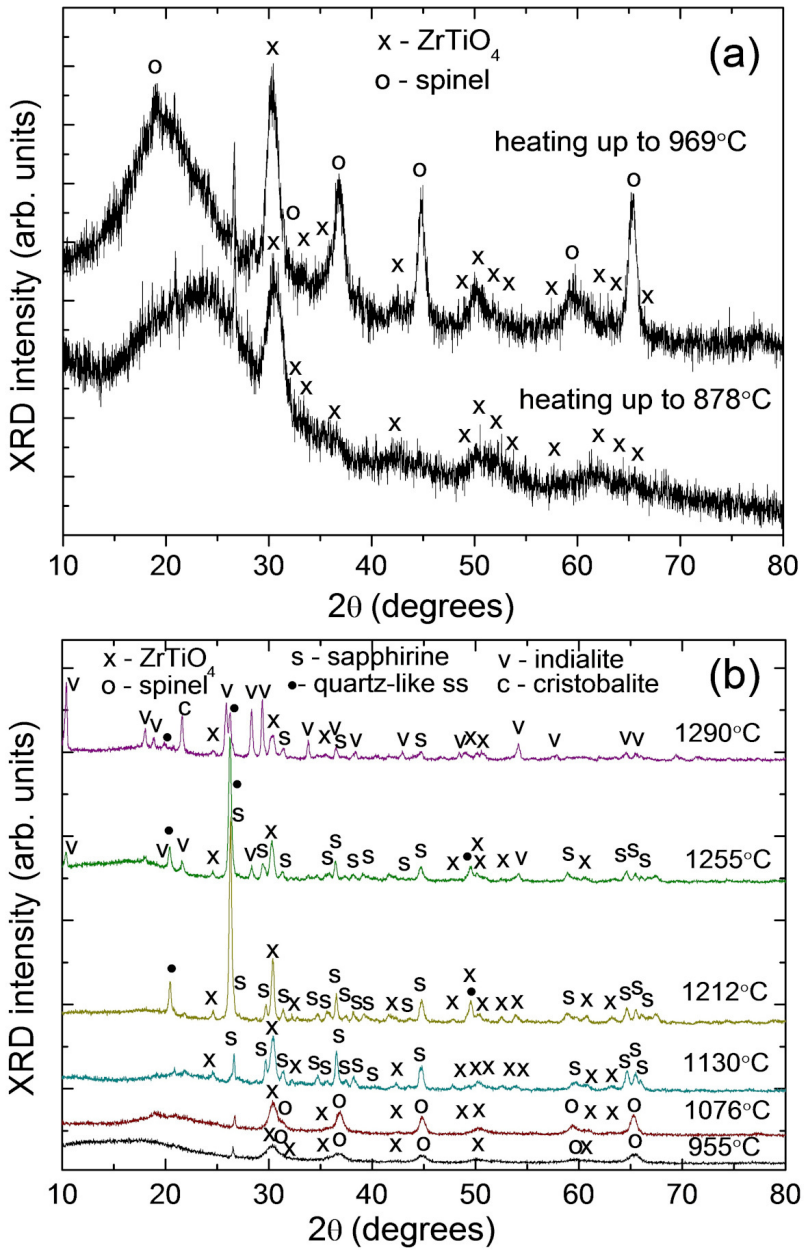

FIG. 3. XRD patterns (a) of the initial glass heat-treated in the DSC furnace up to 878 and 969 °C; (b) of the samples preheated at 800 °C for 6 h and heat-treated in the DSC furnace up to 955, 1076,1130, 1212, 1255, and 1290°C. The patterns are shifted for the convenience of observation

TABLE 1. The average crystal sizes D and spinel unit cell parameter a in glass-ceramics

Heat-treatment schedule	Spinel		$ZrTiO_4$	Sapphirine	Indialite	Cristobalite
	D, nm	a, $\pm$0.003, Å	D, nm	D, nm	D, nm	D, nm
800 °C/6 h	–	–	6.0	–	–	–
800 °C/6 h + 850 °C/6 h	8.5	8.068	6.0	–	–	–
800 °C/6 h + 900 °C/6 h	9.5	8.098	6.5		–	–
800 °C/6 h + 950 °C/6 h	12.0	8.099	8.0			
800 °C/6 h + 1000 °C/6 h	13.5	8.093	9.5	17.5	–	–
800 °C/6 h + 1050 °C/6 h	–	–	14.5	24.0	–	–
800 °C/6 h + 1100 °C/6 h	–	–	22.5	25.0	–	–
800 °C/6 h + 1200 °C/6 h	–	–	30.5		29.0	31.5
800 °C/6 h + 1300 °C/6 h	–	–	26.0		25.0	34.5

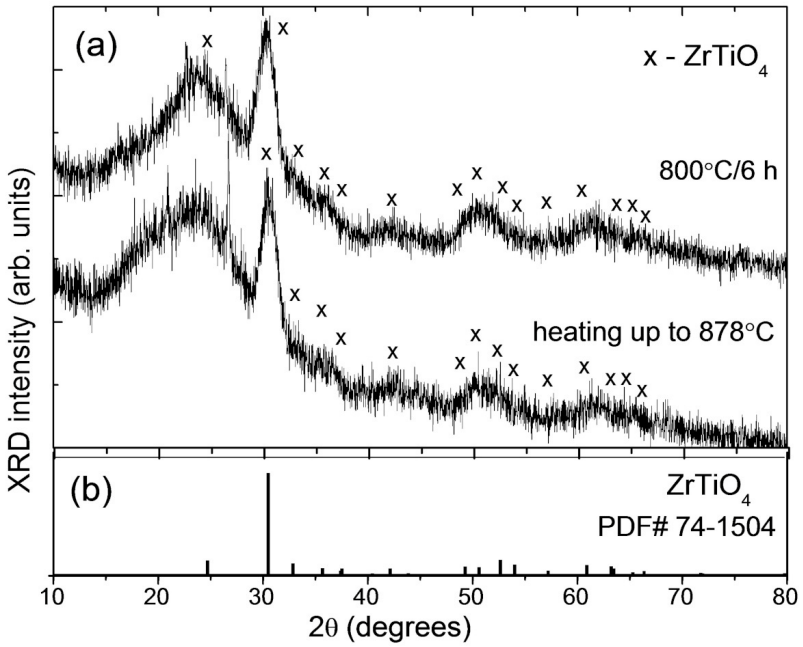

FIG. 4. (a) XRD patterns of the quenched glass heated in the DSC furnace up to 878 °C and the glass heat-treated at 800 °C for 6 h; (b) the standard pattern of $ZrTiO_4$

In the high temperature range of heat-treatments, at 1200 and 1300 °C, the residual glass crystallizes with the formation of crystals of stable phases of indialite, $2MgO{\cdot}2Al_2O_3{\cdot}5SiO_2$, and cristobalite, SiO_2, while preserving sapphirine and zirconium titanate, see Fig. 5(a). Crystals of magnesium aluminosilicates with the quartz-like structure, which is observed in the DSC run, are not observed in glass-ceramics prepared in isothermal conditions. It is probably related to the selected heat-treatment schedules. We speculate that this phase will crystallize during heat-treatments in the temperature range from 1100 to 1200 °C.

Figure 5(b) shows the details of the formation of crystalline phases in transparent glass-ceramics. The position of the maximum of amorphous halo is located at $2\theta = 24.3^\circ$ in the XRD pattern of the initial glass. With increasing the heat-treatment temperature, it constantly shifts to $2\theta = 21.8^\circ$, the position of the maximum of amorphous halo in quartz glass, see Fig. 5(b). The characteristics of the crystalline phases formed during the heat-treatments are presented in Table 1.

Figure 6 demonstrates the Raman spectra of the initial glass and transparent glass-ceramics. The spectrum of the initial glass is typical for aluminosilicate glasses nucleated by a mixture of TiO_2 and ZrO_2 [9] and contains three broad Raman bands at $\sim$ 450, 800 and $\sim$ 920 cm^{-1}. The band at $\sim$ 920 cm^{-1} is related to [TiO_4] tetrahedra in the aluminosilicate network, while the bands with lower frequencies are the characteristics of the vibrations of the aluminosilicate network itself. After the heat-treatment of the initial glass at 800 °C for 6 h, intensity of the $\sim$ 920 cm^{-1} band in its Raman

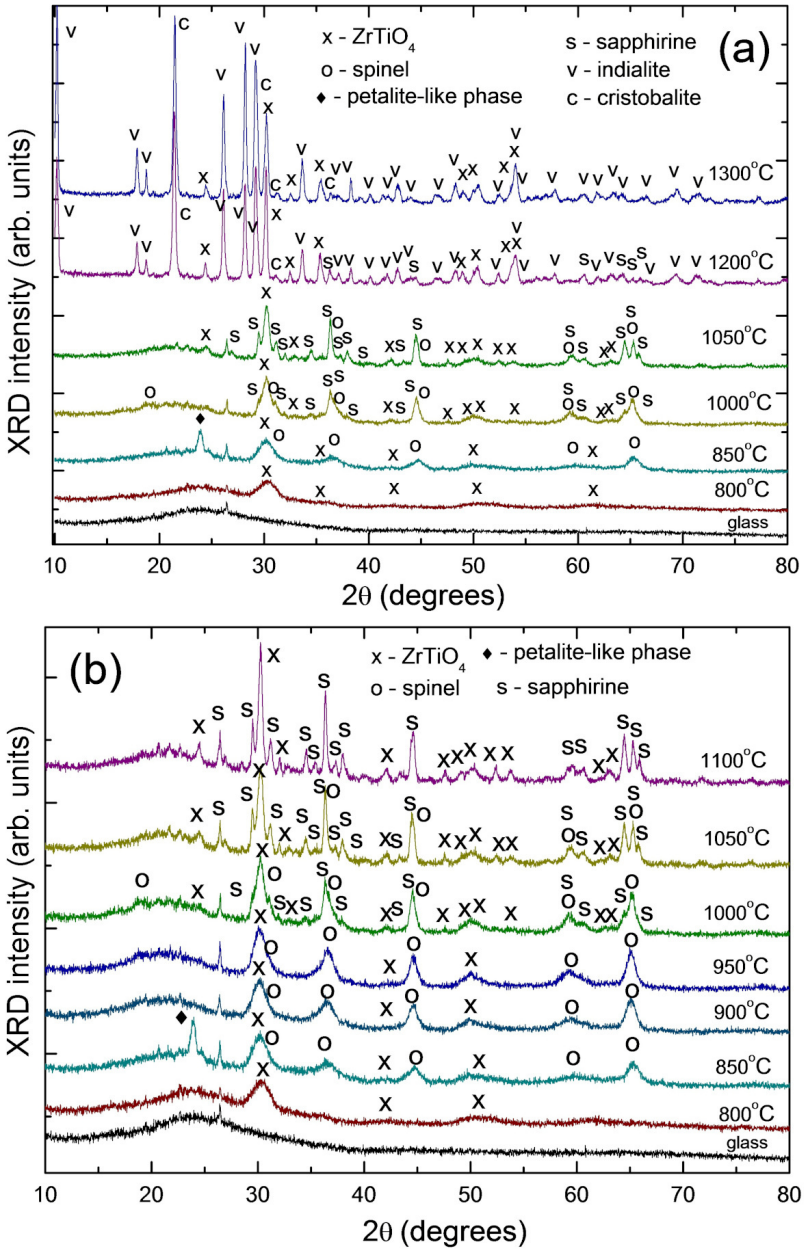

FIG. 5. (a,b) XRD patterns of the initial glass and glass-ceramics. (a) The heat-treatment temperature is from 800 to 1300 °C; (b) The heat-treatment temperature is from 800 to 1000 °C. Labels 850–1300 °C indicate the heat-treatment temperature at the second stage. Holding time at the second stage is 6 h. The nucleation stage is at 800 °C for 6 h

spectrum diminishes while intensity of the ∼800 cm^{-1} band goes up; the spectral features of $ZrTiO_4$ crystals [10–12] are clearly seen in the spectra (the characteristic bands locate at ∼ 154, 269, 334, 416 and 645 cm^{-1}). The redistribution of intensities of the bands located in the high-frequency region in favor of the band centered at ∼ 790 cm^{-1} is the evidence of the development of phase separation [12]. In Raman spectra of glass-ceramics, the heat-treatment temperature increasing causes a further rise of the band at ∼ 800 cm^{-1} and bands related to the continuous precipitation of $ZrTiO_4$. The Raman bands typical for spinel nanocrystals with a partly inverse structure appear at 414, 488, 657, 724, and 796 cm^{-1} [10, 11]. In the spectrum of glass-ceramics prepared by the two-stage heat-treatment with the second stage at 1000 and 1050 °C, the Raman bands of sapphirine appear at 457, 564, and 684 cm^{-1} [13]. Appearance of weak high-frequency bands at 940 and 1100 cm^{-1} in spectra of all glass-ceramics prepared by high-temperature heat-treatments is related to the vibrations of $[TiO_4]$ groupings in the residual highly siliceous glass [14].

Absorption spectra of the initial and heat-treated glasses are formed by an absorption edge located in the UV region of the spectrum, a broad intense unstructured band in the visible spectral range, a broad weak unstructured band with a maximum at ∼ 1000 nm, a strong band with a maximum at ∼ 2000 nm, and an absorption band in the region from 2700 to 3300 nm, see Fig. 7(a). In the spectrum of the glass, the position of the absorption edge corresponds to $\lambda = 362$ nm. A

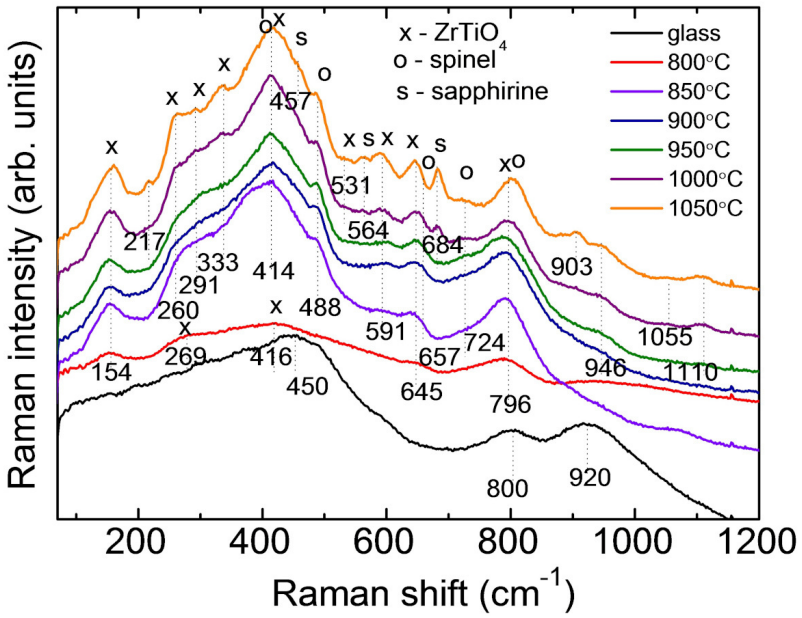

FIG. 6. Raman spectra of the initial glass and transparent glass-ceramics. *Labels* 850–1050 °C indicate the heat-treatment temperature at the second stage. The first stage is at 800 °C. The holding time at each stage is 6 ° h. λ_{exc} = 514 nm. *Numbers* denote the position of the Raman peaks in cm^{-1}. The curves are shifted for the convenience of observation

broad band with a maximum at $\sim$ 1100 nm has absorption coefficient of $\sim$ 5.2 cm^{-1}. This absorption is mainly due to the $^5T_2 \rightarrow ^5E(^5D)$ transition of ferrous ions, Fe^{2+}, in octahedral ligand field (LF). The spectrum of the sample obtained by the heat-treatment at 800 °C for 6 h is similar to that of the initial glass, which means that crystallization of $ZrTiO_4$ does not involve iron ions. The absorption spectrum changes with spinel crystallization in the temperature region from 850 to 1000 °C. The absorption in the visible spectral range is caused by the oxygen to metal charge transfer (OMCT) O^{2-}–Fe^{2+}, O^{2-}–Fe^{3+}, O^{2-}–Ti^{3+}, O^{2-}–Ti^{4+}, as well as intervalent charge transfer (IVCT) Fe^{2+}/Fe^{3+} and Ti^{4+}–Fe^{2+} bands. We cannot rule out a weak absorption of Fe^{3+} and Ti^{3+} ions in octahedral ligand field. A broad band at 1500–2200 nm with a maximum at $\sim$ 1.90 μm appears and grows with increasing the heat-treatment temperature while the band with a maximum at $\sim$ 1100 nm decreases in intensity. An appearance and growth of the band at 1500–2200 nm is due to the entry of Fe^{2+} ions into spinel nanocrystals in the tetrahedral positions (T_d) (the $^5E \rightarrow ^5T_2(^5D)$ transition).

With the increase of the heat-treatment temperature up to 1050 °C, in the spectrum of glass-ceramics a noticeable drop in the intensity of the absorption band in the region of 2000 nm associated with Fe^{2+} ions in T_d sites in spinel is observed. This correlates with the decrease in the amount of spinel nanocrystals and appearance of sapphirine. In sapphirine, Mg^{2+} ions are in sixfold coordination while Al^{3+} ions are in four-and sixfold coordinated sites [15]. Sapphirine is known to accommodate iron ions. There are the substitutions $Mg^{2+} \rightarrow Fe^{2+}$ (predominantly) and $Al^{3+} \rightarrow Fe^{3+}$ with Fe^{3+} ions assigned to tetrahedral positions [16]. Thus, upon sapphirine formation from spinel and residual highly siliceous glass, iron ions are present as the $^{IV}Fe^{3+}$ and $^{VI}Fe^{2+}$ species [4]. It is reflected in the absorption spectrum of glass-ceramic obtained by the heat-treatment at 1050 °C, see Fig. 7. The structuring of the spectrum of OH-groups is due to their incorporation into spinel nanocrystals [17].

4. Conclusions

Model glass of the $MgO - Al_2O_3 - SiO_2$ ternary system intended for the development of transparent glass-ceramics based on the Fe^{2+}:$MgAl_2O_4$ spinel nanocrystals was nucleated by a mixture of TiO_2 and ZrO_2 and doped with 0.6 mol% FeO. The glass was melted at 1580 °C for 4 h with stirring and heat-treated in the temperature range from 800 to 1300 °C.

The structure, phase composition and spectroscopic properties of the initial glass and glass-ceramics were studied by the differential scanning calorimetry and X-ray diffraction analysis, Raman and absorption spectroscopy.

$ZrTiO_4$ nanocrystals 6 nm in size precipitate in the glass during its nucleation heat-treatment at 800 °C. Similar crystal fraction of $ZrTiO_4$ appears during heating of the initial glass to the temperature of ~880 °C. Spinel nanocrystals appear during two different heat-treatment protocols, i.e., in the course of heating of the initial glass up to the temperature of 970 °C and by the two-stage heat-treatments with temperature from 850 to 1000 °C at the second stage. Spinel nanocrystals with average size ranging from 9 to 14 nm and with unit cell parameter a = 8.068 – 8.099 Å are formed in glass-ceramics during heat-treatments at temperatures from 850 to 1000 °C. A broad absorption band spanning from ~1.5 to 2.5 μm is assigned to the $^5E \rightarrow ^5T_2$ (^5D) transition of Fe^{2+} ions in T_d sites in spinel nanocrystals.

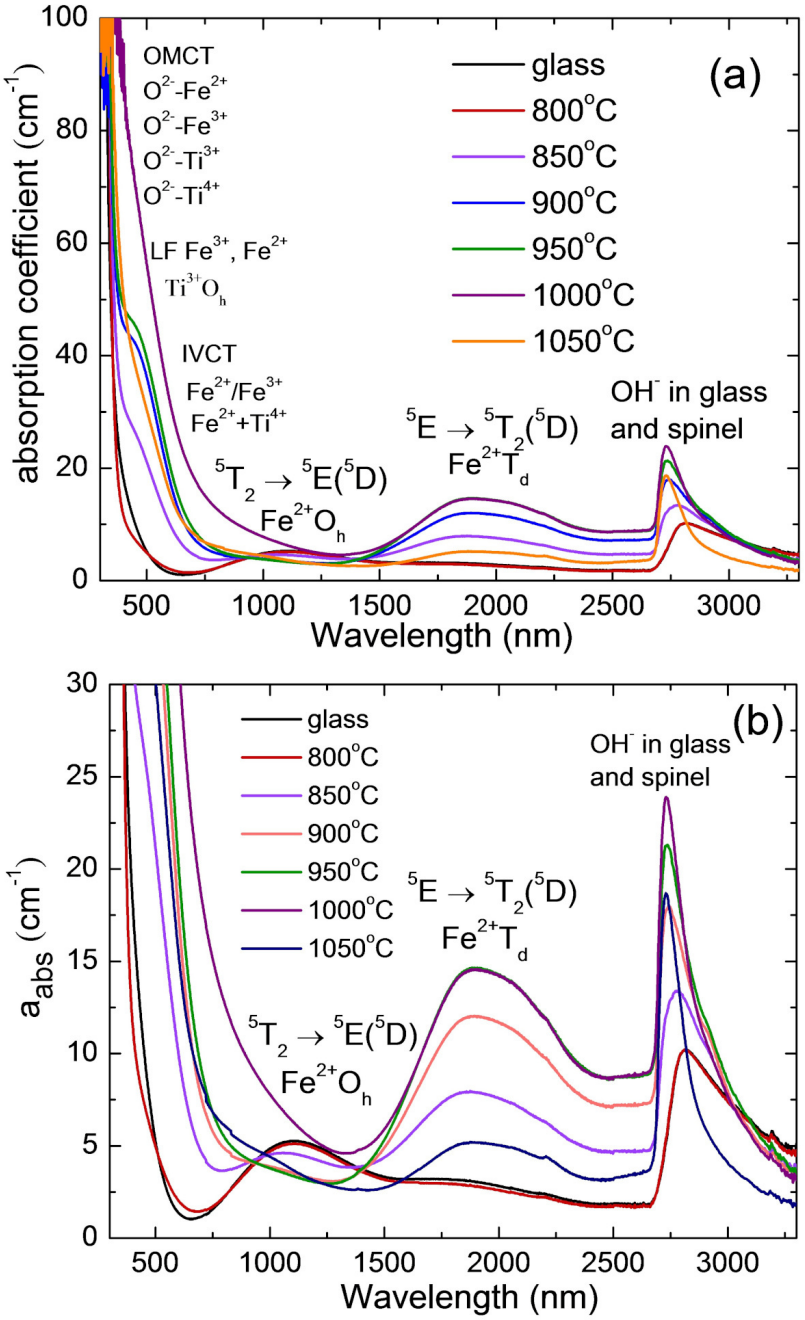

FIG. 7. Absorption spectra of the glass and transparent glass-ceramics in different scales along the Y-axis. *Labels* 850–1050 °C indicate the heat-treatment temperature at the second stage. The first stage of the heat-treatment is always at 800 °C for 6 h

Iron-doped sapphirine nanocrystals with average sizes ranging from 18 to 25 nm appear in glass-ceramics during heat-treatments from 1000 to 1100 °C. Appearance of iron-doped sapphirine nanocrystals results in a decrease of absorption in the spectral range from $\sim$ 1.5 to 2.5 μm. The obtained regularities are important for the development of saturable absorbers for the spectral range of 2–3 μm.

References

[1] Frolov M.P., Korostelin Yu.V., Kozlovsky V.I., Podmar'kov Yu.P., Savinova S.A., Skasyrsky Ya.K. 3 J. pulsed Fe:ZnS laser tunable from 3.44 to 4.19 μm. *Laser Phys. Lett.*, 2015, **12**(5), P. 055001(1-6).

[2] Basyrova L., Balabanov C., Belyaev A., Drobotenko V., Vitkin V., Dymshits O., Loiko P. Synthesis, structure and spectroscopy of Fe^{2+}:$MgAl_2O_4$ transparent ceramics. *J. Phys.: Conf. Ser.*, 2019, **1410**, P. 012123(1-4).

[3] Dymshits O., Shepilov, M., Zhilin A. Transparent glass-ceramics for optical applications. *MRS Bulletin*, 2017, **42**, P. 200–205.

[4] Basyrova L., Bukina V., Balabanov S., Belyaev A., Drobotenko V., Dymshits O., Alekseeva I., Tsenter M., Zapalova S., Khubetsov A., Zhilin A., Volokitina A., Vitkin V., Mateos X., Serres J.M., Camy P., Loiko P. Synthesis, structure and spectroscopy of Fe^{2+}:$MgAl_2O_4$ transparent ceramics and glass-ceramics. *J. Lumin.*, 2021, **236**, P. 118090(1-17).

[5] Dugué A., Dymshits O., Cormier L., Cochain B., Lelong G., Zhilin A., Belin S. In situ evolution of Ni environment in magnesium aluminosilicate glasses and glass–ceramics. Influence of ZrO_2 and TiO_2 nucleating agents. *J. Phys. Chem. Solids*, 2015, **78**, P. 137–146.
[6] Golubkov V.V., Dymshits O.S., Zhilin A.A., Chuvaeva T.I., Shashkin A.V., On the phase separation and crystallization of glasses in the MgO–Al_2O_3–SiO_2–TiO_2 system. *Glass Phys. Chem.*, 2003, **29**, P. 254–266.
[7] Carl G., Höche T., Voigt B. Crystallisation behavior of a MgO–Al_2O_3–SiO_2–TiO_2–ZrO_2 glass. *Phys. Chem. Glasses.*, 2002, **43C**, P. 256–258.
[8] Lipson H., Steeple H., in: McMillan (Ed.), *Interpretation of X-Ray Powder Patterns*, Martins Press, London, N.Y., 1970, p. 344.
[9] Loiko P.A., Dymshits O.S., Zhilin A.A., Alekseeva I.P., Yumashev K.V. Influence of NiO on phase transformations and optical properties of ZnO–Al_2O_3–SiO_2 glass–ceramics nucleated by TiO_2 and ZrO_2. Part II. Optical absorption and luminescence. *J. Non-Cryst. Solids*, 2013, **376**, P. 99–105.
[10] Krebs M.A., Condrate R.A. A Raman spectral characterization of various crystalline mixtures in the ZrO_2-TiO_2 and HfO_2-TiO_2 systems, *J. Mater. Sci. Lett.*, 1988, **7**, P. 1327–1330.
[11] Azough F., Freer R., Petzelt J. A Raman spectral characterization of ceramics in the system ZrO_2–TiO_2. *J. Mater. Sci.*, 1993, **28**, P. 2273–2276.
[12] Alekseeva I.P., Dymshits O.S., Golubkov V.V., Loiko P.A., Tsenter M.Ya., Yumashev K.V., Zapalova S.S., Zhilin A.A. Influence of NiO on phase transformations and optical properties of ZnO–Al_2O_3–SiO_2 glass-ceramics nucleated by TiO_2 and ZrO_2. Part I. Influence of NiO on phase transformations of ZnO–Al_2O_3–SiO_2 glass-ceramics nucleated by TiO_2 and ZrO_2. *J. Non-Cryst. Solids*, 2014, **384**, P. 73–82.
[13] Lamara S., Redaoui D., Sahnoune F., Heraiz M., Saheb N., Microstructure, thermal expansion, hardness and thermodynamic parameters of cordierite materials synthesized from Algerian natural clay minerals and magnesia. *Bol. Soc. Esp.Cerám. V.*, 2021, **60**(5), P. 291–306.
[14] Alekseeva I., Dymshits O., Ermakov V., Golubkov V., Malyarevich A., Tsenter M., Zhilin A., Yumashev K. *Phys. Chem. Glasses Eur. J. Glass Sci. Technol. B*, 2012, **53**(4), P. 167–180.
[15] Povarennykh A.S. *Crystal Chemical Classification of Minerals*. Springer, New York, 1972, p. 286.
[16] Steffen G., Seifert F., Amthauer G. Ferric iron in sapphirine: a Mössbauer spectroscopic study. *Am. Mineral.*, 1984, **69**, P. 339–348.
[17] Bromiley G.D., Nestola F., Redfern S.A.T., Zhang M., Water incorporation in synthetic and natural $MgAl_2O_4$ spinel. *Geochem. Cosmochim. Acta*, 2010, **74**, P. 705–718.

Submitted 10 October 2023; accepted 14 November 2023

Information about the authors:

Vasilisa S. Bukina – Vavilov State Optical Institute, 36 Babushkina St., St. Petersburg, 192171, Russia; ORCID 0009-0006-3752-0722; nakara.orihara@mail.ru

Olga S. Dymshits – Vavilov State Optical Institute, 36 Babushkina St., St. Petersburg, 192171, Russia; Ioffe Institute, 26 Politekhnicheskaya, St Petersburg, 194021, Russia; ORCID 0000-0003-1980-0561; vodym1959@gmail.com

Irina P. Alekseeva – Vavilov State Optical Institute, 36 Babushkina St., St. Petersburg, 192171, Russia; vgolub19@gmail.com

Anna A. Volokitina – Vavilov State Optical Institute, 36 Babushkina St., St. Petersburg, 192171, Russia; ORCID 0000-0002-6091-6534; anna.itmo@gmail.com

Svetlana S. Zapalova – Vavilov State Optical Institute, 36 Babushkina St., St. Petersburg, 192171, Russia; zenii99@yandex.ru

Aleksandr A. Zhilin – D.V. Efremov Institute of Electrophysical Apparatus, 3 Doroga na Metallostroi, pos. Metallostroi, St Petersburg, 196641, Russia; zhilin1311@yandex.ru

Conflict of interest: the authors declare no conflict of interest.

NANOSYSTEMS:
PHYSICS, CHEMISTRY, MATHEMATICS

Original article

Kozhevnikova N.S., et al. *Nanosystems: Phys. Chem. Math.*, 2023, **14** (6), 699–704.
http://nanojournal.ifmo.ru
DOI 10.17586/2220-8054-2023-14-6-699-704

Surface topology, electrophysical properties and formation mechanism of tin(ii) sulfide thin films

N. S. Kozhevnikova[1,a], L. N. Maskaeva[2,b], A. N. Enyashin[1,c], A. P. Tyutyunnik[1,d], O. A. Lipina[1,e], I. O. Selyanin[1,f], V. F. Markov[2,g]

[1]Institute of Solid State Chemistry of the Ural Branch of RAS, Ekaterinburg, Russia
[2]Ural Federal University, Ekaterinburg, Russia

[a]kozhevnikova@ihim.uran.ru, [b]larisamaskaeva@yandex.ru, [c]enyashin@ihim.uran.ru, [d]tyutyunnik@ihim.uran.ru, [e]lipinaolgaa@yandex.ru, [f]sioprostreet@mail.ru, [g]v.f.markov@urfu.ru

Corresponding author: N. S. Kozhevnikova, kozhevnikova@ihim.uran.ru

PACS 81.10.Dn, 82.60.Lf, 82.70.Dd, 81.05.Hd

ABSTRACT Photosensitive nanocrystalline SnS films with a size of coherent X-ray scattering regions of about 30 nm were obtained by chemical bath deposition. It has been demonstrated that the deposition time affects significantly both microstructure and thickness of the film as well as the size of the particles' agglomerates forming the film. The current sensitivity of the obtained films was studied. All synthesized films, regardless of the duration of synthesis, reveal p-type conductivity due to Sn vacancies. Atomic force microscopy measurements and fractal approach provide a detailed description of the processes occurring during film formation. The characteristics of the fabricated SnS films are potentially useful for design of advanced absorbing layers within thin film solar cells.

KEYWORDS tin(II) sulfide, thin films, chemical bath deposition, p-type conductivity, quantum-chemical calculations, formation mechanism

ACKNOWLEDGEMENTS This work was carried out in accordance with the scientific and research plans and state assignment of the ISSC UB RAS and Ural Federal University Program of Development within the Priority-2030 Program (Ministry of Science and Higher Education of the Russian Federation).

FOR CITATION Kozhevnikova N.S., Maskaeva L.N., Enyashin A.N., Tyutyunnik A.P., Lipina O.A., Selyanin I.O., Markov V.F. Surface topology, electrophysical properties and formation mechanism of tin(ii) sulfide thin films. *Nanosystems: Phys. Chem. Math.*, 2023, **14** (6), 699–704.

1. Introduction

Tin (II) sulfide (SnS) belongs to the family of binary semiconductor chalcogenides and occurs in nature in the form of mineral Herzenbergite. The crystal lattice of SnS consists of layers with a strong covalent intralayer Sn-S bonding and with a weak van der Waals interlayer interaction [1]. Effective technology for creating thin film solar cells requires semiconductor materials satisfying certain criteria. The chemical elements comprising a material must be relatively nontoxic, earth abundant and cheap. For high efficiency of solar energy conversion, the material of absorbing layer should have optimal value of optical band gap E_g, high optical absorption coefficient a, high quantum yield of excited charge carriers, large diffusion length of charge carriers and low recombination rate. SnS posseses a direct E_g of 1.2–1.5 eV, indirect E_g of 1.1 eV, large $\alpha > 10^4 - 10^5$ cm^{-1}, and high free carrier concentration around 10^{17} – 10^{18} cm^{-3}, hence, representing a promising material for the absorbing layer of new generation thin film solar cells [1–4].

In this paper, thin SnS films are synthesized by chemical bath deposition from aqueous solutions. The effect of deposition time on the microstructure of the resulting nanocrystalline films is demonstrated, the conductivity type and current sensitivity have been studied. Based on the atomic force microscopy data, a mechanism for the formation of a SnS film on a dielectric substrate is proposed. To substantiate the stoichiometry of chemical composition the quantum chemical calculations have been carried out.

2. Experimental

SnS films were obtained by chemical bath deposition from aqueous solutions using tin chloride $SnCl_2$, sodium thiosulfate $Na_2S_2O_3$ and sodium citrate $Na_3C_6H_5O_7$ (Na_3Cit). Deposition was carried out in a LOIP LT–112a thermostat at 343 K with an accuracy of $\pm 0.5^\circ$ in maintaining temperature. SnS films were deposited on sitall substrates during 30, 60, 90 and 120 minutes. The reaction baths contained 0.06 M $SnCl_2$, 0.15 M Na_3Cit and 0.06 M $Na_2S_2O_3$. The pH value was maintained in the range from 2.5 to 3.0.

TABLE 1. Characteristics of SnS thin films chemically deposited on sitall substrates from $SnCl_2$ and $Na_2S_2O_3$ aqueous solutions at 343 K

Synthesis time, min	Unit cell parameters			Average film thickness, nm	E_g, eV	j, nA/cm^2 at 10 V		
	a, Å	b, Å	c, Å			j_{light}	j_{dark}	j_{light}/j_{dark}
60	11.318(5)	3.9963(11)	4.2865(22)	210	0.94	58.83	32.90	1.79
90	11.3003(3)	3.9963(7)	4.2775(15)	480	1.01	139.60	88.15	1.58
120	11.282(4)	3.9957(6)	4.2807(15)	670	1.12	147.16	78.38	1.89

The crystal structure and phase composition of the films were studied using the X-ray diffractometer Stadi–P (Stoe) in the Bragg-Brentano geometry with CuK_α radiation in the angle range $2\theta = 5 - 100^\circ$ with a step of $\Delta(2\theta)^\circ = 0.03^\circ$ and 70 second exposure. The thickness of the films was determined using the Linnik MII-4M microinterferometer. The light transmission spectra were recorded using a UV-3600 spectrophotometer (Shimadzu, Japan) in the wavelength range of 200–1700 nm with a scanning step of 1 nm.

The morphological characteristics and elemental composition of the films were studied by scanning electron microscopy (SEM) on the TESCAN MIRA 3 LMU electron microscope (TESCAN, Czech Republic). The topology and surface roughness were studied by semi-contact atomic force microscopy (AFM) on the NT-MDT NTEGRA Prima II complex. A silicon cantilever with resonant frequency of 230 kHz and a radius of curvature of the probe less than 10 nm was used to scan the surface. To analyse the surface topology of the films, areas of SnS films with a size of 5×5 μm^2 were selected and captured from the total surface area of the sample. The AFM images were processed by the Gwyddion program.

The type of SnS films conductivity was determined by the thermal probe method. To register the sign of the thermoelectric force, the digital multimeter DT-830 B was used. The volt-ampere characteristics of the films were measured in both the dark room and as illuminated by a light beam from the solar radiation simulator Zolix GLORIA-X500A, equipped with an Osram XBO 500W/H OFR lamp, under standard conditions: AM1.5G spectrum, illumination 100 mW/cm^2, temperature 298 K. The magnitude of the current was recorded by the Keithley 2450 source measure unit.

The density-functional theory (DFT) calculations within periodic boundary conditions were performed using the SIESTA 4.0 package [5]. Generalized Gradient Approximation (GGA) with the Perdew-Burke-Ernzerhof (PBE) parametrization was employed for description of exchange-correlation potential. The core electrons were treated within the frozen core approximation, applying norm-conserving Troullier-Martins pseudopotentials. The double-ζ polarized basis set (DZP) was used for description of the valence orbitals of all elements.

3. Results and discussion

The X-ray diffraction spectra of SnS films revealed a set of reflexes typical for α-SnS (sp. gr. P*nma*). The unit cell parameters with corresponding standard quadratic deviations are given in Table 1. The experimental error is determined to be several times greater than indicated in parentheses, since the diffraction patterns of SnS overlap with patterns from several phases composing sitall substrate as well as due to the SnS peaks widening. The X-ray phase analysis did not reveal any tin-containing crystalline phase except α-SnS. The determination of the exact sizes of the coherent scattering regions (CSR) by the Williamson-Hall extrapolation method is rather evaluative due to the broadening anisotropy of the diffraction reflexes. The CSR average value is 26 nm for all synthesized films, which indicates the growth termination of the SnS single crystallites after 60 min of synthesis.

According to energy dispersive X-ray spectroscopic analysis (EDX), the elemental composition of the synthesized SnS films corresponds to the average contents of Sn and S as 40.3 and 41.1 at.%. The content of O is 18.6 at.% and it is due to surface oxygen. The etching of films with an argon beam allows to clean the surface of samples and get rid of oxygen almost completely (for example, down to $\sim$1 at.% after etching the film with an Ar+ beam to a depth of 6 nm).

According to SEM data, at the initial stage of synthesis (up to 30 min) the grain-like SnS particles of 300–400 nm in length and 50–100 nm in diameter are formed (Fig. 1a). These particles agglomerate into an insular film with a large number of voids and depressions. After 60 minutes, the number of loose large agglomerates with a Feret diameter of $\sim$1 microns, consisting of particles 200–300 nm in length and 50–100 nm in diameter (Fig. 1b), increases. Taking into account the average film thickness of $\approx$210 nm after 60 min (Table 1), these agglomerates should have a flat-like organization and cover the substrate in two-dimensional space. After 90 min of deposition, the film thickens, i.e. the individual large agglomerates are no longer visible, and the film becomes a structure formed from small elongated particles of $\sim$80–200 nm (Fig. 1c). At the end of synthesis (after 120 min), the SnS film completely covers the substrate and consists mainly of particles with linear sizes of 80–200 nm (Fig. 1d).

TABLE 2. Surface roughness parameters and fractal dimension of SnS films obtained by processing of AFM images with a surface area of 5×5 μm^2

Microrelief parameter		Deposition time, min			
		30	60	90	120
Arithmetic mean roughness R_a, nm		158.0	75.4	112.3	91.5
Root-mean-square roughness R_q, nm		194.4	97.2	142.6	115.1
The coefficient of asymmetry of the roughness profile R_{sk}		-0.4	0.1	-0.3	-0.2
Maximum profile height R_z, nm		506.5	393.3	440.3	322.0
Fractal dimension D_f of the surface	Cube counting method	2.35	2.31	2.35	2.38
	Triangulation method	2.44	2.42	2.44	2.48

Thus, with an increase in the synthesis duration, the amount of the SnS solid phase on the substrate increases, the SnS layers become denser, while the shape and size of grain-like SnS particles remain unchanged. The grain-like SnS particles are agglomerates consisting of nanoparticles ∼26 nm in size.

Fig. 2 shows typical AFM images of SnS films illustrating a significant difference in surface topology. The films are formed from agglomerates, the amount and shape of which depend on the deposition time. This is consistent with the SEM data (Fig. 1).

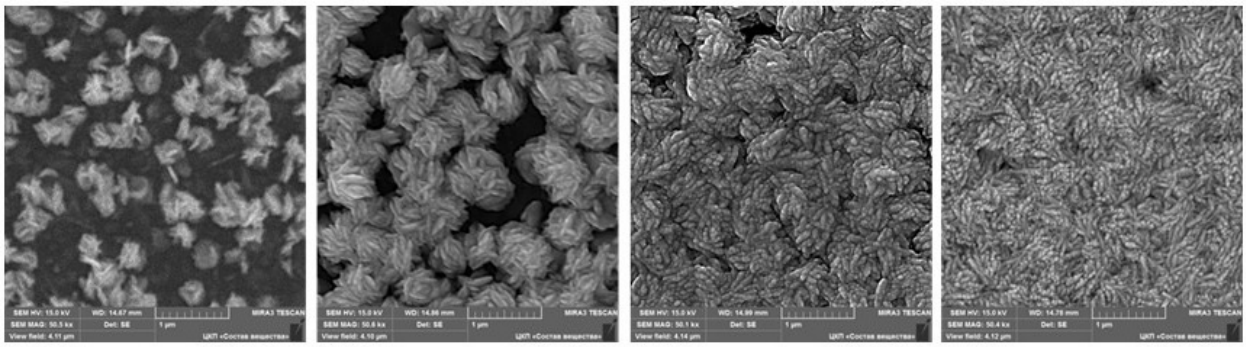

FIG. 1. Morphology evolution of SnS thin films on sitall substrate depending on the deposition time, min: a – 30; b – 60; c – 90; d – 120

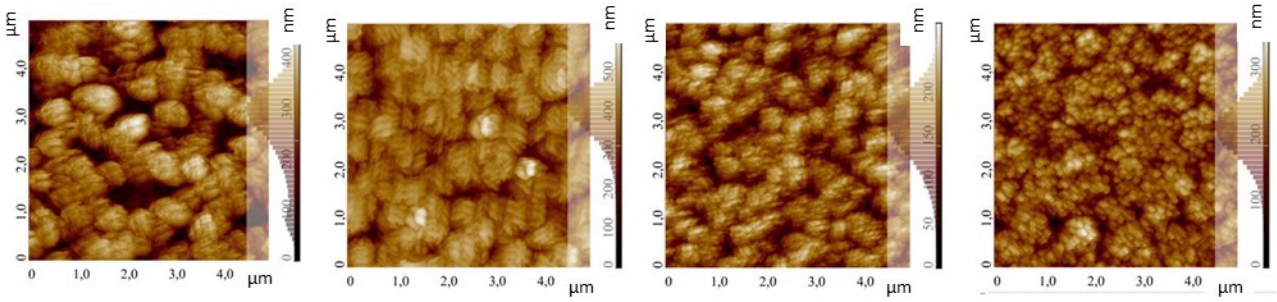

FIG. 2. Surface topology of the SnS thin films on sitall substrate depending on the deposition time, min: a – 30; b – 60; c – 90; d – 120. The dimension of AFM images is 5×5 μm^2

Table 2 presents the parameters describing the surface topology of the SnS films at different duration of synthesis. All samples are characterized by a sufficiently bright heterogeneity of the surface relief, as evidenced by the significant difference between the maximum height of the surface profile R_z and the parameters determining the arithmetic mean R_a and the root-mean-square Ra values of roughness.

The surface of the SnS films reveals a colloid microstructure from the first minutes of deposition. The colloidal particles are represented as the large agglomerates of nanoparticles (Fig. 1,2). Considering a colloidal particle as a fractal cluster (fractal agglomerate), the fractal geometry methods can be applied to describe the thin film microstructure [6–16]. Any fractal cluster as a geometric system is formed as a result of the association (adhesion) of solid particles, and the conditions of association affect the way of cluster growth [12]. The SEM and AFM data (Fig. 2,3) reveal the SnS fractal clusters look like disordered systems, but they may possess an internal order. The parameter characterizing this order numerically is the surface fractal dimension D_f [12]. The D_f values for SnS films are obtained by the processing of AFM images and are tabulated (Table 2). According to [8, 9, 11, 12], the obtained D_f values indicate that the formation of fractal clusters of SnS occurs in three-dimensional space, i.e. mainly within the solution volume according to the "cluster-particle" Witten-Sander model. The role of the free primary particles is performed by SnS nanoparticles.

At the first stage of film deposition, the formation of SnS nanoparticles takes place within the solution bulk. This process obeys the classical crystallization model: a fixed number of crystalline SnS nuclei arises in the supersaturated solution at the initial moment, then SnS nuclei grow to nanoparticles about 26 nm during the first 30 min. At the second stage, the grain-like clusters are formed as a result of collision and agglomeration of these nanoparticles. In the Witten-Sander model, the associating nanoparticles perform Brownian motion in the solution before collision resulting in a cluster. At the third stage, grain-like clusters are deposited on the substrate with film formation (Fig. 1,2). It should be noted that the processes of secondary nucleation due to high supersaturation is quite likely to take place in the solution. After 120 min of deposition, the grain-like clusters/agglomerates are arranged densely on the substrate (Fig. 2d), which excludes the possibility of linear motion trajectories or multiple collisions before sticking and reveals the kinetically controlled agglomeration [10]. This confirms the implementation of the Witten-Sander model. An invariability of D_f (Table 2) indicates that, regardless of the duration of deposition, the mechanism of film formation is preserved [15] and the film surface remains self-similar (self-affine [16]). Thus, the fractal approach provides a deeper understanding of the processes occurring during the formation of SnS thin film on a substrate [15].

The calculation of E_g for SnS was carried out for the case of indirect allowed transitions [6]. Extrapolation of the linear part of function $[\alpha h\nu]^{1/2} = C_2(h\nu - E_g)$ on the abscissa axis allowed to determine the E_g value. The E_g for films deposited after 60, 90 and 120 min are found equal to 0.94, 1.01 and 1.12 eV, respectively (Table 1), which is consistent with the previously published values [2–4].

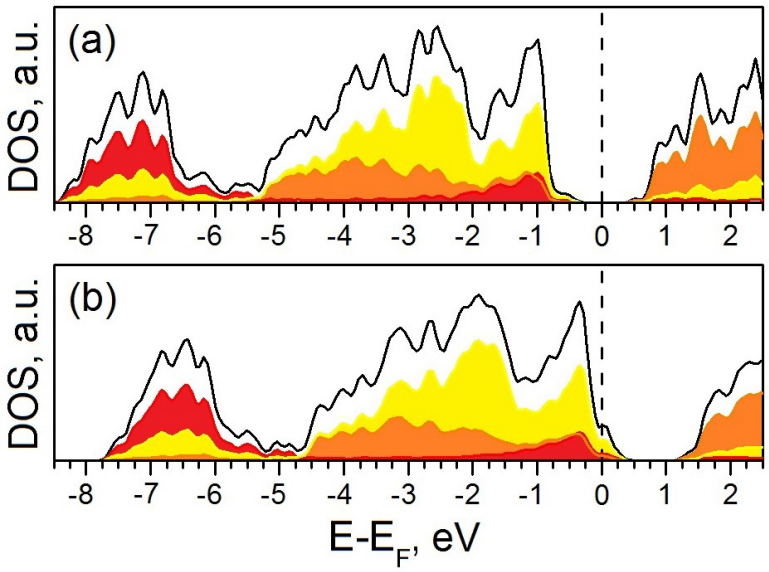

FIG. 3. The total and partial densities of electronic states (DOS) for a (001)SnS slab with perfect stoichiometry (a) or with the Sn atom vacancies in the bulk (b). The Sn5s-, Sn5p- and S3p-states are painted in red, orange and yellow, respectively. DFT GGA calculations

According to the thermo-EMF method, all synthesized SnS films have p-type conductivity. It is known that for binary tin sulfides with only intrinsic lattice defects, the n- or p-type of conductivity is determined by an excess of Sn or S atoms, respectively [7]. In this work, the role of tin vacancies in regulating the type of SnS conductivity is confirmed by DFT calculations of the electronic structure of α-SnS. $3a \times 3b$ supercell of (001)SnS slab of three molecular layers thick was employed as a model of nanoscale SnS. According to the calculations, such a "perfect" film is a semiconductor with the E_g value of at least 1.09 eV (Fig. 3a). The bottom of conduction band is represented by Sn5p-states, while the top of the valence band consists of S3p-states with an admixture of Sn5n and Sn5s-states. These basic features of the SnS electronic structure remain even after introduction of the Sn vacancies, both in the bulk and on the surface. However, the Fermi level

of SnS shifts to the edge of the valence band, which really corresponds to the change from the intrinsic conductivity to the p-type conductivity (Fig. 3b).

The resistivity of the obtained SnS films was studied both under lighting conditions and in the darkness. Fig. 4 shows the volt-ampere $j(U)$ characteristics of SnS thin films in the dark and while illuminated by a light beam of 100 mW/cm^2 at 298 K. A linear course of $j(U)$ curves passing through the origin is observed over the entire area of applied voltages, which indicates the ohmic nature of the obtained SnS films. After illumination of the film surface, the j increased due to the increase in the concentration of free charge carriers. The maximum photocurrent density under illumination $j_{light} = 147.16$ nA/cm^2 at 10 V is observed for SnS film obtained after 120 min, and the maximum value of the dark current density $j_{dark} = 88.15$ nA/cm^2 is found for SnS film after 90 min of synthesis (Table 1).

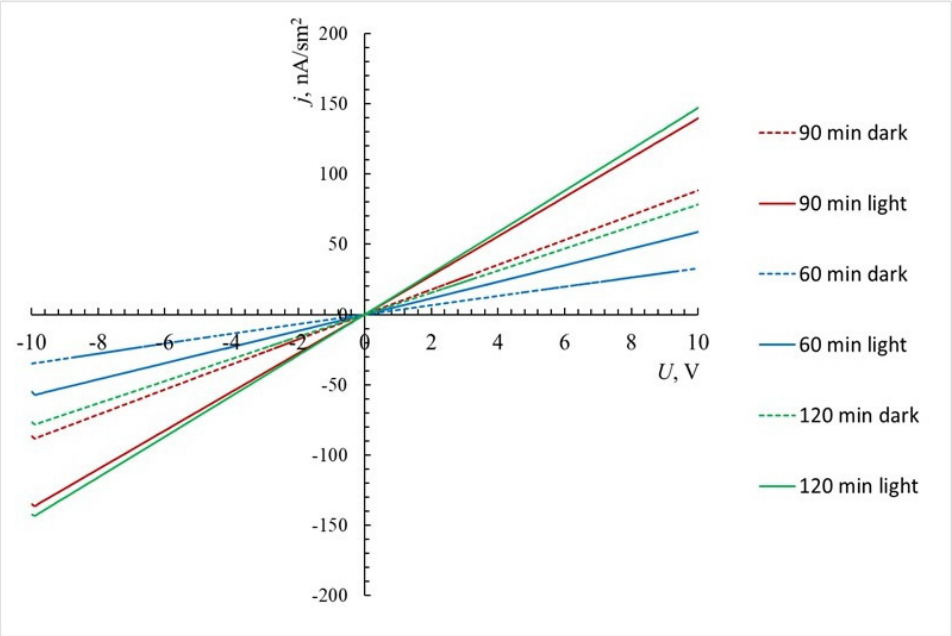

FIG. 4. Current-voltage characteristics of SnS films on sitall substrates at different deposition times either in the dark room or under illumination by a light beam of 100 mW/cm^2 (light)

For the film deposited after 30 min, the values of j_{light} and j_{dark} are close to zero (Table 1), which indicates the absence of photosensitive properties. The latter is related to the morphology of SnS (Fig. 1,2): the layer after 30 min is formed from individual agglomerates and has an insular character, strong difference in the profile height (200 ± 150 nm) and significant roughness (Table 2). SnS films deposited after 60 and 120 min possess the highest values of the ratio j_{light}/j_{dark}, which are 1.8 and 1.9, respectively (Table 1). At the same time, these films have the lowest values of the arithmetic mean roughness $R_a = 75.4$ and 91.5 nm (Table 2), respectively. The thickness of these films varies in the range from 210 to 670 nm. Thus, the continuity and roughness of the substrate coating do affect primarily the value of j_{light}/j_{dark}, while no noticeable effect of the film thickness on the value of j_{light}/j_{dark} was found. To obtain the photosensitive layers based on SnS, solid films with a minimal roughness and with a thickness of at least 200 nm should be deposited.

4. Conclusion

Thin films of α-SnS were obtained by chemical deposition from aqueous solutions. The effect of the deposition time on their microstructure and their surface topology is presented. The volt-ampere characteristics revealed the optimal film thickness of at least 200 nm for obtaining photosensitive layers. The synthesized films possess a superstoichiometric composition of $S \approx 1$ at.%. Quantum-chemical calculations confirm the role of Sn vacancies as the main progenitors of observed p-type conductivity of SnS films. The formation mechanism of a thin SnS film on a dielectric substrate proceeds according to the "cluster-particle" model, and the formation of initial fractal clusters of SnS occurs in three-dimensional space, i.e. within the solution bulk.

References

[1] Brent J.R., Lewis D.J., Lorenz T., Lewis E.A., Savjani N., Haigh S.J., Seifert G., Derby B., O'Brien P. Tin(II) Sulfide (SnS) Nanosheets by Liquid-Phase Exfoliation of Herzenbergite: IV-VI Main Group Two-Dimensional Atomic Crystals. *J. Am. Chem. Soc.*, 2015, **137**(39), P. 12689–12696.

[2] Banai R.E., Horn M.W., Brownson J.R.S. A review of tin(II) monosulfide and its potential as a photovoltaic absorber. *Solar Energy Materials & Solar Cells*, 2016, **150**, P. 112–129.

[3] Sinsermsuksakul P., Heo J., Noh W., Hock A.S., Gordon R.G. Atomic layer deposition of tin monosulfide thin films. *Adv. Energy Mater.*, 2011, **1**, P. 1116–1125.
[4] Reddy K.T.R., Reddy N.K., Miles R.W. Photovoltaic properties of SnS based solar cells. *Sol. Energy Mater. Sol. Cells*, 2006, (90), P. 3041–3046.
[5] García A., Papior N., Akhtar A., Artacho E., Blum V., Bosoni E., Brandimarte P., Brandbyge M., Cerdá J.I., Corsetti F., Cuadrado R., Dikan V., Ferrer J., Gale J., García-Fernández P., García-Suárez V.M., García S., Huhs G., Illera S., Korytár R., Koval P., Lebedeva I., Lin L., López-Tarifa P., Mayo S.G., Mohr S., Ordejón P., Postnikov A., Pouillon Y., Pruneda M., Robles R., Sánchez-Portal D., Soler J.M., Ullah R., Yu V.W., Junquera J.J. Siesta: Recent developments and applications. *J. Chem. Phys.*, 2020, **152**, P. 204108.
[6] Titova L.V., Fregoso B.M., Grimm R.L. Chapter 5: Group-IV monochalcogenides GeS, GeSe, SnS, SnSe, in book Chalcogenide: From 3D to 2D and Beyond. *Woodhead Publishing Series in Electronic and Optical Materials*, 2020, P. 119–151.
[7] Vidal J., Lany S., d'Avezac M., Zunger A., Zakutaev A., Francis J., Tate J. Band-structure, optical properties, and defect physics of the photovoltaic semiconductor SnS. *Applied Physics Letters*, 2012, **100**(3), P. 032104.
[8] Roldughin V.I. Fractal structures in disperse systems. *Russian Chemical Reviews*, 2003, **72**(10), P. 823–847.
[9] Roldughin V.I. The characteristics of fractal disperse systems. Russian Chemical Reviews, 2003, **72**(11), P. 913–937.
[10] Samsonov V.M., Kuznetsova Y.V., D'yakova E.V. Fractal properties of aggregates of metal nanoclusters on solid surface. *Russian Journal of Applied Physics*, 2016, **86**(2), P. 71–77.
[11] Feder E. *Fractals*. Moscow: Mir, 1991, 260 p. (In Russian).
[12] Smirnov B.M. Physics of fractal clusters. Moscow: Nauka, 1991. 136 p, (In Russian).
[13] Antonov A.S., Sdobnyakov N.Y., Ivanov D.V., Podbolotov K.B. Morphology investigation study of the copper films relief on a mica surface. Fiziko-khimicheskie aspekty izucheniya klasterov, nanostruktur i nanomaterialov [Physical and chemical aspects of the study of clusters, nanostructures and nanomaterials], 2017, **9**, P. 19–26, (In Russian).
[14] Sdobnyakov N.Y., Antonov A.S., Ivanov D.V. Morphological characteristics and fractal analysis of metal films on dielectric surfaces. Tver: Tver State University, 2019, 168 p, (In Russian).
[15] Brylkin Y.V., Kustov A.L.Correlation between fractal dimension and different roughness for copper samples. *Fiziko-khimicheskie aspekty izucheniya klasterov, nanostruktur i nanomaterialov* [Physical and chemical aspects of the study of clusters, nanostructures and nanomaterials], 2013, **5**, P. 33–38, (In Russian).
[16] Panin A.V., Shugurov A.R. Application of fractal description for image analysis in scanning probe microscopy. *Poverkhnost* [Surface], 2003, 6, P. 62–69, (In Russian).

Submitted 17 October 2023; revised 25 October 2023; accepted 8 November 2023

Information about the authors:

N. S. Kozhevnikova – Institute of Solid State Chemistry of the Ural Branch of RAS, Ekaterinburg, Russia; kozhevnikova@ihim.uran.ru

L. N. Maskaeva – Ural Federal University, Ekaterinburg, Russia; larisamaskaeva@yandex.ru

A. N. Enyashin – Institute of Solid State Chemistry of the Ural Branch of RAS, Ekaterinburg, Russia; enyashin@ihim.uran.ru

A. P. Tyutyunnik – Institute of Solid State Chemistry of the Ural Branch of RAS, Ekaterinburg, Russia; tyutyunnik@ihim.uran.ru

O. A. Lipina – Institute of Solid State Chemistry of the Ural Branch of RAS, Ekaterinburg, Russia; lipinaolgaa@yandex.ru

I. O. Selyanin – Institute of Solid State Chemistry of the Ural Branch of RAS, Ekaterinburg, Russia; sioprostreet@mail.ru

V. F. Markov – Ural Federal University, Ekaterinburg, Russia; v.f.markov@urfu.ru

Conflict of interest: the authors declare no conflict of interest.

NANOSYSTEMS:
PHYSICS, CHEMISTRY, MATHEMATICS

Original article

Chebanenko M.I., et al. *Nanosystems: Phys. Chem. Math.*, 2023, **14** (6), 705–712.
http://nanojournal.ifmo.ru
DOI 10.17586/2220-8054-2023-14-6-705-712

Planetary grinding's impact on the structure and photocatalytic characteristics of urea-derived g-C_3N_4 nanocrystals

Maria I. Chebanenko[1], Lev A. Lebedev[1], Maksim I. Tenevich[1], Ekaterina Yu. Stovpiaga[1], Vadim I. Popkov[1]

[1]Ioffe Institute, St. Petersburg, Russia

Corresponding author: Maria I. Chebanenko, m_chebanenko@list.ru

PACS 61.43.Gt, 61.46.+w

ABSTRACT The burgeoning interest in two-dimensional materials derived from graphite carbon nitride (g-C_3N_4) stems from its non-toxicity, exceptional charge carrier mobility, and UV-vis absorption capabilities. Crucially, g-C_3N_4's performance hinges on its specific surface area. We investigate how planetary grinding impacts the crystal and electronic structures of g-C_3N_4 nanocrystals. Six samples, subjected to varying durations of mechanical treatment, underwent comprehensive characterization using a complex of physico-chemical methods. Notably, planetary grinding substantially increases the specific surface area of g-C_3N_4 nanocrystals while preserving their electronic structure. Furthermore, we assessed the photocatalytic performance of these samples in decomposing antibiotics under visible light. The nanocrystalline powder with an enhanced specific surface area demonstrated a remarkable efficiency in tetracycline hydrochloride decomposition. In summary, our study highlights the potential of planetary grinding as a means to augment g-C_3N_4's specific surface area, positioning it as a promising platform for the development of contemporary, eco-friendly photocatalysts.

KEYWORDS g-C_3N_4, graphitic carbon nitride, two-dimensional structures, mechanical processing, photocatalysis

ACKNOWLEDGEMENTS This work was supported by the Russian Science Foundation (project No. 23-23-00328).

FOR CITATION Chebanenko M.I., Lebedev L.A., Tenevich M.I., Stovpiaga E.Yu., Popkov V.I. Planetary grinding's impact on the structure and photocatalytic characteristics of urea-derived g-C_3N_4 nanocrystals. *Nanosystems: Phys. Chem. Math.*, 2023, **14** (6), 705–712.

1. Introduction

The rapid expansion of the pharmaceutical industry, characterized by the continuous development and large-scale production of medicinal products, has brought about a pressing need for the safe disposal of industrial wastewater [1–4]. Presently, the photocatalytic oxidation of pharmaceutical compounds under solar irradiation has emerged as a promising and eco-friendly method for treating wastewater generated during pharmaceutical manufacturing processes [5–8]. This technique harnesses the synergistic interplay of a photocatalyst and visible light. By absorbing photons, the photocatalyst generates electron-hole pairs, which actively engage in subsequent reactions. These reactions culminate in the production of potent oxidizing agents that effectively degrade organic contaminants.

Many established photocatalysts primarily function within the ultraviolet domain of the electromagnetic spectrum are often composed of costly elements [9–11]. Consequently, the scientific community has turned its attention to graphitic carbon nitride (g-C_3N_4) in recent years. g-C_3N_4 stands out as a semiconductor material comprised of readily available chemical components, exhibiting remarkable chemical stability and the capacity to absorb visible light [7, 10, 12]. However, the photocatalytic performance of this material is constrained by its relatively modest specific surface area and a propensity for rapid charge carrier recombination [2].

To address this limitation, researchers have explored various strategies for exfoliating bulk graphitic carbon nitride into nanosheets. This exfoliation process enhances both the specific surface area and the number of active sites on g-C_3N_4, thereby reducing volumetric charge carrier recombination [13]. For example, a study outlined in [14] introduces a thermal exfoliation method conducted at 550 °C for 1 – 3 hours, resulting in an increased specific surface area and improved photocatalytic capabilities for NO removal under visible light. Research detailed in [15] describes the successful exfoliation of g-C_3N_4 using sulfuric acid for 8 hours, followed by ultrasonic treatment, rendering the material suitable for use as a photocatalyst in hydrogen evolution reactions. An effective approach to ultrasonic exfoliation of g-C_3N_4 is proposed in [16], where bulk g-C_3N_4 powder, dispersed in a N-Methyl pyrrolidone (NMP) solution, is subjected to ultrasonic treatment, yielding nanosheets suitable for photocatalytic hydrogen production. Additionally, article [12] highlights the beneficial impact of steam exfoliation on the electrochemical properties of g-C_3N_4. Nevertheless, all these

methods are characterized by their complex and time-consuming procedures, reliance on expensive chemical reagents, and the need for specialized equipment.

The present study introduces a promising approach to exfoliate bulk graphitic carbon nitride utilizing mechanical forces in a planetary mill. The investigation shows the influence of the duration of mechanical treatment on the crystalline and electronic structure of the resultant g-C_3N_4. Notably, it is revealed that the mechanical grinding exerts a positive impact on the specific surface area. The study culminates in a photocatalytic assessment involving the oxidation of tetracycline hydrochloride under visible light. The research findings strongly suggest that exfoliation via a planetary mill holds significant potential for enhancing the photocatalytic activity of graphitic carbon nitride. This, in turn, opens up promising avenues for the utilization of such materials as the foundation for catalysts employed in the neutralization of hazardous compounds present in pharmaceutical wastewater.

2. Materials and methods

2.1. Materials

Urea (99.8 %, CH_4N_2O) was purchased from NevaReaktiv. Tetracycline hydrochloride (95 %, $C_{22}H_{24}N_2O_8{\cdot}HCl$) was obtained from neoFroxx. All the reagents used in this research work are analytical grade. Deionized water was obtained from the analytical laboratory.

2.2. Synthesis of g-C_3N_4 nanopowder

To obtain graphitic carbon nitride, urea powder was placed in a quartz crucible. Thermal polymerization was conducted for 1 hour at a temperature of 550 °C in an ambient air atmosphere. The yield of the target product when using urea as a precursor was 2 % by mass [17, 18].

The resulting powder was divided into 6 portions for subsequent grinding. 1 gram of the sample, along with 10 mL of ethanol and 7 agate balls, were loaded into a 30 mL capacity ball mill jar. The duration of mechanical treatment varied from 30 to 150 minutes, and the milling was performed at a drum rotation speed of 300 revolutions per minute. The obtained suspensions were dried at 100 °C until complete removal of ethanol. As a result, a series of six samples was obtained, differing in the duration of planetary milling (CN-0, CN-30, CN-60, CN-90, CN-120, and CN-150).

2.3. Physico-chemical characterization

Structural changes of the g-C_3N_4 sample during grinding were recorded by Shimadzu XRD-6000 X-ray diffractometer equipped (CuKα radiation, $\lambda = 0.154051$ nm) in the range 5 – 80° (2θ) with a scanning step of 0.01° and integration time for each point 1 s. The average size of the crystallites was estimated using Debye–Scherrer's equation [19]:

$$D = \frac{0.94 \cdot \lambda}{\beta \cdot \cos\theta},$$

where λ is the wavelength of the incident radiation (CuK$\alpha = 0.154$ nm); β is the full width at half maximum in radians; θ is the Bragg angle in radians [19].

The degree of crystallinity of the samples was calculated based on the analysis of X-ray diffraction pattern profile:

$$\text{Crystallinity degree } = \frac{\text{Area of all the crystalline peaks}}{\text{Area of all the crystalline and amorpous peaks}}.$$

The nanopowder morphology was examined through scanning electron microscopy (SEM) using a Tescan Vega 3 SBH scanning electron microscope.

N_2 adsorption-desorption measurements were conducted with an 3FLEX Surface Area and Porosity Analyzer at a standard mode, at a temperature of 77 K. The specific surface area was calculated using the Brunauer–Emmett–Teller (BET) method. Pore size distribution plots were generated from the desorption branch of the isotherm using the Barrett–Joyner–Halenda (BJH) method.

Diffuse reflection spectra were acquired at room temperature within the 350 – 700 nm range using an Avaspec-ULS2048CL-EVO spectrometer equipped with an AvaSphere-30-REFL refractometric integration sphere. The obtained diffuse reflection spectra were analyzed using the Kubelka–Munk function [7, 20]:

$$F(R) = \frac{(1-R)^2}{2R},$$

where R represents the diffuse reflection of the sample.

To determine the values of the optical bandgap, the Tauc plot was utilized:

$$h\upsilon \cdot F(R)^{1/n} = A(h\upsilon - E_g),$$

where A is the proportionality coefficient, n is the power index indicating the nature of the transition, $h\upsilon$ is the photon energy, and E_g is the optical bandgap.

2.4. Photocatalytic measurements

Tetracycline hydrochloride (TCHCl) was selected as the model antibiotic, with an initial solution concentration of 0.03 g/L. A 1 mg quantity of catalyst powder was thoroughly dispersed in the initial antibiotic solution and placed within a 10 mL capacity photocatalytic reactor cuvette. The solution was then stirred in the dark for 1 hour to establish an adsorption-desorption equilibrium.

Subsequently, the solution was exposed to LEDs with a power consumption of 24 W and a peak wavelength of 405 nm, while being continuously stirred under visible radiation. In-situ measurements were conducted using an Avaspec-ULS2048CL-EVO spectrometer equipped with an Avalight-XE Pulsed Xenon Lamp.

The degree of antibiotic decomposition under the influence of visible radiation in the presence of the catalyst was determined using the following formula:

$$\text{Rem. Eff.} = \frac{(C_0 - C)}{C_0} \cdot 100\ \%,$$

where C_0 represents the initial concentration of the TCHCl solution, and C is the concentration of the TCHCl solution after exposure to light.

3. Results and discussion

3.1. Powder X-ray diffraction

The crystalline structure and phase purity of the prepared series of samples were confirmed through X-ray phase analysis. Fig. 1(a) illustrates diffraction patterns for the initial CN-0 sample and samples subjected to mechanical grinding with varying durations (CN-30, CN-60, CN-90, CN-120, and CN-150). All obtained graphs exhibit a typical pattern for graphitic carbon nitride.

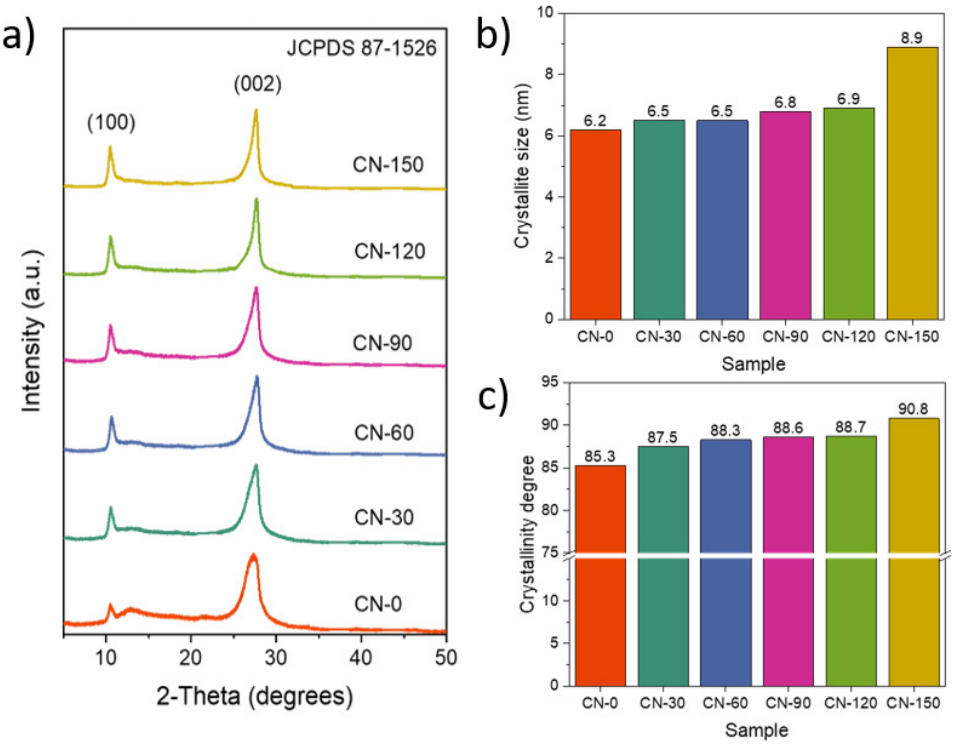

FIG. 1. (a) Powder X-ray diffraction patterns; (b) crystallinity degree and (c) crystallite size of CN-0, CN-30, CN-60, CN-90, CN-120 and CN-150 samples

The X-ray diffraction patterns display two prominent reflections at approximately 13° and 27°, corresponding to the diffraction planes (100) and (002), respectively (JCPDS card 87-1526) [21, 22].

The concurrent increase in X-ray reflection intensity and reduction in their width as grinding time increases may indicate an expansion of the coherent scattering domain. The average crystallite size, determined along the crystallographic direction (002), is presented in Fig. 1(b) as a bar chart.

Considering that nanocrystalline graphitic carbon nitride comprises a plethora of irregularly shaped and randomly oriented flakes, it is posited that mechanical treatment induces the ordering and straightening of the edges of individual nanosheets. This phenomenon suggests a transition towards a more planar configuration, as supported by the heightened degree of crystallinity observed in the samples (Fig. 1(c)).

3.2. Scanning electron microscopy

The alterations in the morphology of graphitic carbon nitride due to the impact of planetary milling were documented using scanning electron microscopy (SEM). In Fig. 2(a), the original graphitic carbon nitride powder is depicted as consisting of randomly oriented two-dimensional sheets with irregular edges. Mechanical treatment induces a transformation in the shape of these sheets, accompanied by their partial agglomeration.

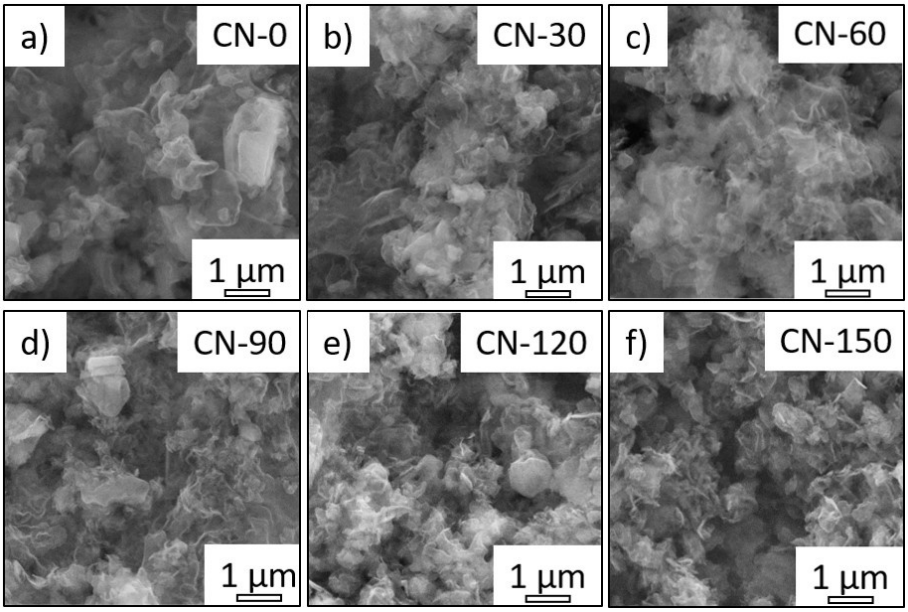

FIG. 2. SEM images of (a) CN-0; (b)CN-30; (c) CN-60; (d) CN-90; (e) CN-120 and (f) CN-150 nanopowders

3.3. N_2 adsorption-desorption analysis

The textural characteristics of the CN-0, CN-30, CN-60, CN-60, CN-90, CN-120, and CN-150 samples were investigated using the low-temperature nitrogen adsorption-desorption method. The resulting isotherms, as depicted in Fig. 3(a), are classified as Type IV, indicating the mesoporous nature of this material. Notably, the hysteresis loops displayed pronounced features associated with the capillary condensation of gas within the mesopores. This behavior is indicative of mesoporous structures.

Further analysis, as shown in Fig. 3(b), through pore size distribution plotting, confirms the presence of pores with diameters falling within the range of 2 – 50 nm. It is noteworthy that the porosity of the samples experiences a marginal increase during the planetary milling process, primarily attributed to the creation of additional interlayer space within the graphitic carbon nitride material, as evidenced in Fig. 3(c).

The specific surface area was determined using the linear form of the BET equation, and the resulting specific surface area values are illustrated in Fig. 3(c). It is evident that consecutive increases in specific surface area values occur during the grinding process in the planetary mill.

Graphitic carbon nitride is characterized by a layered structure comprising tri-s-triazine units, as depicted in Fig. 4 [23]. These layers in g-C_3N_4 are weakly bonded together by van der Waals forces, facilitating easy exfoliation and, consequently, an increase in the available surface area for sorption. It is postulated that the sequential rise in specific surface area values is achieved by reducing the stack thickness (h) during mechanical treatment. Prolonged mixing in the planetary mill leads to partial particle agglomeration, resulting in a further decrease in specific surface area and an increase in stack thickness.

3.4. Diffuse reflectance spectroscopy

The optical properties of the sample series were investigated through diffuse reflectance spectroscopy. In Fig. 5(a), absorption spectra within the UV-visible range are presented for the CN-0, CN-30, CN-60, CN-90, CN-120, and CN-150 samples. The results reveal that the grinding process in the planetary mill leads to a shift in the absorption edge towards the visible spectrum ($\lambda \geq 400$ nm). This observed "redshift" effect signifies an enhanced light absorption capability of graphitic carbon nitride within the visible portion of the spectrum, resulting in an increased generation of electron-hole pairs.

To determine the optical bandgap width for the samples, Tauc plots were constructed. Fig. 5(b) illustrates the spectral dependencies $[R(F)h\nu]^{1/2}$ derived from the obtained spectral absorption coefficient data. The bandgap width values were obtained through extrapolation of the linear region of the spectrum to the abscissa axis. As anticipated, there were

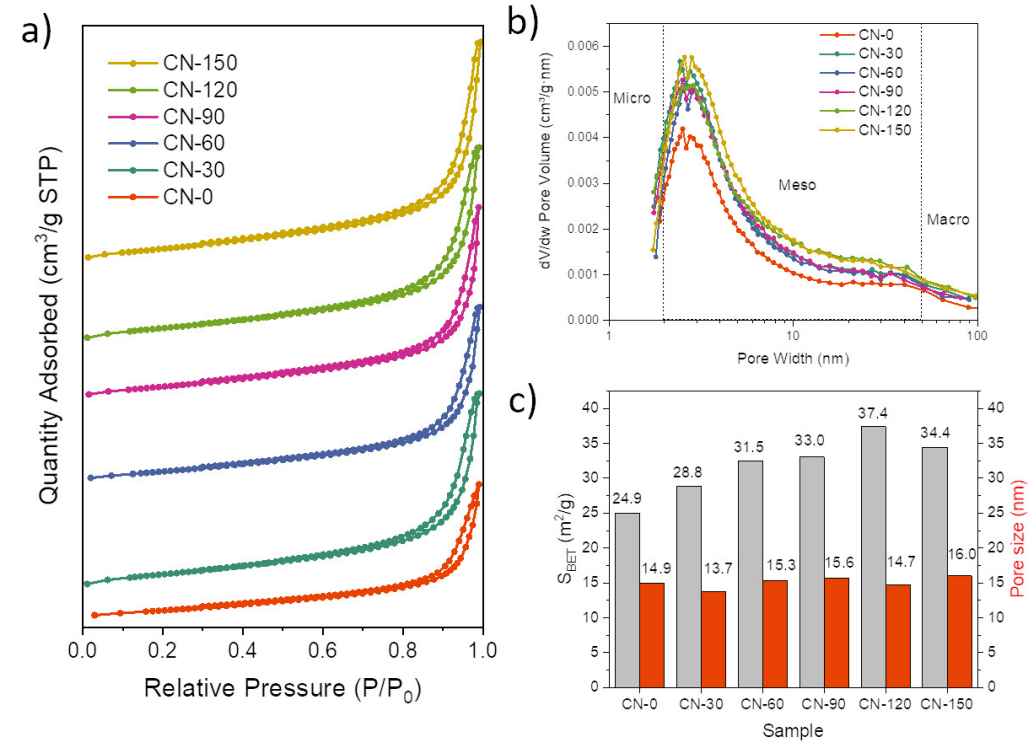

FIG. 3. (a) Nitrogen adsorption-desorption isotherms; (b) the pore size distribution results calculated from the BJH desorption pore volume data; (c) BET surface area and pore size of CN-0, CN-30, CN-60, CN-90, CN-120 and CN-150 samples

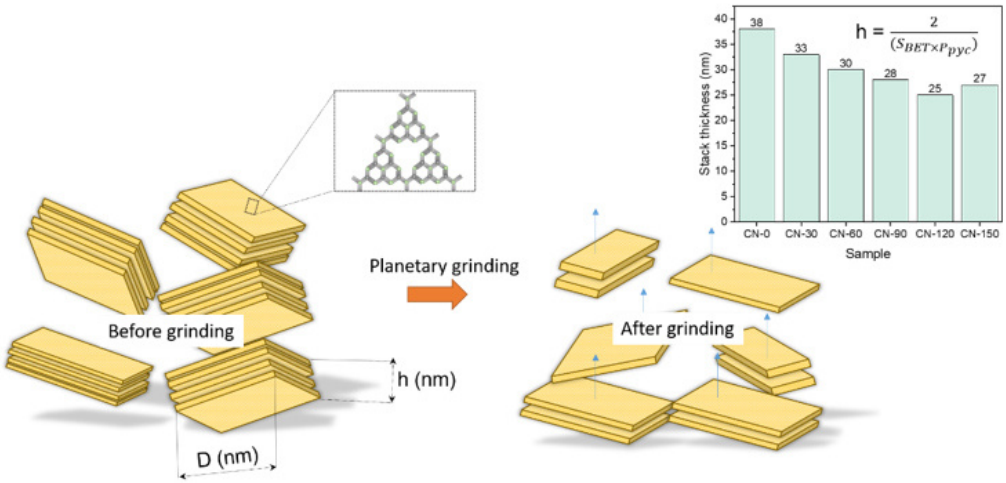

FIG. 4. Schematic representation of the mechanical grinding process

no substantial alterations in the electronic structure after mechanical grinding. The optical bandgap width for the sample series exhibited variations within the range of 3.84 – 3.85 eV.

3.5. Photocatalytic test

The influence of mechanical grinding on the photocatalytic performance of graphitic carbon nitride was evaluated during the oxidation of tetracycline hydrochloride under visible light ($\lambda = 405$ nm). The photocatalytic experiment was preceded by a dark control test. Solutions containing specified quantities of CN-0, CN-30, CN-60, CN-90, CN-120, and CN-150 powders were agitated in darkness for 15 minutes to establish an adsorption equilibrium. Additionally, a control solution of tetracycline hydrochloride was exposed to visible light to rule out the possibility of its spontaneous degradation under illumination. Fig. 6(a) illustrates the representative absorption spectra of tetracycline hydrochloride recorded over a 60-minute duration in the presence of the CN-150 sample. Fig. 6(b) depicts the concentration ratios

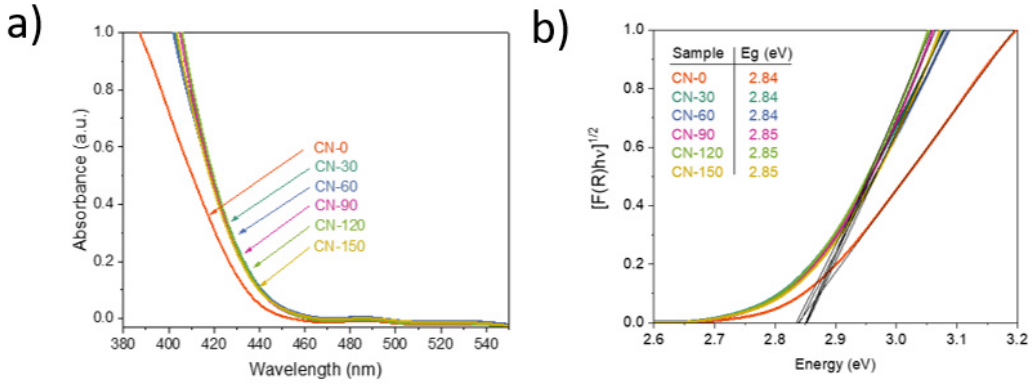

FIG. 5. (a) UV-vis diffuse reflectance spectroscopy; (b) Tauc plots of CN-0, CN-30, CN-60, CN-90, CN-120 and CN-150 samples

(C/C_0). It is evident that the duration of mechanical treatment on the nanocrystalline graphitic carbon nitride powder exerts a favorable influence on its photocatalytic activity.

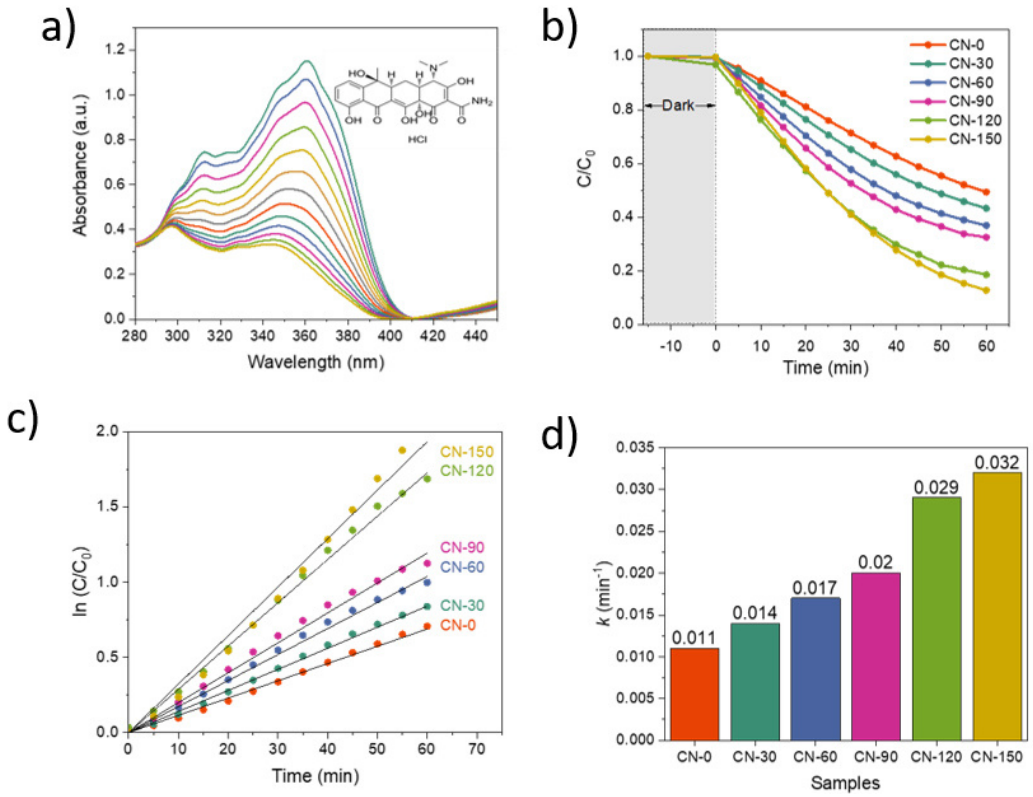

FIG. 6. (a) The decomposition spectrum of tetracycline hydrochloride in the presence of CN-150; (b) photocatalytic degradation curves of TCHCl; (c) pseudo-first-order kinetic curves of the samples; (d) the calculated kinetic constants

To quantitatively assess the catalytic activity, the apparent first-order rate constant was determined by plotting the natural logarithm of (C/C_0) against the duration of the photocatalytic experiment. The resulting values are presented as a bar chart in Fig. 6(d). It was ascertained that this exfoliation method engenders a threefold enhancement in the photocatalytic capabilities of the material.

The findings affirm a consistent augmentation in photocatalytic activity with prolonged mechanical exfoliation time. It is notable that the most significant increase in photocatalytic activity is observed for the CN-120 sample, characterized by the highest specific surface area and the thinnest stack thickness of graphitic carbon nitride. It is postulated that further extension of the mechanical treatment may lead to a gradual reduction in photocatalytic activity due to the re-agglomeration of g-C_3N_4 nanolayers.

4. Conclusions

The original nanocrystalline powder of graphitic carbon nitride was synthesized via the thermal polymerization of urea at 550 °C in an ambient air atmosphere. Subsequently, the resulting calcined powder underwent mechanical grinding in a planetary mill for various durations, ranging from 0 to 150 minutes. This extended mechanical treatment led to a notable improvement in the powder's crystallinity, concomitant with the straightening and ordering of the nanosheets comprising the graphitic carbon nitride. Notably, there was an expansion in the coherent scattering domain as the synthesis temperature increased. Remarkably, the electronic structure of the powder remained largely unaltered, with the bandgap width consistently hovering around 2.8 eV for both the initial and processed samples.

The specific surface area values exhibited a progressive increase, ranging from 24.9 to 37.4 m^2/g with a grinding time of 120 minutes. However, when subjected to prolonged mechanical treatment beyond 120 minutes, re-agglomeration occurred, resulting in a reduction in the specific surface area to 34.4 m^2/g.

The photocatalytic activity of the obtained powders was assessed through the photocatalytic oxidation of tetracycline hydrochloride. The study demonstrated that planetary milling facilitated the production of graphitic carbon nitride powder with significantly enhanced photocatalytic properties. This enhancement was evident in the threefold increase in the degradation rate constant of the antibiotic under solar light exposure.

Consequently, this investigation has underscored the viability of developing an efficacious and environmentally sustainable foundation for photocatalytic materials rooted in graphitic carbon nitride, which holds promise for the removal of hazardous organic pollutants from pharmaceutical wastewater.

References

[1] Caban M., Stepnowski P. How to Decrease Pharmaceuticals in the Environment? A Review. *Environ. Chem. Lett.*, 2021, **19**, P. 3115–3138.

[2] Abdel S.M., Gad-allah T.A., El-Shahat M.F., Ashmawy A.M., Ibrahim H.S. Novel Application of Metal-Free Graphitic Carbon Nitride (g-C_3N_4) in Photocatalytic Reduction – Recovery of Silver Ions. *J. of Environmental Chemical Engineering*, 2016, **4**, P. 4165–4172.

[3] Sammut Bartolo N., Azzopardi L.M., Serracino-Inglott A. Pharmaceuticals and the Environment. *Early Hum. Dev.*, 2021, **155**, P. 39–42.

[4] Paut Kusturica M., Jevtic M., Ristovski J.T. Minimizing the Environmental Impact of Unused Pharmaceuticals: Review Focused on Prevention. *Front. Environ. Sci.*, 2022, **10**, P. 1–8.

[5] Rapti I., Kourkouta T., Malisova E.M., Albanis T., Konstantinou I. Photocatalytic Degradation of Inherent Pharmaceutical Concentration Levels in Real Hospital WWTP Effluents Using g-C_3N_4 Catalyst on CPC Pilot Scale Reactor. *Molecules*, 2023, **28** (3), 1170.

[6] Song J., Zhao K., Yin X., Liu Y., Khan I., Wang K. Photocatalytic Degradation of Tetracycline Hydrochloride with g-C_3N_4/Ag/AgBr Composites. *Front. Chem.*, 2022, **10**, 1069816.

[7] García-López E.I., Pomilla F.R., Bloise E., Lü X., Mele G., Palmisano L., Marcì G. C_3N_4 Impregnated with Porphyrins as Heterogeneous Photocatalysts for the Selective Oxidation of 5-Hydroxymethyl-2-Furfural Under Solar Irradiation. *Top. Catal.*, 2021, **64**, P. 758–771.

[8] Rodríguez-López L., Santás-Miguel V., Cela-Dablanca R., Núnez-Delgado A., Álvarez-Rodríguez E., Pérez-Rodríguez P., Arias-Estévez M. Ciprofloxacin and Trimethoprim Adsorption/Desorption in Agricultural Soils. *Int. J. Environ. Res. Public Health*, 2022, **19** (14), 8426.

[9] Seroglazova A.S., Chebanenko M.I., Popkov V.I. Synthesis, Structure, and Photo-Fenton Activity of $PrFeO_3$–TiO_2 Mesoporous Nanocomposites. *Condens. Matter Interphases*, 2021, **23**, P. 548–560.

[10] Zhurenok A.V., Vasichenko D.B., Berdyugin S.N., Gerasimov E.Yu., Saraev A.A., Cherepanova S.V., Kozlova E.A. Photocatalysts Based on Graphite-like Carbon Nitride with a Low Content of Rhodium and Palladium for Hydrogen Production under Visible Light. *Nanomaterials*, 2023, **13**, 2176.

[11] Gupta B.K., Kedawat G., Agrawal Y., Kumar P., Dwivedi J., Dhawan S.K. A Novel Strategy to Enhance Ultraviolet Light Driven Photocatalysis from Graphene Quantum Dots Infilled TiO_2 Nanotube Arrays. *RSC Adv.*, 2015, **5**, P. 10623–10631.

[12] Chebanenko M.I., Omarov S.O., Lobinsky A.A., Nevedomskiy V.N., Popkov V.I. Steam Exfoliation of Graphitic Carbon Nitride as Efficient Route toward Metal-Free Electrode Materials for Hydrogen Production. *Int. J. Hydrogen Energy*, 2023, **48**, P. 27671–27678.

[13] Rodionov I.A., Zvereva I.A. Photocatalytic Activity of Layered Perovskite-like Oxides in Practically Valuable Chemical Reactions. *Russ. Chem. Rev.*, 2016, **85**, P. 248–279.

[14] Papailias I., Todorova N., Giannakopoulou T., Ioannidis N., Boukos N., Athanasekou C.P., Dimotikali D., Trapalis C. Chemical vs Thermal Exfoliation of g-C_3N_4 for NOx Removal under Visible Light Irradiation. *Appl. Catal. B Environ.*, 2018, **239**, P. 16–26.

[15] Xu J., Zhang L., Shi R., Zhu Y. Chemical Exfoliation of Graphitic Carbon Nitride for Efficient Heterogeneous Photocatalysis. *J. Mater. Chem. A*, 2013, **1**, P. 14766–14772.

[16] Yuan Y.J., Shen Z., Wu S., Su Y., Pei L., Ji Z., Ding M., Bai W., Chen Y., Yu Z.T. Liquid Exfoliation of g-C_3N_4 Nanosheets to Construct 2D-2D MoS2/g-C_3N_4 Photocatalyst for Enhanced Photocatalytic H_2 Production Activity. *Appl. Catal. B Environ.*, 2019, **246**, P. 120–128.

[17] Chebanenko M.I., Zakharova N.V., Popkov V.I. Synthesis and Visible-Light Photocatalytic Activity of Graphite-like Carbon Nitride Nanopowders. *Russ. J. Appl. Chem.*, 2020, **93**, P. 494–501.

[18] Chebanenko M.I., Zakharova N.V., Lobinsky A.A., Popkov V.I. Ultrasonic-Assisted Exfoliation of Graphitic Carbon Nitride and Its Electrocatalytic Performance in Process of Ethanol Reforming. *Semiconductors*, 2019, **53**, P. 2072–2077.

[19] Bokuniaeva A.O., Vorokh A.S. Estimation of Particle Size Using the Debye Equation and the Scherrer Formula for Polyphasic TiO_2 Powder. *J. Phys. Conf. Ser.*, 2019, **1410**, 012057.

[20] Qu D., Liu J., Miao X., Han M., Zhang H., Cui Z., Sun S., Kang Z., Fan H., Sun Z. Peering into Water Splitting Mechanism of g-C_3N_4-Carbon Dots Metal-Free Photocatalyst. *Appl. Catal. B Environ.*, 2018, **227**, P. 418–424.

[21] Fina F., Callear S.K., Carins G.M., Irvine J.T.S. Structural Investigation of Graphitic Carbon Nitride via XRD and Neutron Diffraction. *Chem. Mater.*, 2015, **27**, P. 2612–2618.

[22] Azizi-Toupkanloo H., Karimi-Nazarabad M., Shakeri M., Eftekhari M. Photocatalytic Mineralization of Hard-Degradable Morphine by Visible Light-Driven Ag@g-C_3N_4 Nanostructures. *Environ. Sci. Pollut. Res.*, 2019, **26**, P. 30941–30953.

[23] Zhu B., Zhang L., Cheng B., Yu J. First-Principle Calculation Study of Tri-s-Triazine-Based g-C_3N_4: A Review. *Appl. Catal. B Environ.*, 2018, **224**, P. 983–999.

Submitted 22 October 2023; revised 30 October 2023; accepted 31 October 2023

Information about the authors:

Maria I. Chebanenko – Ioffe Institute, Politechnicheskaya, 26, St. Petersburg, 194021, Russia; ORCID 0000-0002-1461-579X; m_chebanenko@list.ru

Lev A. Lebedev – Ioffe Institute, Politechnicheskaya, 26, St. Petersburg, 194021, Russia; ORCID 0000-0001-9449-9487; 1595lion@gmail.com

Maksim I. Tenevich – Ioffe Institute, Politechnicheskaya, 26, St. Petersburg, 194021, Russia; ORCID 0000-0003-2003-0672; chwm420@gmail.com

Ekaterina Yu. Stovpiaga – Ioffe Institute, Politechnicheskaya, 26, St. Petersburg, 194021, Russia; ORCID 0000-0003-0434-5252; kattrof@gvg.ioffe.ru

Vadim I. Popkov – Ioffe Institute, Politechnicheskaya, 26, St. Petersburg, 194021, Russia; ORCID 0000-0002-8450-4278; vadim.i.popkov@mail.ioffe.ru

Conflict of interest: the authors declare no conflict of interest.

NANOSYSTEMS:
PHYSICS, CHEMISTRY, MATHEMATICS

Original article

Potapenko K.O., Kozlova E.A. *Nanosystems: Phys. Chem. Math.*, 2023, **14** (6), 713–718.
http://nanojournal.ifmo.ru
DOI 10.17586/2220-8054-2023-14-6-713-718

Effect of triethanolamine and sodium hydroxide concentration on the activity of Pt/g-C_3N_4 catalyst in the reaction of photocatalytic hydrogen evolution under visible light irradiation

Ksenia O. Potapenko[a], Ekaterina A. Kozlova[b]

Boreskov Institute of Catalysis, SB RAS, Novosibirsk, 630090, Russia

[a]potapenko@catalysis.ru, [b]kozlova@catalysis.ru

Corresponding author: Ksenia O. Potapenko, kozlova@catalysis.ru

PACS 82.65.+r, 68.43.-h

ABSTRACT In this work, the dependences of the rate of photocatalytic hydrogen evolution under visible light irradiation on the concentration of triethanolamine and sodium hydroxide for 0.1 wt.% Pt/g-C_3N_4 photocatalyst were studied. The kinetic dependences of the reaction rate versus substrate initial concentration described by the Langmuir–Hinshelwood monomolecular model. Optimal initial conditions for highly efficient hydrogen evolution have been studied. It is shown that under such conditions the catalyst is a stable material in long-term experiments. The maximum rate of hydrogen evolution was 7.2 mmol·$g^{-1}h^{-1}$.

KEYWORDS photocatalysis, hydrogen evolution, carbon nitride, triethanolamine, visible light

ACKNOWLEDGEMENTS This work was supported by the Russian Science Foundation, project No. 21-13-00314. Authors thanks to Dr. D. B. Vasilchenko for the photocatalyst synthesis.

FOR CITATION Potapenko K.O., Kozlova E.A. Effect of triethanolamine and sodium hydroxide concentration on the activity of Pt/g-C_3N_4 catalyst in the reaction of photocatalytic hydrogen evolution under visible light irradiation. *Nanosystems: Phys. Chem. Math.*, 2023, **14** (6), 713–718.

1. Introduction

With annual population growth, there is a sharp increase in energy demand. However, the world energy industry is based on fossil raw materials [1]. At the same time, oil and coal combustion products (CO_2, SO_x, and NO_x) cause serious damage to the environment, animals and people [2]. Therefore, the issue of decarbonization of the economy and the search for new environmentally friendly energy sources is becoming acute [3]. Hydrogen is considered as a promising alternative energy source because of its high energy density, zero pollution, etc [4–6] The only method of hydrogen production from renewable energy sources is photocatalytic splitting of water. In this case, the hydrogen produced acts as an energy carrier [1].

Photocatalysts based on graphitic carbon nitrate g-C_3N_4 have attracted attention because of their chemical and thermal stability [7–9]. Also the position of the valence band (VB) and conduction band (CB) corresponds to the thermodynamic conditions of water splitting with the formation of hydrogen and oxygen [10–12]. However, a considerable disadvantage of g-C_3N_4 is, firstly, the low specific surface area, and secondly, the rapid recombination of photogenerated electrons and holes, which significantly reduces the activity of photocatalysts [13, 14]. To increase the efficiency of photocatalytic hydrogen evolution, electron donors, so-called "sacrificial agents", are added to the solution. Electron donors are oxidized by photogenerated holes in the valence band of g-C_3N_4, which avoids recombination of electrons and holes, and hence spatial charge separation occurs. Further, photoexcited electrons from the conduction band of g-C_3N_4 participate in the process of water reduction with the formation of hydrogen. Typically, the sacrificial agents for g-C_3N_4-based catalysts are methanol, ethanol and triethanolamine [15]. However, methanol is decarbonylated at room temperature during the reaction and carbon dioxide is adsorbed on the catalyst surface, so, self-poisoning of the catalyst occurs. In the case of titanium dioxide, surface purification by highly electrophilic forms of oxygen (holes) is possible. Thus, the use of methanol is inefficient for g-C_3N_4-based catalysts due to the lack of surface active oxygen [16]. The use of triethnolamine is of great interest, firstly, because the adsorbed TEOA molecules on the surface of the photocatalyst protect it from photocorrosion and degradation of the p-conjugated graphite-likecarbon nitride structure [17]. Secondly, photocatalytic hydrogen evolution results in the oxidation of TEOA, which is attractive in terms of its carcinogenic nature in the pristine state [16]. Thus, it is possible to combine hydrogen evolution with the destruction of TEOA structure during photocatalytic process.

For efficient photocatalytic process, it is necessary to study the influence of reaction conditions on the activity of the catalyst in the target process. The acidity of the medium is known to have a complex effect on the reaction rate due to changes in the state of the catalyst surface, redox potential H^+/H_2 [18, 19]. The aqueous solution of triethanolamine

exhibits weak basic properties. When alkali is added to the reaction suspension, deprotonation of TEOA occurs, which leads to an increase in the pH of the solution. In terms of zeta potential, g-C_3N_4 has zero surface in the pH range of 4.4 – 5.1 [20]. Consequently, the pH of the reaction suspension plays a significant influence on the adsorption-desorption properties on the surface of g-C_3N_4, because at alkaline pH, the surface of carbon nitride is negatively charged, while at acidic pH, on the contrary, it is positively charged.

Previously, our group suggested a new method for the synthesis of graphitic carbon nitride. Synthesis of g-C_3N_4 proceeded through the formation of a supramolecular complex melamine-cyanuric acid between melamine and cyanuric acid, which was further calcined at 550 °C for 1 hour [21, 22]. According to X-ray phase analysis data, the coherent scattering region, which characterizes the average crystallite size, is 10.1 nm, which confirms the nanoscale of the obtained material [21,22]. Due to the branched network of pores in the obtained material, easy access of reagents to the co-catalyst is provided. A method of platinum deposition on the surface of the catalyst from labile Pt(IV) nitrate complexes was also developed, which provides a uniform distribution of platinum ionic particles on graphitic carbon nitride [23,24]. The size of platinum nanoparticles is 1 – 2 nm according to the data of transmission electron microscopy [21,22]. The combination of g-C_3N_4 material preparation and Pt particles deposition methods allowed to achieve high activity in the photocatalytic hydrogen production.

Therefore, the aim of this work was studying the influence of triethanolamine and sodium hydroxide concentration on the activity of the previously proposed catalyst 0.1 wt.% Pt/g-C_3N_4 in the reaction of photocatalytic hydrogen evolution under visible light irradiation. Selection of optimal initial conditions for highly efficient process of photocatalytic hydrogen evolution.

2. Experimental

2.1. Photocatalyst synthesis

2.1.1. Synthesis of g-C_3N_4. Graphitic carbon nitrate g-C_3N_4 was prepared according to the procedure described in [21, 22]. Briefly, a suspension consisting of melamine and cyanuric acid was suspended in water, stirred on a magnetic stirrer for 12 hours, and heated at 90 °C. A supramolecular melamine-cyanuric acid (MCC) complex was obtained. After that, the MCC, was washed with water several times, dried in vacuum, and then calcined at 550 °C for 1 hour (heating rate 1 C/min). The prepared sample of graphite-like carbon nitride is hereinafter denoted by the abbreviation CN.

2.1.2. Synthesis of 0.1 wt.% Pt/g-C_3N_4. Platinum deposition on the surface of g-C_3N_4 was carried out according to the procedure described in detail in [24]. A sample of g-C_3N_4 was suspended in acetone, the required amount of previously prepared platinum precursor $(Me_4N)_2[Pt_2(\mu\text{–}OH)_2(NO_3)_8]$ was added, and stirred for 12 hours. Then the precipitate was washed with acetone several times, dried in an air current. Then the obtained powder was calcined in a hydrogen atmosphere at 500 °C for 1 hour at a heating rate of 10 °C/min. A 0.1 wt.% Pt/g-C_3N_4 catalyst, hereinafter referred to as Pt–CN, was obtained.

2.2. Photocatalytic experiments

The photocatalytic hydrogen evolution experiment was carried out in a horizontally illuminated reactor (Fig. 1). A 50 mL suspension consisting of 25 mg of Pt–CN catalyst, (0 – 70) vol. % triethanolamine (TEOA), and (0 – 5) M NaOH was placed in the reactor. The catalyst was pre-suspended in an ultrasonic bath. The reactor was purged with argon for 15 minutes to remove the oxygen present in the system. An LED with emission maximum at 430 nm, power 50 mW/cm^2, distance from the quartz window to the suspension 6 cm was used as a radiation source. Gas phase analysis for quantitative determination of the evolved hydrogen was carried out using a gas chromatograph CHROMOS GC-1000 equipped with a thermal conductivity detector with a NaX zeolite column.

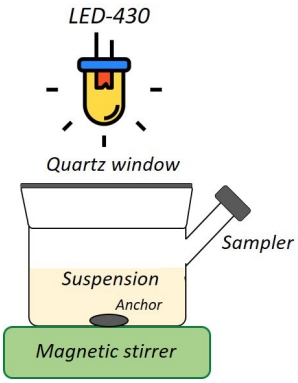

FIG. 1. Schematic representation of the reactor for photocatalytic hydrogen evolution

The apparent quantum efficiency (AQE) was calculated using the following formula:

$$\text{AQE} = \frac{2 \cdot W(\text{H}_2)}{N_f},$$

where $W(\text{H}_2)$ is the rate of photocatalytic hydrogen release (mol/min), N_f is the photon flux.

The photon flux was $3 \cdot 10^{-4}$ mol/min for a 430 nm LED.

3. Results and discussion

3.1. Photocatalytic activity

At the first stage of the work, the effect of TEOA concentration on the activity of Pt–CN in the reaction of photocatalytic hydrogen evolution under visible irradiation (maximum emission of LED 430 nm) was studied. In the absence of electron donor, the rate of hydrogen evolution is low and equals 0.31 mmol·g^{-1}h^{-1}. When TEOA is added to the reaction suspension, there is a sharp increase in the reaction rate, a linear increase is observed up to 30 vol.% TEOA. The reaction rate in this case is 3.92 mmol·g^{-1}h^{-1}. Further, with increasing TEOA concentration, the reaction rate reaches a plateau (Fig. 2a).

The dependence is described by the Langmuir–Hinshelwood model of monomolecular adsorption (Fig. 2b), implying a one-step oxidation of the adsorbed substrate, with hydrogen release occurring via photoreduction of oxygen-containing molecules proceeding in several stages [25]. Therefore, the obtained data were approximated by the Langmuir-Hinshelwood model according to the following equation:

$$W_0 = k\frac{K \cdot C_0}{1 + K \cdot C_0},$$

where W_0 is the initial rate of photocatalytic hydrogen evolution, k is the apparent rate constant of the reaction, K is the adsorption constant of TEOA, C_0 is the initial concentration of triethanolamine.

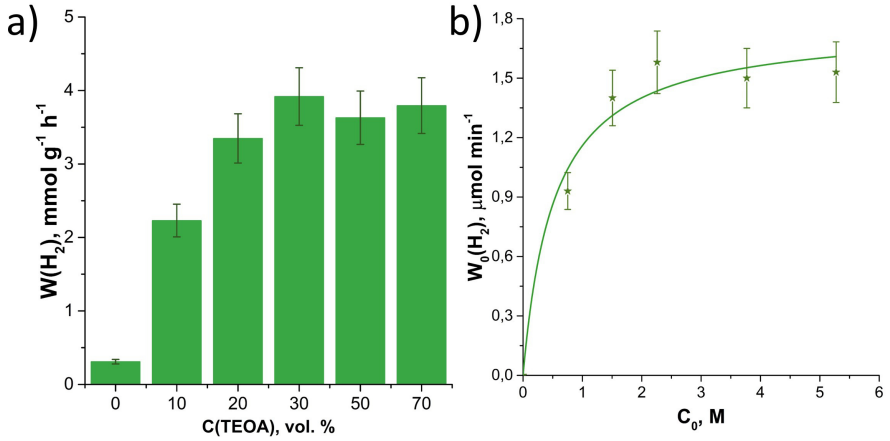

FIG. 2. Dependence of hydrogen evolution rate on TEOA concentration (a) and approximation of experimental data by the Langmuir–Hinshelwood model (b) in the presence of Pt–CN. Experimental conditions: $C(\text{TEOA})$ =0 – 70 vol.%, $m_{cat} = 25$ mg, $V_{susp} = 50$ mL, $\lambda = 430$ nm

Table 1 shows the obtained values of approximation of experimental data using the above model. The coefficient of determination R^2 is 0.97, which shows the high accuracy of the proposed model.

TABLE 1. Values of approximation parameters of experimental data of TEOA adsorption on catalyst Pt–CN

Parameter	Values
k, μmol·min^{-1}	1.8 ± 0.1
K, M^{-1}	1.9 ± 0.7
R^2	0.97

3.2. Influence of pH value

According to the experimental data on determination of the optimum concentration of the sacrificial agent – triethanolamine – the best hydrogen evolution rate was achieved at a volume concentration of 30 vol.% TEOA. Therefore, the influence of pH of the reaction suspension on the activity of the Pt–CN was further studied by adding different amounts of sodium hydroxide to 30 vol.% TEOA. The NaOH concentration value was varied from 0 to 5 mol/L.

The dependence of hydrogen evolution rate on NaOH concentration is presented in Fig. 3. The pH value of the reaction suspension strongly affects the hydrogen evolution. The dissociation constant pKb of TEOA is 6.2, hence, in acidic media, the amino groups of TEOA are protonated, which can deactivate the α-CH bond [26]. When the pH increases, two forms coexist in solution: molecular and deprotonated. The latter is more efficient as a reducing agent [27], reacting efficiently with hydroxyl radicals.

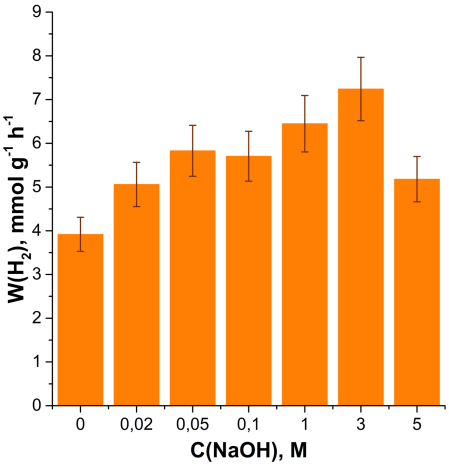

FIG. 3. Dependence of hydrogen evolution rate on NaOH concentration at fixed TEOA concentration in the presence of Pt–CN. Experimental conditions: $C(\text{TEOA}) = 30$ vol.%, $C(\text{NaOH}) = 0.02$ –5 M, $m_{cat} = 25$ mg, $V_{susp} = 50$ mL, $\lambda = 430$ nm

Based on the experimental data (Fig. 3), the addition of NaOH leads to an increase in the reaction rate, which takes place due to the formation of hydroxyl radicals [28]. The photocatalytic reaction involves the oxidation of TEOA, which is characterized by a low oxidative potential of $+0.64$ V vs. SCH. Therefore, from the thermodynamic point of view, the one-electron transfer of the lone nitrogen pair is more favorable [29]. In [30], the authors confirm that the oxidation of TEOA proceeds not by the hydroxyl group but by the lone nitrogen pair. Next, the formation of iminium cation occurs. The iminium cation undergoes hydrolysis to form diethanolamine and glycolaldehyde [29].

In the NaOH concentration range of 0 – 3 M, a linear increase in the reaction rate is observed, reaching a maximum at conditions of 30 vol.% TEOA + 3M NaOH. The hydrogen evolution rate under these conditions is 7.24 mmol·g^{-1}h^{-1}, with an apparent quantum efficiency of 1.9 %. However, further, there is a sharp decrease in the activity of Pt–CN. Probably at high pH the amount of H^+ cations become very small for the subsequent reduction to form hydrogen H_2, which is one of the reasons for the decrease in the reaction rate. The process of photocatalytic hydrogen evolution becomes more difficult. Thus, the optimal conditions for hydrogen evolution are a solution of 30 vol.% TEOA and 3M NaOH.

3.3. Photocatalytic stability

One of the important characteristics of the photocatalyst is not only the activity of the material in the target process, but also its stability in long-term experiments and the possibility of reuse, which is attractive from the practical point of view. Therefore, cyclic experiments were carried out to study the stability of Pt–CN. According to the results on determining the optimal composition of the electron donor solution, the following systems were used: a) 30 vol.% TEOA; b) 30 vol.% TEOA + 3M NaOH. The number of runs was 4, after each run the reactor was purged with argon to remove hydrogen and oxygen.

As shown in Fig. 4(a,b), in the absence of NaOH, the activity of the Pt–CN photocatalyst does not decrease significantly after four runs, indicating that the catalyst exhibits high stability. However, when 3M NaOH is added, the hydrogen evolution rate decreases almost twofold after the first run. In the case of runs in 3M NaOH medium, a decrease in the hydrogen evolution rate by almost 2.5 times is observed already after the second run. After the fourth run, the hydrogen evolution rate was 1.39 mmol·g^{-1}h^{-1}. Thus, a fourfold decrease in activity was observed. Probably, carbonization of the Pt–CN catalyst surface occurs in alkaline medium [21].

Thus, the optimum conditions for hydrogen evolution on Pt–CN is 30 vol.% TEOA, since the addition of NaOH results in catalyst deactivation.

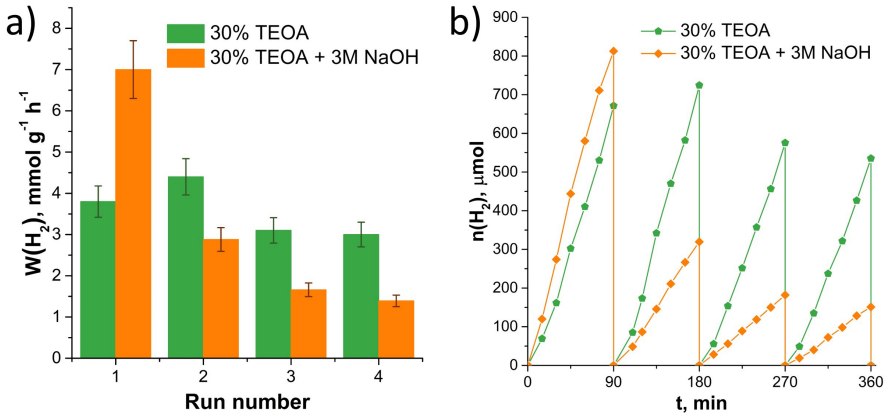

FIG. 4. Dependence of hydrogen evolution rate on the reaction cycle (a) and kinetic curves of hydrogen formation (b) for Pt–CN catalyst. Experimental conditions: $C(\text{TEOA}) = 30$ vol.% / $C(\text{TEOA}) = 30$ vol.% + C(NaOH)=3M, $t_{run} = 90$ min, $m_{cat} = 25$ mg, $V_{susp} = 50$ mL, $\lambda = 430$ nm

4. Conclusion

In this work, the dependences of the rate of photocatalytic hydrogen evolution under the visible light irradiation (wavelength 430 nm) on the concentration of TEOA and NaOH in the presence of 0.1 wt.% Pt/g-C_3N_4 catalyst were obtained. The kinetic dependences of hydrogen evolution rate on TEOA concentration were approximated by Langmuir–Hinshelwood model with high accuracy, the optimum electron donor concentration was found, which was 30 vol.% TEOA. In alkaline medium, a linear increase in rate was observed with increasing NaOH concentration, the maximum activity was observed at 30 vol.% TEOA + 3M NaOH and was 7.24 mmol·g^{-1}h^{-1}, AQE = 2.1 %. The obtained reaction rate is currently very high for the photocatalytic hydrogen evolution process in the presence of a catalyst with such a low platinum content of 0.1 wt.% Pt/g-C_3N_4. The stability of 0.1 wt.% Pt/g-C_3N_4 catalyst was studied in long-term photocatalytic hydrogen evolution experiments. The catalyst is shown to be a stable material in the absence of sodium hydroxide. On the contrary, upon addition of alkali, a decrease in activity by a factor of almost 5 is observed, which is associated with carbonization of the 0.1 wt.% Pt/g-C_3N_4 surface.

References

[1] Zhu Q., Xu Z., Qiu B., Xing M., Zhang J. Emerging Cocatalysts on G-C_3N_4 for Photocatalytic Hydrogen Evolution. *Small*, 2021, **17**, 2101070.
[2] Bairrao D., Soares J., Almeida J., Franco J.F., Vale Z., Jiang B., Xie H., Zhou H., Wang K., Xin K., et al. Green Hydrogen and Energy Transition: Current State and Prospects in Portugal. *Energies*, 2023, **16**, 551.
[3] Lee C.C., Wang F., Lou R., Wang K. How Does Green Finance Drive the Decarbonization of the Economy? Empirical Evidence from China. *Renew. Energy*, 2023, **204**, P. 671–684.
[4] Singla M.K., Nijhawan P., Oberoi A.S. Hydrogen Fuel and Fuel Cell Technology for Cleaner Future: A Review. *Environ. Sci. Pollut. Res.*, 2021, **28**, P. 15607–15626.
[5] Preethi V., Kanmani S. Photocatalytic Hydrogen Production. *Mater. Sci. Semicond. Process.*, 2013, **16**, P. 561–575.
[6] Sharma R., Almáši M., Nehra S.P., Rao V.S., Panchal P., Paul D.R., Jain I.P., Sharma A. Photocatalytic Hydrogen Production Using Graphitic Carbon Nitride (GCN): A Precise Review. *Renew. Sustain. Energy Rev.*, 2022, **168**, 112776.
[7] Wang X., Maeda K., Thomas A., Takanabe K., Xin G., Carlsson J.M., Domen K., Antonietti M. A Metal-Free Polymeric Photocatalyst for Hydrogen Production from Water under Visible Light. *Nat. Mater.*, 2008, **8**, P. 76–80.
[8] Fan Z., Guo X., Jin Z., Li X., Li Y. Bridging Effect of S-C Bond for Boosting Electron Transfer over Cubic Hollow CoS/g-C_3N_4 Heterojunction toward Photocatalytic Hydrogen Production. *Langmuir*, 2022, **38**, P. 3244–3256.
[9] Liu X., Zhang Q., Cui Z., Ma F., Guo Y., Wang Z., Liu Y., Zheng Z., Cheng H., Dai Y., et al. Morphology and Defects Design in G-C_3N_4 for Efficient and Simultaneous Visible-Light Photocatalytic Hydrogen Production and Selective Oxidation of Benzyl Alcohol. *Int. J. Hydrogen Energy*, 2022, **47**, P. 18738–18747.
[10] Maeda K., Wang X., Nishihara Y., Lu D., Antonietti M., Domen K. Photocatalytic Activities of Graphitic Carbon Nitride Powder for Water Reduction and Oxidation under Visible Light. *J. Phys. Chem. C*, 2009, **113**, P. 4940–4947.
[11] Cao S., Low J., Yu J., Jaroniec M. Polymeric Photocatalysts Based on Graphitic Carbon Nitride. *Adv. Mater.*, 2015, **27**, P. 2150–2176.
[12] Wen J., Xie J., Chen X., Li X. A Review on G-C_3N_4-Based Photocatalysts. *Appl. Surf. Sci.*, 2017, **391**, P. 72–123.
[13] Zhurenok A.V., Vasilchenko D.B., Kozlova E.A. Comprehensive Review on G-C_3N_4-Based Photocatalysts for the Photocatalytic Hydrogen Production under Visible Light. *Int. J. Mol. Sci.*, 2022, **24**, 346.
[14] Cao S., Yu J. G-C_3N_4-Based Photocatalysts for Hydrogen Generation. *J. Phys. Chem. Lett.*, 2014, **5** (12), P. 2101-2107.
[15] Liao G., Gong Y., Zhang L., Gao H., Yang G.J., Fang B. Semiconductor Polymeric Graphitic Carbon Nitride Photocatalysts: The "Holy Grail" for the Photocatalytic Hydrogen Evolution Reaction under Visible Light. *Energy Environ. Sci.*, 2019, **12**, P. 2080–2147.
[16] Jones W., Martin D.J., Caravaca A., Beale A.M., Bowker M., Maschmeyer T., Hartley G., Masters A. A Comparison of Photocatalytic Reforming Reactions of Methanol and Triethanolamine with Pd Supported on Titania and Graphitic Carbon Nitride. *Appl. Catal. B Environ.*, 2019, **240**, P. 373–379.
[17] Kumaravel V., Imam M.D., Badreldin A., Chava R.K., Do J.Y., Kang M., Abdel-Wahab A. Photocatalytic Hydrogen Production: Role of Sacrificial Reagents on the Activity of Oxide, Carbon, and Sulfide Catalysts. *Catal.*, 2019, **9**, 276.

[18] Kozlova E.A., Parmon V.N. Heterogeneous Semiconductor Photocatalysts for Hydrogen Production from Aqueous Solutions of Electron Donors. *Russ. Chem. Rev.*, 2017, **86**, P. 870–906.
[19] Li Y., Zhou M., Cheng B., Shao Y. Recent Advances in G-C_3N_4-Based Heterojunction Photocatalysts. *J. Mater. Sci. Technol.*, 2020, **56**, P. 1–17.
[20] Zhu B., Xia P., Ho W., Yu J. Isoelectric Point and Adsorption Activity of Porous G-C_3N_4. *Appl. Surf. Sci.*, 2015, **344**, P. 188–195.
[21] Vasilchenko D., Zhurenok A., Saraev A., Gerasimov E., Cherepanova S., Tkachev S., Plusnin P., Kozlova E. Highly Efficient Hydrogen Production under Visible Light over G-C_3N_4-Based Photocatalysts with Low Platinum Content. *Chem. Eng. J.*, 2022, **445**, 136721.
[22] Vasilchenko D., Tkachenko P., Tkachev S., Popovetskiy P., Komarov V., Asanova T., Asanov I., Filatov E., Maximovskiy E., Gerasimov E., et al. Sulfuric Acid Solutions of $[Pt(OH)_4(H_2O)_2]$: A Platinum Speciation Survey and Hydrated Pt(IV) Oxide Formation for Practical Use. *Inorg. Chem.*, 2022, **61**, P. 9667–9684.
[23] Vasilchenko D., Topchiyan P., Tsygankova A., Asanova T., Kolesov B., Bukhtiyarov A., Kurenkova A., Kozlova E. Photoinduced Deposition of Platinum from $(Bu_4N)_2[Pt(NO_3)_6]$ for a Low Pt-Loading Pt/TiO_2 Hydrogen Photogeneration Catalyst. *ACS Appl. Mater. Interfaces*, 2020, **12**, P. 48631–48641.
[24] Vasilchenko D., Topchiyan P., Berdyugin S., Filatov E., Tkachev S., Baidina I., Komarov V., Slavinskaya E., Stadnichenko A., Gerasimov E. Tetraalkylammonium Salts of Platinum Nitrato Complexes: Isolation, Structure, and Relevance to the Preparation of PtO_x/CeO_2 Catalysts for Lowerature CO Oxidation. *Inorg. Chem.*, 2019, **58**, P. 6075–6087.
[25] Kurenkova A.Y., Kozlova E.A., Kaichev V.V. The Influence of Reaction Conditions on the Rate of Hydrogen Evolution in Aqueous Solutions of Glycerol over Pt/TiO_2 Photocatalysts. *Kinet. Catal.*, 2021, **62**, P. 62–67.
[26] Li Y., Zhang K., Peng S., Lu G., Li S. Photocatalytic Hydrogen Generation in the Presence of Ethanolamines over Pt/$ZnIn_2S_4$ under Visible Light Irradiation. *J. Mol. Catal. A Chem.*, 2012, **363–364**, P. 354–361.
[27] Chowdhury P., Gomaa H., Ray A.K. Sacrificial Hydrogen Generation from Aqueous Triethanolamine with Eosin Y-Sensitized Pt/TiO_2 Photocatalyst in UV, Visible and Solar Light Irradiation. *Chemosphere*, 2015, **121**, P. 54–61.
[28] Markovskaya D.V., Kozlova E.A. Formal Kinetic Description of Photocatalytic Hydrogen Evolution from Ethanol Aqueous Solutions in the Presence of Sodium Hydroxide. *Kinet. Catal.*, 2018, **59**, P. 727–734.
[29] Savateev O., Zou Y. Identification of the Structure of Triethanolamine Oxygenation Products in Carbon Nitride Photocatalysis. *Chemistry Open*, 2022, **11**, e202200095.
[30] Ghosh T., Das A., König B. Photocatalytic N-Formylation of Amines via a Reductive Quenching Cycle in the Presence of Air. *Org. Biomol. Chem.*, 2017, **15**, P. 2536–2540.

Submitted 02 November 2023; revised 10 November 2023; accepted 11 November 2023

Information about the authors:

Ksenia O. Potapenko – Boreskov Institute of Catalysis, SB RAS, Novosibirsk, 630090, Russia; ORCID 0000-0002-7868-3409; potapenko@catalysis.ru

Ekaterina A. Kozlova – Boreskov Institute of Catalysis, SB RAS, Novosibirsk, 630090, Russia; ORCID 0000-0001-8944-7666; kozlova@catalysis.ru

Conflict of interest: the authors declare no conflict of interest.

NANOSYSTEMS:
PHYSICS, CHEMISTRY, MATHEMATICS

Original article

Kruchinin N.Yu. *Nanosystems: Phys. Chem. Math.*, 2023, **14** (6), 719–728.
http://nanojournal.ifmo.ru
DOI 10.17586/2220-8054-2023-14-6-719-728

Molecular dynamics simulation of the rearrangement of polyampholyte conformations on the surface of a charged oblate metal nanospheroid in a microwave electric field

Nikita Yu. Kruchinin[1,a]

[1]Orenburg State University, Center of Laser and Informational Biophysics, Orenburg, Russia

[a]kruchinin_56@mail.ru

PACS 36.20.-r, 02.70.Ns, 61.46.+w

ABSTRACT Using molecular dynamics, the rearrangement of the conformational structure of polyampholytes on the surface of a gold oblate nanospheroid in an alternating electric field was studied depending on the value of its total charge. On the surface of the nanospheroid, at its high total charge and at small amplitude of the alternating electric field strength vector, polyampholyte loops stretched over the entire surface of the nanospheroid. With an increase in the amplitude of the electric field in the equatorial region of the nanospheroid, an annular polyampholytic fringe was formed, ordered by the types of links depending on the distance to the polarization axis of the nanoparticle. In the case of high simulation temperature, the shape of the annular fringe changed twice over a period: in one case, ordering according to the types of links along the polarization axis of the nanospheroid, and in the other case, perpendicular to it.

KEYWORDS polyampholyte, oblate metallic nanospheroid, conformational changes, adsorption, molecular dynamics

ACKNOWLEDGEMENTS This work was supported by the Ministry of Science and Higher Education of the Russian Federation within the framework of project no. FSGU-2023-0003.

FOR CITATION Kruchinin N.Yu. Molecular dynamics simulation of the rearrangement of polyampholyte conformations on the surface of a charged oblate metal nanospheroid in a microwave electric field. *Nanosystems: Phys. Chem. Math.*, 2023, **14** (6), 719–728.

1. Introduction

Gold nanoparticles that form conjugates with polymer molecules are widely used in the creation and modification of various chemical sensors based on the effects of surface-enhanced Raman scattering, surface plasmon resonance, and F?rster energy transfer between macrochain-bound nanoobjects [1–6]. In addition, such hybrid nanosystems are used for drug delivery, as nanoprobes in biomedicine, and also in other elements of nanoelectronic devices [7–13]. In this case, not only spherical gold nanoparticles can be used, but also ellipsoidal nanoparticles, for example, in the form of elongated and oblate nanospheroids, to obtain nanosystems with adjustable plasmon characteristics [14–17].

One way to control the functional characteristics of such nanosystems is to change the conformational structure of a polyelectrolyte macrochain adsorbed on a nanoparticle under the influence of both an external static electric field and electromagnetic radiation [18–21]. In this case, various functional molecules can be associated with the macrochain, for example, molecules of organic luminophores, as well as small atomic clusters.

In the case of adsorption of polyelectrolyte macromolecules on a charged metal surface, under the influence of electric charges distributed over the metal surface, the conformational structure of the adsorbed macrochain is rearranged. In this case, the conformational changes in the adsorbed polyelectrolyte are affected by the shape of the metal nanoobject and the distribution of the surface density of electric charges on it [22–28]. The conformational structure of a macromolecule adsorbed on a nanoparticle is also significantly affected by the distribution order of charged units in the macrochain. Thus, for generally neutral polyampholyte macromolecules and uniformly charged polyelectrolytes, the character of changes in their conformations during adsorption on the surface of metal nanoparticles charged or polarized in an external electric field is very different [22–28].

When a metal nanoparticle is placed in an external uniform electric field, nonuniformly distributed electric charges are induced on its surface, the surface density of which depends on the shape of the nanoparticle. In this case, the electric field near the surface of the nanoparticle is strongly distorted. The non-uniform distribution of induced electric charges will have a significant effect on the conformational structure of adsorbed polyelectrolytes. For generally neutral polyampholytic polypeptides, as a rule, the extension of macrochain loops along the direction of the induced dipole moment of the metal nanoparticle was observed [22–25].

When a metal nanoparticle is exposed to electromagnetic radiation, the distribution of induced electric charges on the surface of the nanoparticle changes periodically. These temporary changes in the surface charge density lead to a change in the conformational structure of the adsorbed polyelectrolyte macromolecule [29–31]. Previously, conformational changes

in an external alternating electric field of generally neutral polyampholytic polypeptides on the surface of a generally neutral gold nanoparticle of an oblate spheroidal shape were studied [30]. With a periodic change in the polarity of a metal oblate nanospheroid, the links of the polyampholytic macrochain shifted from the poles to the central region and a girdle annular macromolecular fringe was formed, the density and width of which depended on the amplitude of the external polarizing alternating electric field.

A different picture will be observed when a charged metallic oblate nanospheroid with adsorbed polyampholyte is placed in an external alternating electric field. In this case, the electric charges distributed over the surface, due to the presence of a charge in an oblate nanospheroid, will be added to the charges induced by an external electric field. And this will lead to a significant change in the distribution of the surface charge density on the surface of the nanoparticle. Therefore, the conformational structure of a generally neutral polyampholytic macrochain on the surface of a charged oblate nanospheroid in an alternating field will depend on its charge and differ significantly from the previously considered case of a generally neutral oblate nanospheroid [30], as well as from the case of a uniformly charged macrochain [31]. By changing the magnitude and sign of the charge of an oblate metallic nanospheroid, as well as the magnitude of the external alternating electric field, it is possible to control the change in the conformational structure of the adsorbed polyampholyte macrochain.

Thus, the purpose of this work is to study the conformational changes of generally neutral polyampholytic polypeptides on the surface of an oblate charged metal nanospheroid upon changing its polarity at an ultrahigh frequency.

2. Molecular dynamics simulation

Molecular dynamics (MD) simulation of polyampholytic polypeptides on the surface of an oblate spheroidal gold nanoparticle was performed using the NAMD 2.14 software package [32], the model of which was obtained by cutting an ellipsoid of rotation from a gold crystal with major semiaxes 3 nm long and minor semiaxes 1.5 nm long. During the simulation, its atoms remained fixed. Four generally neutral polyampholytic polypeptides have been considered:

1) **P1** polypeptide consisting of 402 amino acid residues with 268 Ala (A) units with evenly distributed 67 Asp units (D, charge $-1e$) and 67 Arg units (R, charge $+1e$) – $(\mathrm{ADA_2RA})_{67}$;

2) **P2** polypeptide consisting of 400 amino acid residues with 320 Ala units with evenly distributed 40 Asp units and 40 Arg units – $(\mathrm{A_2DA_4RA_2})_{40}$;

3) **P3** polypeptide consisting of 400 amino acid residues with 320 Ala units with evenly distributed 20 pairs of Asp units and 20 pairs of Arg units – $(\mathrm{A_4R_2A_8D_2A_4})_{20}$;

4) **P4** polypeptide consisting of 412 amino acid residues with 368 Ala units with evenly distributed 11 pairs of Asp units and 11 pairs of Arg units – $\mathrm{A_8(A_8D_2A_{16}R_2A_8)_{11}A_8}$.

For polypeptides, the CHARMM36 force field was used [33, 34]. The CHARMM all-atom force field is a widely used and well-proven force field for molecular dynamics simulations of proteins, peptides, nucleic acids and lipids. This is a non-reactive force field that includes the following bonded potential energy terms in the potential energy function: valence bonds and angles, torsion angles (dihedrals), impropers, Urey–Bradley, as well as nonbonded potential energy terms: electrostatic Coulombic potential and Lennard–Jones potential. The parameters of the potential energy function terms were determined by fitting an extended set of experimental and ab initio results. The parametrization was based on results for a wide variety of model compounds that represent the protein backbone and the individual side chains. Internal parametrizations (bond length, bond angle, Urey–Bradley, dihedral, and improper dihedral terms) were chosen to reproduce geometries from crystal structures, infrared and Raman spectroscopic data, and ab initio calculations. Interaction parameters (electrostatic and van der Waals terms) were chosen to fit 6–31G* ab initio interaction energies and geometries for water molecules bonded to polar sites of the model compounds and experimental condensed-phase properties such as heats of vaporization and molecular volumes [33, 34].

Noncovalent interactions with a gold nanospheroid were described by the Lennard–Jones potential parameterized in [35], which is widely used in studying the adsorption of molecules on the surface of gold nanoparticles [36–41]. The van der Waals potential was cut off at a distance of 1.2 nm using a smoothing function between 1.0 and 1.2 nm. Electrostatic interactions were calculated directly at a distance of 1.2 nm, and at a larger distance, the particle mesh Ewald (PME) [42] was used with a grid step of 0.11 nm. The entire nanosystem was placed in a cube with 24 nm edges filled with TIP3P water molecules [43]. Although the TIP3P water model is rigid and coarser compared to many other water models, including the flexible model, the CHARMM force field with this type of water model is well balanced, accurate and computationally efficient, and is therefore widely used in calculations for studying conformational changes of macromolecular chains using the molecular dynamics [44–47].

Polypeptide conformations enveloping an oblate spheroidal nanoparticle (Fig. 1a) obtained as a result of MD simulation on the surface of a neutral nanospheroid in the absence of an external electric field were used as starting points [25]. To obtain the starting conformations, MD simulation was carried out at a constant temperature at 900 K, followed by a decrease to 300 K for a polypeptide macromolecule, which was located in the form of a nonequilibrium coil near the surface of a flattened uncharged and unpolarized nanospheroid. The length of the time trajectory reached 15 ns. This made it possible to achieve deeper conformational minima of the macrochain energy, including on a shorter trajectory section.

To control the obtaining of equilibrium conformations, the change in the root mean square distance between polypeptide atoms in different conformations (RMSD) was monitored [25].

The surface of a spheroidal nanoparticle was charged by assigning partial charges to atoms located on its surface [47, 48].The distribution of surface charge density on the surface of an oblate metal spheroid charged with a total charge Q is inhomogeneous [49]:

$$\sigma_Q = \frac{Q}{4\pi a^2 c\sqrt{\frac{x^2+y^2}{a^4}+\frac{z^2}{c^4}}}, \tag{1}$$

Where a is the length of the major semiaxes, and c is the length of the minor semiaxis directed along the axis z, which coincides with the axis of rotation of the spheroid. Gold nanospheroids charged with different total positive charges were considered: $Q_1 \approx 37.5e$, $Q_2 \approx 75e$ and $Q_3 \approx 150e$. At such values of the total charge of an oblate nanospheroid, the atoms that were located on the surface at its poles had partial charges equal to $+0.025e$, $0+0.05e$, and $+0.1e$, respectively, and the partial charges of atoms located at the equator were 2 times greater (1).

The partial charges on the surface of a charged oblate spheroidal nanoparticle were further summed up with partial charges induced by an external electric field. On the surface of an oblate spheroid polarized in an external uniform electric field directed along the axis of rotation, the surface charge density is distributed according to the formula [49]:

$$\sigma_p = \frac{\sigma_{\max} z}{c^2\sqrt{\frac{x^2+y^2}{a^4}+\frac{z^2}{c^4}}}, \tag{2}$$

where $\sigma_{\max} = \dfrac{p_z}{V}$ is the value of the surface charge density at the pole of an oblate polarized spheroid, p_z is the dipole moment of the spheroid, V is the volume of the spheroid.

In the process of modeling, the densities of induced charges periodically changed in time according to the sine law with an oscillation period $T = 2.4$ ns during 4 oscillation periods. The following peak values of the induced dipole moment of a polarized nanospheroid were considered: $p_1 \approx 7.7$ and $p_2 \approx 15.4$ kD. At such values of the dipole moment of an oblate nanospheroid, the atoms on the surface of its positively charged pole had partial charges of $+0.25e$ and $+0.5e$. Each oscillation period was divided into 8 equal time segments of 0.3 ns each, during which the field remained unchanged, and the value of the dipole moment of the nanospheroid on the selected segment was set by averaging it over the entire length of the segment. The dipole moment of the nanoparticle changed in the following sequence, starting from the starting conformation of the polypeptide: $+0.69p$ (mean value in the range of oscillations from $\pi/8$ to $3\pi/8$), $+0.97p$, $+0.69p$, 0, $-0.69p$, $-0.97p$, $-0.69p$ and 0. The MD simulation was performed at constant temperatures of 300 and 900 K (NVT, Berendsen thermostat). During periodic repolarization of a charged oblate nanospheroid, a narrow belt of atoms appeared in its equatorial region, the charge sign of which did not change and they remained positively charged throughout the entire period (1, 2). To compensate for the excess charge of the entire molecular system, chloride ions were added, which were randomly distributed over the entire simulation cell.

Based on the results of MD simulation, the distributions of the linear density of polypeptide atoms along the axis of rotation of the oblate nanospheroid, as well as the radial distributions of the density of polypeptide atoms in the equatorial region of the nanospheroid, were calculated.

3. Results

As a result of MD simulation at a temperature of 300 K of a polyampholyte macrochain on the surface of a neutral oblate metal nanospheroid with a periodic change in time of its polarity at the peak value of the dipole moment p1, the amino acid residues of the polypeptide shifted from the vast subpolar regions of the nanoparticle to its narrow equatorial region (Figs. 1b and 1c) [30]. In this case, polyampholyte units were adsorbed on the surface in the vicinity of the equator, regardless of their type. As the peak value of the dipole moment of an oblate nanospheroid increased during modeling with a periodic change in its polarity, the area of strongly charged subpolar regions of the generally neutral nanoparticle increased and, accordingly, the weakly charged equatorial region narrowed (2). Therefore, the narrowing and swelling of the polyampholytic fringe in the equatorial region of the oblate uncharged nanospheroid occurred with a significant ejection of macrochain loops, as well as desorption of some of the links from the surface [30].

A different picture was observed when modeling polyampholytic polypeptides at a temperature of 300 K on the surface of a charged oblate nanospheroid. With an increase in the total charge of an oblate nanospheroid, the force with which negatively charged polyampholyte units are attracted to a positively charged surface increased. Therefore, when modeling with the peak value of the dipole moment p_1 of the nanospheroid, as its total charge increased, the displacement of links from the subpolar regions to the equatorial region became more and more difficult, and at the maximum considered total charge of the nanospheroid, there was almost no displacement of the macrochain to the equator (Figs. 1d,e). On the surface of a strongly charged oblate nanospheroid, at the end of the simulation, with a periodic change in its polarity with a peak value of the dipole moment p_1, loops were formed over its entire surface from polyampholyte units (Figs. 1d,e) due to the repulsion of like-charged units of the macrochain with respect to the total charge of the nanoparticle.

With an increase in the peak value of the dipole moment of an oblate nanospheroid to p_2, the absolute value of induced electric charges in the subpolar regions of an oblate nanospheroid increased. Therefore, the charged units of

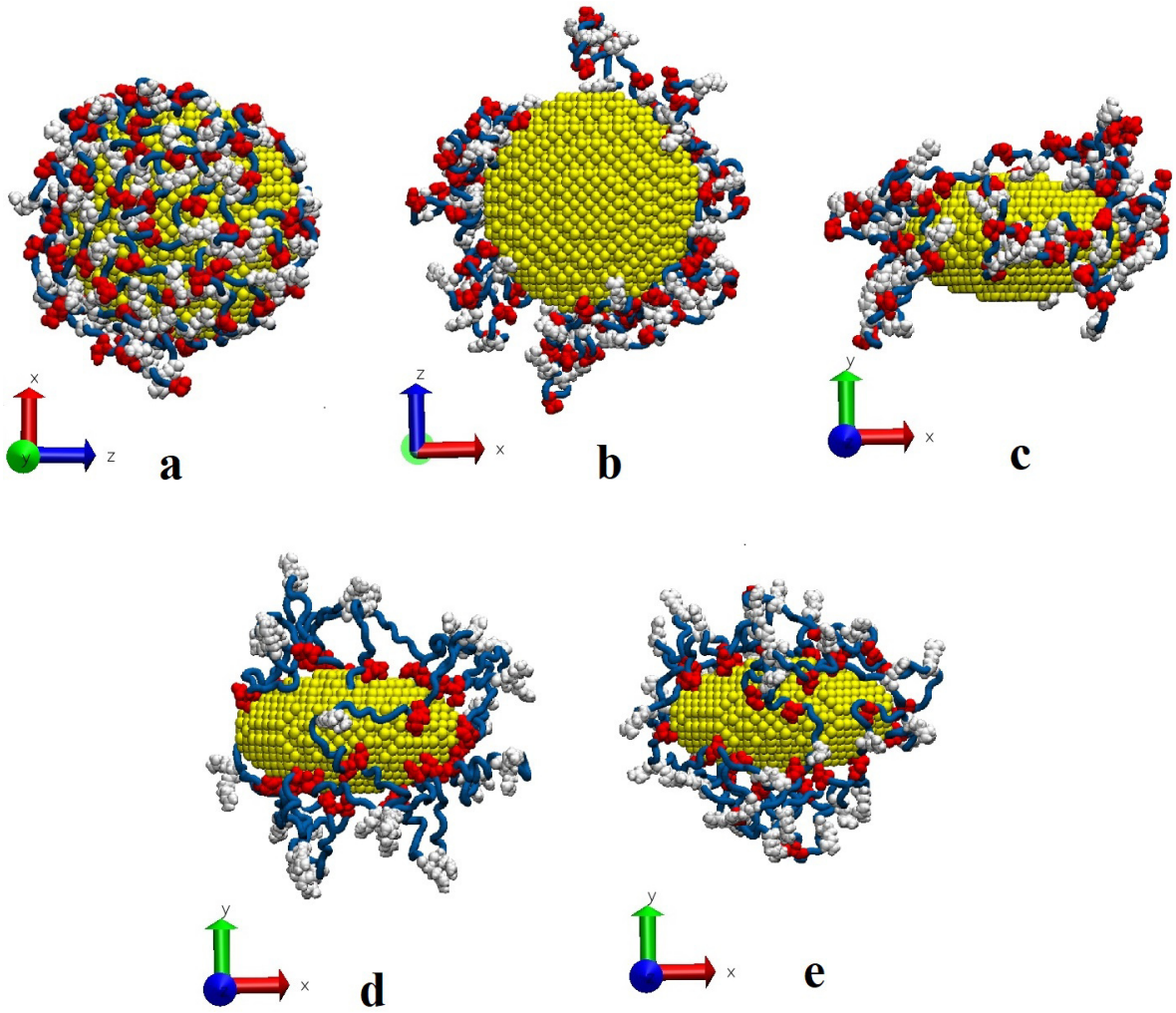

FIG. 1. Starting conformation of polypeptide P1 (a), as well as conformations of polypeptides P1 (b, c), P3 (d) and P2 (e) after MD simulation at a temperature of 300 K with periodic change in polarity on the surface of neutral (b, c) and a charged (d, e) oblate nanospheroid with a total charge Q_3 at the peak value of the dipole moment p_1 (a, b – view along the rotation axis; b, c, d – side view; rotation axis of the nanospheroid and the external electric field are directed along the y axis; blue tube – Ala units, Asp units are shown in red, and Arg units in white)

polyampholyte were pushed out from the similarly charged subpolar regions and gradually, upon repolarization of the oblate nanospheroid, shifted to its equatorial region (Fig. 2), remaining there. This was due to the strong attraction of negatively charged macrochain units to the surface near the equator, in contrast to the case of a neutral oblate spheroidal nanoparticle, where desorption of a large number of macromolecule units was observed [30]. Thus, on the surface of a charged oblate nanospheroid, the ordering of the polyampholytic fringe encircling its edge occurred due to the repulsion of positively charged Arg units from the surface. In this case, the loops of the polyampholyte macrochain were stretched mainly perpendicular to the polarization axis (Fig. 2). It is obvious that when the sign of the total charge of the nanospheroid changes, the order of distribution of concentric layers of charged units of the macrochain in the surrounding annular polyampholytic fringe will change. In this case, on the surface in the equatorial region of the oblate negatively charged nanospheroid there will be a layer of Arg units, and on the periphery, a layer of Asp amino acid residues of the polyampholyte polypeptide.

Figure 3 shows the radial distributions of the atomic density of polyampholytic polypeptides P3 and P1 in the equatorial region of an oblate gold nanospheroid 1 nm wide in the starting conformation (Fig. 3a), as well as at the end of the simulation at a temperature of 300 K with a periodic change in polarity (Fig. 3b,c) of a nanospheroid charged with charge Q_3 at the peak dipole moment p_2. It can be seen that, in the starting conformation (Fig. 3a), regardless of their type, polyampholyte units are concentrated near the surface of the oblate nanospheroid. In cases where a girdle polyampholyte fringe ordered by unit types was formed in the equatorial region of an oblate spheroidal nanoparticle (at full charge Q_3 and at the peak dipole moment p_2 of an oblate nanospheroid (Fig. 2)), characteristic radial distributions of the density of polyampholyte atoms were formed (Fig. 3b,c). In this case, the profile of the radial distribution of the density of atoms

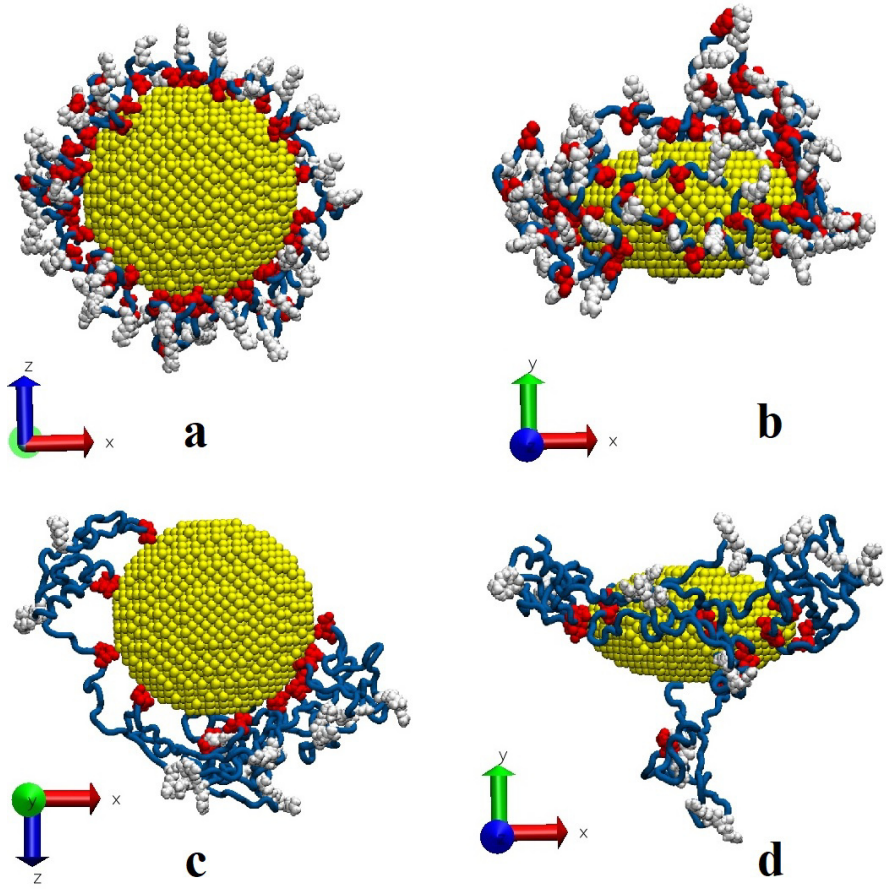

FIG. 2. Conformations of polypeptides P1 (a, b) and P4 (c, d) after MD simulation at a temperature of 300 K with a periodic change in polarity on the surface of an oblate nanospheroid charged with charge Q_3 at the peak value of the dipole moment p_2 (a, c – view along the polarization axis; c, d – side view; rotation axis of the nanospheroid and the external electric field are directed along the y axis, blue tube – Ala units, Asp units are shown in red, and Arg units in white)

over Asp units, which are charged opposite to the narrow charged equatorial belt of atoms on the surface of the nanoparticle, which do not change the sign of the charge during repolarization, was located closest to the axis of rotation of the nanospheroid. As one moves away from the axis of rotation of the nanospheroid, there is a layer of neutral Ala units, which connect the Arg units repelled from the surface located on the periphery. At the same time, the greater the length of the polypeptide fragment of Ala units, which binds oppositely charged units, the more Arg units moved away from the edge of the oblate nanospheroid in the equatorial region and, thus, the diameter of the formed girdle edge in the transverse direction to the polarization axis increased.

Figure 4 shows the distributions of the linear density of atoms of polyampholytic polypeptides along the axis of rotation of an oblate gold nanospheroid. It can be seen that in the starting conformations (Figs. 4a,b, curves 1) at a distance slightly less than 2 nm on both sides of the beginning of the z axis, which coincides with the center of the nanospheroid, two characteristic peaks of the linear density of macrochain atoms are observed, corresponding to the adsorption of macrochain units on vast polar regions of the nanospheroid. In the case of modeling at the peak dipole moment p_1 and total charge Q_3 of an oblate nanospheroid, when macrochain loops were ejected over the entire surface of the nanoparticle (Figs. 1c,d), the profile of the linear distribution of the density of polypeptide atoms significantly broadened (Figs. 4a,b, curves 2), and the peaks of these distributions on both sides of the origin of the z axis were significantly reduced. And at the end of the simulation, at the full charge Q_3 and the peak dipole moment p_2 of the nanospheroid (Figs. 4a,b, curves 3), a single peak was formed on the curves of the linear distribution of the density of polyampholyte atoms at the beginning of the z axis, which corresponds to the shift of the macrochain links to the equatorial region (Fig. 2).

Figure 5 shows the distributions of the linear density of atoms of the polypeptide P3 along the axis of rotation of the oblate nanospheroid at full charge Q_3 and the peak value of the dipole moment p_2 at the last simulation period for all atoms of the polypeptide (Fig. 5a), as well as for the amino acid residues Arg (Fig. 5b) and Asp (Fig. 5c). It can be seen that at the end of the simulation segments at a temperature of 300 K (Fig. 5, curves 1 and 2), when the dipole moment with the maximum value of the nanospheroid is directed in different directions along the rotation axis, the distribution of the linear density of polypeptide atoms (Fig. 5a, curves 1 and 2) are different from each other. This is due to the displacement

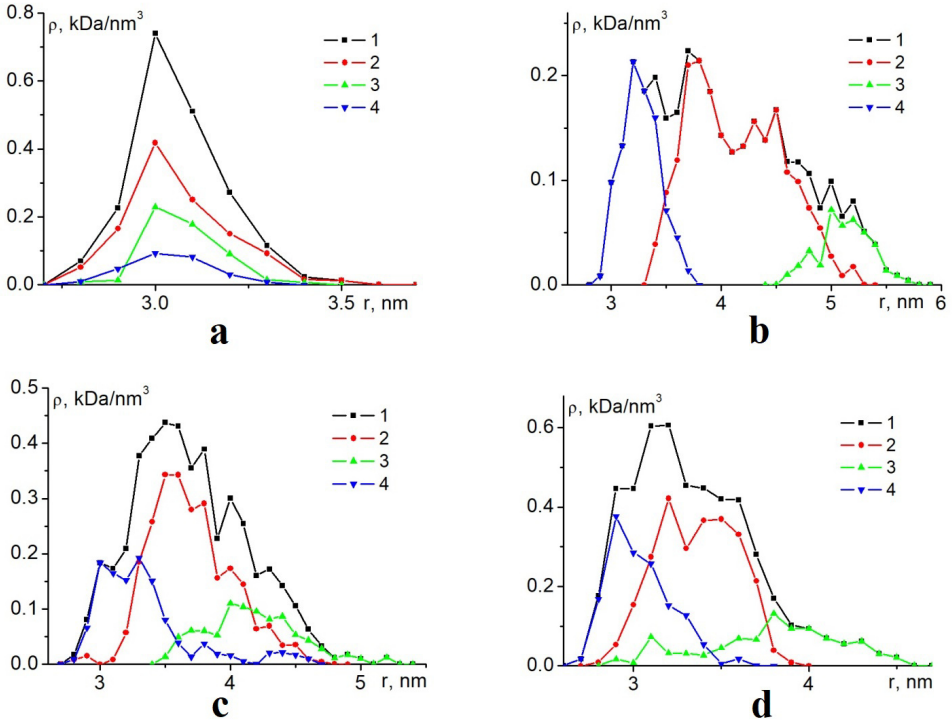

FIG. 3. Radial density distributions of atoms of polypeptides P3 (a, b) and P1 (c, d) in the equatorial region of an oblate gold nanospheroid in the starting conformation (a), as well as at the end of MD simulation at temperatures of 300 K (b, c) and 900 K (d) with a periodic change in the polarity of the nanospheroid charged with charge Q_3 and at the peak dipole moment p_2 (1 – for all atoms of the polypeptide, and 2, 3, and 4 – for amino acid residues Ala, Arg, and Asp)

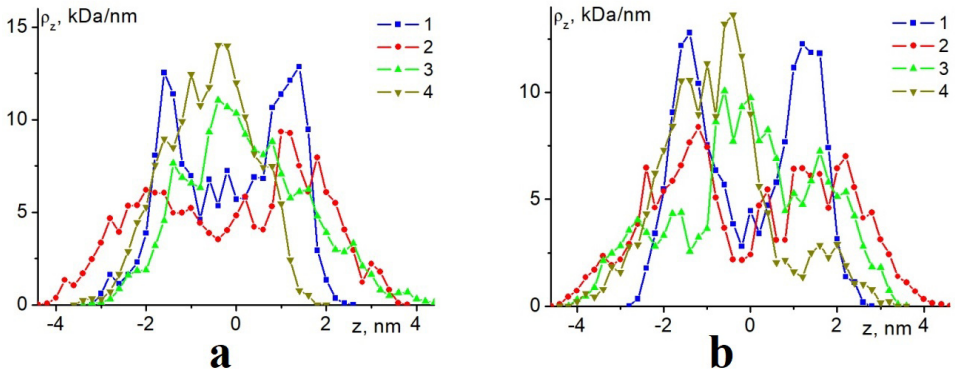

FIG. 4. Linear density distributions of atoms of polypeptides P2 (a) and P3 (b) along the axis of rotation of an oblate gold nanospheroid in the starting conformation (1), as well as at the end of MD simulation at temperatures of 300 K (2, 3) and 900 K (4) s a periodic change in its polarity with a total charge Q_3 at the peak dipole moment p_1 (2) and p_2 (3, 4)

of the charged Arg units (Fig. 5b, curves 1 and 2) from the equatorial region, in contrast to the Asp units, which mostly remained concentrated near the equator (Fig. 5c, curves 1 and 2).

In the MD simulation of polyampholyte polypeptides at a temperature of 900 K on the surface of an oblate gold nanospheroid with a periodic change in its polarity over time, potential barriers that prevent conformational changes in the macrochain were easily overcome, and the conformational structure of the polyampholyte periodically changed following a change in the external electric field. At the end of the simulation segments, when the dipole moment of the nanospheroid was equal to zero, the polyampholyte was concentrated in the narrow equatorial region of the oblate spheroidal nanoparticle (Fig. 6a), as in the simulation with a temperature of 300 K. At the same time, at the maximum considered charge Q_3 of the oblate nanospheroid, as in the simulation with low temperature, the conformational structure of polyampholyte ordered by unit types was formed in the equatorial region (Fig. 6a). For all the considered polypeptides, at the end of the simulation segments, when the dipole moment of the nanospheroid was equal to zero, radial distributions

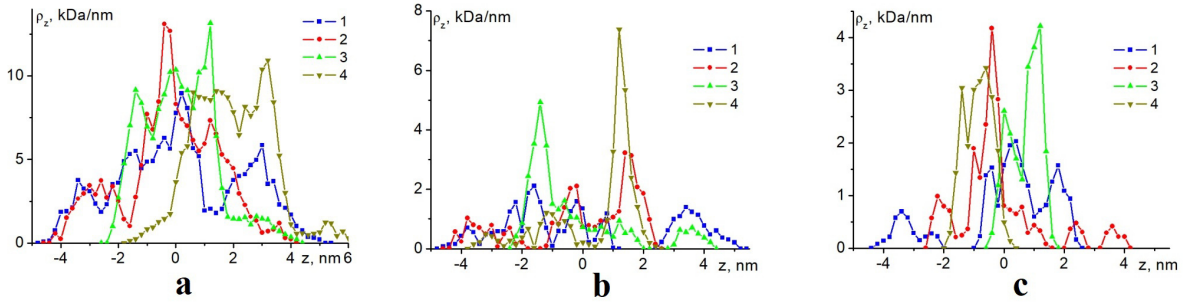

FIG. 5. Linear density distributions of P3 polypeptide atoms along the axis of rotation of an oblate nanospheroid at Q_3 in the last simulation period at temperatures of 300 K (1, 2) and 900 K (3, 4) at the end of time intervals with a peak dipole moment of $+0.97p_2$ (1, 3) and $-0.97p_2$ (2, 4) for all atoms of the polypeptide (a), as well as for the amino acid residues Arg (b) and Asp (c)

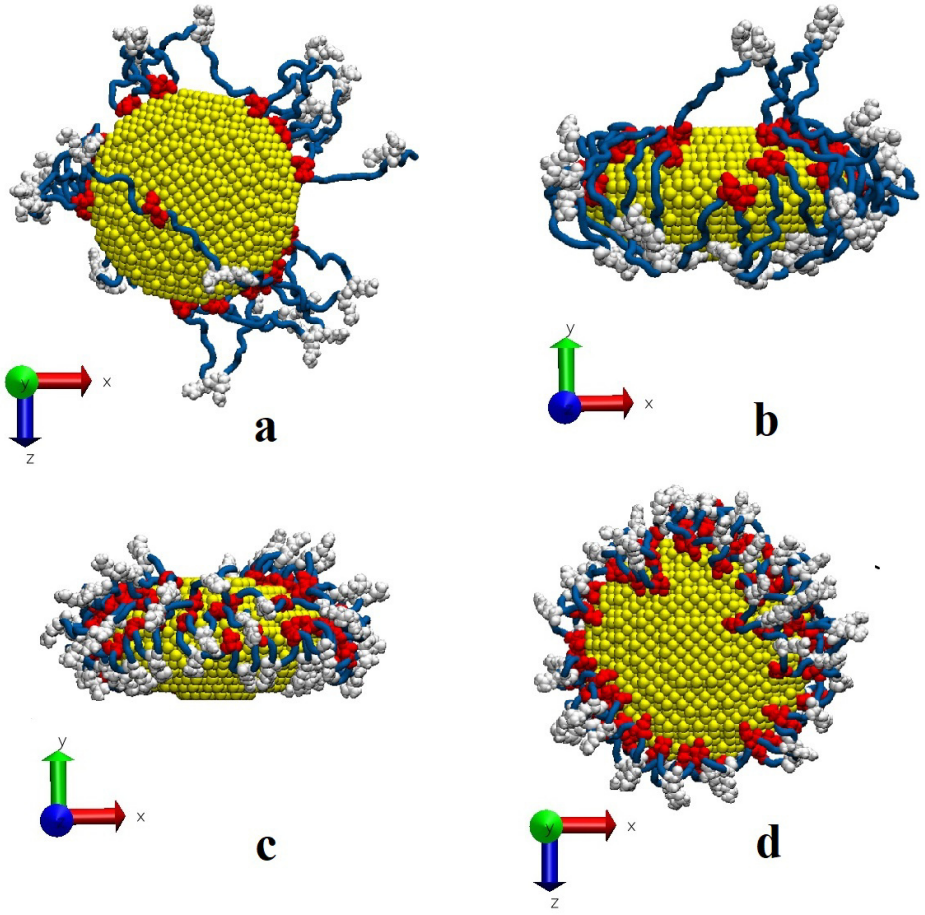

FIG. 6. Conformation of the P3 polypeptide (a) on the surface of an oblate gold nanospheroid at its full charge Q_3 and at the peak dipole moment p_2 at the end of MD simulation with a periodic change in its polarity at a temperature of 900 K (a), as well as the conformations of the P3 polypeptides (b) and P1 (c, d) at the moment of time in the last oscillation period, when the dipole moment has a maximum value (a, d – view along the rotation axis; b, c – side view; rotation axis of the nanospheroid and the external electric field are directed along the y axis; blue tube – Ala units, Asp units are shown in red, and Arg units in white)

of macrochain atomic density similar to those in the case of low temperature were obtained, with differentiation by unit types (Fig. 3d). And on the distributions of the linear density of polypeptide atoms along the axis of rotation of an oblate gold nanospheroid (Fig. 4, curves 4), a peak is observed near the origin of the coordinates of the z axis, which is much higher than in the simulation with a temperature of 300 K. This is due to the fact that at a higher temperature, the macrochain links are more mobile and they are more easily displaced to the equator and concentrated there.

However, at the end of the MD simulation segments at a temperature of 900 K, when the dipole moment of the oblate charged gold nanospheroid was maximal, in contrast to the case of simulation with a low temperature, the charged units of both Arg and Asp were displaced from the equatorial plane to the edge of oppositely charged polar regions (Fig. 6b,c,d). Moreover, upon repolarization of the nanospheroid, the arrangement of the Arg and Asp units of the polypeptide changed in a mirror manner, and the polar regions of the polarized oblate nanospheroid, as a rule, remained free of adsorbed units of the macrochain (Fig. 6d). As can be seen (Figs. 6b,c,d), at the moments of time when the dipole moment of an oblate nanospheroid is maximum, the conformational structure of the polyampholyte has a clear separation according to the types of units along the rotation axis, encircling the nanoparticle. This is reflected in the distribution curves of the linear density of polypeptide atoms along the axis of rotation of the oblate nanospheroid (Fig. 5, curves 3 and 4). It can be seen that the profiles of linear density distributions over all atoms of the polypeptide (Fig. 5a, curves 3 and 4) at a temperature of 900 K are significantly shifted along the rotation axis for different directions of the dipole moment of the nanoparticle, in contrast to the simulation at a temperature of 300 K (Fig. 5a, curves 1 and 2). The shift of the atomic density profiles along the Arg units at a temperature of 900 K (Fig. 5b, curves 3 and 4) is clearer, and the peaks of these curves are much higher than at low temperature (Fig. 5b, curves 1 and 2). At a low simulation temperature, during polarization reversal of a charged oblate nanospheroid, the profiles of oppositely charged Asp units almost did not shift (Fig. 5c, curves 1 and 2), and at a high temperature, their significant shift relative to the equatorial plane is observed (Fig. 5c, curves 3 and 4).

4. Conclusion

On the surface of a charged oblate gold nanospheroid, when modeling at low temperature with a periodic change in time of its polarity along the axis of rotation at low values of its total charge, as well as at a small amplitude of the polarizing electric field near its equator, a polyampholytic ring-shaped fringe, similar to the case of a generally neutral oblate nanospheroid [30]. As the total charge of the oblate nanospheroid increased and at small amplitude of the polarizing electric field, the macrochain loops stretched over the entire surface of the nanospheroid. At high values of the total charge of an oblate nanospheroid and large amplitude of the polarizing electric field in the equatorial region of the nanospheroid, the annular fringe located perpendicular to the axis of rotation of the nanospheroid was ordered according to the types of polyampholyte units. At the equator, on the surface, there were links of the macrochain, which were charged opposite to the total charge of the nanospheroid. When moving away from the axis of rotation, there was a ring-shaped layer of neutral amino acid residues of the polypeptide. Its thickness in the transverse direction with respect to the polarization axis of the nanospheroid was the greater, the greater was the distance between oppositely charged amino acid residues in the polypeptide. The diameter of the formed girdle ring-shaped macromolecular fringe depended on this distance. On the periphery of the ring-shaped fringe, there was a concentric layer of polyampholyte units, similarly charged with respect to the total charge of the nanospheroid.

When modeling polyampholytic polypeptides on the surface of a charged oblate metal nanospheroid with a periodic change in time of its polarity with high temperature at times when its dipole moment was minimal, the formation of a conformational structure of the adsorbed macrochain was observed, similar to the case of modeling at low temperature. In particular, at the maximum considered total charge of the nanospheroid and the maximum considered amplitude of the polarizing field strength vector at the given time instants, an annular edge ordered by the types of links was formed around the equator of the nanoparticle, depending on the distance to the polarization axis. At other times, when the dipole moment of the nanospheroid was maximal, the annular fringe located near the equator changed its shape and became already ordered along the polarization axis. At the same time, during polarization reversal, the arrangement of oppositely charged links of the macrochain changed in a mirror manner with respect to the equatorial plane. That is, the annular polyampholyte edge changes its shape twice during the period: in one case, ordering according to the types of links along the polarization axis, and in the other case, ordering perpendicular to it.

Thus, in the considered nanosystem, the rearrangement of the macromolecular fringe by the action of an external alternating electric field is possible, depending on the charge of the oblate metal nanospheroid. An annular encircling macromolecular shell with a controlled atomic density is formed on the surface of the nanoparticle. The dielectric properties of such a shell significantly change the characteristics of the polarizability of such a “core-layer” hybrid nanosystem, and the possibility of field modulation of the layer geometry makes it possible to consider it as a control factor for the plasmonic properties of the nanosystem. The macrochain may contain photoactive centers that act as a sensor with light indication. In this case, due to the proximity of the glow center to the surface of the plasmonic nanoparticle, its radiation and kinetic characteristics will have a strong dependence on the distance to the surface, which can be changed under the influence of the electric field of the nanoparticle. Therefore, such a rearrangement of the conformational structure of adsorbed polyampholytes by the action of an external alternating electric, taking into account the charge of an oblate

nanospheroid, can be used to create new and modify existing sensors and nanoprobes based on the effects of surface-enhanced Raman scattering or Förster energy transfer between nanoobjects connected by a macrochain, as well as to create sensitive elements of measuring nanoelectronics and nanomaterials.

References

[1] Manikas A.C., Causa F., Moglie R.D., Netti P.A. Tuning gold nanoparticles interfaces by specific peptide interaction for surface enhanced raman spectroscopy (SERS) and separation applications. *ACS Appl. Mater. Interfaces*, 2013, **5**(16), P. 7915–7922.

[2] Miyazaki C.M., Martin C.S., Constantino C.J.L. Gold conjugated-magnetite nanoparticles for magnetic concentration towards reproducibility and repeatability of SERS measurements. *Colloids and Surfaces A: Physicochemical and Engineering Aspects*, 2023, **671**, P. 131661.

[3] Qiu M., Zheng S., Li P., Tang L., Xu Q., Weng S. Detection of 1-OHPyr in human urine using SERS with injection under wet liquid-liquid self-assembled films of β-CD-coated gold nanoparticles and deep learning. *Spectrochimica Acta Part A: Molecular and Biomolecular Spectroscopy*, 2023, **290**, P. 122238.

[4] Zanetti-Polzi L., Charchar P., Yarovsky I., Corni S. Origins of the pH-Responsive photoluminescence of peptide-functionalized Au nanoclusters. *ACS Nano*, 2022, **16**(12), P. 20129–20140.

[5] Pradhan S.P., Swain S., Sa N., Pilla S.N., Behera A., Sahu P.K., Si S.C. Photocatalysis of environmental organic pollutants and antioxidant activity of flavonoid conjugated gold nanoparticles. *Spectrochimica Acta Part A: Molecular and Biomolecular Spectroscopy*, 2022, **282**, P. 121699.

[6] Natarajan P., Sukthankar P., Changstrom J., Holland C.S., Barry S., Hunter W.B., Sorensen C.M., Tomich J.M. Synthesis and characterization of multifunctional branched amphiphilic peptide bilayer conjugated gold nanoparticles. *ACS Omega*, 2018, **3**(9), P. 11071–11083.

[7] Wu T., Chen K., Lai W., Zhou H., Wen X., Chan H.F., Li M., Wang H., Tao Y. Bovine serum albumin-gold nanoclusters protein corona stabilized polystyrene nanoparticles as dual-color fluorescent nanoprobes for breast cancer detection. *Biosensors and Bioelectronics*, 2022, **215**, P. 114575.

[8] Mao M., Xie Z., Ma P., Peng C., Wang Z., Wei X., Liu G. Design and optimizing gold nanoparticle-cDNA nanoprobes for aptamer-based lateral flow assay: Application to rapid detection of acetamiprid. *Biosensors and Bioelectronics*, 2022, **207**, P. 114114.

[9] Li X., Mao X., Xie W., Liu B., Chen F. Intracellular biosynthesis of gold nanoparticles for monitoring microalgal biomass via surface-enhanced raman spectroscopy. *ACS Sustainable Chem. Eng.*, 2022, **10**(15), P. 4872–4880.

[10] Zhang H., Wang Z., Wang F., Zhang Y., Wang H., Liu Y. In situ formation of gold nanoparticles decorated Ti_3C_2 MXenes nanoprobe for highly sensitive electrogenerated chemiluminescence detection of exosomes and their surface proteins. *Anal. Chem.*, 2020, **92**(7), P. 5546–5553.

[11] Zhang Y., Tan J., Zhou L., Shan X., Liu J., Ma Y. Synthesis and application of AS1411-functionalized gold nanoparticles for targeted therapy of gastric cancer. *ACS Omega*, 2020, **5**(48), P. 31227–31233.

[12] Shivashankarappa A., Sanjay K.R., Shah D., Tagat A. Decalepis hamiltonii derived gold nanoparticles and photodynamic cytotoxic evaluation on skin melanoma ($B_{16}F_{10}$) cells as an effective drug delivery vehicle. *Journal of Drug Delivery Science and Technology*, 2022, **76**, P. 103766.

[13] Farhadian N., Kazemi M.S., Baigi F.M., Khalaj M. Molecular dynamics simulation of drug delivery across the cell membrane by applying gold nanoparticle carrier: Flutamide as hydrophobic and glutathione as hydrophilic drugs as the case studies. *Journal of Molecular Graphics and Modelling*, 2022, **116**, P. 108271.

[14] Rajput P., Shishodia M.S. FRET sensing, and field enhancement near spheroidal nanoparticle: Multipole spectral expansion approach. *Optics Communications*, 2022, **519**, P. 128391.

[15] Lermé J., Bonnet C., Lebeault M., Pellarin M., Cottancin E. Surface plasmon resonance damping in spheroidal metal particles: quantum confinement, shape, and polarization dependences. *J. Phys. Chem. C*, 2017, **121**(10), P. 5693–5708.

[16] Pazos-Perez N., de Abajo F.J.G., Fery A., Alvarez-Puebla R.A. From nano to micro: synthesis and optical properties of homogeneous spheroidal gold particles and their superlattices. *Langmuir*, 2012, **28**(24), P. 8909–8914.

[17] Alsawafta M., Wahbeh M., Truong V. Plasmonic modes and optical properties of gold and silver ellipsoidal nanoparticles by the discrete dipole approximation. *Journal of Nanomaterials*, 2012, **2012**, P. 457968.

[18] Gomes B.S., Cantini E., Tommasone S., Gibson J.S., Wang X., Zhu Q., Ma J., McGettrick J.D., Watson T.M., Preece J.A., Kirkman-Brown J.C., Publicover S.J., Mendes P.M. On-demand electrical switching of antibody-antigen binding on surfaces. *ACS Appl. Bio Mater.*, 2018, **1**(3), P. 738–747.

[19] Zhao J., Wang X., Jiang N., Yan T., Kan Z., Mendes P.M., Ma J. Polarization effect and electric potential changes in the stimuli-responsive molecular monolayers under an external electric field. *J. Phys. Chem. C*, 2015, **119**(40), P. 22866–22881.

[20] Cantini E., Wang X., Koelsch P., Preece J.A., Ma J., Mendes P.M. Electrically responsive surfaces: experimental and theoretical investigations. *Acc. Chem. Res.*, 2016, **49**(6), P. 1223–1231.

[21] Ghafari A.M., Domínguez S.E., Järvinen V., Gounani Z., Schmit A., Sjöqvist M., Sahlgren C., Salo-Ahen O.M.H., Kvarnström C., Torsi L., Österbacka R. In situ coupled electrochemical-goniometry as a tool to reveal conformational changes of charged peptides. *Advanced Materials Interfaces*, 2022, **9**, P. 2101480.

[22] Kruchinin N.Yu., Kucherenko M.G. Molecular dynamics simulation of the conformational structure of polyampholyte polypeptides at the surface of a charged gold nanoparticle in external electric field. *Polymer Science Series A*, 2023, **65**(2), P. 224–233.

[23] Kruchinin N.Yu., Kucherenko M.G. Rearrangements in the conformational structure of polyampholytic polypeptides on the surface of a uniformly charged and polarized nanowire: molecular dynamics simulation. *Surfaces and Interfaces*, 2021, **27**, P. 101517.

[24] Kruchinin N.Yu., Kucherenko M.G. Molecular dynamics simulation of conformational rearrangements in polyelectrolyte macromolecules on the surface of a charged or polarized prolate spheroidal metal nanoparticle. *Colloid Journal*, 2021, **83**(5), P. 591–604.

[25] Kruchinin N.Yu., Kucherenko M.G. Statistical and molecular-dynamics simulation of electrically induced changes in the conformational structure of polyampholytes on the surface of a flattened metal nanospheroid. *Colloid Journal*, 2022, **84**(2), P. 169–182.

[26] Kucherenko M.G., Kruchinin N.Yu., Neyasov P.P. Modeling of conformational changes of polyelectrolytes on the surface of a transversely polarized metal nanowire in an external electric field. *Eurasian Physical Technical Journal*, 2022, **19**(2), P. 19–29.

[27] Kruchinin N.Yu., Kucherenko M.G. Molecular dynamics simulation of the conformational structure of uniform polypeptides on the surface of a polarized metal prolate nanospheroid with varying pH. *Russian Journal of Physical Chemistry A*, 2022, **96**(3), P. 624–632.

[28] Kruchinin N.Yu., Kucherenko M.G., Neyasov P.P. Modeling conformational changes in uniformly charged polyelectrolytes on the surface of a polarized metallic oblate nanospheroid. *Russian Journal of Physical Chemistry A*, 2022, **96**(12), P. 2718–2728.

[29] Kruchinin N.Yu., Kucherenko M.G. Modeling the conformational rearrangement of polyampholytes on the surface of a prolate spheroidal metal nanoparticle in alternating electric field. *High Energy Chemistry*, 2021, **55**(6), P. 442–453.

[30] Kruchinin N.Yu., Kucherenko M.G. Conformational changes in polyampholyte macrochains on the surface of an oblate metallic nanospheroid in alternating electric field. *High Energy Chemistry*, 2022, **56**(6), P. 499–510.

[31] Kruchinin N.Yu., Kucherenko M.G. Rearrangements in the conformational structure of polyelectrolytes on the surface of a flattened metal nanospheroid in an alternating electric field. *Colloid Journal*, 2023, **85**(1), P. 44–58.
[32] Phillips J.C., Braun R., Wang W., Gumbart J., Tajkhorshid E., Villa E., Chipot C., Skeel R.D., Kalé L., Schulten K. Scalable molecular dynamics with NAMD. *J Comput Chem.*, 2005, **26**, P. 1781–1802.
[33] MacKerell Jr. A.D., Bashford D., Bellott M., Dunbrack Jr. R.L., Evanseck J.D., Field M.J., Fischer S., Gao J., Guo H., Ha S., Joseph-McCarthy D., Kuchnir L., Kuczera K., Lau F.T.K., Mattos C., Michnick S., Ngo T., Nguyen D.T., Prodhom B., Reiher W.E., Roux B., Schlenkrich M., Smith J.C., Stote R., Straub J., Watanabe M., Wiórkiewicz-Kuczera J., Yin D., Karplus M. All-atom empirical potential for molecular modeling and dynamics studies of proteins. *J. Phys. Chem. B.*, 1998, **102**(18), P. 3586–3616.
[34] Huang J., Rauscher S., Nawrocki G., Ran T., Feig M., de Groot B.L., Grubmüller H., MacKerell Jr. A.D. CHARMM36m: an improved force field for folded and intrinsically dis-ordered proteins. *Nature Methods*, 2016, **14**, P. 71–73.
[35] Heinz H., Vaia R.A., Farmer B.L., Naik R.R. Accurate simulation of surfaces and interfaces of face-centered cubic metals using 12–6 and 9–6 Lennard-Jones potentials. *J. Phys. Chem. C*, 2008, **112**(44), P. 17281–17290.
[36] Jia H., Zhang Y., Zhang C., Ouyang M., Du S. Ligand-ligand-interaction-dominated self-assembly of gold nanoparticles at the oil/water interface: an atomic-scale simulation. *J. Phys. Chem. B*, 2023, **127**(10), P. 2258–2266.
[37] Cappabianca R., De Angelis P., Cardellini A., Chiavazzo E., Asinari P. Assembling biocompatible polymers on gold nanoparticles: toward a rational design of particle shape by molecular dynamics. *ACS Omega*, 2022, **7**(46), P. 42292–42303.
[38] Xiong Q., Lee O., Mirkin C.A., Schatz G. Ethanol-induced condensation and decondensation in DNA-linked nanoparticles: a nucleosome-like model for the condensed state. Journal of the American Chemical Society, 2023, **145**(1), P. 706–716.
[39] Wei X., Harazinska E., Zhao Y., Zhuang Y., Hernandez R. Thermal transport through polymer-linked gold nanoparticles. *The Journal of Physical Chemistry C*, 2022, **126**(43), P. 18511–18519.
[40] Yokoyama K., Thomas J., Ardner W., Kieft M., Neuwirth L.S., Liu W. An approach for in-situ detection of gold colloid aggregates amyloid formations within the hippocampus of the Cohen's Alzheimer's disease rat model by surface enhanced raman scattering methods. *Journal of Neuroscience Methods*, 2023, **393**, P. 109892.
[41] Wang X., Ham S., Zhou W., Qiao R. Adsorption of rhodamine 6G and choline on gold electrodes: a molecular dynamics study. *Nanotechnology*, 2023, **34**, P. 025501.
[42] Darden T., York D., Pedersen L. Particle mesh Ewald: An N·log(N) method for Ewald sums in large systems. *J. Chem. Phys.*, 1993, **98**, P. 10089–10092.
[43] Jorgensen W.L., Chandrasekhar J., Madura J.D., Impey R.W., Klein M.L. Comparison of simple potential functions for simulating liquid water. *J. Chem. Phys.*, 1983, **79**, P. 926–935.
[44] Chen Y., Cruz-Chu E.R., Woodard J.C., Gartia M.R., Schulten K., Liu L. Electrically induced conformational change of peptides on metallic nanosurfaces. *ACS Nano*, 2012, **6**, P. 8847–8856.
[45] Mahinthichaichan P., Tsai C., Payne G.F., Shen J. Polyelectrolyte in electric field: disparate conformational behavior along an aminopolysaccharide chain. *ACS Omega*, 2020, **5**, P. 12016–12026.
[46] Si W., Yu M., Wu G., Chen C., Sha J., Zhang Y., Chen Y. A nanoparticle-DNA assembled nanorobot powered by charge-tunable quad-nanopore system. *ACS Nano*, 2020, **14**, P. 15349–15360.
[47] Shankla M., Aksimentiev A. Conformational transitions and stop-and-go nanopore transport of single-stranded DNA on charged grapheme. *Nature Communications*, 2014, **5**, P. 5171.
[48] Chen P., Zhang Z., Gu N., Ji M. Effect of the surface charge density of nanoparticles on their translocation across pulmonary surfactant monolayer: a molecular dynamics simulation. *Molecular Simulation*, 2018, **44**, P. 85–93.
[49] Landau L.D., Pitaevskii L.P., Lifshitz E.M. *Electrodynamics of Continuous Media*, 2nd Edition, Elsevier Ltd., 1984, 460 p.

Submitted 8 September 2023; revised 30 October 2023; accepted 5 November 2023

Information about the authors:

Nikita Yu. Kruchinin – Orenburg State University, Center of Laser and Informational Biophysics, Orenburg, Russia; ORCID 0000-0002-7960-3482; kruchinin_56@mail.ru

NANO
ФИХМ

NANOSYSTEMS:

PHYSICS, CHEMISTRY, MATHEMATICS

INFORMATION FOR AUTHORS

The journal publishes research articles and reviews, and also short scientific papers (letters) which are unpublished and have not been accepted for publication in other magazines. Articles should be submitted in English. All articles are reviewed, then if necessary come back to the author to completion.

The journal is indexed in Web of Science Core Collection (Emerging Sources Citation Index), Chemical Abstract Service of the American Chemical Society, Zentralblatt MATH and in Russian Scientific Citation Index.

Author should submit the following materials:

1. Article file in English, containing article title, the initials and the surname of the authors, Institute (University), postal address, the electronic address, the summary, keywords, MSC or PACS index, article text, the list of references.
2. Files with illustrations, files with tables.
3. The covering letter in English containing the article information (article name, MSC or PACS index, keywords, the summary, the literature) and about all authors (the surname, names, the full name of places of work, the mailing address with the postal code, contact phone number with a city code, the electronic address).
4. The expert judgement on possibility of publication of the article in open press (for authors from Russia).

Authors can submit a paper and the corresponding files to the following addresses: nanojournal.ifmo@gmail.com, popov1955@gmail.com.

Text requirements

Articles should be prepared with using of text editors MS Word or LaTex (preferable). It is necessary to submit source file (LaTex) and a pdf copy. In the name of files the English alphabet is used. The recommended size of short communications (letters) is 4-6 pages, research articles– 6-15 pages, reviews – 30 pages.

Recommendations for text in MS Word:

Formulas should be written using Math Type. Figures and tables with captions should be inserted in the text. Additionally, authors present separate files for all figures and Word files of tables.

Recommendations for text in LaTex:

Please, use standard LaTex without macros and additional style files. The list of references should be included in the main LaTex file. Source LaTex file of the paper with the corresponding pdf file and files of figures should be submitted.

References in the article text are given in square brackets. The list of references should be prepared in accordance with the following samples:

[1] Surname N. *Book Title*. Nauka Publishing House, Saint Petersburg, 2000, 281 pp.
[2] Surname N., Surname N. Paper title. *Journal Name*, 2010, **1** (5), P. 17-23.
[3] Surname N., Surname N. Lecture title. In: Abstracts/Proceedings of the Conference, Place and Date, 2000, P. 17-23.
[4] Surname N., Surname N. Paper title, 2000, URL: http://books.ifmo.ru/ntv.
[5] Surname N., Surname N. Patent Name. Patent No. 11111, 2010, Bul. No. 33, 5 pp.
[6] Surname N., Surname N. Thesis Title. Thesis for full doctor degree in math. and physics, Saint Petersburg, 2000, 105 pp.

Requirements to illustrations

Illustrations should be submitted as separate black-and-white files. Formats of files – jpeg, eps, tiff.

NANOSYSTEMS:

PHYSICS, CHEMISTRY, MATHEMATICS

Журнал зарегистрирован
Федеральной службой по надзору в сфере связи, информационных технологий и массовых коммуникаций
(свидетельство ПИ № ФС 77 - 49048 от 22.03.2012 г.)
ISSN 2220-8054

Учредитель: федеральное государственное автономное образовательное учреждение высшего образования
«Национальный исследовательский университет ИТМО»

Издатель: федеральное государственное автономное образовательное учреждение высшего образования
«Национальный исследовательский университет ИТМО»

Отпечатано в Учреждении «Университетские телекоммуникации»
Адрес: 197101, Санкт-Петербург, Кронверкский пр., 49

Подписка на журнал НФХМ
На первое полугодие 2024 года подписка осуществляется через
ОАО «АРЗИ», подписной индекс Э57385